

Department of Civil and Environmental Engineering

University of Strathclyde

An experimental investigation into the mechanics of clay erosion

A thesis presented for the Degree of Doctor of Philosophy

By

Raniero Beber

2025

Declaration of authenticity and author's right

This thesis is the result of the author's original research. It has been composed by the author and has not been previously submitted for examination which has led to the award of a degree.

The copyright of this thesis belongs to the author under the terms of the United Kingdom Copyright Acts as qualified by University of Strathclyde Regulation 3.50. Due acknowledgement must always be made of the use of any material contained in, or derived from, this thesis.

Signed: 

Date: 21/02/2025

Abstract

This thesis presents an experimental investigation of the erosion behaviour of clay, both in saturated and unsaturated states and a numerical simulation study to promote the adoption of performance-based design in flood embankments retrofitting.

The erosion detachment mechanism of saturated reconstituted clay have been investigated with a miniaturized jet erosion device (μ -jet) and a imaging system. Direct observation of the detaching unit, identified as 'flake', during erosion has been performed and characterized based on sample preparation. A layered fabric within the samples has been identified as root cause of flake detachment and further investigated based on clay particle physio-chemical interaction. A micro-mechanical interpretation of the observed detaching unit and layered fabric have been put forward.

The unsaturated soil mechanics framework have been used to re-interpret a well known, standard de facto, test to measure soil erosion: the Jet Erosion Test. Different erosion responses at varying compaction water contents and dry densities were detected using a laser scanner. This enabled the measurement of both scour depth and scoured volume. The experimental study also investigated the effect of submergence time. The experimental results have shown that the submerged water jet generates a scour with a relatively complex geometry, made of a step extending over the entire cross-sectional area of the sample and a scour hole localised in the centre of the sample. The depths of both the erosion step and the scour hole evolve with the submersion time in a different fashion depending on the compaction water content. At the same time, the compaction water content generates different rates and mode of penetration of the waterfront that propagates from the surface of the sample once the sample is submerged in water before the Jet Erosion Test starts. The step developing at the top of the sample was modelled successfully by considering the failure of a horizontal infinite layer subjected to the tangential hydrodynamic stresses generated by the impinging jet. The central scour hole was assumed to be generated by a bearing capacity mode of failure triggered by the normal hydrodynamic stresses and modelled accordingly.

The numerical simulation work examines the case of flood embankments in the tidal area of the Elbe River in Germany. These embankments require to be retrofitted by raising their crest from 5m to 7m because of the new projection of extreme river levels due to climate change. The

conventional 'prescriptive' design consisting of raising the embankment by maintaining the 1:3 inclination of the landside slope is compared with the 'performance-based' design where the inclination of the slope on the landside could be potentially increased up to 1:1, which is shown to be sustainable if partial saturation and transient water flow are considered. Raising the flood embankment with 1:1 landside slope (rather than 1:3) could lead to expropriation cost savings of the order of €3.9M/km. For the case of a newly built embankment of 7 m height, the saving would become €4.5M/km. An approximate estimation of embodied carbon suggests that the carbon saving would be of the order of 3,100-4,200tCO_{2e}/km.

***Ai miei genitori,
Rita e Marcello.***

Acknowledgments

I would like to express my special appreciation and thanks to my main supervisor, *Professor Alessandro Tarantino*, for the time, patience and effort you dedicated to me, and to my second supervisor, *Professor Rebecca Lunn*, for your assistance and guidance.

I feel obliged to thank you, *Matteo Pedrotti*, not only for lacing up your running shoes to bag the Scottish Munros with me but, more importantly, for wearing the critical reviewer's hat while discussing experiments.

I would also like to thank the team of technicians for their support in my experimental work, especially *Derek McNee* and *Mara Knapp*.

I would like to thank *Patrick Becker* from Kempfert for tutoring me while in Hamburg.

I am grateful for the funding I received for my PhD from the Department of Civil and Environmental Engineering and the Marie Skłodowska-Curie scholarship within the European Training Network project TERRE.

A special thanks to my *Family* and *Friends* for their unwavering support and understanding.

Finally, I thank everyone who has been part of this journey—for your help, support, kindness, love, and laughter.

Table of Contents

Abstract	5
Acknowledgments.....	8
Chapter I: Introduction	13
1 Research Context and Publications.....	14
2 Aim, Research Questions and Specific Objectives.....	15
RQ1: What is the erosion detachment mechanism in reconstituted clay?	16
RQ2: Is partial saturation controlling the results of JET erosion test performed in compacted clay?.....	16
RQ3: Does unsaturated soil mechanics-based design help minimize the material required to upgrade flood embankments?	16
3 Structure of the Thesis	17
Chapter II: Background	19
1 Erosion processes in geotechnical infrastructures	19
2 Erosion processes in natural environments	22
References.....	25
Chapter III: Experimental investigation into the erosion detachment mechanisms in reconstituted clay	29
1 Introduction.....	299
2 Background	32
3 Materials and methods	34
3.1 Materials	34
3.2 Sample preparation	35
3.3 Micro-jet erosion test device (μ -jet).....	39
3.4 Testing procedure	42
3.5 Image processing	43
4 Results	48
4.1 Detachment mechanism in reconstituted samples at pH ₄	48

4.2	Interplay between detachment mechanism and fabric as induced by different hydraulic, mechanical, and chemical loading.....	53
4.3	Further observations of layered fabric	66
5	Discussion	72
5.1	First detachment shear stress	72
5.2	Considerations about mobilization of clusters/aggregates in clays.....	78
5.3	Layered fabric	79
6	Conclusions.....	84
	References.....	86
	Appendix I: Drag coefficient estimation of the plate detachment.....	89
	Appendix II – Interaction of clay particles in Face-to-Face configuration.....	94

Chapter IV: Effect of Submergence Time on Erosion Mechanisms of Clay in JET Erosion Test 105

1	Introduction.....	105
2	Methods.....	107
2.1	Material and Specimen Preparation.....	105
2.2	Jet erosion test procedure	109
2.3	Scour morphology	109
3	Results	113
3.1	Effect of compaction water content and density.....	113
3.2	Effect of submergence time	115
4	Discussion	120
4.1	Hydro-mechanical characterisation.....	120
4.2	Numerical modelling of hydraulic flow during submersion period.....	122
4.3	Hydrodynamic loading.....	123
4.4	Formation of the erosion step	125
4.5	Formation of the erosion hole.....	127
5	Conclusions.....	128
	References.....	130

Chapter V: Climate Change Adaptation of Elbe River Flood Embankments via Suction-Based Design 133

1	Introduction.....	133
2	Hamburg Flood Defence System.....	135
2.1	Historical floods and upgrade of flood protection infrastructure.....	135
2.2	Embankment typical cross section and geological setting.....	131
2.3	Design storm surge.....	137
3	Methodology.....	137
3.1	Flood embankment cross section.....	138
3.2	Materials.....	138
3.3	Water-flow model.....	141
3.4	Stability analysis model.....	143
4	Results and Discussion.....	144
4.1	Conventional versus suction-based design.....	144
4.2	Sensitivity analysis: effect of the hydraulic conductivity of the klei cover.....	149
4.3	Sensitivity analysis: Rainfall effects.....	150
5	Economic and environmental implications of performance-based design.....	153
5.1	Land expropriation.....	153
5.2	Habitat suppression.....	154
5.3	Embodied carbon savings.....	154
6	Conclusions.....	155
	References.....	157
	Appendix I. Klei Shear Strength Parameters.....	160
	Appendix II. Embodied Carbon for Cobbins Brook Embankment.....	162
	Appendix III – Supplemental Materials.....	164

Chapter VI: Summary and Conclusions..... 169

	Perspective.....	170
--	------------------	-----

Chapter I: Introduction

Cohesive soils are ubiquitous in the world around us and are often essential in creating substrates for life to thrive in. They are needed in smaller percentages for the creation of macro-aggregates in agricultural soils and they dominate within mudflat habitats in coastal areas.

The erosion of cohesive soils represents a fundamental geophysical process with far-reaching implications for both natural systems and human infrastructure. Unlike non-cohesive soils, the complex physicochemical interactions within cohesive materials create unique erosional behaviours that challenge conventional understanding and management approaches. These fine-grained materials, predominantly composed of clay and silt particles, form the base of numerous critical environments and man-made structures worldwide.

In riverine and estuarine ecosystems, cohesive soil erosion governs sediment fluxes that determine channel morphology, water quality, and habitat availability. The detachment and transport of these materials directly influence the fate of nutrients, contaminants, and organic matter throughout watersheds. This is particularly evident in urbanized watersheds where altered hydrological regimes accelerate erosional processes, threatening both ecological integrity and infrastructure stability. The resulting sedimentation in reservoirs and navigation channels necessitates costly dredging operations, while the associated turbidity impacts aquatic ecosystems by reducing light penetration and altering benthic habitats.

Within coastal environments, cohesive soil erosion plays a decisive role in shoreline evolution, especially in regions dominated by fine-grained sediments such as mudflats, salt marshes, and mangrove forests. These environments serve as critical buffers against storm surge and wave action, while simultaneously supporting highly productive ecosystems. The accelerated erosion of these cohesive shorelines, driven by sea level rise and increased storm intensity, threatens both coastal communities and ecosystem services valued in the billions of dollars annually. Furthermore, the mobilization of historically contaminated cohesive sediments in industrial harbours and estuaries presents substantial environmental management challenges, as these materials often serve as repositories for legacy pollutants including heavy metals, persistent organic compounds, and emerging contaminants.

In the context of engineered systems, the erosion of cohesive soils poses significant risks to critical infrastructure including levees, dams, embankments, and foundation systems. The progressive nature of cohesive soil erosion—often beginning with subtle subsurface processes before manifesting in catastrophic failures—necessitates sophisticated monitoring and intervention strategies. Surface erosion affecting levees and earthen dam embankments start small in magnitude but soon lead to dangerous and catastrophic outcomes compromising structural integrity, potentially leading to devastating failures that threaten downstream communities and environments. Motivated by this reason is paramount to address the surface erosion process and progress in its understanding at different scales, from the micro scale involving soil particles to the application scale of engineering infrastructures or the modelling of natural processes at scale.

1 Research Context and Publications

The research performed within this thesis work was part of a larger ecosystem of Institutions and researchers called TERRE. With the aim of ‘*Training Engineers and Researchers to Rethink geotechnical Engineering for a low carbon future*’ the [TERRE](#) project involved academic as well as industry partners and was financed by the Marie Skłodowska-Curie Innovative Training Network (ITN-ETN) under grant agreement ETN-GA-2015-675762. As one of the ESRs I was involved in a secondment year at [Kempfert GmbH](#) in Hamburg, Germany. During the secondment the collaboration with the industry partner, a geotechnical consulting firm, lead to the publication that has been included as chapter five. This work is a first step towards the application of the findings of the previous chapters in the engineering practice.

Publications in this thesis

This dissertation is a compilation thesis and consists of one published article and two manuscripts ready to be submitted.

Beber, R., Tarantino, A. and Becker, P., 2023. Climate change adaptation of Elbe river flood embankments via suction-based design. *International Journal of Geomechanics*, 23(3), p.05023001.

Beber, R., Pedrotti, M. Lunn, R. and Tarantino, A., 2025. Effect of Submergence Time on Erosion Mechanisms of Clay in Jet Erosion Test. *Manuscript to be submitted to Journal of Hydraulic Engineering*.

Beber, R., Tarantino, A., Lunn, R. and Pedrotti, M. 2025. Experimental investigation into the erosion detachment mechanisms in reconstituted clay. *Manuscript to be submitted to Journal of Sedimentary Research or Water Resources Research or Journal of Geophysical Research*.

Other publications and works

During the last year of the PhD, thanks to the successful submission of two experimental proposals, I was given the opportunity to investigate the behaviour of clay aggregates by means of Xrays and Neutron imaging at the [NEXT](#) facility of Institut Laue-Langevin in Grenoble, France. In preparation for such experimentation a Xrays imaging campaign was performed at the Advance Material Research Laboratory ([AMRL](#)) of Strathclyde. These datasets are not featured in the thesis since they require further processing. Below the additional publications and datasets relevant to the topic that were published by the author:

Beber, R., Helfen L., Lenoir N., Migliorelli, M.G., Pedrotti M., Tarantino A. and Tengattini A., 2021. Unveiling Processes at Particle/Aggregate Scale Controlling Hydro-Mechanical Behaviour of Compacted Clays. Institut Laue-Langevin (ILL) doi:10.5291/ILL-DATA.1-05-52

Beber, R., Helfen L., Lenoir N., Martini M., Pedrotti M., Tarantino A. and Tengattini A., 2020. Mechanisms of cracking-induced layering associated with the propagation of a water front in an initially unsaturated clay. Institut Laue-Langevin (ILL) doi:10.5291/ILL-DATA.UGA-116

Beber, R., Becker, P. and Tarantino, A., 2020. Suction as an untapped natural soil reinforcement to reduce embodied carbon in geotechnical structures: the case study of flood embankments in Hamburg area. In *E3S Web of Conferences* (Vol. 205, p. 12001). EDP Sciences.

Beber, R., Tarantino, A., Pedrotti, M. and Lunn, R., 2019. The effect of clay water content in the Jet Erosion Test. In *E3S Web of Conferences* (Vol. 92, p. 02016). EDP Sciences.

Beber, R., Pedrotti, M. and Tarantino A. 2019. Xray micro tomography of compacted clay formation, wetting and drying. University of Strathclyde, to be published on Zenodo

2 Aim, Research Questions and Specific Objectives

The aim of the thesis is to investigate the erosion processes in clay geomaterials in natural sediments and engineered clays at different scales, from the micro-scale of clay particles interaction, to the testing of Representative Element Volumes samples in the Jet Erosion Test, towards the application of this findings at the project scale of a engineering infrastructure such as the flood embankment considered. For natural sediments the attention was paid to the mechanism of first detachment by testing kaolin reconstituted from slurry. For the engineered clay the research focused on the effects of submergence time and compaction on the response of the clay subjected to the impinging jet.

To guide the research, and to fill the gaps in knowledge, three key research questions (**RQ**) were defined. Each of these were broken down into specific objectives (**SO**) as follows:

RQ1: What is the erosion detachment mechanism in reconstituted clay?

SO-1 Setup a miniaturized μ -JET Erosion Test and camera to observe detachment mechanism.

SO-2 Observe detachment mechanism under different at formation conditions.

SO-3 Hypotheses formulation and testing on the observed detachment mechanism/s.

RQ2: Is partial saturation controlling the results of JET erosion test performed in compacted clay?

SO-4 Perform JET Erosion Test on compacted clay samples at different compaction water content and induce different wetting stages.

SO-5 Introduce a new method to measure scour volume and parametrize the scour.

SO-6 Develop a conceptual model for clay erosion in JET test accounting for the effect of submergence time and water content at compaction.

Towards the application of the answers to the previous research questions, with particular focus on the feasibility of applying the insight from RQ2 at scale, a full scale engineering problem has been addressed into upgrading flood embankment, maintaining their resistance to erosion and overflow, by minimizing ecological, economical and carbon costs.

RQ3: Does unsaturated soil mechanics–based design help minimize the material required to upgrade flood embankments?

SO-7 Gather input data for Elbe river flood protection use case design.

SO-8 Perform steady-state hydraulic simulation and slope stability analysis to determine safety factor of the embankment.

SO-9 Introduce transient conditions and unsaturated soil mechanics to determine realistic performances of the embankment.

SO-10 Estimate ecological, carbon and economical saving of performance-based design compare to prescriptive design to increase uptake.

3 Structure of the Thesis

This thesis contains three main research chapters, that are written as individual journal papers.

Chapter 2 set the background context for the research and report the relevant literature attaining to the chapters that follows. The surface erosion processes in natural environment and man made structures are described in detail as well as the latest advances in their understanding via numerical modelling and experimental works.

Chapter 3 look into the mechanism of detachment involved in reconstituted clay. By means of a miniaturized JET device and the coupling with an underwater camera the incipient of motion has been investigated and a new detachment mechanism generated by a mesoscale structure in the samples has been observed. The interpretation of the experimental evidence is performed via subsequent hypothesis testing and implementation of clay micro-mechanics concepts.

Chapter 4 applies the unsaturated soil mechanics and the continuous mechanics framework to interpret the experimental data gathered with a standard de facto instrument used in characterizing the erosion of geomaterial both in the laboratory and the field. The JET erosion test was conducted on clay compacted samples mimicking the compaction process in embankments construction for levees. The sample have been subsequently wetted to mimic the action of flooding water on the erodibility of such samples;

Chapter 5 uses the continuo mechanics framework and the unsaturated soil mechanics relations to analyse the problem of flood embankment retrofitting posed by raising sea level and intense storms. This is performed on the Elbe river flood defence as a case study to promote the spread and adoption of unsaturated soil mechanics design moving from prescriptive design to performance-based design in order to benefit the environment both in terms of carbon and ecological impact as well as economically for the agency that need to uptake climate adaptation measures.

Finally **chapter 6** concludes the key findings of the thesis. This chapter builds on chapter 3 to 5 and merge the findings as well as it answer to the research question presented in the introductory chapter.

Chapter II: Background

The erosion of cohesive soils manifests in two distinct domains, each characterized by unique material properties and erosion mechanisms. In engineered environments, compacted clay soils form the critical components of infrastructure such as dams, levees, and embankments, where erosion processes are governed by the material's artificially enhanced density, controlled moisture content, and engineered layering. The erosion threshold in these compacted materials typically exceeds that of their natural counterparts, yet when this threshold is breached—often through concentrated flow paths or internal seepage—the resulting erosion can progress rapidly, threatening structural integrity through mechanisms such as piping, headcut advancement, or surface degradation.

In stark contrast, the natural realm of riverine channels, estuaries, and coastal zones is dominated by soft, recently deposited mud sediments with high water content, where the cohesive particles exhibit complex flocculation/sedimentation behaviours and biomechanical influences from organic content. These natural deposits typically present lower erosion resistance than engineered clays, mainly due to the difference in density, with their erosion thresholds and rates being highly sensitive to biological activity, seasonal variations, salinity gradients, and consolidation history.

Given the substantial differences in soil/sediment formation between these two domains of cohesive soil erosion a separate background section is hereafter presented for each of them.

1 Erosion processes in geotechnical infrastructures

Compacted soils, the core of geotechnical infrastructures

Earthen geotechnical infrastructure such as dams, levees, and embankments have been built for centuries for flood defence and water resources management purposes. These infrastructures are the most important, due to their extensive volumes, and are built by compacting clayey soil in layers at prescribed water content and density (Romero et al., 2008). Two types of erosion affect these engineering infrastructures: external erosion, where there is overflow on the face of the structure, and internal erosion, associated with mechanisms induced by infiltration flows

within the structure and its foundations. Both, and nearly in the same proportions, are responsible for almost all of the reported earth dam failures (Foster et al., 2000; Richards et al., 2007). The internal erosion mechanisms have been extensively studied over the last twenty years and are so-called concentrated leak erosion, contact erosion or backward piping erosion in its development phase and suffusion (Bonelli, 2012).

On the other hand surface erosion is triggered when overflow occurs and the level of the water body (i.e. river, reservoir, sea) exceeds the embankment crest, then water flows towards the protected land with increasing velocity due to the relatively steep slopes characterizing the downstream side of the embankment. Overflow is the result of the insufficient hydraulic capacity of the defence structure that is typically observed during extreme floods (Zhang et al., 2016). This is made worst and more catastrophic by increasing of extreme weather events by climate change (Michelazzo, 2014).

Importance of transient and unsaturated conditions during embankments lifespan

Under ordinary service conditions these embankments are mostly unsaturated and the transient nature of a overflow changes the boundary conditions temporarily. The importance of partial saturation and transient-state conditions for a realistic assessment of the existing safety conditions of flood embankments is also highlighted by Gragnano et al., 2021 who monitored a river embankment on the river Secchia (northern Italy) for 36 months. In the literature the importance of partial saturation in the analysis of the response of flood embankments is now widely acknowledged (Ngo et al. 2022; Zhang et al. 2021; Vahedifard et al. 2020; Johari et al. 2019; Khalilzad et al. 2015). A more detailed description of the flood embankment behaviour under unsaturated conditions and the implication on levee stability can be found in Beber et al., 2023.

Embankment breach initiation and headcut progression

It is generally assumed that the water flowing along the downstream slope generates hydraulic shear stresses that induce the removal of soil particles (i.e. surface erosion) once a critical soil resistance threshold is exceeded. This is the reason why embankment breaching by overflow is often referred to as overflow/overtopping erosion in the literature. A comprehensive overview of the mechanics of overflow erosion is provided by Powledge et al. 1989. The primary erosion mechanism observed during the overflow of fine-grained embankments is known as headcutting. The headcut is defined as a vertical or nearly vertical drop in elevation of the embankment slope (Hahn et al., 2000). However, little quantitative information is currently available about breach initiation (Mohamed et al., 2002). The understanding of surface erosion on compacted clay considering the unsaturated state and the transient dynamics could

therefore improve the understanding of the underlying mechanism to breach initiation, of particular relevance for flood protection infrastructure design, construction and maintenance as well as for transportation embankments (Johnston et al., 2021).

Surface erosion and erodimeters

Recently Philippe et al., 2024 published a review of the surface erosion in geomaterials. They stressed the importance for the need of a predictive model for soil erodibility and highlighted the gap existing in a unifying framework due to the complexity of the erosion in cohesive materials.

The conceptual framework mostly accepted, currently based on an empirical erosion law, is the one defined by a linear relation between the excess critical shear stress and the erosion kinetic coefficient (Sanford et al., 2001; Walder, 2016; Marot et al., 2011). Even though numerous studies proved the dependence of these two parameters from soil properties (Knapen et al., 2007) and external factors such as fluid conditions and biota (Grabowski et al., 2011) in the current conceptual framework these two parameters are still considered intrinsic soil properties due to the scatter of the data in the literature (Philippe et al., 2024).

Measuring soil erosion parameters is challenging and different erodimeters have been presented in the literature, each with its advantages and limitations, the three most common are reported. The most diffuse for its usability and portability is the JET – Jet Erosion Test (Hanson et al., 2004; Al-Madhhachi et al., 2013; Fox et al., 2022). The HET – Hole Erosion Test has been developed for cohesive soils able to withstand a hole through the sample where erosion is measured (Wan et al., 2004; Benahmed et al., 2012; Fattahi et al., 2017; Xie et al., 2018). The EFA – Erosion Function Apparatus has been standardized and commercialized by a company specialized in construction materials testing equipment, the soil sample to be tested is collected in the field using a Shelby tube and then placed in a circular opening at the bottom of a rectangular tube hydraulic flume (Briaud et al., 2001; Bennabi et al., 2012; Briaud et al., 2017).

The Jet Erosion Test and its interpretation

The Jet Erosion Test (JET) (Hanson et al., 2004; Al-Madhhachi et al., 2013; Fox et al., 2022) is a standard de facto laboratory and in-situ methodology used to quantify the erodibility characteristics of cohesive soils and sediments by measuring their resistance to concentrated hydraulic shear stress. During the test, a submerged impinging jet of water is directed vertically downward onto the soil surface from a fixed height, creating a localized scour hole whose dimensions are measured at regular time intervals. The jet generates a known shear stress distribution at the soil-water interface, with maximum shear stress occurring near the

stagnation point directly beneath the jet centerline. As erosion progresses, the geometry of the developing scour hole is monitored using depth measurements, allowing to calculate the erosion rate as a function of applied shear stress. The test results yield critical erosion parameters including the critical shear stress (τ_c) below which no erosion occurs, and the erodibility coefficient (k_d) which quantifies the rate of erosion above the critical threshold. These parameters follow the excess shear stress erosion equation: $\dot{e} = k_d(\tau - \tau_c)$, where \dot{e} represents the erosion rate, τ is the applied shear stress, and the relationship enables prediction of erosion behavior under various hydraulic conditions. The JET has proven particularly valuable for characterizing streambank materials, earthen dam cores, and other geotechnical applications where erosion resistance is a critical design parameter.

The background just present is of most interest for the reader of chapter 4 and chapter 5.

2 Erosion processes in natural environments

Ubiquitous presence of cohesive sediments

The spatiotemporal dynamics of fine cohesive sediments in tidal mud flats constitute a fundamental component of estuarine and coastal morphodynamics, with significant implications for ecosystem functionality, coastal defence, and sediment management strategies (Winterwerp et al., 2022). These intertidal environments serve as critical transition zones between terrestrial and marine ecosystems, providing essential habitat for numerous species while simultaneously functioning as natural buffers against wave action and storm surges (Wolanski et al., 2011). The erosion and transport of cohesive sediments within mud flat environments govern not only their geomorphological evolution but also influence water quality, contaminant fate, and navigability of adjacent channels (Lick, 1982; Mehta et al., 1989; Voermans et al., 2018; Gupta et al., 2023).

The dynamics of sediment transport are significantly affected by tidal actions, where both flood and ebb tides contribute differently to sediment redistribution within these environments (Geng et al., 2020; Moore et al., 2009). The morphological evolution of estuarine systems is often governed by the asymmetrical flow patterns created by tidal forces, which can lead to varying sediment deposition and erosion rates across the tidal flats (Moore et al., 2009).

Physical models versus empirical relations

Despite extensive research on cohesive sediment dynamics, a comprehensive understanding of the specific detachment mechanisms operating at the microscale level remains conspicuously absent from the scientific literature. Previous investigations have primarily focused on quantifying bulk erosion rates and empirical relationships between applied shear stress and mass erosion (Partheniades, 1965; Winterwerp et al., 2004), while the fundamental physical processes governing detachment mechanism have received comparatively limited attention. This knowledge gap significantly impedes the development of physically-based predictive models for cohesive sediment erosion in natural environments.

Complexity of factors affecting cohesive sediment behaviour

Mud flat sediments present particular complexity due to their variable consolidation states, significant spatial heterogeneity, and the influence of biological factors such as microphytobenthos and extracellular polymeric substances (EPS) on erosion resistance (Tolhurst et al., 2002; Malarkey et al., 2015; Pivato et al., 2019). Conversely, increased shear stress from hydrodynamic forces can lead to the erosion of these biological mats, resulting in the detachment of sediment particles and altering the sediment dynamics within the ecosystem (Mendoza-Lera et al., 2016).

These complexities have historically complicated efforts to isolate and characterize the specific mechanical processes governing sediment detachment. The use of reconstituted clay in controlled laboratory conditions, as often done in the literature, therefore represents a strategic approach to systematically investigate the fundamental physical mechanisms of cohesive sediment erosion, establishing a baseline understanding that can subsequently be extended to incorporate the additional complexities present in natural systems.

Erosion detachment mechanisms as base to inform physical-based modelling

Improving mechanistic understanding of cohesive sediment erosion processes has significant practical applications, including enhanced predictive capabilities for estuarine morphodynamic models, improved design criteria for coastal protection schemes, and more effective strategies for managing sediment-bound contaminants in industrialized estuaries. By bridging the gap between empirical observations and theoretical frameworks, this research aims to contribute in the development of more robust and physically-based approaches to modelling cohesive sediment dynamics in tidal environments.

The background just present is of most interest for the reader of chapter 3.

References

- Al-Madhhachi, A.S.T., Hanson, G.J., Fox, G.A., Tyagi, A.K. and Bulut, R., 2013. Deriving parameters of a fundamental detachment model for cohesive soils from flume and jet erosion tests. *Transactions of the ASABE*, 56(2), pp.489-504.
- Beber, R., Tarantino, A. and Becker, P., 2023. Climate change adaptation of Elbe river flood embankments via suction-based design. *International Journal of Geomechanics*, 23(3), p.05023001.
- Benahmed, N. and Bonelli, S., 2012. Investigating concentrated leak erosion behaviour of cohesive soils by performing hole erosion tests. *European Journal of Environmental and Civil Engineering*, 16(1), pp.43-58.
- Bennabi, A., Karoui, T., Benamar, A. and Wang, H.Q., 2012. Some elements of comparison between two laboratory devices for soil erosion testing. *ICSE10 Paris*, pp.1089-1096.
- Bonelli, S. ed., 2012. Erosion of geomaterials. John Wiley & Sons.
- Briaud, J.L., Ting, F.C.K., Chen, H.C., Cao, Y., Han, S.W. and Kwak, K.W., 2001. Erosion function apparatus for scour rate predictions. *Journal of geotechnical and geoenvironmental engineering*, 127(2), pp.105-113.
- Briaud, J.L., Govindasamy, A.V. and Shafii, I., 2017. Erosion charts for selected geomaterials. *Journal of geotechnical and geoenvironmental engineering*, 143(10), p.04017072.
- Fattahi, S.M., Soroush, A. and Shourijeh, P.T., 2017. The hole erosion test: a comparison of interpretation methods. *Geotechnical Testing Journal*, 40(3), pp.494-505.
- Foster, M., Fell, R. and Spannagle, M., 2000. The statistics of embankment dam failures and accidents. *Canadian Geotechnical Journal*, 37(5), pp.1000-1024.
- Fox, G.A., Guertault, L., Castro-Bolinaga, C., Allen, P., Bigham, K.A., Bonelli, S., Hunt, S.L., Kassa, K., Langendoen, E.J., Porter, E. and Shafii, I., 2022. Perspective: Lessons learned, challenges, and opportunities in quantifying cohesive soil erodibility with the jet erosion test (JET). *J. ASABE*, 65(2), pp.197-207.
- Geng, L., Gong, Z., Zhou, Z., Lanzoni, S. and D'Alpaos, A., 2020. Assessing the relative contributions of the flood tide and the ebb tide to tidal channel network dynamics. *Earth Surface Processes and Landforms*, 45(1), pp.237-250.
- Grabowski, R.C., Droppo, I.G. and Wharton, G., 2011. Erodibility of cohesive sediment: The importance of sediment properties. *Earth-Science Reviews*, 105(3-4), pp.101-120.
- Gragnano, C.G., Rocchi, I. and Gottardi, G., 2021. Field monitoring and laboratory testing for an integrated modeling of river embankments under transient conditions. *Journal of Geotechnical and Geoenvironmental Engineering*, 147(9), p.05021006.
- Gupta, L.K., Pandey, M., Raj, P.A. and Shukla, A.K., 2023. Fine sediment intrusion and its consequences for river ecosystems: a review. *Journal of Hazardous, Toxic, and Radioactive Waste*, 27(1), p.04022036.
- Hahn, W., Hanson, G.J. and Cook, K.R., 2000. Breach morphology observations of embankment overtopping tests. In *Building partnerships* (pp. 1-10).
- Hanson, G.J. and Cook, K.R., 2004. Apparatus, test procedures, and analytical methods to measure soil erodibility in situ. *Applied engineering in agriculture*, 20(4), pp.455-462.
- Hanson, G.J., Robinson, K.M., Cook, K.R. and Temple, D.M., 2004. Modeling of erosion from headcut development in channelized flow. *Advances in hydro-science and engineering*, 6.
- Hanson, G.J. and Hunt, S.L., 2007. Lessons learned using laboratory JET method to measure soil erodibility of compacted soils. *Applied engineering in agriculture*, 23(3), pp.305-312.

- Johari, A. and Talebi, A., 2019. Stochastic analysis of rainfall-induced slope instability and steady-state seepage flow using random finite-element method. *International Journal of Geomechanics*, 19(8), p.04019085.
- Johnston, I., Murphy, W. and Holden, J., 2021. A review of floodwater impacts on the stability of transportation embankments. *Earth-Science Reviews*, 215, p.103553.
- Khalilzad, M., Gabr, M.A. and Hynes, M.E., 2015. Deformation-based limit state analysis of embankment dams including geometry and water level effects. *International Journal of Geomechanics*, 15(5), p.04014086.
- Knapen, A., Poesen, J., Govers, G., Gyssels, G. and Nachtergaele, J., 2007. Resistance of soils to concentrated flow erosion: A review. *Earth-Science Reviews*, 80(1-2), pp.75-109.
- Lick, W., 1982. The transport of contaminants in the Great Lakes. *Annual Review of Earth and Planetary Sciences*, Vol. 10, p. 327, 10, p.327.
- Malarkey, J., Baas, J.H., Hope, J.A., Aspden, R.J., Parsons, D.R., Peakall, J., Paterson, D.M., Schindler, R.J., Ye, L., Lichtman, I.D. and Bass, S.J., 2015. The pervasive role of biological cohesion in bedform development. *Nature communications*, 6(1), p.6257.
- Marot, D., Regazzoni, P.L. and Wahl, T., 2011. Energy-based method for providing soil surface erodibility rankings. *Journal of Geotechnical and Geoenvironmental Engineering*, 137(12), pp.1290-1293.
- Mehta, A.J., Hayter, E.J., Parker, W.R., Krone, R.B. and Teeter, A.M., 1989. Cohesive sediment transport. I: Process description. *Journal of Hydraulic Engineering*, 115(8), pp.1076-1093.
- Mendoza-Lera, C., Federlein, L.L., Knie, M. and Mutz, M., 2016. The algal lift: Buoyancy-mediated sediment transport. *Water Resources Research*, 52(1), pp.108-118.
- Mercier, F., Bonelli, S., Pinettes, P., Golay, F., Anselmet, F. and Philippe, P., 2014. Comparison of computational fluid dynamic simulations with experimental jet erosion tests results. *Journal of Hydraulic Engineering*, 140(5), p.04014006.
- Mercier, F., Golay, F., Bonelli, S., Anselmet, F., Borghi, R. and Philippe, P., 2014. 2D axisymmetrical numerical modelling of the erosion of a cohesive soil by a submerged turbulent impinging jet. *European Journal of Mechanics-B/Fluids*, 45, pp.36-50.
- Mohamed, M.A., Samuels, P.G., Morris, M.W. and Ghataora, G.S., 2002, September. Improving the accuracy of prediction of breach formation through embankment dams and flood embankments. In *River Flow* (Vol. 2002, p. 1st).
- Moore, R.D., Wolf, J., Souza, A.J. and Flint, S.S., 2009. Morphological evolution of the Dee Estuary, Eastern Irish Sea, UK: A tidal asymmetry approach. *Geomorphology*, 103(4), pp.588-596.
- Ngo, P.S.N., Garciano, L.E.O., De Leon, M.P., Lopez, N.S.A., Ishii, H., Iimura, K., Valdez, J.J.P. and Shibayama, T., 2022. Experimental and numerical modeling of a tide embankment section subjected to storm surge in Tacloban City, Philippines. *Natural Hazards Review*, 23(4), p.05022007.
- Partheniades, E., 1965. Erosion and deposition of cohesive soils. *Journal of the Hydraulics Division*, 91(1), pp.105-139.
- Philippe, P. and Benahmed, N., 2024. Quantifying soil surface erosion. *Comptes Rendus. Physique*, 25(S3), pp.1-36.
- Pivato, M., Carniello, L., Moro, I. and D'Odorico, P., 2019. On the feedback between water turbidity and microphytobenthos growth in shallow tidal environments. *Earth Surface Processes and Landforms*, 44(5), pp.1192-1206.
- Powledge, G.R., Ralston, D.C., Miller, P., Chen, Y.H., Clopper, P.E. and Temple, D.M., 1989. Mechanics of overflow erosion on embankments. I: Research activities. *Journal of Hydraulic Engineering*, 115(8), pp.1040-1055.
- Rajaratnam, N. and Beltaos, S., 1977. Erosion by impinging circular turbulent jets. *Journal of the Hydraulics Division*, 103(10), pp.1191-1205.

- Rajaratnam, N. and Berry, B., 1977. Erosion by circular turbulent wall jets. *Journal of Hydraulic Research*, 15(3), pp.277-289.
- Regazzoni, P.L. and Marot, D., 2011. Investigation of interface erosion rate by Jet Erosion Test and statistical analysis. *European Journal of Environmental and Civil Engineering*, 15(8), pp.1167-1185.
- Richards, K.S. and Reddy, K.R., 2007. Critical appraisal of piping phenomena in earth dams. *Bulletin of Engineering Geology and the Environment*, 66, pp.381-402.
- Romero, E. and Jommi, C., 2008. An insight into the role of hydraulic history on the volume changes of anisotropic clayey soils. *Water Resources Research*, 44(5).
- Sanford, L.P. and Maa, J.P.Y., 2001. A unified erosion formulation for fine sediments. *Marine Geology*, 179(1-2), pp.9-23.
- Tolhurst, T.J., Gust, G. and Paterson, D.M., 2002. The influence of an extracellular polymeric substance (EPS) on cohesive sediment stability. In *Proceedings in marine science* (Vol. 5, pp. 409-425). Elsevier.
- Voermans, J.J., Ghisalberti, M. and Ivey, G.N., 2018. A model for mass transport across the sediment-water interface. *Water Resources Research*, 54(4), pp.2799-2812.
- Vahedifard, F., Jasim, F.H., Tracy, F.T., Abdollahi, M., Alborzi, A. and AghaKouchak, A., 2020. Levee fragility behavior under projected future flooding in a warming climate. *Journal of Geotechnical and Geoenvironmental Engineering*, 146(12), p.04020139.
- Walder, J.S., 2016. Dimensionless erosion laws for cohesive sediment. *Journal of Hydraulic Engineering*, 142(2), p.04015047.
- Wan, C.F. and Fell, R., 2004. Investigation of rate of erosion of soils in embankment dams. *Journal of geotechnical and geoenvironmental engineering*, 130(4), pp.373-380.
- Winterwerp, J.C. and Van Kesteren, W.G., 2004. Introduction to the physics of cohesive sediment dynamics in the marine environment (Vol. 56). Elsevier.
- Winterwerp, J.C., Van Kessel, T., van Maren, D.S. and Van Prooijen, B.C., 2022. *Fine sediment in open water: From fundamentals to modeling*.
- Wolanski, E., McLusky, D., Uncles, R.J. and Monismith, S.G., 2011. Water and Fine-Sediment Circulation.
- Xie, L., Liang, X. and Su, T.C., 2018. Measurement of pressure in viewable hole erosion test. *Canadian Geotechnical Journal*, 55(10), pp.1502-1509.
- Zhang, Z., Fu, X., Sheng, Q., Du, Y., Zhou, Y. and Huang, J., 2021. Stability of cracking deposit slope considering parameter deterioration subjected to rainfall. *International Journal of Geomechanics*, 21(7), p.05021001.

Chapter III: Experimental investigation into the erosion detachment mechanisms in reconstituted clay

1 Introduction

The spatiotemporal dynamics of fine-grained sedimentary soils is a critical aspect in the stewardship of estuarine and coastal aquatic systems and the evaluation of the impact of anthropogenic infrastructure on ecosystem integrity (Winterwerp et al., 2022). This includes major port developments, maintenance dredging operations, and coastal protection schemes. A fundamental component governing these transport mechanisms is the mass flux of fine sediments occurring at bed-water interface (Partheniades, 1965). The detachment mechanism that leads to sediment mobilization from the coastal and river beds is responsible for this exchange process and its understanding is paramount (Mehta et al., 1989). Such knowledge directly informs sediment management strategies in navigation channels, optimization of dredging protocols, and assessment of contaminant transport in industrialized estuaries, where pollutants often preferentially bind to fine sediment particles (Lick, 1982; Voermans et al., 2018; Gupta et al., 2023).

In fine-grained sediments, three different erosion modes have been identified in the literature namely i) surface erosion, ii) mass erosion and iii) fluid mud entrainment/generation (Partheniades, 2009; Mehta, 2013; Winterwerp et al., 2022).

The first two mechanisms have been widely investigated in the literature (Harrison et al., 1971; Mehta et al., 1982; Lick, 1982; Sheng, 1986) and are the object of this research. The latter mechanism involves bed under formation from suspensions or stable suspensions governed by turbulent-mixing processes (McAnally et al., 2007) but it is not investigated further in this work.

Surface erosion and mass erosion are often modelled via the erosion law as formulated by Kandiah et al. (1974) and Ariathurai et al. (1978) as follows:

$$E = M \left(\frac{\tau_b - \tau_c}{\tau_c} \right)^n \quad \text{for } \tau_b > \tau_c \quad [1]$$

where E [kg/m²/s] is the erosion rate, M [kg/m²/s] is the erosion flux parameter, n is a soil parameter often assume to be equal to unity, τ_b is the mean bed hydrodynamic shear stress applied by the flow, and τ_c is the critical shear stress above which erosion is observed. This equation is generally referred to as

Partheniades' erosion formula thanks to pioneering work of this author (Partheniades, 1965). The critical shear stress τ_c in equation [1], also referred to as erosion threshold parameter, is a key parameter to estimate in practical engineering problems.

For sandy materials, τ_c is estimated using a semi-empirical model based on the assumption that incipient motion is associated with the mobilisation of a single grain. Shields (1936) considered the destabilising and stabilising forces acting on a single grain to identify the non-dimensional variables controlling the incipient motion, i.e., the dimensionless shear stress against the Reynolds number. Experimental data were therefore represented in this non-dimensional plane and fitted with an empirical curve to develop a predictive tool.

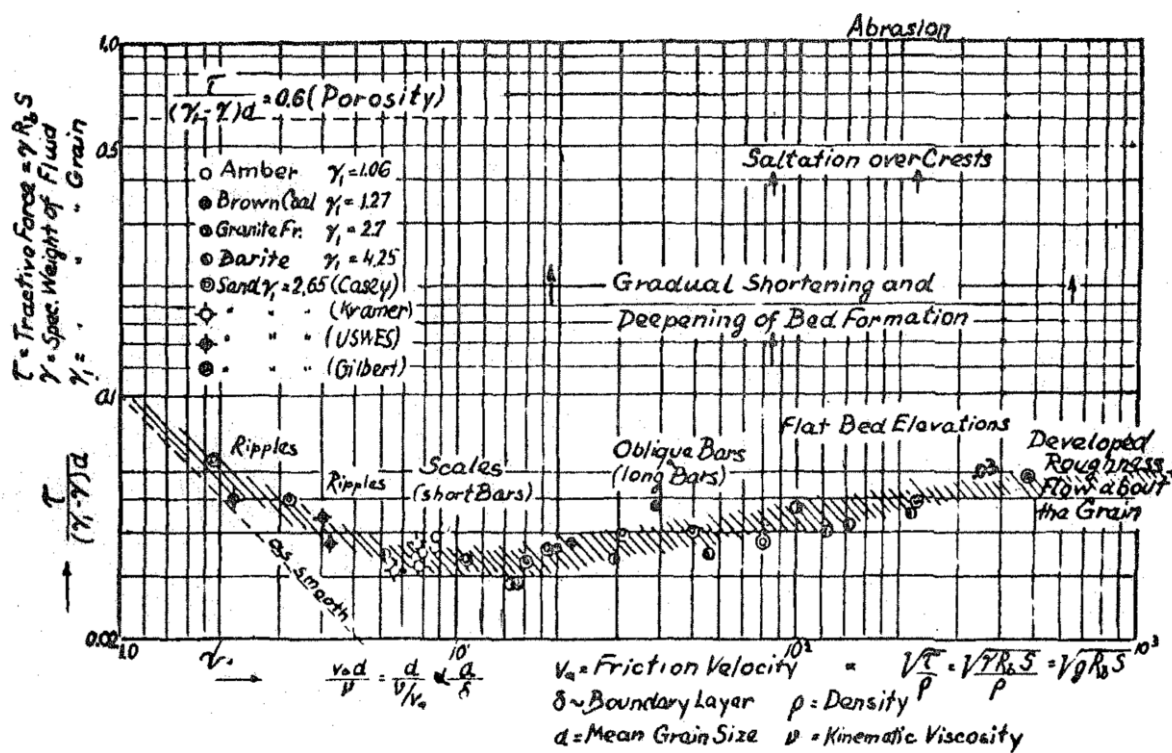


Figure 1. Log-Log Shields Diagram depicting the adimensionalized grain diameter on the x-axis and the adimensionalized shear stress on the y-axis leading to incipient of motion of the single grain (after Shields (1936))

Advancements have been made to extend the Shields' semi-empirical approach to fine-grained silty sediments. Miedema (2013) considered a mechanism whereby incipient motion is associated with the mobilisation of an assemblage of particles (i.e. smaller particles bound to larger particles by van der Waals forces). A semi-empirical model was proposed that could capture the experimental data by Roberts et al. (1998), who presented data on the detachment of quartz particles ranging from sand to silt size showing that τ_c increases as particle size decreases into the silt range as opposed to the case of sand size (where τ_c decrease as particle size decreases). Yao et al. (2022) presented similar results as Roberts et al. (1998) investigating experimentally the erosion threshold of sand-silt mixtures. Chen et al. (2022) addressed the increase of τ_c as particle size decreases into the silt range by adopting a fractal analysis of the aggregate

without making explicit reference to any detachment mechanism. Righetti et al. (2007) studied the detachment of flocs from lacustrine benthic sediments in flume experiments. He extended the Shields's semi-empirical approach by modelling the floc as an aggregate of mineral particles and organic material by accounting for cohesion and adhesion forces in floc-to-floc interactions.

For clayey sediments, attempts have been made to relate the threshold shear stress empirically to the plasticity index (Winterwerp et al., 2012), dry density (Mehta et al., 1994) and other macroscopic soil properties (Debnath et al., 2010). However, the performance of these empirical approaches to predict the threshold shear stress is quite poor (Grabowski et al., 2011). No attempts have been made to model the threshold shear stress in clays based on a detachment mechanism focused on the identification of the detaching unit, which has likely hindered the identification of the variables controlling the first detachment.

Winterwerp et al. (2012) have implicitly assumed that the critical shear stress marks the transition from sporadic detachment of flocs (floc erosion) to the detachment of aggregates affecting the entire bed (surface erosion). Their schematisation of erosion of clayey sediments, though intuitive, has rarely been supported by direct observations of the elements detaching from the clay sediment bed, with the exception of aggregates collected post-mortem by sieves traps at end of flume devices (Perkey et al., 2020). The assumption that the threshold shear stress is associated with the detachment of clay particle assemblages (e.g., aggregates) is in line with the observation of the detachment mechanism assumed to control the initiation of erosion in fine-grained silty sediments. It can be tentatively assumed that the main difference between the erosion of coarse-grained and fine-grained sediments is the detaching unit, individual particles for sandy sediments and assemblages of particles for silty and clayey sediments. However, there is little experimental evidence about the mechanisms of erosion initiation in clays. This will be key to develop robust semi-empirical models for the characterisation of the shear stress threshold in clayey sediments.

This work addresses experimentally and conceptually the following research questions:

R1: What are the mechanisms of first detachment in clay and to directly observe them?

R2: What is the representative unit, or what is the scale controlling the above mechanism?

R3: Is there a fundamental difference between the mechanisms of erosion initiation in clay and granular sediments?

To this end, a micro-jet erosion device was developed to observe the mechanisms of the onset detachment on reconstitute kaolin clay.

2 Background

This section reviews the dataset on the critical shear stress for a silt as presented by Roberts et al. (1998). This is the most comprehensive dataset on materials with particle size smaller than sand and closer to clay. These experimental data are then compared with the semi-empirical model by Shields (1936) for granular materials as parametrised by Miedema (2012). These data will serve as a benchmark for the data on reconstituted clay presented later in this chapter.

Roberts et al. (1998) used quartz particles with median size d_{50} ranging from 5 to 1350 μm . Samples were prepared from slurry and consolidated to achieve bulk densities in the range 1.65-1.95 g/cm^3 . Hydrodynamics shear stresses were imposed in a flume device in the range 0.2-6.4 Pa. Experimental data are shown in Figure 2 in terms of critical shear stress versus particle size d_{50} for different values of soil density tested. The relationship between critical shear stress versus particle diameter appeared to be non-monotonic. As d_{50} increases, the minimum detachment shear stress also increases. At the same time, the shear stress increases with soil density, an effect ascribed to ‘cohesive’ interparticle forces.

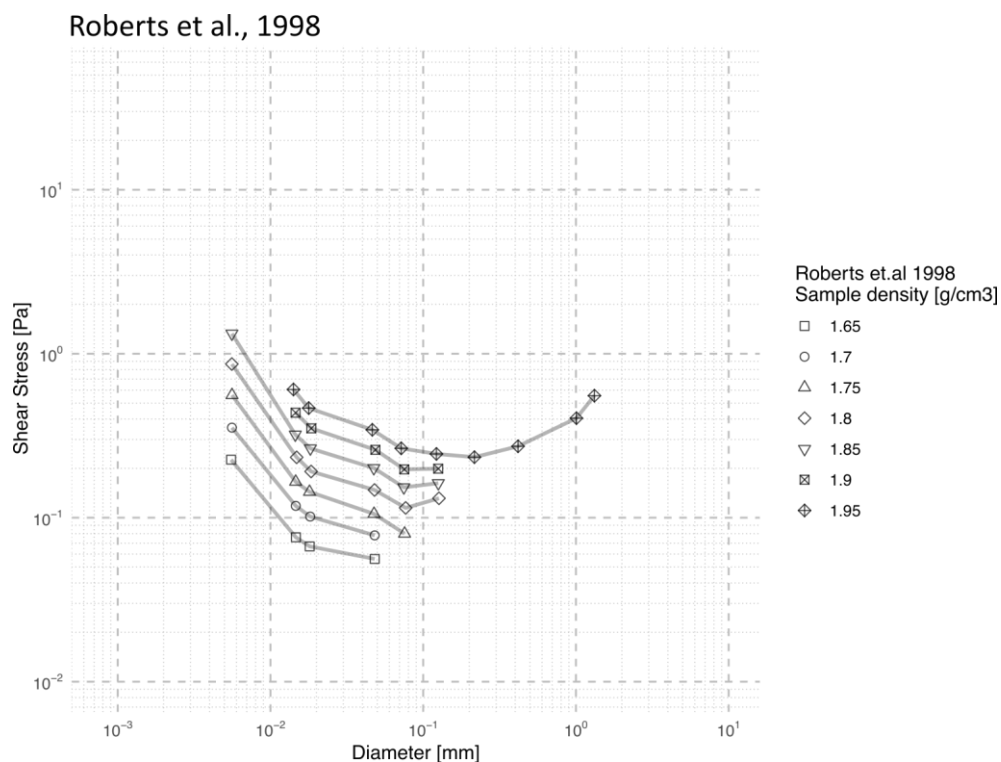


Figure 2. Detachment shear stress versus median particle size d_{50} of different densities of quartz samples (Roberts et al., 1998)

Miedema (2012) developed a model for the entrainment of particles as a result of fluid flow over a bed of sand-size spherical particles distinguishing between the mechanisms of sliding, rolling and lifting.

Sliding was intended by the author as the mechanism that occurs when many particles are starting to move, and it is assumed to be controlled by the macroscopic angle of shearing resistance. Rolling and lifting are assumed to be individual particle mechanisms controlled by particle-scale parameters such as pivot angle and exposure and protrusion rate. The model of Miedema (2012) is the most comprehensive theoretical formulation of the semi-empirical model introduced by Shields (1936) and is based on a detailed derivation of the friction velocity at the top of the sphere. It accounts for the effect of turbulence, particle shape and exposure on drag and lift and the transition from laminar to turbulent regime.

In their work, Miedema (2012) tested the different theoretical formulations (sliding, rolling, and lifting) against numerous experimental dataset on granular materials made available since Shield's work including Amber (0.38-3mm), Brown Coal (0.75-5mm), Granite Fragments(0.75-3mm), and Barite(0.25 – 5mm). The Shield's curves by Miedema appear to match the experimental data by Roberts (1998) on silt only for the samples with d_{50} larger than 0.2mm.

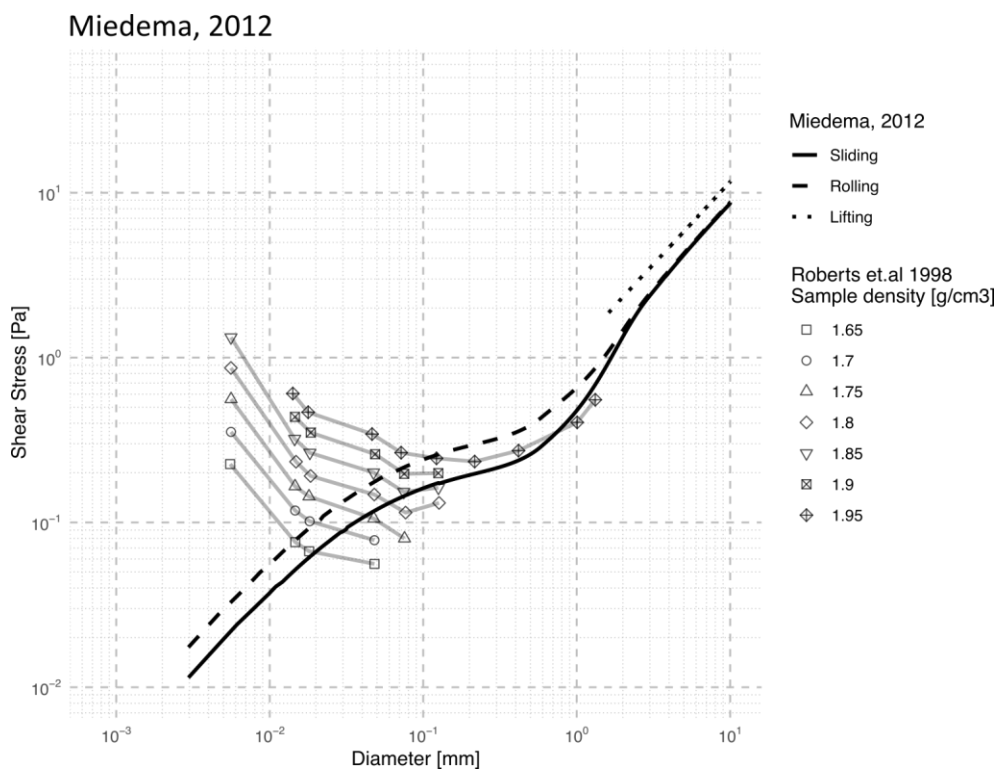


Figure 3. Theoretical derivation of Shield's curve for three different mechanisms, i.e. sliding (continuous curve), rolling (dashed curve), and lifting (dotted curve), for he case of turbulent regime (Miedema, 2012)

3 Materials and Methods

3.1 Materials

Speswhite™ Kaolin from Imerys with a plastic limit $w_P = 0.32$ and a liquid limit $w_L = 0.64$ was chosen for the tests presented hereafter. The particle size distribution shows it to have a 0.20 silt fraction and a 0.80 clay fraction. Figure 4 shows the aggregate size distribution for suspensions at pH 4 and at pH 9 at zero electrolyte concentration. Suspension prepared at pH 9 shows a median Stokes' diameter of 0.98 μm . On the other side, suspension prepared at pH 4 has a median Stokes' diameter of 6.4 μm .

Deionized deaired water was found to be acidic (pH=4). To prepare alkaline water, potassium hydroxide, KOH, was used to increase the pH to the value of 9 (the increase in molarity due to the addition of KOH was less than 0.01 M).

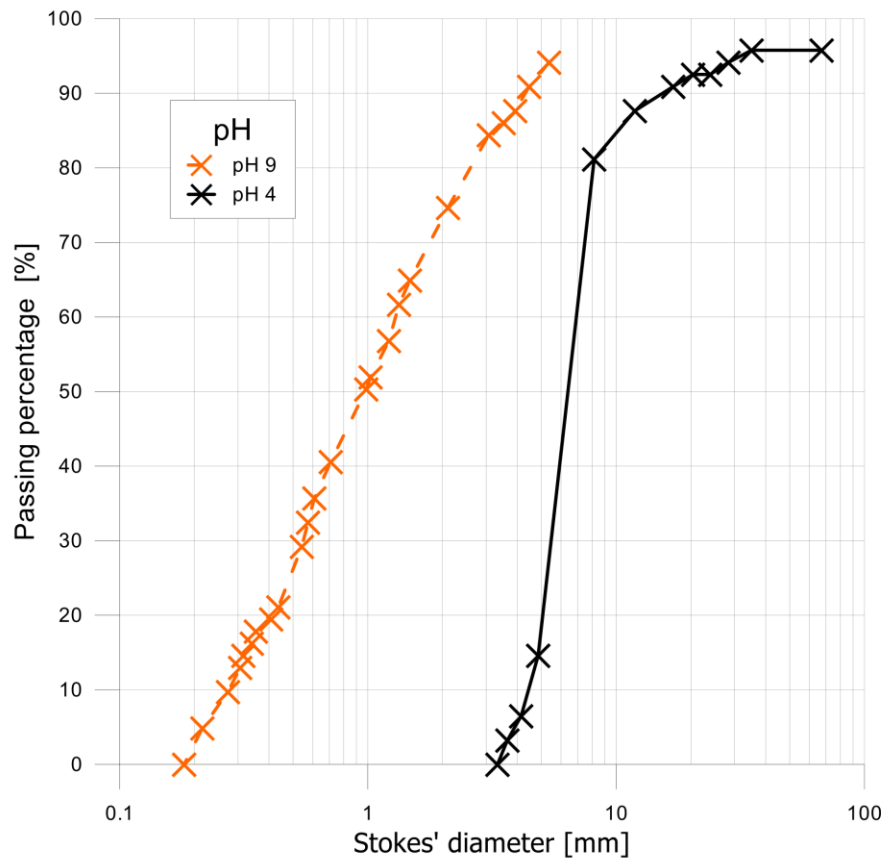


Figure 4. Aggregate Size distribution of Speswhite™ Kaolin from Imerys (after Pedrotti, 2016)

3.2 Sample preparation

Two series of samples were prepared. The first series is referred to as pH₄ with samples prepared by using deionised water ‘as is’. The second series is referred to as pH₉ with samples prepared by adding alkaline water.

For the samples at pH₄, the slurry was prepared by mixing dry powder with deionised water. After mixing, the slurry was de-aired. For the samples at pH₉, the slurry was prepared by mixing dry powder and alkaline water. After mixing, the slurry was de-aired and the pH was measured again. If found to be less than 9, additional KOH were added in order to restore the value equal to 9.

The choice of mixing kaolin with water at different pH was motivated by the different ‘fabric’ generated by either acidic or alkaline water. Water at pH₄ generates a ‘flocculated’ open fabric, due to the edge-to-face attraction between the negatively charged face and positively charged edge of the kaolinite particle (Pedrotti and Tarantino, 2018). Water at pH₉ generates a ‘dispersed’ close fabric due to the particles becoming negatively charged all around, which promotes arrangement of particles in sub-parallel configuration (Pedrotti and Tarantino, 2018).

3.2.1 Samples reconstituted from slurry and consolidated by self-weight

The slurry was prepared by mixing dry powder with deionized (acidic) or alkaline water in ratio of 1:2 by weight. The slurry was placed in a column made of 3 superposed oedometer rings to reach a height of 60mm plus an extension made of a Perspex tube of the same inner diameter of 75mm. During self-weight consolidation, the sample surface was left covered with water to preserve the saturation of the slurry. The sample was always maintained submerged with water before and during its transfer to the JET device. These samples will be referred to as ‘reconstituted self-weight samples’.

3.2.2 Samples reconstituted from slurry by external stress (oedometer)

The slurry was prepared by mixing dry powder with deionized (acidic) or alkaline water in ratio of 1:1 by weight. The slurry was de-aired and then placed inside an oedometer cell for consolidation to target vertical stress of either 89kPa or 888kPa. The samples were loaded and unloaded in steps, each step of sufficiently long duration to allow for full consolidation. Two samples were consolidated to 888 kPa following a different loading sequence as shown in Figure 5. Sample A was loaded by considering stress increments not exceeding 288 kPa whereas sample B was loaded first to 88 kPa and then to 888 kPa in one single step. Unloading steps were equal to 44kPa for both samples.

After the last load was removed and swelling completed, the loading cap and the top porous stone were removed to transfer the sample to the testing device. The sample was always maintained submerged

with water before and during its transfer to the JET device. These samples will be referred to as ‘reconstituted samples’.

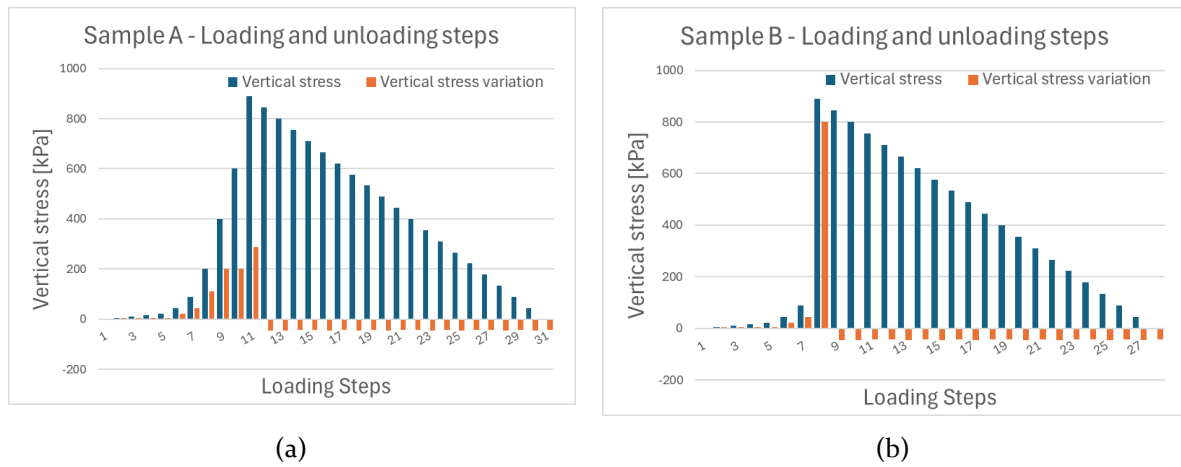


Figure 5. Loading and unloading steps for sample A & B consolidated to 888 kPa vertical stress. (a) Sample A consolidated with loading increments not exceeding ~290 kPa. (b) Sample B consolidated with final loading increment of 800 kPa.

3.2.3 Samples reconstituted from slurry by imposing non-conventional boundary conditions

In order to test some hypotheses on the observed detachment mechanism, more samples were consolidated from slurry by imposing non-conventional boundary conditions as follows.

Consolidation in oedometer with impervious surface

This sample was prepared with the same loading sequence as per sample A consolidated at 888 kPa with the exception that the top porous stone was replaced by a impervious aluminium disk to enable drainage only from the bottom porous stone.

Consolidation at slow deformation rate

Sample was consolidated at the constant displacement rate of 0.002 mm/min (sufficiency slow to allow for drained conditions) until the vertical stress reached 888 kPa as measured through a load cell.

Radial consolidation

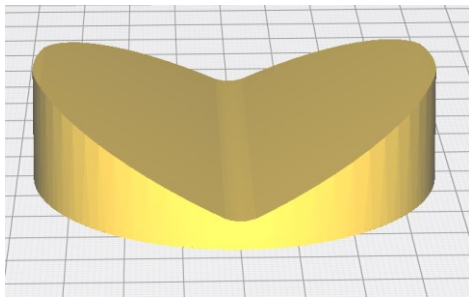
The sample was loaded at the constant displacement rate of 0.002 mm/min with drainage occurring radially thanks to the mould made of high-conductivity sandstone as shown in Figure 6. Two impervious aluminium discs were placed on top and bottom surfaces of the sample.



Figure 6. Radially consolidated sample ready to be tested in the micro-jet test device

Cusped top surface

The top cap was 3D printed to create a cusped top surface. The top cup was printed in 'all-fill' mode in order to ensure the maximum stiffness allowed by the ABS material. The cusped top surface was maintained impervious to flow during consolidation. The design of the top cap and the sample consolidated to 89 kPa are shown in Figure 7.



(a)

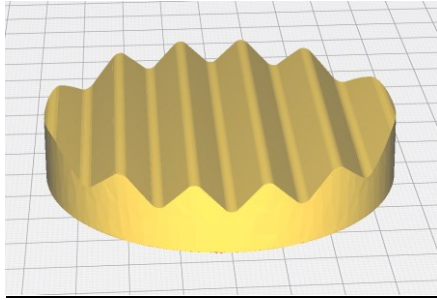


(b)

Figure 7. Sample consolidated to 89 kPa with a cusped loading cap. (a) 3D model of the cusped loading cap. (b) Sample with cusped surface ready to be tested in the micro-jet erosion test device.

Zigzag top surface

The top cap was 3D printed to create a zigzag top surface. The top cup was printed in 'all-fill' mode in order to ensure the maximum stiffness allowed by the ABS material. The zigzag top surface was maintained impervious to flow during consolidation. The design of the top cap and the sample consolidated to 888 kPa are shown in Figure 8.



(a)



(b)

Figure 8. Sample consolidated to 888 kPa with a zigzag loading cap. (a) 3D model of the zigzag loading cap. (b) Sample with zigzag surface ready to be tested in the micro-jet erosion test device.

Slurry at repose – flat surface

The slurry, prepared with dry powder and water at a ratio 1:1, has a yogurt-like viscosity. After being de-aired, the slurry was placed inside the oedometer ring, and the ring was lifted and dropped on the table (i.e. tapping) several times until the sample surface became nearly horizontal. The sample was left exposed to the air for a few minutes before placing it underwater in the micro JET device.



Figure 9. Slurry at repose- flat sample ready to be tested.

Slurry at repose – irregular surface

The slurry prepared with dry powder and water at a ratio 1:1 has a yogurt-like viscosity. After being de-aired, the slurry was placed inside the oedometer ring and after exposure to air for few minutes gently placed underwater in a tank. The slurry was left in place for 2h in order to allow for any pore-water pressure (positive and negative) redistribution. Figure 10 shows the sample ready to be tested.



Figure 10. Slurry at repose - weird-shape sample ready to be tested

Self-weight in plastic beaker

Similarly to the samples consolidated by self-weight, the slurry prepared at pH 4 and pH 9 in 2:1 water/dry kaolin ration has been placed in 250 mL plastic beakers.

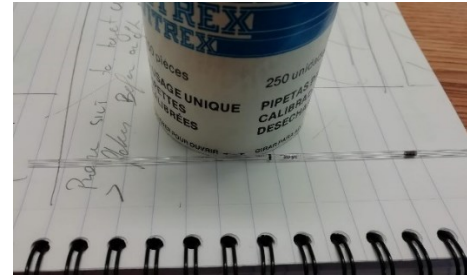
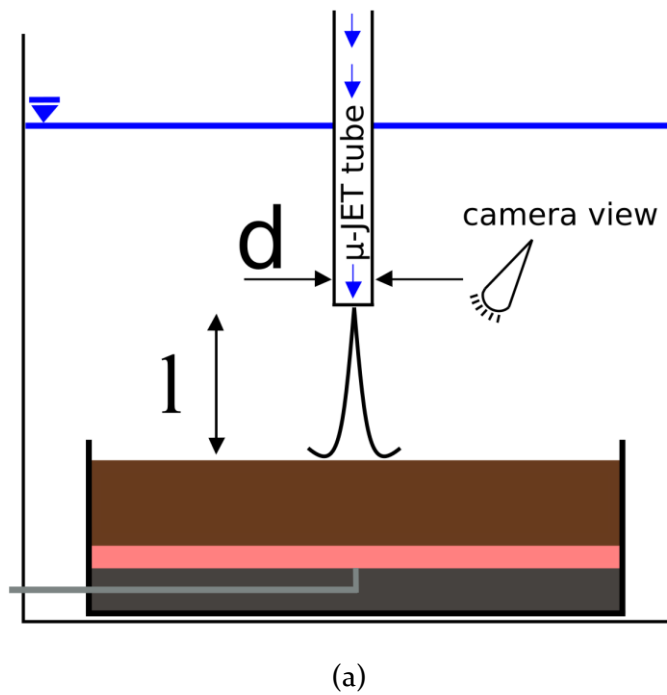
3.3 Micro-jet erosion test device (μ -jet)

To investigate the detachment mechanisms in clay, a miniaturized Jet Erosion Test (Hanson et al., 1994) was assembled and equipped with video system to film the surface of the sample subjected to erosion. The jet erosion test was chosen among other test devices for the following reasons:

- i) Hydraulic flume (Partheniades, 1965): the sample surface and core is disturbed during its placement in the testing apparatus; moreover due to the protrusion of the sample by design in the guide leading to erosion the detachment is more likely to be initiated at the sample boundary;
- ii) Hole Erosion Test (HET) (Lüthi, 2011): the HET would allow for better control of the fluid regime but it would not be easy to observe detachment mechanisms inside the hole ;
- iii) Impeller rotation test (Dunne et al., 2022): the centrifugal flow generates a diffuse detachment making the mechanisms difficult to observe. In addition, the water becomes turbid again making the visual observation of detachment mechanisms relatively difficult;
- iv) The laminar flow established in the JET allows for an easier estimation of the shear stresses applied to the soil surface (Benseghier et al., 2020);
- v) The erosion is localised compared to a Flume or HET because the shear stresses declines relatively rapidly from the impinging jet, thus facilitating the observation of the detachment of particles/aggregates.

The testing apparatus is shown schematically in Figure 11a and includes the components of an ordinary JET device (Hanson et al., 1994). It is referred to as micro-JET (μ -jet) because of the reduced diameter of the nozzle compared to ordinary JET. It is composed of a tank to host the submerged sample, a glass nozzle, and an adjustable head tank to provide the driving hydraulic head. The nozzle internal diameter is $d=0.634\text{mm}$ and the distance l between the nozzle and the sample surface can be adjusted in the range 0-50mm with a resolution of 0.01mm thanks to an arm holding the pipette attached to micrometric screw. The nozzle velocity u could be varied by raising or lowering a constant head tank connected to the glass

nozzle, which could be positioned at 11 different elevations. The velocity generated by the constant head was measured in the ranges from 0.14 to 0.99 m/s.



(b)



(c)

Figure 11. (a) μ -jet schematic layout (d =nozzle diameter, l =nozzle – sample distance). (b) Pipette used as μ -jet nozzle. (c) laminar flow in μ -jet highlighted by fluorescein.

The nozzle consisted of a glass pipette 125 mm long and 1.6mm outer diameter (Figure 11b). The smooth surface of glass favours the establishment of laminar flow in the pipette as observed in Figure 11c.

The Jet Reynolds number, Re_{jet} is given by

$$Re_{jet} = \frac{u * d}{\nu} \quad [2]$$

where u is the fluid velocity in the nozzle, d is the diameter of the nozzle, and ν is the kinematic viscosity of the fluid. Considering a kinematic viscosity of $\nu = 1E-6 \text{ m}^2/\text{s}$ for the water, $d=0.634 \text{ mm}$, and $u=0.14$ to 0.99 m/s , one obtains a Reynolds number in the range $Re_{jet} = 9 - 63$, which indicates laminar flow in the pipette prior the exiting the nozzle.

The jet impinging on the surface of the sample can also be considered to be laminar considering that non-dimensional nozzle distance $l^*=l/d$ from the sample surface ranges from 15.8 ($l=10\text{mm}$) to 31.5 ($l=20\text{mm}$). According to Badr et al. (2014, Figure 2 in their paper), these values of Re_{jet} and l^* are associated with free laminar regime (FLR).

3.3.1 Tangential shear stress

The maximum value of the shear stress at sample surface generated by the impinging jet was calculated based on Brunier-Coulin et al. (2020) as follows:

$$\tau_{max} = 0.00469 \frac{\rho u^2 Re_{jet}^{7/2}}{(l + 0.048 Re_{jet} d)^2} \quad [3]$$

where ρ is the fluid density. This maximum occurs at a normalized radial distance from the jet centreline $r/l \sim 0.12$, where r is the distance from the jet centreline and l is the distance of the nozzle from the sample surface. Figure 12 shows the maximum shear stress as a function of the water flow velocity in the nozzle.

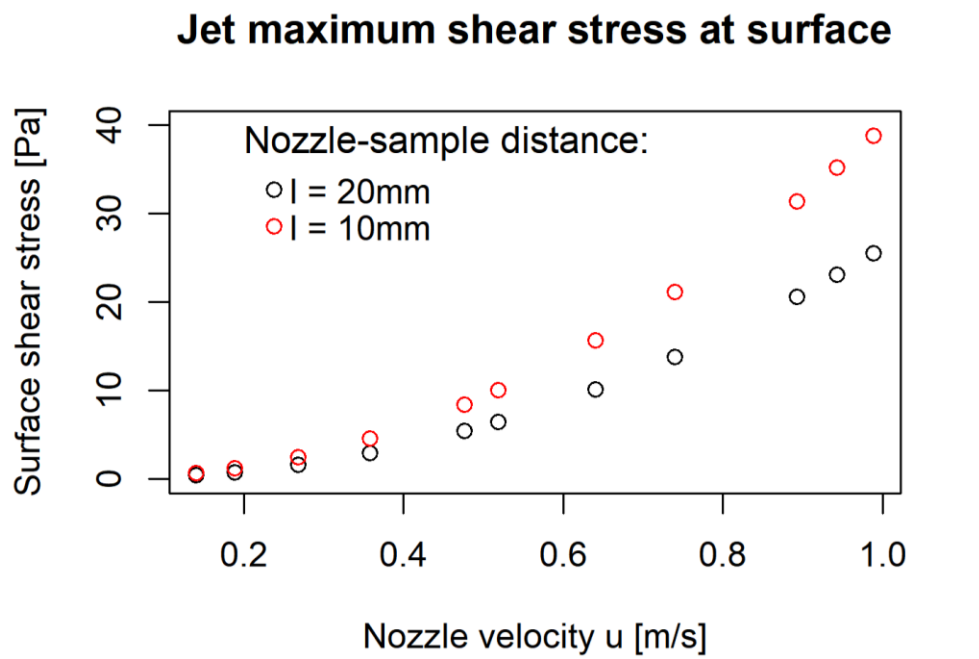


Figure 12. Maximum shear stress applied to sample surface by the impinging jet

3.3.2 Submersible camera

The μ -jet was equipped with a submersible camera (Teslong, 2019) recording RGB videos at 25 frames per second with a 1280x720 resolution. It was connected to a PC via a USB port with videos made available in AVI format. The camera was set at an angle with respect to the sample surface due to the presence of the pipette that did not allow the camera to be positioned facing the sample surface in coaxial nadiral position with the jet.

3.4 Testing procedure

The testing procedure consists of the following steps:

- i) Check that the sample had remained submerged with water following consolidation from slurry;
- ii) Place the sample in the tank where the JET is carried out sliding the sample underwater to avoid exposing the sample to accidental air-drying (this step is only carried out if the sample is removed from the consolidation cell, otherwise the JET is carried out directly in the submerged oedometer consolidation cell as shown in Figure 13);
- iii) Position the camera to have an adequate field of view of the area to be eroded by the impinging jet;
- iv) Lower the nozzle in close proximity of the sample surface and zero its position;
- v) Start video recording and move back the nozzle vertically to the testing position [$l=10\text{mm}$ or $l=20\text{mm}$];
- vi) Start the jet with the lower hydraulic head and maintain it for 5 minutes. If no erosion is observed, the hydraulic head is increased further and maintained for 5 min. The process is reiterated until the detachment of clay is observed.

The aforementioned procedure could be applied to up to 5 different locations on the sample surface (the surface of the sample consolidated in the oedometer is $\sim 50\text{ cm}^2$ compared to the jet footprint that is $< 0.8\text{ cm}^2$).



Figure 13. μ -jet testing procedure . (a) glass nozzle, tilted submersible camera and oedometer cell. (b) zoom on area of interest where some fluorescein has been added to visualise the laminar flow moving outwards in radial direction from the jet centre line.

3.5 Image processing

The impinging jet caused the detachment of flakes from the clay surface. To determine their dimension, images were processed in two steps as summarised below. Before the jet erosion test, the homography transformation matrix was calibrated, this matrix being used to ‘rectify’ the image taken with an oblique camera. After the jet erosion test, the flake was first identified (via image subtraction), its contour was detected and finally rectified using the previously calibrated transformation matrix. These steps are detailed hereafter.

3.5.1 Homography transformation

Principles of homography transformation

A general camera transformation from a point with coordinates X, Y, Z in the 3D space to a point (pixel) with coordinates u, v in the 2D image is represented by a 4×3 matrix that accounts for intrinsic parameters (i.e. focal length, principal point offset and axis skewness) and extrinsic parameters (i.e. 3D rigid roto-translation from camera to point reference system) (Hartley and Zisserman, 2003). Due to the complexity of determining these 12 parameters separately, they are usually determined by calibration procedure utilizing check boards and other calibration patterns of known dimensions (Bacakoglu and Kamel, 1997).

The transformation matrix can be simplified for the case where the points represented in the image belongs to a plane (i.e., the sample surface prior testing), with the problem reducing to the case of planar homography (Jawahar and Jain, 2006). The 3D points are now represented as $(X, Y, 0)$ with the ‘physical’ plane associated with the coordinate plane $X-Y (Z=0)$. The transformation matrix H has dimensions 3×3 as shown in Eq. [4]:

$$\begin{bmatrix} u \\ v \\ 1 \end{bmatrix} = \begin{bmatrix} h_{11} & h_{12} & h_{13} \\ h_{21} & h_{22} & h_{23} \\ h_{31} & h_{32} & 1 \end{bmatrix} \begin{bmatrix} X \\ Y \\ 1 \end{bmatrix} \quad [4]$$

where (u, v) are the image coordinates, h_{ij} are the components of the transformation matrix H , and (X, Y) are the coordinates on the plane of interest. The homography matrix is first determined by considering the pixel as unit length by setting $h_{33} = 1$. In order to estimate the remaining 8 parameters at least 4 points in the plane (X_i, Y_i) and in the image coordinate systems (u_i, v_i) need to be known. The back-projection error for the four points (X_i, Y_i) is given by :

$$Err = \sum_i \left[\left(u_i - \frac{h_{11} * X_i + h_{12} * Y_i + h_{13}}{h_{31} * X_i + h_{32} * Y_i + h_{33}} \right)^2 + \left(v_i - \frac{h_{21} * X_i + h_{22} * Y_i + h_{23}}{h_{31} * X_i + h_{32} * Y_i + h_{33}} \right)^2 \right] \quad [5]$$

and is minimized in order to calibrate the 8 parameters characterising the matrix in Eq. [4].

The demo visualization in Figure 14 is used to clarify the planar homography transformation. Figure 14a shows the orthorectified nadiral view of a circle on a plane, but it would appear distorted as an ellipse if such plane was viewed from an angle as shown in Figure 14b. By using the four vertices of the ellipse and with the prior knowledge that these points are associated with four cardinal points on a circle, the

nadiral view can be recovered by applying the homography transformation as shown in Figure 14c. The choice of selecting points on a circle does not make the transformation rotationally invariant, i.e. orientation of the 2D object in the nadiral view cannot be determined. However, this does not affect the dimension of the flake, which is the main objective of the image processing.

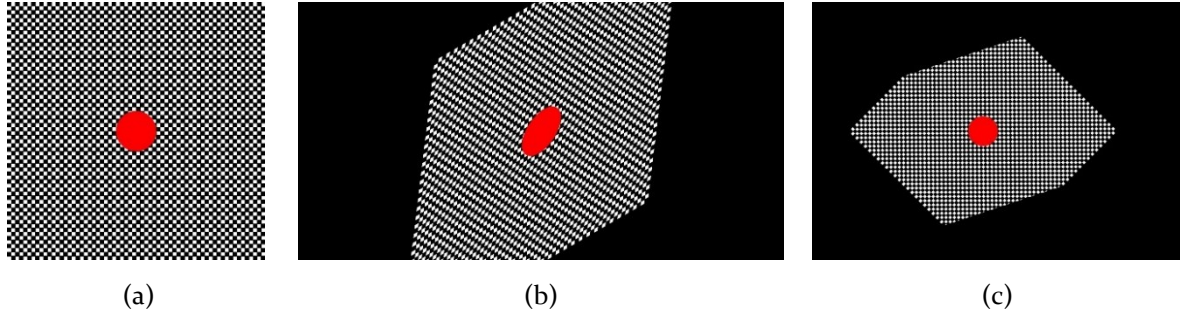


Figure 14. Homography transformation for the case of a circle on plane. (a) nadiral view of the circle on the plane (X,Y) . (b) slanted view of the circle in the plane $e(u,v)$. (c) restored nadiral view by applying the homography transformation.

Homography transformation applied to μ -jet images

The homography transformation was used to rectify the slanted images acquired by the camera and obtain the nadiral view. The determination of the H matrix coefficients was performed at the beginning of each video by considering the deformed circle represented by the ‘footprint’ of the glass nozzle as shown in Figure 15a. At this stage, the glass nozzle is in very close proximity of the sample surface. The outer diameter of the nozzle identifies the circle on the sample surface in the nadiral view. Via a GUI created in Python and OpenCV library (Bradski, 2000), an ellipse (in yellow in Figure 15b) is fitted to 5 points (in green) manually positioned on the virtual contact between cylindrical glass nozzle and the sample surface. Once the ellipse is determined, the 4 vertices are mapped to the cardinal points of a circle to calibrate the H matrix coefficients. The scaling parameter h_{33} was determined by imposing that the glass nozzle footprint, transformed into a circle after applying the homography transformation, matched the outer diameter of glass nozzle (1.6mm). The H matrix is then used to rectify the selected frames of interest as shown in Figure 15c.

The calibration of the homography transformation matrix was repeated any time the glass nozzle was moved to a new location on the sample surface.



(a)

(c)



(b)

Figure 15. Homography transformation calibration in μ -jet initial frame. (a) original frame from slanted camera. (b) GUI fitting of an ellipse (yellow) by manually positioning 5 points (green) on the virtual contact between cylindrical glass nozzle and sample surface. (c) rectified image in nadiral view.

3.5.2 Image subtraction and flake segmentation

The detached flakes were segmented to derive quantitative information about their geometry. To better identify the flake to segment, two frames were selected before and after flake detachment. Figure 16a shows a frame prior flake detachment whereas Figure 16b shows a frame post-detachment (the flake before detachment is shown by a yellow curve). The two frames were subtracted to identify clearly the flake before and after detachment as shown in Figure 16c. Image difference consists in the square of a pixel by pixel subtraction, this better highlight the difference amongst frames. Pixel by pixel difference was performed in the ImageJ software (Rueden et al., 2017) and the Region of Interest ROI segmented were saved. This process has been chosen in order not to convert a full video that in most cases ranges over one hour span (~10GB) but to apply the transformation only to the frames and ROIs of interest.

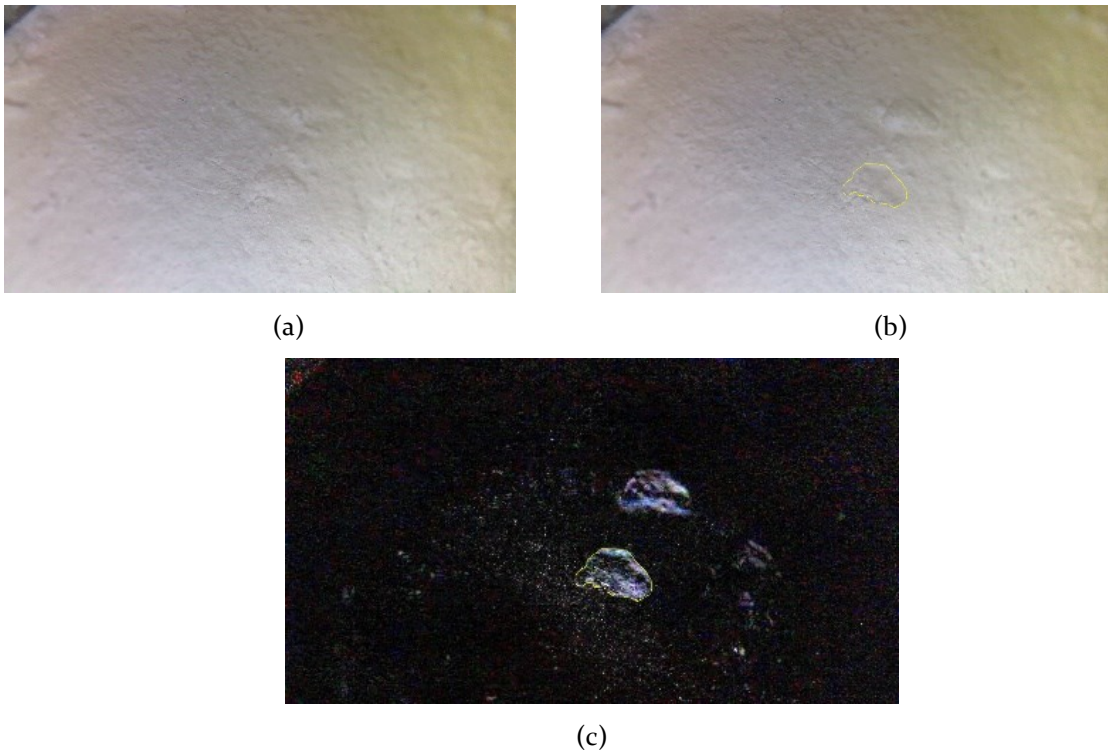


Figure 16. Flake identification aided by image difference. (a) frame prior detachment. (b) frame post-detachment with over imposed segmented flake (yellow). (c) frame to frame difference with over imposed segmented flake (yellow).

The flake highlighted in the image resulting from the subtraction, was contoured manually (in yellow in Figure 17a) and the homography transformation was applied (Figure 17b). As a reference, Figure 17b also shows the footprint of the glass nozzle. Finally, the area of the flake was calculated.

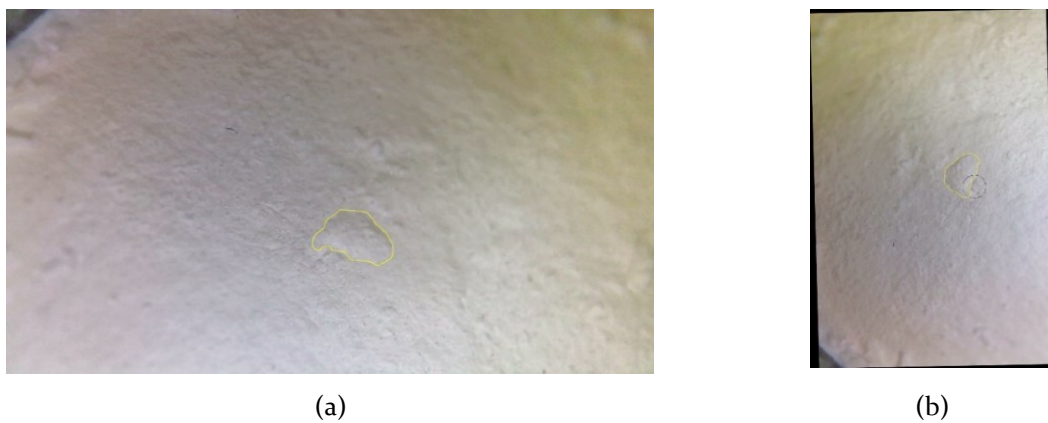


Figure 17. Output of flake dimension retrieval pipeline. (a) the manually segmented flake in yellow (ROI) in the camera view. (b) the rectified ROI and image after the application of the homography transformation, quantitative information on the flake dimensions can now be retrieved.

3.5.3 Summary of the procedure to characterize the geometry of the flake

Calibration of the homography transformation matrix

1. Retrieve initial frames for the determination of the homography transformation matrix coefficients (Figure 15a);
2. Via a Python-based GUI and OpenCV library, mark five points on the nozzle footprint ellipse on the slanted frame (Figure 15b);
3. Calibrate the transformation matrix to obtain a unit circle in the 'rectified' image and use the known dimension of the outer diameter of the nozzle (1.6mm) to scale the nadiral view (Figure 15c).

Substruction, ROIs segmentation, and homography transformation:

4. Select two frames from the video at the time stamps of interest imaging the flake before and after detachment;
5. Perform frame to frame difference (as in Figure 16c);
6. Contour the flakes manually into ROIs (Figure 17Error! Reference source not found.a);
7. Apply the homography transformation to the ROIs (Figure 17b) to obtain the 'rectified' flake ;
8. Retrieve the geometric information from the nadiral ROIs, i.e., the area of the flake.

4 RESULTS

4.1 Detachment mechanism in reconstituted samples at pH4

4.1.1 Flake detachment

The observed detachment mechanism mainly consisted of the detachment of clay flakes, i.e., flat and thin pieces of clay lifted by the impinging jet. They are referred to as ‘flakes’ according to the Oxford dictionary, “a small, very thin layer or piece of something, especially one that has broken off from something larger. i.e. flakes of snow/paint”.

Figure 18a shows the schematic layout of the detachment mechanism observed in the samples reconstituted by self-weight and in the oedometer to 89 and 888 kPa vertical stress. The jet undermines the uppermost layer, possibly through an existing discontinuity, causing the bending and lifting of the layer and then the detachment of the flake.

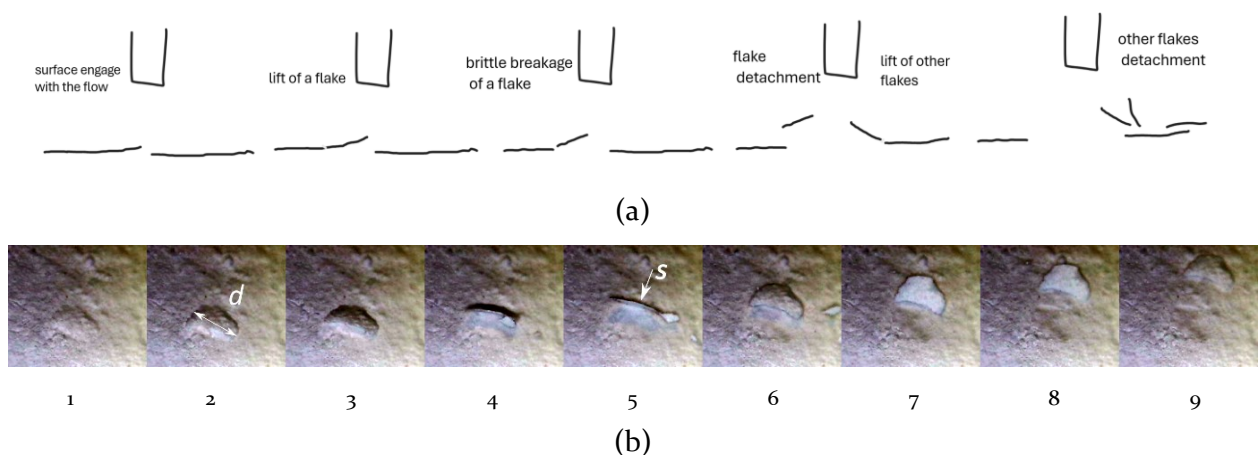


Figure 18. Detachment of single flake. (a) Schematic layout of the detachment mechanism. (b) Video frames showing the different detachment stages, lifting (frames 1-5), breakage and overturning (frames 6-7); sweeping away (frames 8-9).

Figure 18b shows the frame sequence of a single flake undermined by the flow generated by the impinging jet, i.e., layer lifted from sample surface in ‘cantilever mode’, breakage of the layer and detachment of the flake, and flake overturned and swept away outside the area of influence of the jet. It can be observed from frames 2 and 5 in Figure 18b that the planar dimension of the flake, d , is much larger than its thickness s .

4.1.2 Effect of pre-consolidation stress on flake detachment

Figure 19a shows an example of the flake detaching from the sample consolidated by self-weight under an overburden pressure 0.88 kPa and subjected to 0.38 Pa shear stress. The clay layer curls as if it was peeled by the impinging jet and then detaches from the surface.

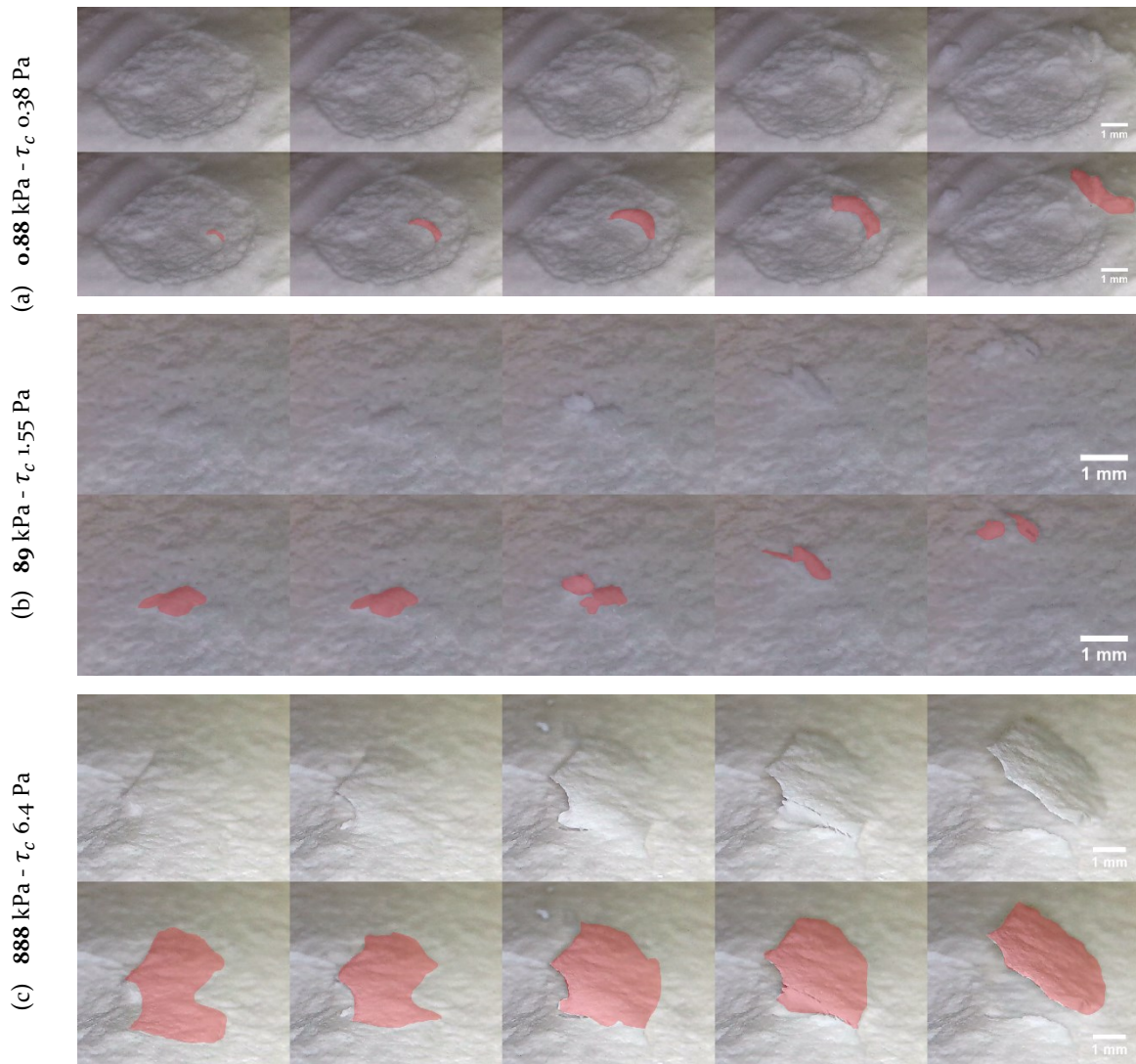


Figure 19. Frames sequence of flake detachment for different consolidation vertical stress. The first row shows the original frames, the second row shows the detaching flake highlighted in red. (a) sample consolidated by self-weight ~ 0.88 kPa. (b) sample consolidated to 89 kPa. (c) sample consolidated to 888 kPa.

Figure 19b shows an example of the flake detaching from the sample consolidated to 89 kPa and subjected to 1.55 Pa shear stress. In this case, the layer lifted by the impinging is more rigid, and part of the lifted layer breaks down generating the two flakes that are swept away.

Figure 19c shows the detaching flake from the sample consolidated to 888 kPa and subjected to 6.4 Pa shear stress. The lift of the layer is clearly visible and its detachment following the breakage of the layer that resembles to the failure of a cantilever plate. The initial lift of a clay layer is also visible in the area below the detached flake.

4.1.3 Planar dimension of first detached flake

Reconstituted samples at pH 4 were consolidated by self-weight and in the oedometer. The results are presented for one sample consolidated by self-weight tested at a depth associated with an overburden pressure of ~ 0.88 kPa, one sample consolidated in the oedometer to 89 kPa vertical stress, and two

samples consolidated in the oedometer to 888 kPa vertical stress (samples A and B respectively, see Figure 5). Each sample was tested at different locations on its surface and, in some cases, multiple flakes detached simultaneously.

Table 1 reports the size of the flakes and the shear stresses associated with first detachment. The planar dimension of the flake was chosen as the diameter of a circle of area equal to the area of the detached flake.

The shear stress of first detachment for a given sample, τ_{first} , was calculated as the weighted average of the shear stresses causing the detachment of flakes at different locations on the sample surface. The hydraulic head was increased in discrete steps and so did the shear stress imposed by the impinging jet. Some flakes detached at one imposed shear stress; some others detached at a next imposed shear stress. The shear stress of first detachment was calculated as follows:

$$\tau_{first} = \sum_{i=1}^2 \frac{n_i * \tau_i}{n} \quad [6]$$

where n_i are the number of flakes detaching at the imposed shear stress τ_i , and n is the total number of flakes. The first flake detachment occurred at the shear stresses of 0.5, 1.20, 2.2 and 5.4 Pa for the samples reconstituted by self-weight, 89kPa, and samples B and A consolidated to 888 kPa, respectively.

Table 1. First flake detachment stress and dimensions for sample

Sample	Tau [Pa]	Area [mm ²]	Equivalent diameter [mm]	τ_{first} [Pa]	
~ 0.88 kPa	0.38	0.24	0.55	0.5	
~ 0.88 kPa	0.38	0.27	0.59		
~ 0.88 kPa	0.38	0.34	0.66		
~ 0.88 kPa	0.38	0.43	0.74		
~ 0.88 kPa	0.38	0.66	0.91		
~ 0.88 kPa	0.38	0.66	0.92		
~ 0.88 kPa	0.72	0.98	1.12		
~ 0.88 kPa	0.72	1.77	1.50		
~ 0.88 kPa	0.72	1.82	1.52		
89 kPa	1.55	0.30	0.62		1.2
89 kPa	1.55	0.32	0.64		
89 kPa	0.72	0.78	0.99		
89 kPa	0.72	0.87	1.05		
89 kPa	1.55	1.00	1.13		
89 kPa	1.55	1.05	1.16		
89 kPa	1.55	1.32	1.30		
89 kPa	0.72	1.50	1.38		
89 kPa	0.72	2.73	1.86		
89 kPa	1.55	2.99	1.95		
89 kPa	0.72	4.29	2.34		
89 kPa	1.55	5.98	2.76		
888 kPa - B	1.55	2.57	1.81	2.2	
888 kPa - B	2.90	4.36	2.35		
888 kPa - B	2.90	4.79	2.47		
888 kPa - B	1.55	7.41	3.07		
888 kPa - A	2.90	0.49	0.79	5.4	
888 kPa - A	2.90	0.62	0.89		
888 kPa - A	2.90	0.90	1.07		
888 kPa - A	6.41	1.32	1.30		
888 kPa - A	13.70	2.99	1.95		
888 kPa - A	6.41	4.20	2.31		
888 kPa - A	2.90	7.41	3.07		

All flakes detaching from the same sample were grouped together to derive the cumulative distribution of the flake size shown in Figure 20. The equivalent diameter D_{50} appears to generally increase with the pre-consolidation increases although the samples consolidated to 89 kPa and the sample A consolidated to 888 kPa show very similar D_{50} .

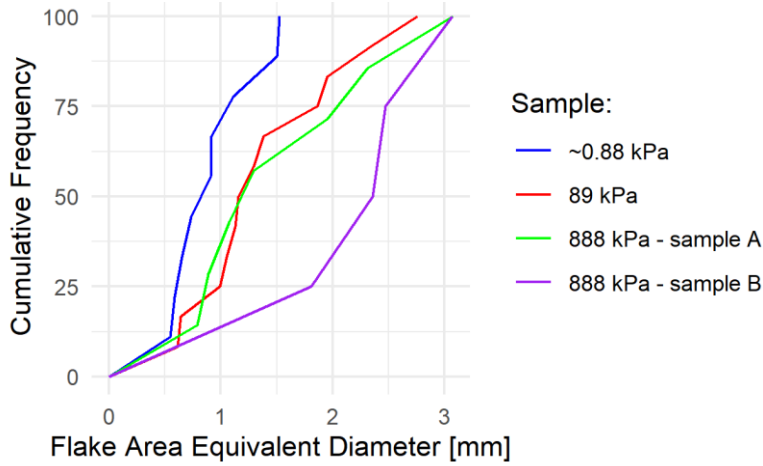


Figure 20. Cumulative distribution of size of first detachment flakes for samples consolidated at different pre-consolidation stress.

4.1.4 Planar dimension of first and subsequent detached flakes

Figure 21 shows the cumulative distribution of the dimension of all flakes detaching from the sample surface. When considering all flakes detaching from the surface, the equivalent diameter D_{50} clearly increases with the pre-consolidation stress. The detachment shear stresses recalculated according to Eq.[6] by including first and subsequent detached flakes were 0.5, 3.2, 9.7, 16.5 Pa for the samples consolidated by self-weight, to 89kPa, and samples B and A consolidated to 888 kPa, respectively.

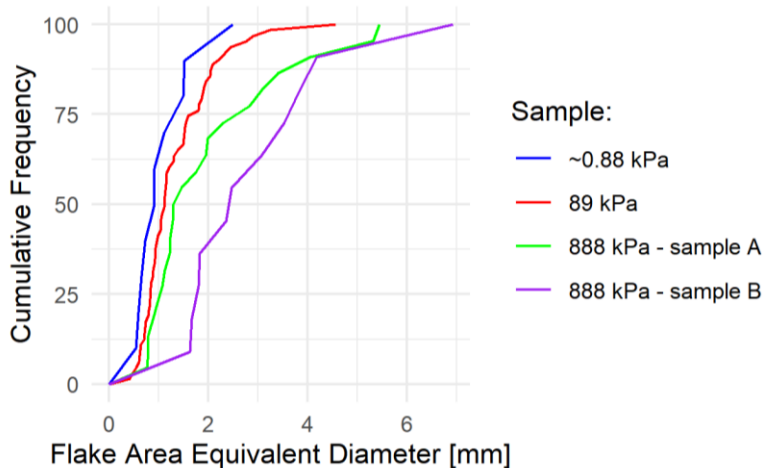


Figure 21. Cumulative distribution of size of first and subsequent detachment flakes for samples consolidated at different pre-consolidation stress.

4.1.5 Flake thickness

The thickness of the flakes detaching from the surface was investigated for the samples consolidated to different pre-consolidation pressures (Figure 22). For the sample consolidated by self-weight, it is difficult to detect the thickness directly on the flake because the flake curls. It is much easier to identify the flake thickness from the scar left by the flake on the sample surface as shown in Figure 22a. For the sample consolidated to 89 kPa, the flake thickness appears clear in Figure 22b, where the flake side is visible to the camera in the second frame (i.e., the flake plane is quasi-orthogonal to the camera view). Similarly, the thickness of the flake detaching from the sample consolidated to 888 kPa can be viewed in the second frame of Figure 22c.

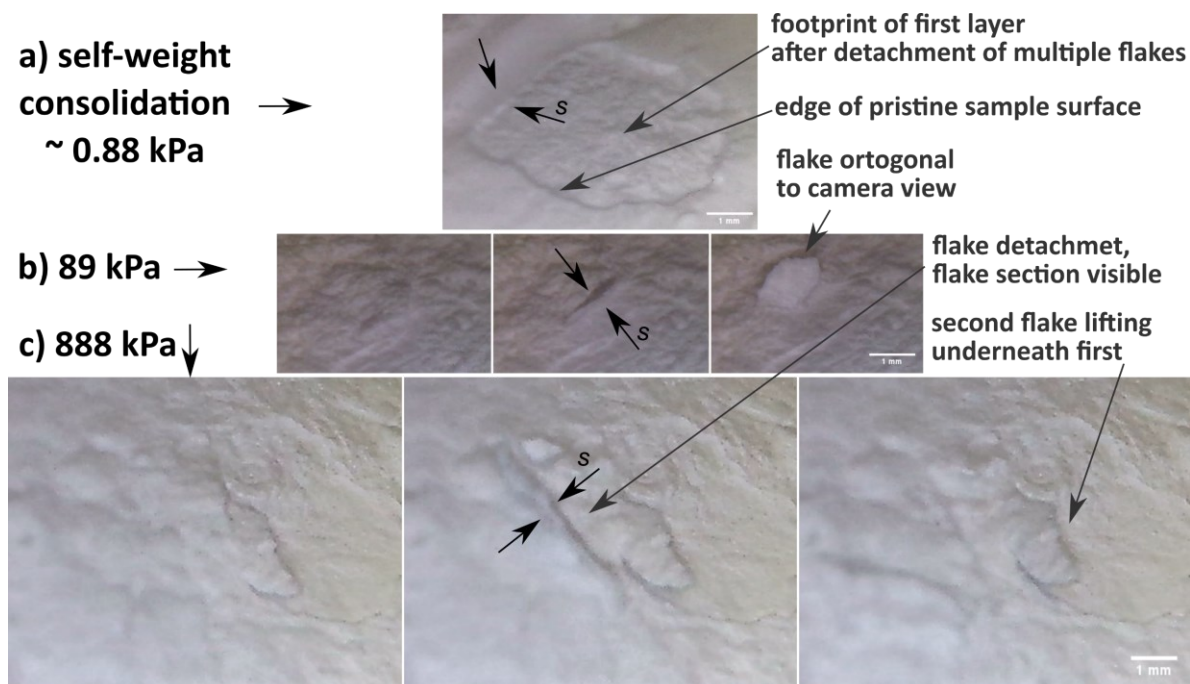


Figure 22. Comparison of flake thickness observed for the samples consolidated to different pre-consolidation stress.

4.1.6 Summary of findings on detachment mechanisms

The schema of Figure 23 comes to hand in looking more in depth at the detachment kinematics with regards to sample formation conditions. Erosion occurred in the form of detachment of flakes with two main features observed: i) the planar dimension d of the flakes increase as the sample is consolidated to a higher stress and ii) the thickness of the flake, s , also increases with the consolidation stress. Moreover, the flexural stiffness of the clay layer that is lifted by the impinging jet also appears to increase with the pre-consolidation stress (the clay layer consolidated by self-weight was ‘peeled off’ by the jet whereas the clay layer of the samples consolidated to the highest stress remained planar when lifted before breakage). These two experimental observations are consistent with the flexural stiffness D of a plate increasing with cube of the plate thickness, s ($D \propto s^3$).

Figure 23 presents a graphical summary of the detachment mechanisms observed experimentally. As the pre-consolidation stress increases, the planar dimension, the thickness, and flexural stiffness of the flakes increase. On the x-axis is represented the time evolution of the eroding samples while on the y-axis the flake thicknesses increase as the consolidation load increases.

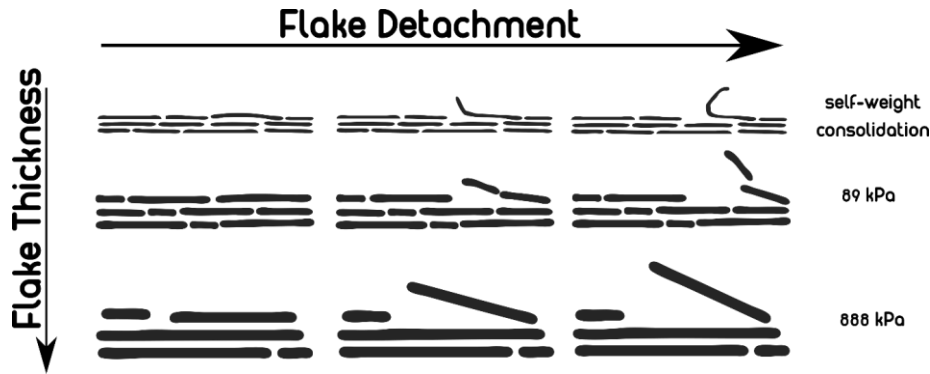


Figure 23. Schema depicting the dynamic of flake detachment observed with increasing consolidation vertical stress.

4.2 Interplay between detachment mechanism and fabric as induced by different hydraulic, mechanical, and chemical loading

From the visual inspection of samples subjected to flake detachment due to the impinging jet, it appears that the reconstituted clay sample exhibits a 'layered' fabric, which extends below the sample surface. This layered fabric triggers the detachment of flakes instead of individual particles or equidimensional aggregates (or fragments) and therefore plays a key role in the erosion mechanisms of reconstituted clay.

To investigate more in depth the interplay between the detachment mechanism and the fabric generated by different modes of loading (hydraulic, mechanical, and chemical) and the factors controlling the genesis of the layered fabric, different bespoke tests were carried out to address research questions arisen from the jet erosion tests or cascaded directly from these bespoke tests as new observations were made.

4.2.1 Underlying fabric of samples consolidated to different pre-consolidation stress

Figure 24 shows the pristine surface (o in the figure) before erosion and the scour hole for the sample consolidated by self-wight under 0.88 kPa overburden pressure. Up to four layers can be identified as indicated by the arrows. Some 'debris' originated by the breakage of the layers into flakes can also be observed on the left of the scour hole.

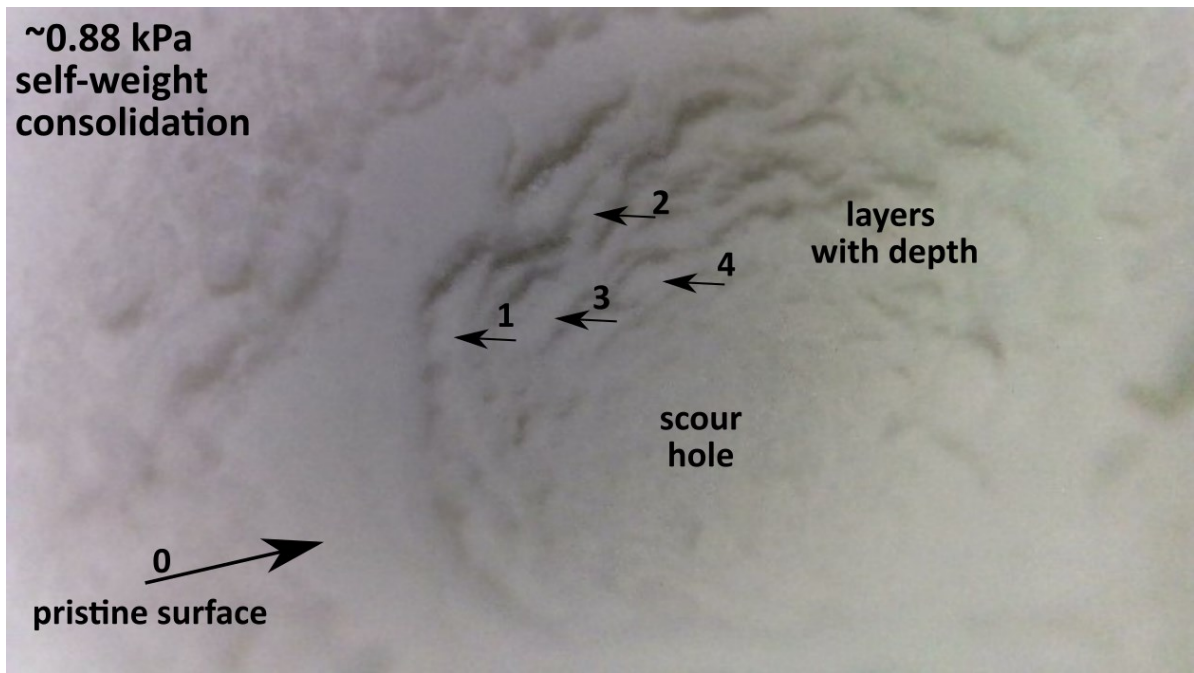


Figure 24. Layered fabric observed with depth for sample consolidated by self-weight to ~ 0.88 kPa.

Figure 25 shows a scour hole for the sample consolidated to 89 kPa. Four layers can be detected as indicated by the arrows, which form a 'terraced' profile. The sample consolidated to 888 kPa also shows a 'terraced' profile (Figure 26), that is a very similar fabric as the sample consolidated to 89 kPa. However, the detaching flakes become larger and thicker.

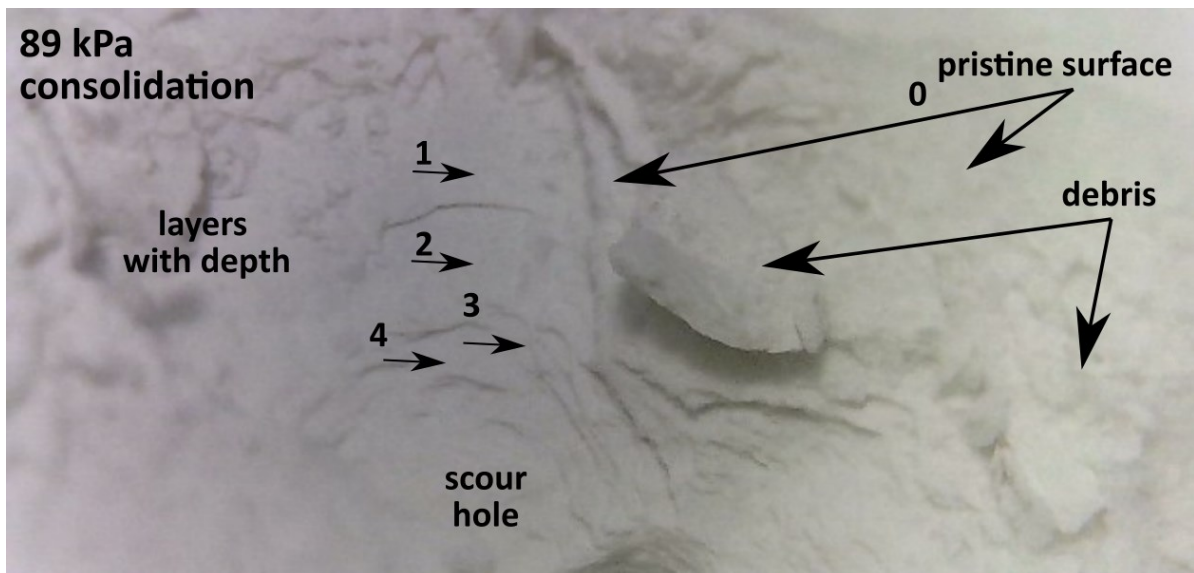


Figure 25. Layered fabric emerging as multiple flakes detach from the sample consolidated to 89 kPa.

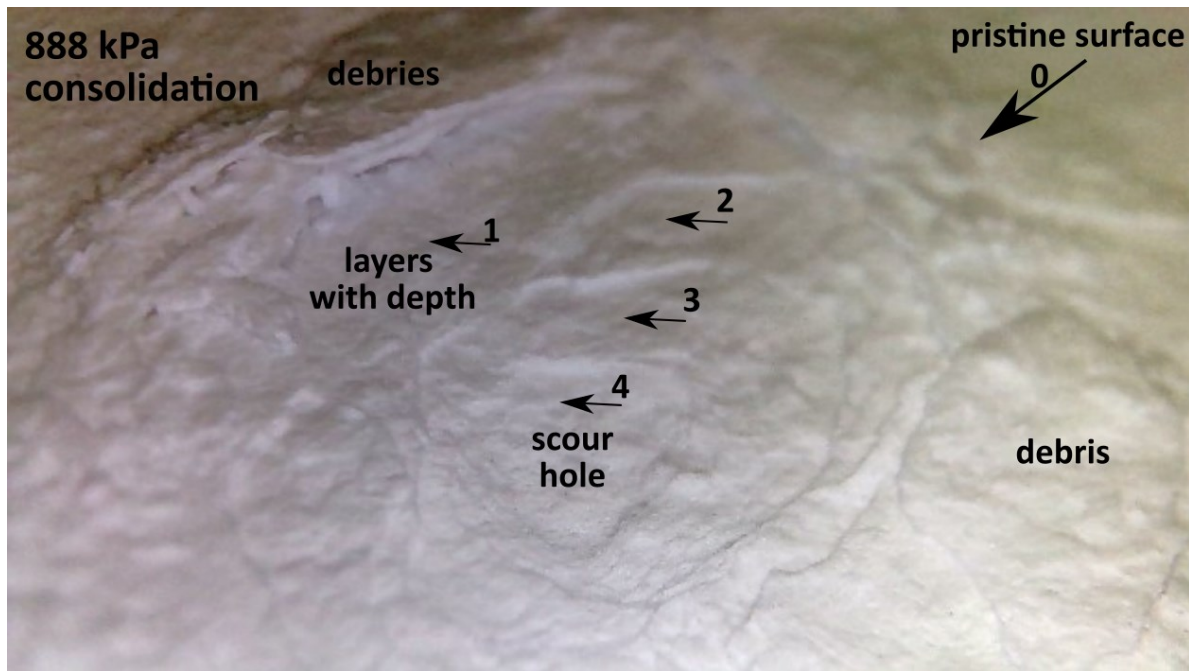


Figure 26. Layered fabric emerging as multiple flakes detach from the sample consolidated to 888 kPa.

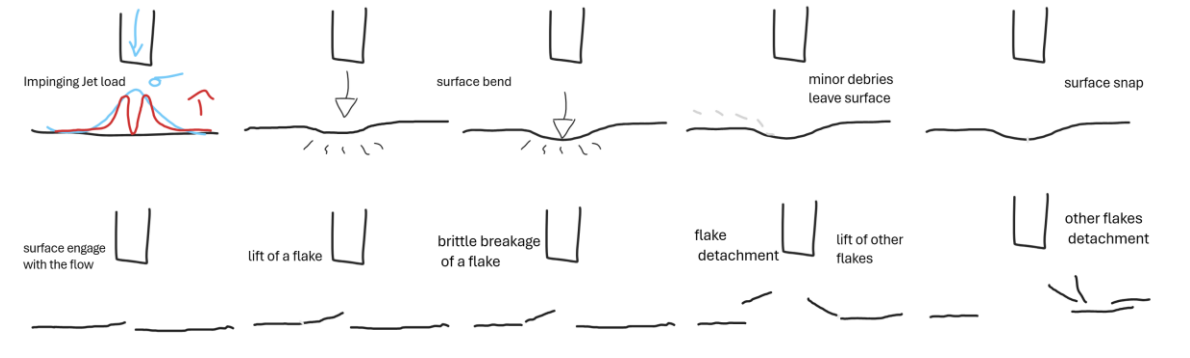
4.2.2 Detachment from non-draining surface during consolidation

Figure 27a shows the detachment mechanism observed in the sample consolidated in the oedometer to 888 kPa with an impervious top surface, i.e., no drainage occurred across the top surface during consolidation. The surface of the sample first undergoes an ‘elastic’ deformation with the sample surface ‘bending’ under the pressure generated by the impinging jet. Over time, very small ‘debris’ leave the surface until the jet punctures the uppermost layer generating a flexural cracks similar to a plate undergoing excessive deflection. The impinging jet undermined the first layer causing the layer to deflect upward (like a cantilever plate) until the layer breaks and a flake detaches. Following the first detachment, other flakes are observed to detach.

This mechanism is represented schematically in Figure 27b showing at first a stage consisting of surface indentation (first row), which was not observed in the samples consolidated with a top draining surface (Figure 18). However, the lift, deflection, and breakage of the first layer and the consequent detachment of flakes is similar to the samples consolidated with a top draining surface (Figure 18). It is noted that the non-draining surface required a very high shear stress (23 Pa) to generate the surface indentation and first flake detachment.



(a)



(b)

Figure 27. Flake detachment from non-draining surface during consolidation (a) Video frames representing the corresponding sequence (e.g. surface puncture and subsequent detachment). (b) Schematization of the extended detachment mechanism from indentation of the surface by the jet to the flake detachment

Following the detachment of the first flakes underneath the jet centre line, further detachments from the surface occur away from jet centre as highlighted by the yellow and red shaded area in Figure 28. The yellow and red shaded flakes are still part of the original sample surface and are swept away from the impingement area. Subjected to the same jet shear stress (23 Pa), a second flake detaches from the area that was previously covered by the yellow flake after 3 minutes (Figure 28-second row). This second flake is detaching from a layer underneath the first ‘crust’ and is thinner and more flexible.

This test shows that the drainage history of the surface affects the shear stress required to generate a first detachment and also the size of the detached flakes. When the surface did not experience drainage during stress-controlled consolidation, flakes were larger and thicker compared to the sample consolidated in stress control but with the draining top surface.

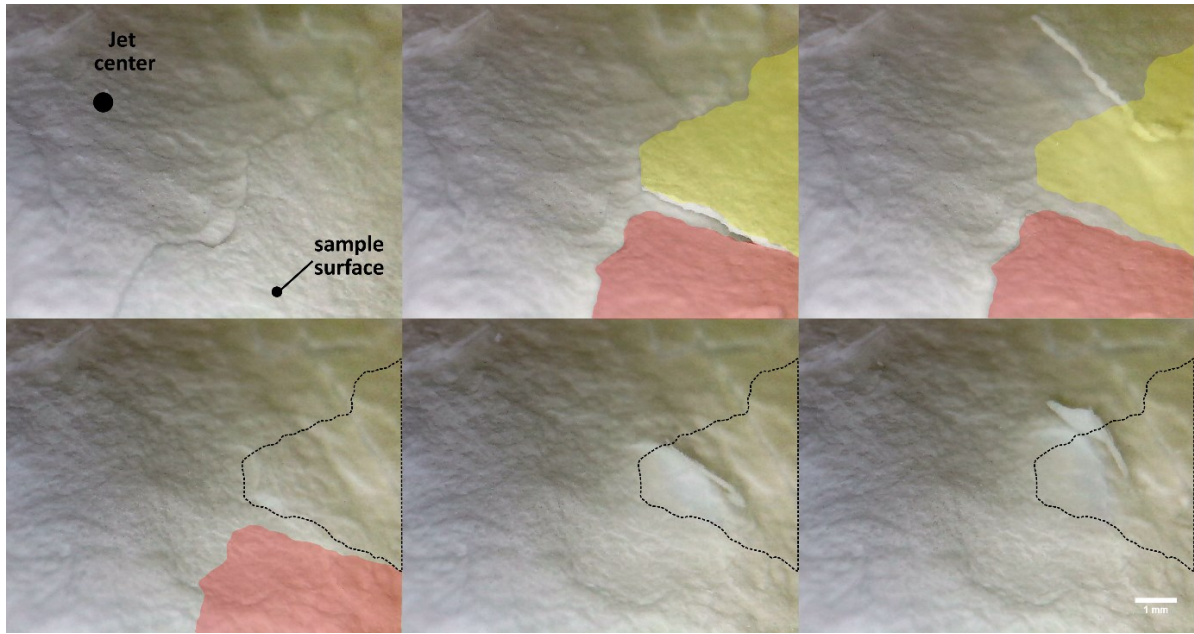


Figure 28. Large flake detachment in the sample consolidated in oedometer with impervious ‘non-draining’ top surface. The flake shaded in yellow detaches first followed by the flak shaded in red (frame progression from left to right and top to bottom). A second layer is lifted and a flake detaches under the foot print of the yellow flake.

4.2.3 Detachment from draining surface upon consolidation at slow deformation rate

Figure 29 show the flake detachment occurring on the surface of the sample consolidated at slow deformation rate (0.002 mm/min) to 888 kPa vertical stress (as opposed to the sample in Figure 19 consolidated in load control). A shear stress of 39 Pa was required to cause the first flake detachment. After the detachment of smaller flakes just underneath the jet centreline, a very large semi-annulus flake detaches from the sample surface, which then breaks in two pieces that move out of the impingement area of the jet. Both the shear stress required for flake detachment and its size are the biggest among all tested samples. This sample presented an erosion mechanism similar to the one described in Figure 25a for the sample consolidated with ‘non-draining’ impervious top surface.

This test shows again that the drainage history, associated with the low flow rate through the top surface during consolidation in this case, affects the shear stress required to generate a first detachment and the size of the detached flakes.



Figure 29. Very large semi-annulus flake detachment in sample consolidated at slow deformation rate. Frame progression from top left to bottom right.

4.2.4 Detachment from non-draining surface of sample subjected to radial consolidation

Figure 30 shows the detachment mechanism occurring in the sample subjected to radial consolidation. Small fragments initially detached for the surface at 2.9 Pa (Figure 30-frame 1), the scour hole deepened when the shear stress imposed by the impinging jet is increased to 5.3 and 6.4 Pa (Figure 30-frames 1-15) with the detachment of small fragments (e.g., red shaded fragment in frames 8 and 9 in Figure 30 detaching at 5.3 Pa shear stress). The scour hole in the sample consolidated radially deepens as opposed to the scour hole expanding laterally as observed for the sample consolidated by vertical drainage. Increasing further the shear stress to 10.1 Pa, two large fragments detach (Figure 30-frame 17).

To better elucidate the failure mode, the detachment of the fragments is schematically represented along the cross section AA' in the inset in frame 17. The fragments show higher sphericity ('less platy') compared to the flakes detaching from the samples consolidated under vertical drainage. Thus the radially consolidated sample is eroding by smaller units at lower stress or by big fragments if the load is increased above a certain threshold and the scour hole allow to erode the sample from the side of the scour it-self. The radially-consolidated sample is eroded by lower shear stresses compared to the samples consolidated under vertical drainage through the top surface (Figure 19c).

This test shows that the direction of flow during consolidation affect the layered fabric. Horizontal layers are formed if drainage occurs in vertical direction causing the detachment of platy fragments (flakes). When the sample is consolidated radially, there is no evidence of horizontal layers and fragments detaching form the surface are more rounded.

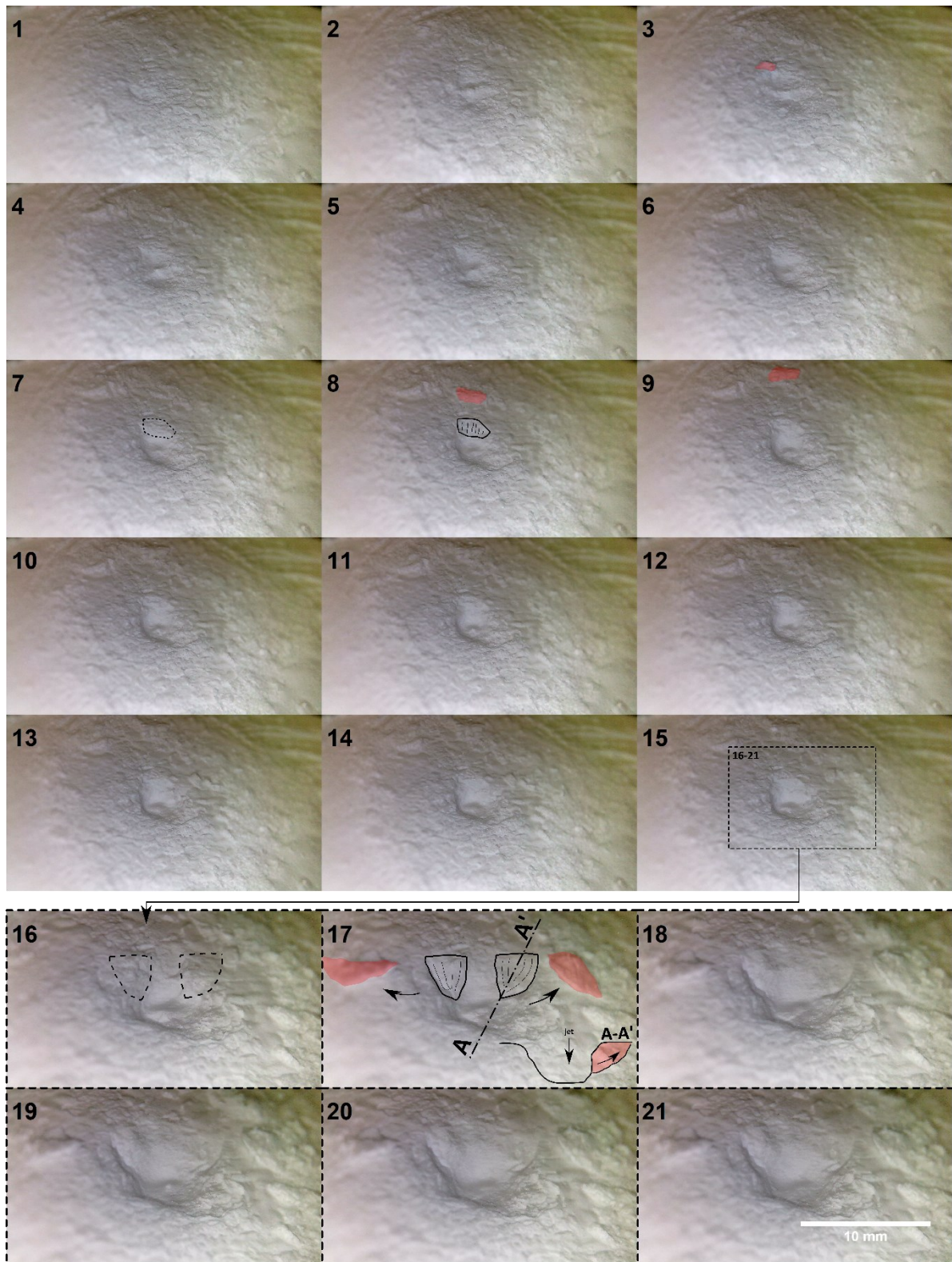


Figure 30. Erosion of radially consolidated sample. Frames 1-15 show the scour hole deepening with the detachment of small fragments. Frames 16-18 show the detachment of two large fragments.

4.2.5 Detachment from surface draining during suction-induced consolidation

Slurry with flat surface

Figure 31a shows a slurry sample ($w=100\% \sim 1.5 w_L$) submerged with water and ready to be tested. Prior to submergence, the slurry sample was exposed to air drying for few minutes, i.e. capillary suction generated at the horizontal surface and suction-induced drainage occurred vertically (normal to the drying surface). Figure 31b shows the detachment of flakes from the sample surface (occurring at 2.9 Pa shear stress). A flake appears to have already detached from the surface (top right in the image) while flakes around the jet centre are being lifted and prone to detachment.

This test shows once again that the drainage history (in this case associated with water removal by air-drying) affects the fabric with layering forming in the direction orthogonal to the drainage path. In turn, this causes detachment in form of flakes.

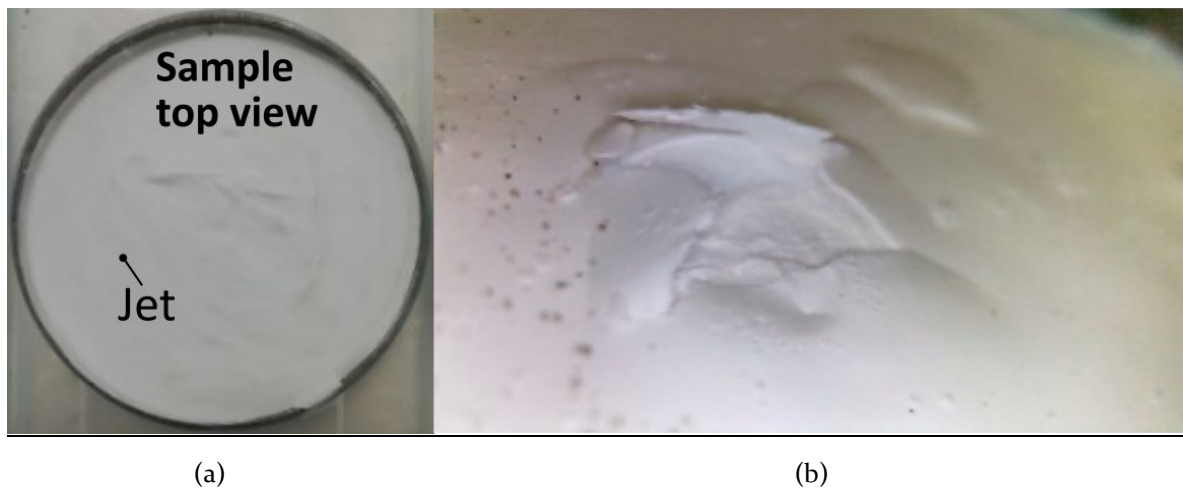


Figure 31. Slurry at repose-flat sample. (a) top view of sample ready to be tested. (b) Flake detachment from pristine surface.

Slurry with irregular surface

Figure 32 shows the slurry dropped from a spoon into the oedometer ring and left as is, i.e., the slurry surface remained irregular. Again, the sample was exposed to air drying for few minutes, i.e. capillary suction generated at the surface and suction-induced drainage occurred in the direction normal to the drying surface. As shown in Figure 32, the area of the sample tested was nearly vertical with some bulges on the surface. Figure 33 shows the scour hole evidencing a layered fabric with layers parallel to the surface. These layers caused the detachment of flakes parallel to the surface (at a shear stress estimated to 0.7 Pa).

This test confirms that layering is directly associated with the direction of flow in proximity of the surface during consolidation, which is suction-induced in this case. At the same time, gravity does not seem to play a role in the formation of the layers (otherwise layers would have been sub horizontal even on the quasi-vertical surface).

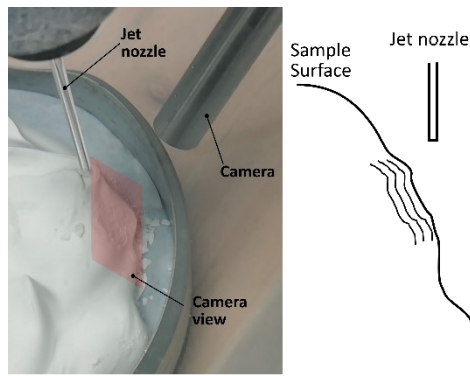


Figure 32. Slurry placed in oedometer ring-irregular-shape sample erosion setup.

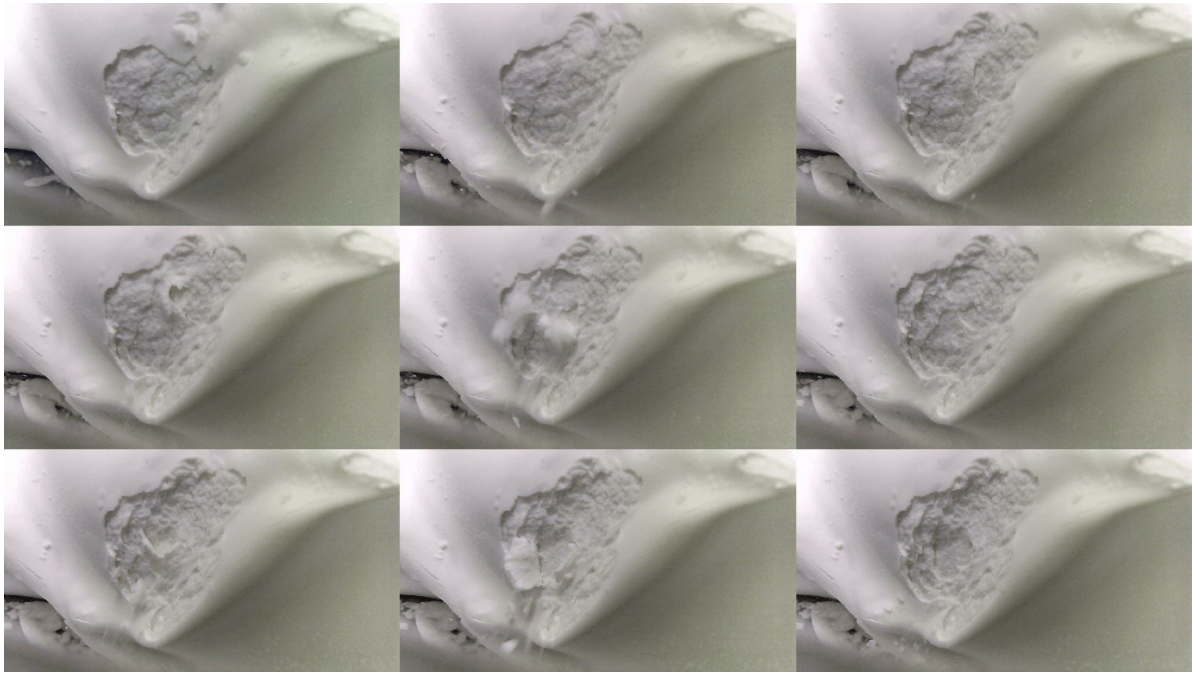


Figure 33. Slurry at repose-irregular-shape sample erosion. Flakes detaches from sample surface (first row). Further flake detachment in subsequent layers (2nd and 3rd row).

4.2.6 Detachment from outer surface and inner surfaces in sample consolidated by self-weight

This test has been designed to estimate the magnitude of consolidation stress required to form a layered fabric. The slurry was first let to consolidated by self-weight and the top surface was exposed to the impinging jet. Afterwards, a soil layer was removed and the impinging jet applied to the exposed inner surface. Figure 34 shows the procedure followed for this test. The drawings on the left report the sample preparation prior to the jet testing and the drawings on the right report the jet testing and the observed detaching units. The images are showing the detachment in a sequence of three frames.

After self-weight consolidation, erosion occurs in small aggregates and a stream of clusters of a few particles (row 1, shear stress applied equal to 0.4 Pa). As the shear stress is increased to 0.7 Pa, a relatively big fragment detached from the sample surface (row 2). After lowering the sample surface by using a siphon to gently suck up the overburden layer, sample surface was again subjected to the impinging jet by applying the same shear stress (0.7 Pa). The jet created a scour hole with the detachment of flake-like fragments (rows 3 and 4). The sample surface was then lowered further by means of the water siphon reaching a depth associated with a pre-consolidation overburden stress of ~ 0.7 kPa. At this stage, detachment occurred in form of flakes (rows 5 and 6).

This test shows that a layered fabric forms very rapidly as the (overburden) stress increases to values well below 1 kPa.

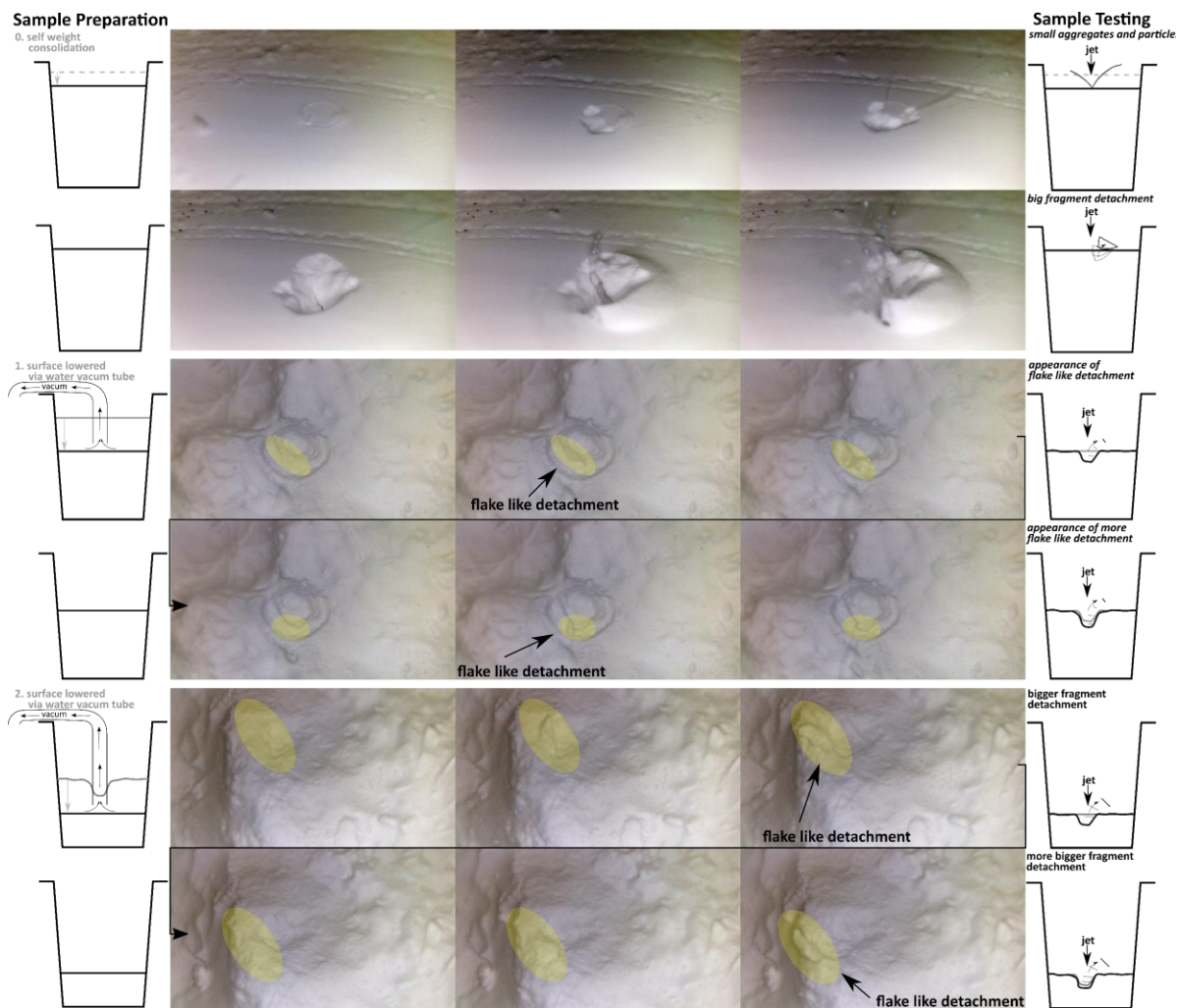


Figure 34. Self-weight in plastic beaker sample. Figure is divide in 3 main frame sequence eroding the sample surface at different depths. Drawings on the left depict sample preparation prir testing with the μ -jet. Drawings on the right depict μ -jet testing and observed detaching units. The sample erode in different detaching units based on jet hydrodynamic load and testing depth: particle or small aggregates (row1), big fragment (row2), embryonic flake detachment (rows 3and4), flake detachment (rows 5and6).

4.2.7 Detachment from draining surface of samples prepared at pH 9

Samples prepared at pH=9 were consolidated by self-weight, and to 89 kPa and 888 kPa vertical stress respectively, similarly to the samples prepared at pH=4. Markers were spread on sample surface to allow easier detection of sample erosion mechanisms due to low contrast associated with non-detectable sample fabric. The markers were made of black sand particles of ~ 100 μm diameter.

Figure 35 shows the sample consolidated by self-weight. When imposing the first shear stress (0.38 Pa), the sample behaved like a viscous-fluid with the formation of a crater. The jet created a 'fountain' with a suspension moving outwards from the impingement area. In the self-weight consolidated sample, this created a milk like liquid that quickly obfuscated the camera view. No aggregates detaching from the surface were visible and the erosion therefore involved the detachment of particles or small clusters of particles 'invisible' to the camera.

Upon the application of the following shear stress (0.72 Pa), a fountain-like outward flow was observed again. After a few seconds, the markers become visible again and also the interface between the fluidised bed and the 'undisturbed' position of the sample surface. After few minutes, the markers that has initially sunk into the sample surface started to move outwards from the jet centre line showing the increase of the depth and size of the scour hole. This sample clearly did not show any layered fabric and detachment in form of flakes as observed in the clay samples prepared at pH 4.



Figure 35. Sample prepared at pH9 by self-weight consolidation. First row: μ -jet applied to pristine sample surface at lowest imposed shear stress (0.4 Pa) causing bed 'fluidification'. Second row: μ -jet applied by imposing higher shear stress (0.7 Pa) on the already fluidized bed creating a 'fountain' like outward flow.

Figure 36 shows the erosion process of the sample prepared at pH 9 and consolidated to 89 kPa. Similarly to the previous sample, the sample surface fluidizes upon the application of the first shear stress increment at 0.4 Pa even if in this sample the process is much slower. Moreover, the markers did not sink into the sample surface but remained sparsely distributed across the pristine surface. Upon applying the second shear stress increment (0.7 Pa) a crater forms more clearly with the markers pushed towards the periphery of the crater. No major differences are identified between the sample reconstituted to 0.88 kPa and the one reconstituted to 89 kPa, besides the ease to fluidify the bed keeping the magnitude and time of the load the same. The fluidified bed did not mix with the eroding fluid in this sample.



Figure 36. Sample prepared at pH9 by consolidation to 89 kPa vertical stress. First row: jet applied to pristine sample surface imposing low shear stress (0.4 Pa). Second row: jet applied by imposing higher shear stress (0.7 Pa) dislodging the fluidized bed.

Figure 37 shows the erosion of the sample prepared at pH 9 and consolidated to 888 kPa vertical stress. The behaviour of the sample appears to be similar to the other samples prepared at pH 9. The main difference is represented by the markers that are not mobilised into the sample surface and a smaller diameter of the scour hole.

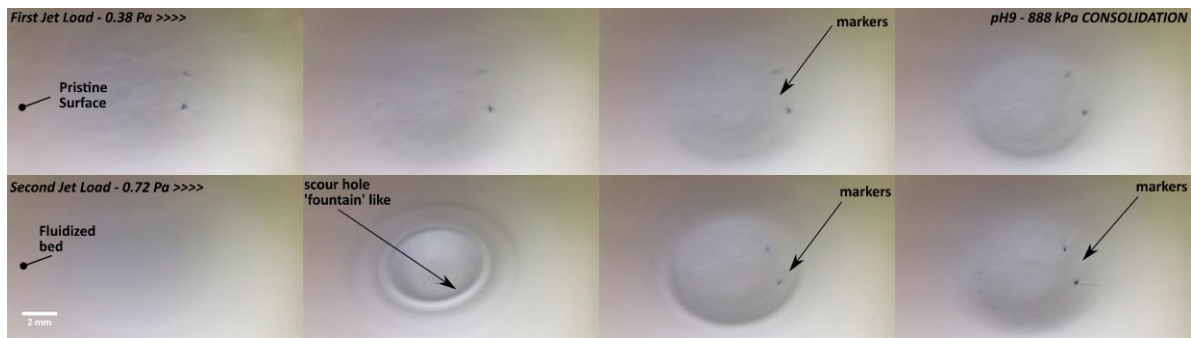


Figure 37. Sample prepared at pH9 by consolidation to 888 kPa vertical stress. First row: jet applied to pristine sample surface imposing low shear stress (0.4 Pa). Second row: jet applied by imposing higher shear stress (0.7 Pa) dislodging the fluidized bed.

This series of tests show that no layered fabric is generated in alkaline clay samples and that no major differences in the mechanism of erosion are observed in the samples consolidated at different pre-consolidation stress, all showing a 'fluidification' of the surface when exposed to the impinging jet (Figure 38).

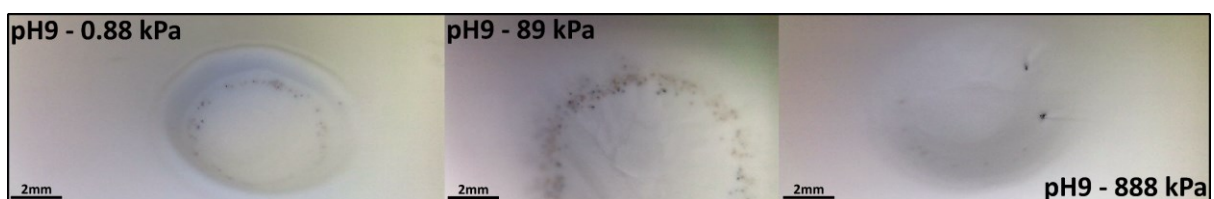


Figure 38. Comparison of scour hole observed at shear stress of 0.7 Pa at the end of 5 minutes in samples prepared at pH=9 and consolidated self-weight, and to 89 kPa and 888 kPa vertical stress respectively

4.2.8 Summary of findings on layered fabric and detachment unit

Figure 39 shows a summary for the different bespoke tests presented in this section to investigate the factors controlling the genesis of the layered fabric. The main difference in detachment mechanism and underlying fabric is associated with the chemistry of the pore-fluid used in sample preparation. All the samples prepared at pH9 do not show any layered fabric and, hence, detachment in the form of flakes. On the other hand, almost all samples prepared at pH4 presented a layered fabric and detachment in form of flakes (with the exception of the top surface of the sample consolidated by self-weight consolidation, which was subjected by zero effective stress).

The second major role is played by the hydraulic boundary conditions imposed to the samples prepared at pH4 during consolidation, which appears to control the thickness of the layers forming in the sample and, hence, the dimension and thickness of the detaching flakes. Compared to the samples prepared under 'ordinary' oedometer drainage (top and bottom of the sample), different mechanisms and fabric were observed when making the sample surface non-draining during consolidation. For the case of impervious surface with zero flow orthogonal to the tested boundary (i.e. impervious surface), the detachment shear stress and flake dimensions both increased. For the case of impervious surface due to consolidation flow occurring parallel to the tested boundary (i.e. radial consolidation), the sample eroded in more rounded fragments of different size, similarly to the self-weight consolidated sample at the top surface.

Another role is played by the magnitude of the pre-consolidation effective stress imposed to the sample during consolidation. At zero pre-consolidation stress (top surface of the sample consolidated by self-weight), there is no layering forming. However, as the pre-consolidation stress increase to about 1 kPa, either generated mechanically or hydraulically by the suction induced by air-drying, the clay shows a layered fabric and flake detachment.

Sample detachment units and shear stress for different loading conditions: hydraulic, mechanical and chemical

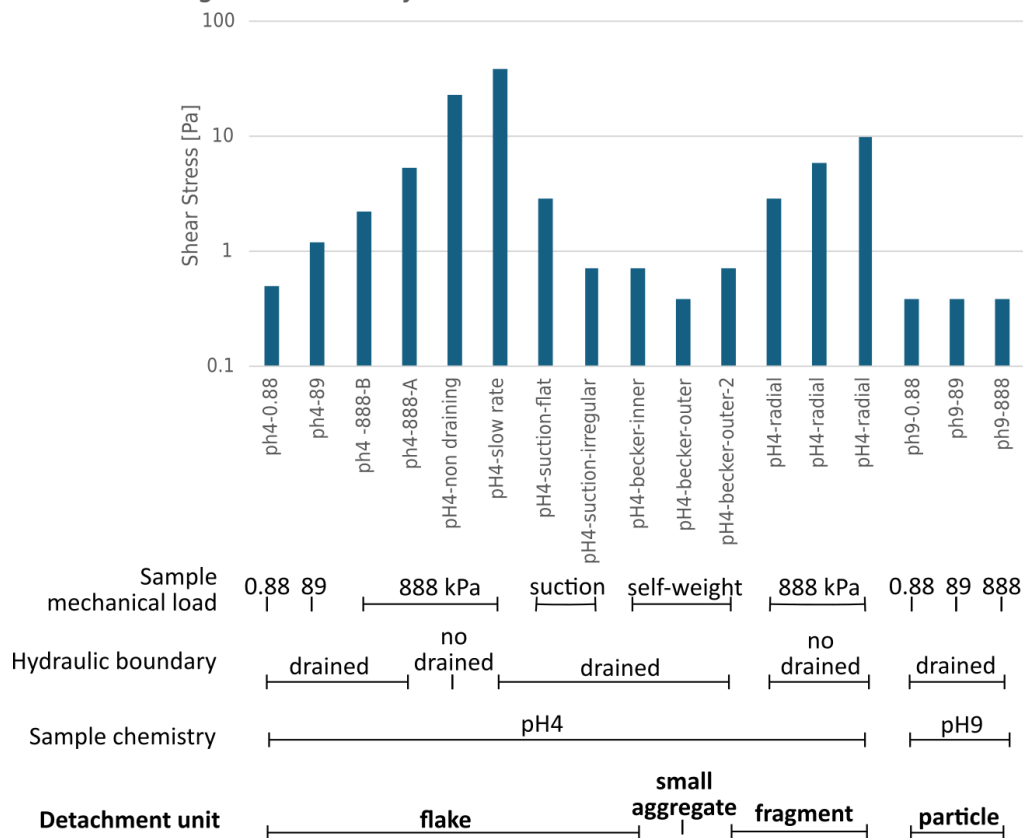


Figure 39. Sample detaching unit and shear stress summary as pre sample hydraulic, mechanical and chemical conditions.

4.3 Further observations of layered fabric

4.3.1 Direct observation of fabric in “standard” sample

To investigate sample fabric, a sample consolidated to 888 kPa in the oedometer was split in two halves under water with a spatula and the fracture surface observed more closely. Figure 40 shows the layered fabric observed at two different locations of the fracture surface (note that the different colours is only due to different lighting conditions). The layered fabric extends over the entire thickness of the sample .

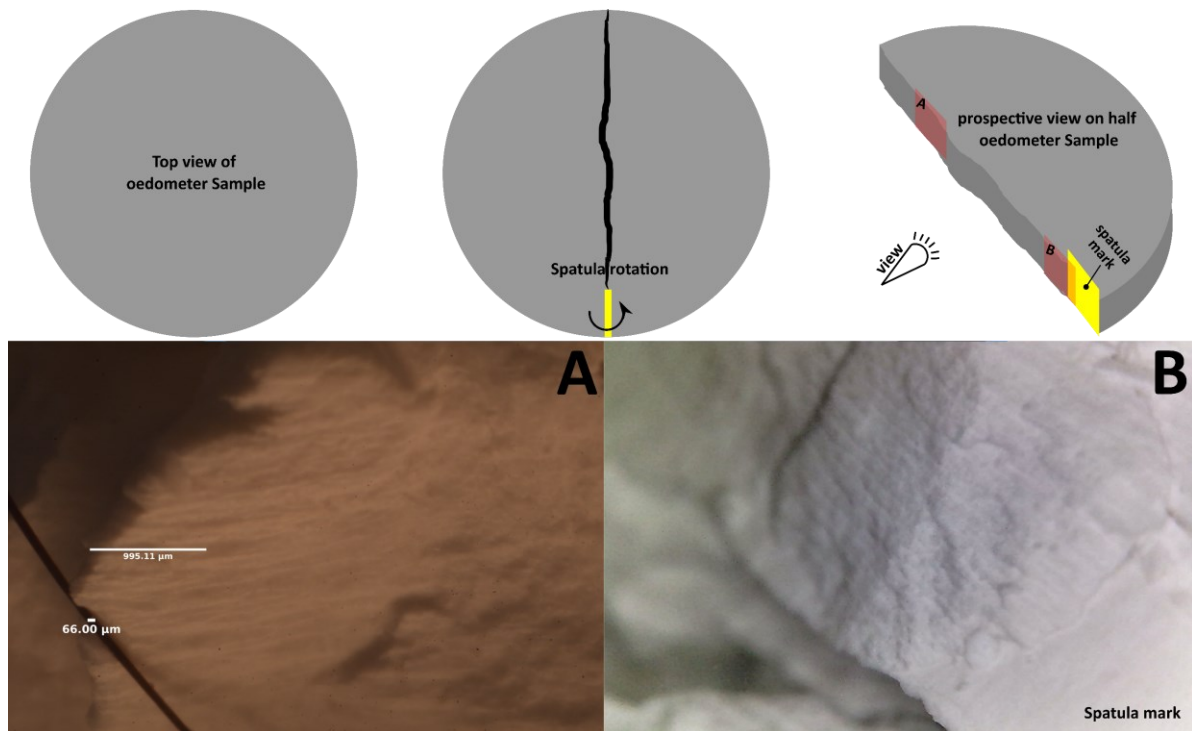


Figure 40. Layered fabric extending over the entire sample thickness observed on the fracture surface of a split sample.

4.3.2 Fabric generated by cusped top cap

In order to test whether the orientation of the layers depends on the direction of the principal strain applied to the clay boundary, a sample was loaded using a cusped top cap. The sample has been tested with the jet applied to 4 opposite location on the slopes of the cusp. The flakes detached from the surface progressively with depth revealing a layered fabric (Figure 41). Layers appeared to be parallel to the surface, i.e., normal to the direction of the principal strain. Due to the inclined surface the scour hole is asymmetrical nevertheless the layered fabric parallel to the two slopes of the sample have become apparent. The two shear stresses generating scour on the two sides of the cupola were 5.3 Pa and 10.0 Pa respectively.

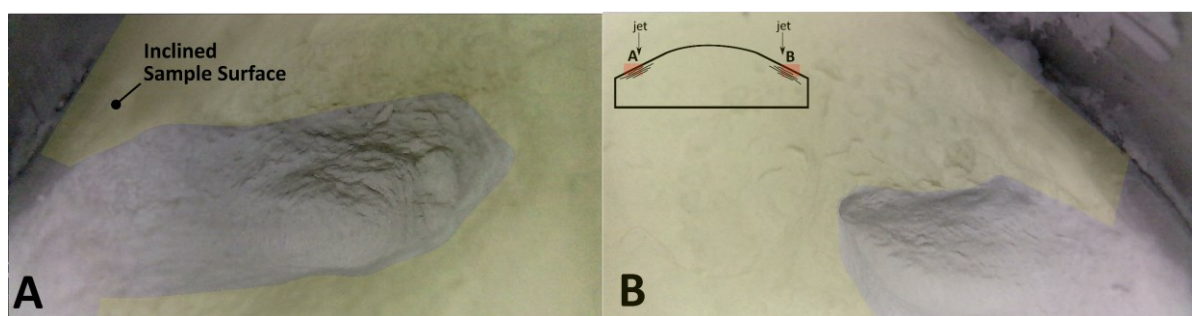


Figure 41. Layered fabric unveiled by erosion in the sample consolidated with cusped top cap. Original sample surface highlighted in yellow, location of the two areas exposed to the jet in the inset.

4.3.3 Fabric generated by zigzag top cap

To further investigate the finding that layers form normal to the direction of principal strain in proximity of the boundary, a sample was consolidated by using a zigzag top cap. After jet testing (with flakes detached from the inclined surfaces), the sample was bisected underwater with a spatula. Figure 42 shows the orientation of the layers parallel to the sample surface, especially near the left and right sides of the cusp.

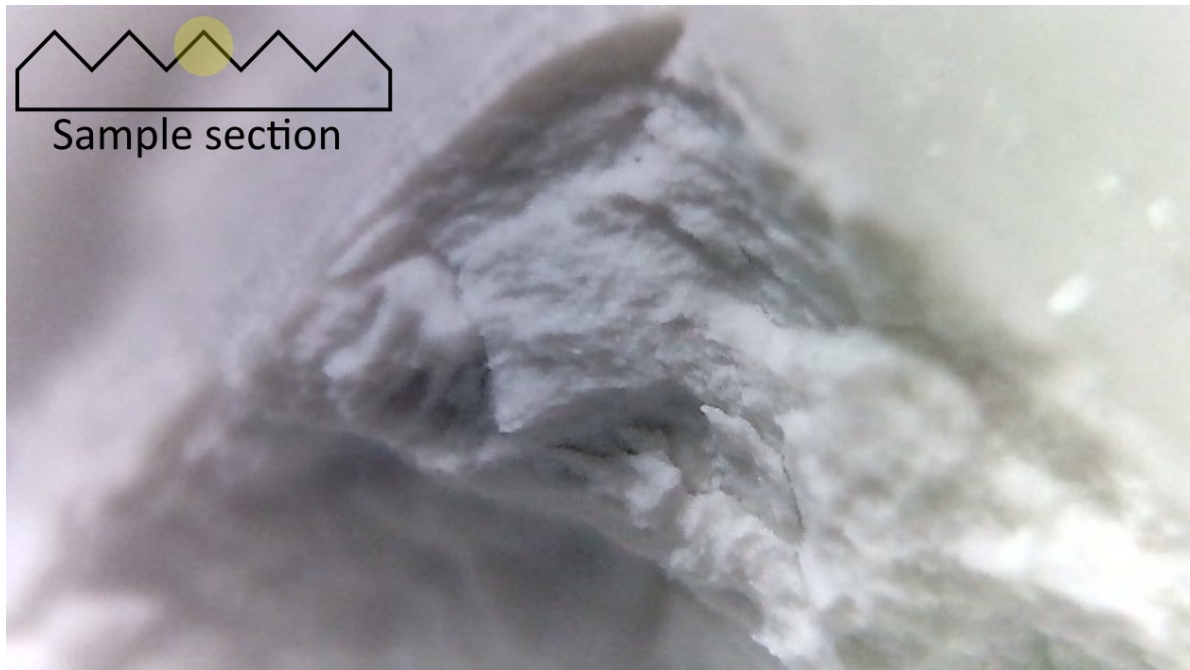


Figure 42. Detailed view of 'zigzag' sample after being split under water.

Encouraged by this observation, a second sample was prepared to investigate more closely the orientation of the fabric in the cross section. The entire sample was air-dried, then broken to isolate the central longitudinal cusp, then further broken to view the cross section of the central cusp (marked in red in Figure 43a). The cross section was then observed at the microscope with 4x magnification (Figure 43b). The location of the microscope images (T, L, R, B) are marked on the sample surface. Figure 43c shows the colour scale marking the orientation of the pixels from the microscope image.

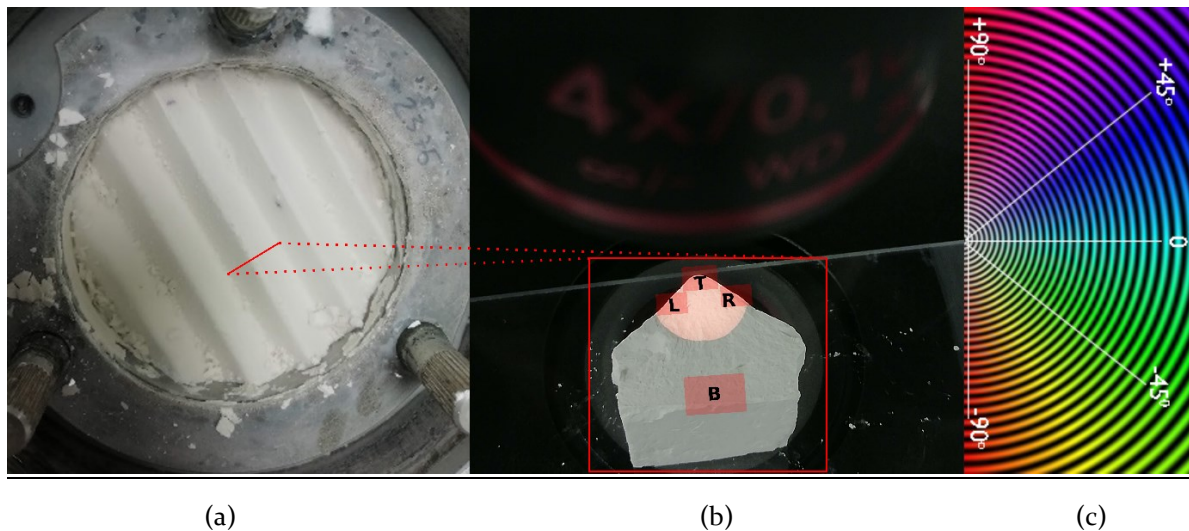


Figure 43. 'Zigzag' sample. (a) Sample ready to be tested and cross section observed at the microscope highlighted in red (b) Sample cross section observed at the optical microscope with locations marked as L,T,R, and B. (c) Colour scale used to represent pixel orientation.

Figure 44 reports the pixel orientation analysis performed with OrientationJ (Püspöki et al., 2017) within the ImageJ suite (Rueden et al.,2017). The first column shows the original image, the second the colour map of pixel orientation, and the third column the histogram of the pixel orientation values. The four rows refer to the four locations as indicated in Figure 43b. The image taken close to the cusp (T) shows two peaks, at $\sim +45$ and -45 degrees from the horizontal respectively. The image on the left-hand side of the cusp (L) presents a peak at $\sim +45$ degrees whereas the image on the right-hand side of the cusp (R) presents a peak at -45 degrees. The image taken at the bottom of the cusp (B) shows a modal value close to zero, i.e., pixels oriented horizontally.

This test confirms that layers tend to form parallel to the boundary (i.e., normal to the direction of the principal strain in proximity of the surface).

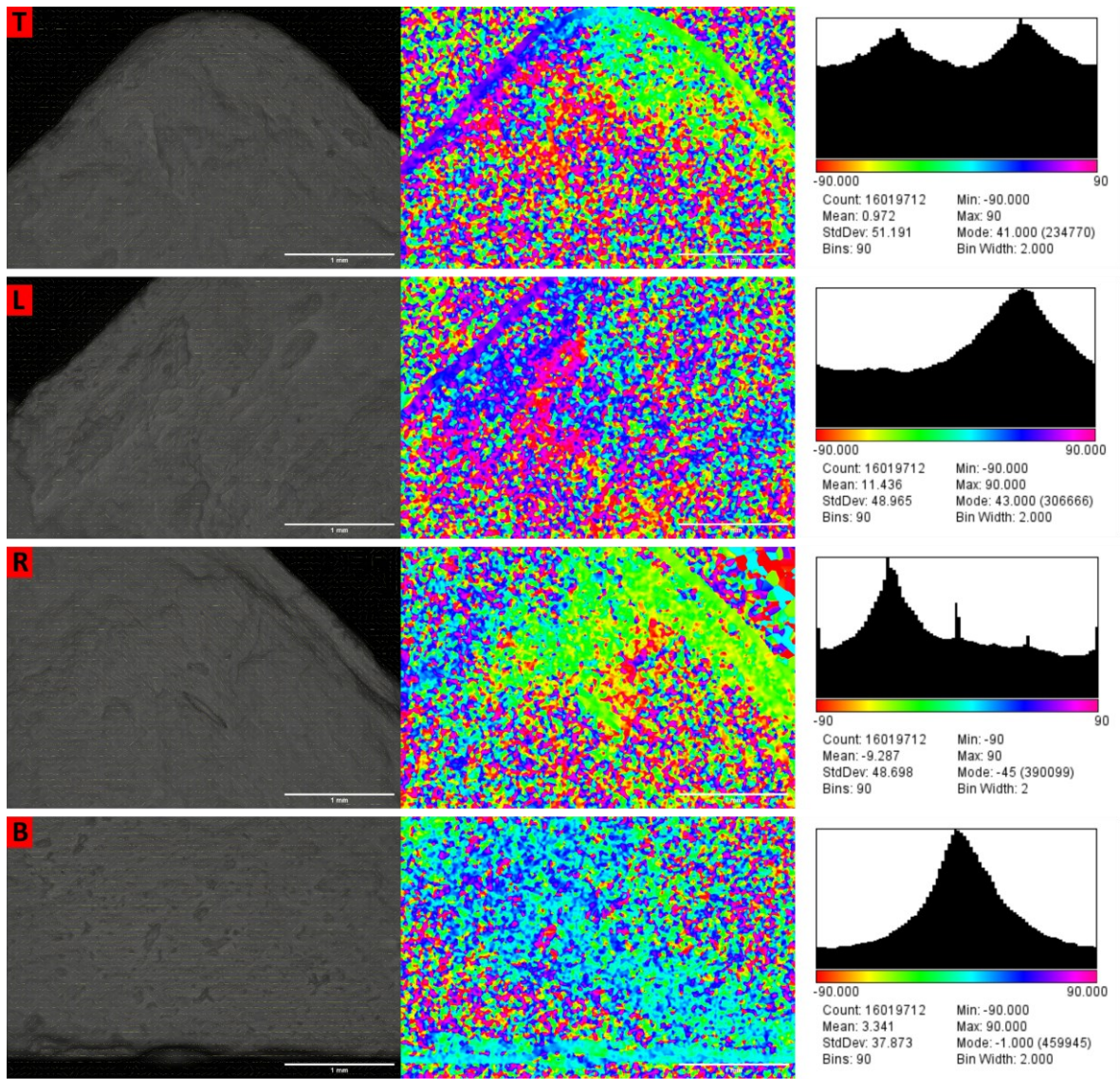


Figure 44. Image orientation results for sample of Figure 43. The 4 rows represent the location L,T,R,B of Figure 43b. First column report the original image with direction arrows as overlay. Second column report the hue coloured direction aggregating the arrows by homogeneous areas. Third column report the histogram of the direction values of each image.

4.3.4 Tilted jet on slurry sample

To test if the observed layered fabric in the sample is an artefact of the testing device when the surface is horizontal and the jet perpendicular to it, a slurry sample was tested by inclining the nozzle by 45 degrees. Figure 45 shows that the inclined nozzle almost touching the surface during the calibration stage. The nozzle is later moved vertically 20mm above the sample surface for the jet test.



Figure 45. Tilted μ -Jet testing at 45 degrees. (a) testing setup showing: inclined nozzle, sample, camera and low head container. (b) detailed view of the inclined nozzle.

The scour hole visible in Figure 46 is asymmetrical due to the inclined jet nozzle. The slurry sample presents a layered fabric similar to the one observed when the impinging jet was orthogonal to the sample surface. This strengthens the experimental observation that the layered fabric is generated during the consolidation process, in this case by the suction generated by the short exposure of the sample to air-drying.

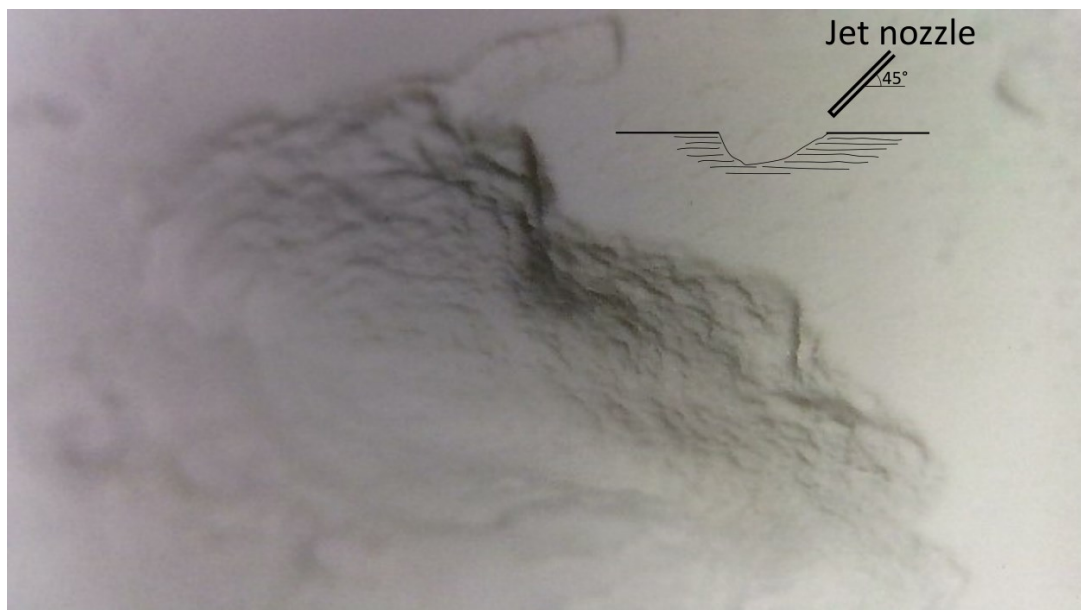


Figure 46. Scour hole upon testing on the Slurry at repose – flat sample tested with μ -jet nozzle inclined by 45 degrees.

5 DISCUSSION

5.1 First detachment shear stress

The experimental observation for the samples prepared at pH₄ (regardless of the pre-consolidation stress, from the self-weight consolidation stress to the 888 kPa consolidation vertical stress) is that the detachment unit is represented by a flake. On the other hand, particles or clusters of a small number of particles were inferred to detach from the samples at pH₉.

5.1.1 Elementary particle versus particle assemblage (flake)

Figure 47 shows the shear stress imposed by the impinging jet at the onset of first detachment against the characteristic size of the material. For the case of samples prepared at pH₉, the detachment involved elements undistinguishable by the camera (erosion took place in the form of ‘milky’ suspension). The dimension of the detaching unit can be estimated in the range from 1 μm (individual particle) to 10 μm (cluster individual particle). Erosion took place as soon as the first shear stress of 0.38 Pa was applied. This shear stress can therefore be considered an upper bound of the detachment shear stress. The detachment shear stress and the size of the detaching unit fall in the range identified by the shaded area in Figure 47, which is not inconsistent with the critical stress observed for granular materials as reported by the continuous and dashed lines curves.

For the case of samples prepared at pH₄, the experimental data points are first represented by considering the diameter $d_{50} = 0.9\mu\text{m}$ of the clay tested, following Roberts et al. (1998) who tested silt quartz particles. The dataset by Roberts et al. (1998) is also reported in Figure 47 showing that i) the critical shear stress decreases as d_{50} increases and ii) the critical shear stress is bulk density dependent. The data on the reconstituted kaolin prepared at pH₄, if represented in terms d_{50} , appear to be consistent with the dataset presented by Roberts et al. (1998), if one ideally extrapolates the experimental curves traced by Roberts et al. (1998). It should be noted that the empirical curves traced by Roberts et al. (1998) suggest a decreasing function between the critical shear stress-and the characteristic particle size, opposite to the increasing function observed for granular materials, as if the detachment mechanisms in fine-grained and coarse-grained materials were fundamentally different.

The data on the reconstituted clay at pH₄ were also reported by considering the size of detaching flake (diameter of the disk of equivalent area). The size of the flakes falls in the millimetre range and shifts the experimental data on the right-hand side in the plot, very close to the curves derived by Miedema (2012) representing the fits detachment in granular materials. At first glance, by considering the dimension of the flakes, the response of fine-grained and coarse-grained materials does not appear fundamentally different. It should be noted, however, that the curves for granular materials were derived by considering the typical density of a sand grain (2.6 g/cm³) whereas the density of the detaching flakes is much lower (equal to the bulk density in the consolidated clay sample. At the same time, the curves for granular

materials were derived by considering the drag coefficient of a sphere whereas the platy flake is expected to be characterised by a different drag coefficient. These two effects are analysed separately in the next section.

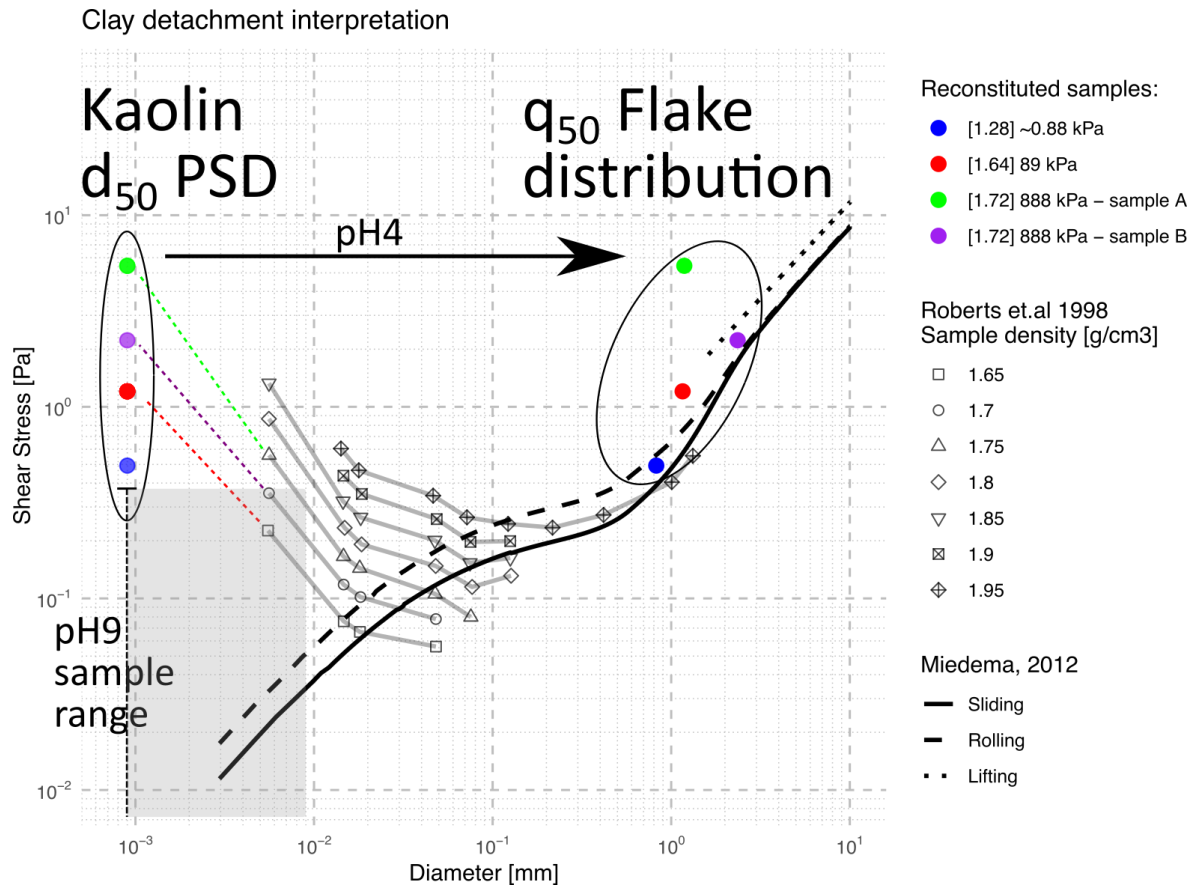


Figure 47. Critical shear stress versus characteristic size for the reconstituted clay at pH4. Data are represented by considering either the d_{50} of the particle size distribution or the diameter of the disk of equivalent area of the first detaching flake.

5.1.2 Effect of flake density and drag coefficient on the critical shear stress

Miedema (2012) developed a model to derive the critical shear stress in granular materials based on the force equilibrium on a spherical particle. Equation [7] is associated with the sliding mechanism and stems from the equilibrium in horizontal direction between the drag force (left-hand side of side Equation [7]) and frictional resistance, in turn dependent on the submerged weight of the sphere:

$$C_D \frac{1}{2} \rho_w u_*^2 f_D \frac{\pi d^2}{4} = \mu (\rho_s - \rho_w) g \frac{\pi d^3}{6} \quad [7]$$

where $C_D(Re)$ is the drag coefficient function of the Reynolds number, Re , ρ_w and ρ_s are the densities of water and the grain respectively, u_* is the friction velocity on the grain, f_D a factor accounting for the grain exposure to the flow, d is the grain diameter, μ the friction coefficient between the grain and the

bed, and g is the acceleration of gravity. The force balance depends explicitly on the drag coefficient C_D , in turn dependent on the grain shape, and the grain density ρ_s .

The density of the flake can be assumed to be equal to the bulk density of the sample. Figure 48 shows the effect of reducing the grain density from the value of an individual sand grain ($\rho_s=2.6 \text{ g/cm}^3$) to the bulk density of the flake, in this case assumed to be equal to 1.64 g/cm^3 as per the bulk density of the sample consolidated to 89 kPa vertical stress. The reduced grain density shifts downward the critical shear stress (blue curves).

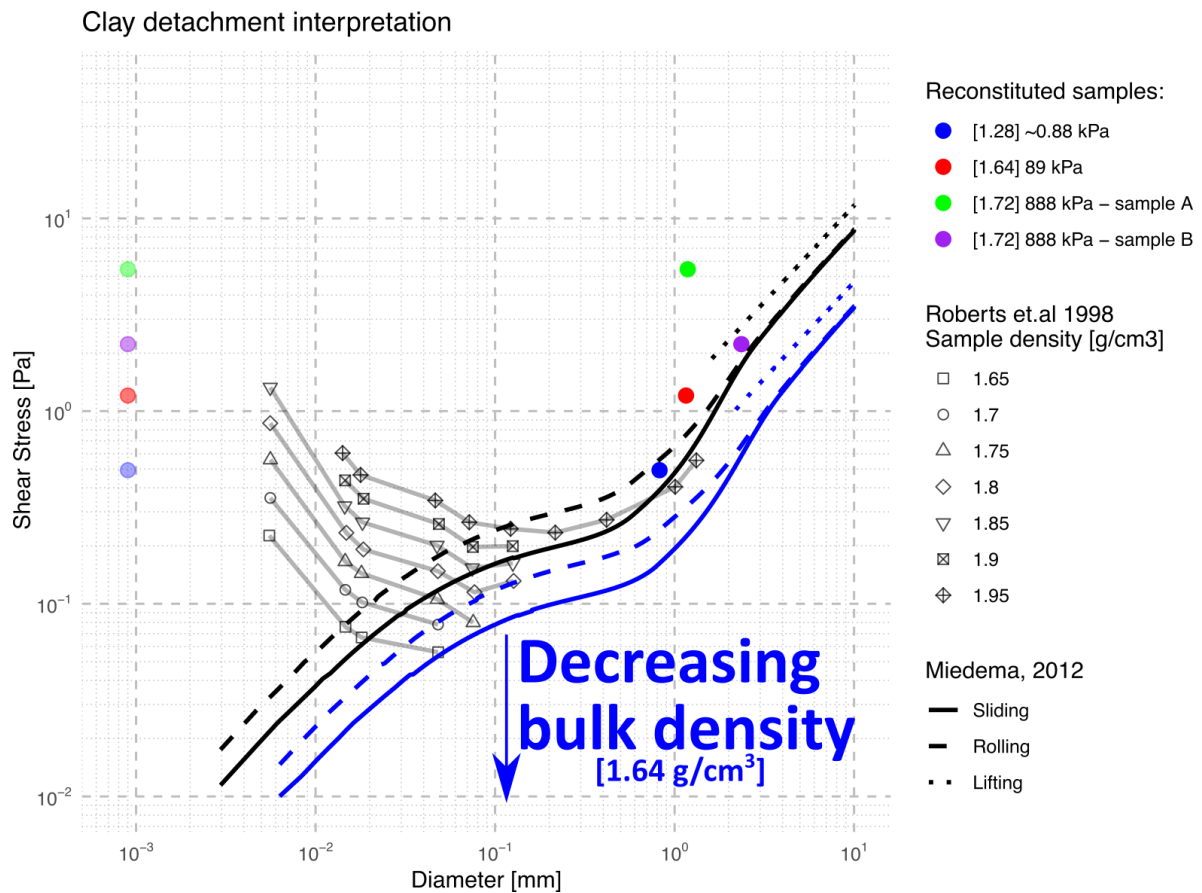


Figure 48. Effect of bulk density of the detaching grain on the critical shear stress by considering the Shields-based model as parametrised by Miedema (2012).

The drag coefficient C_D for the detaching flake is different from the sphere. Figure 49 shows the case of an inclined flake dragged by a flow parallel to the pristine surface. The drag coefficient for this inclined flake was derived by reviewing data in the literature about flat plates immersed in a fluid as shown in the Appendix I. This drag coefficient, expressed as a function of the Reynolds number, Re , is reported by the red curve in Figure 50, where it is compared with the drag coefficient of the sphere (blue curve) adopted to derive the critical shear stress in granular materials.

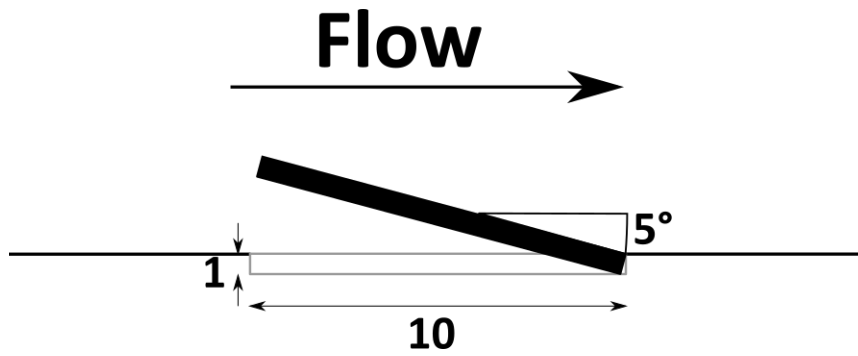


Figure 49. Schematic representation of flake detachment engaging with the flow at 5-degree angle.

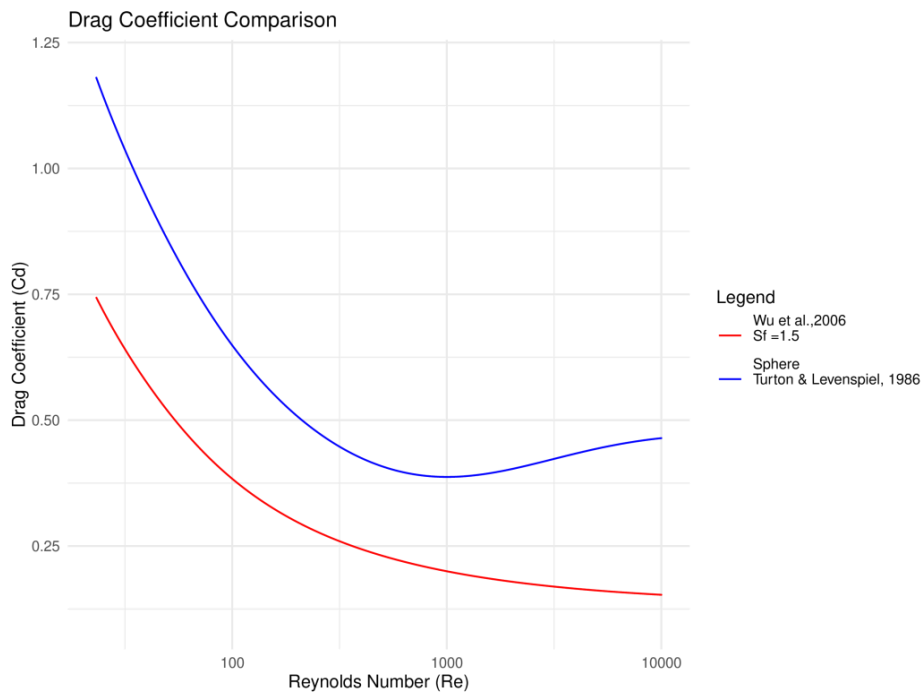


Figure 50. Comparison of drag coefficient of a sphere (blue) and a plate inclined by 5 degrees against the flow direction (see Appendix I for the derivation of the drag coefficient of the inclined plate).

By introducing the reduced drag coefficient for the inclined plate as shown in Figure 50 in Equation [7], and assuming that the flake thickness s is proportional to the flake dimension d , consistent with the observations in Figure 22, the critical shear stress for the flakes can be derived as shown by the red curves in Figure 51. The critical shear stress increases compared to the case of spherical particles indicated by the black curves.

Clay detachment interpretation

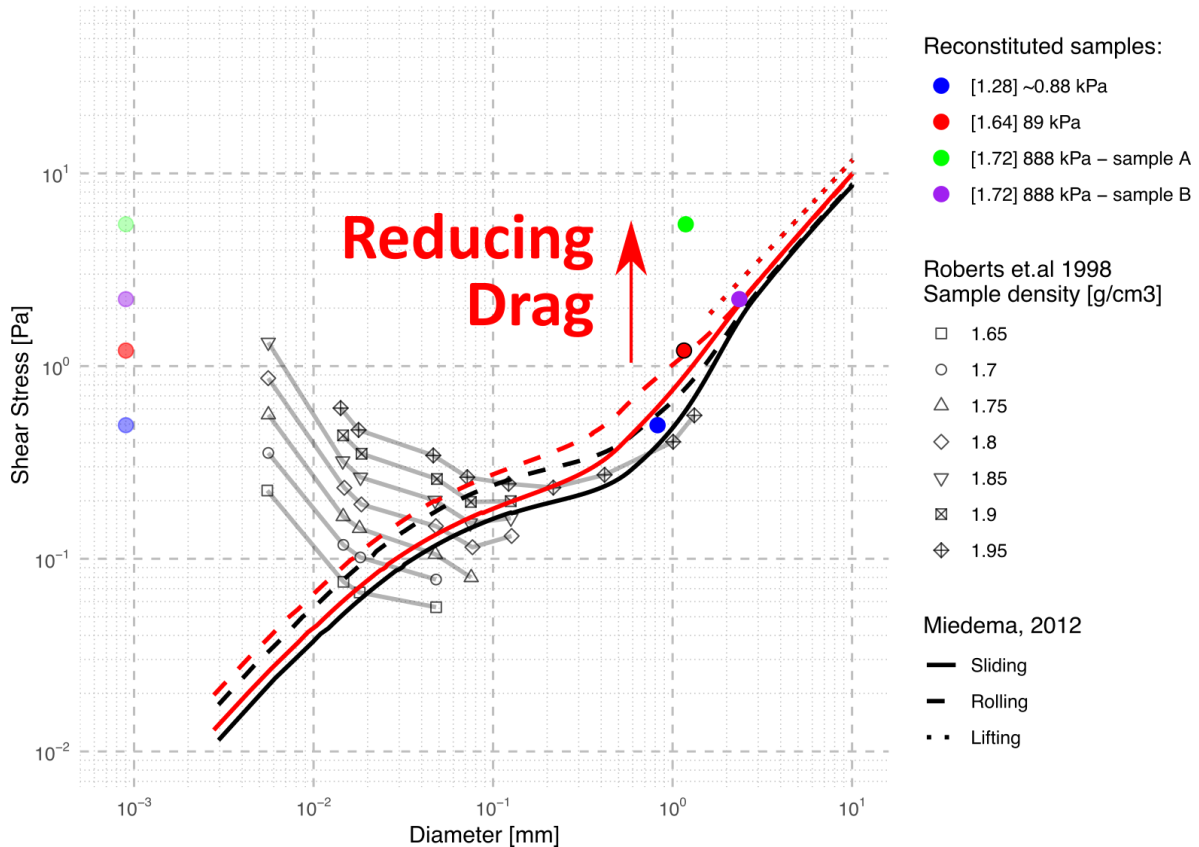


Figure 51. Drag coefficient decrease effect on Shield curve as parametrized by Miedema, 2012. The drag reduction has been conservatively underestimated for the plate case.

Figure 48 and Figure 51 have shown that the decreasing density and decreasing drag coefficient for the flake (compared to the sphere) have opposite effect on the threshold shear stress. They are possibly offsetting each other and this is the reason why the traditional Shields' curve reported in Figure 47 for a sphere as parametrized by Miedema (2012) appears to be in reasonable agreement with the critical shear stress observed for the flakes.

5.1.3 Considerations about the mechanisms of detachment in silt (Roberts et al., 1998)

Roberts et al. (1998) investigated the critical shear stress of silt-size quartz particles represent the data in terms of d_{50} of the particle size distribution as shown in Figure 47 . However, Roberts et al. (1998) stated:

“For $d_{50} < 40 \mu\text{m}$, the sediments behave in a cohesive manner, i.e., they consolidate slowly with time and they erode in chunks. These chunks of sediment, some as large as 1 cm at higher shear stresses, generally disintegrate as they are transported downstream”

If the data by Roberts et al. (1998) are replotted by considering the characteristic size of the ‘chunk’ (10 mm) instead of the d_{50} , the data points would shift to the right, i.e. the shaded ellipse as shown in

Figure 52. Moreover, if one considers the lower density of the ‘chunks’, the critical shear stress curve shifts downward (blue curve in Figure 52 for the case of bulk density equal to 1.65 g/cm³). These two corrections would make the datapoints Roberts et al. (1998) for silty materials very close to the critical shear stress curve derived for the case of spherical ‘granular’ particles, similarly to the case of clay flakes discussed in the previous section.

Additionally, the same author in a follow up study (Roberts et al., 2003) state:

“The 19 μm quartz (referring to the d₅₀) was visually observed to erode as both aggregates and individual particles (although it may be impossible to see the smallest particles), however, aggregates quickly disintegrated and were not visible beyond a few centimetres downstream from the erosion test section. This is consistent with the observations of Roberts et al. 1998 and is indicative of sediment with weak cohesive properties.”

This further strengthens the observation that for the smaller range of silt diameter even for pure quartz particles with d₅₀ ranging from 5 to 19 μm and no clay content the detachment occurs as aggregates.

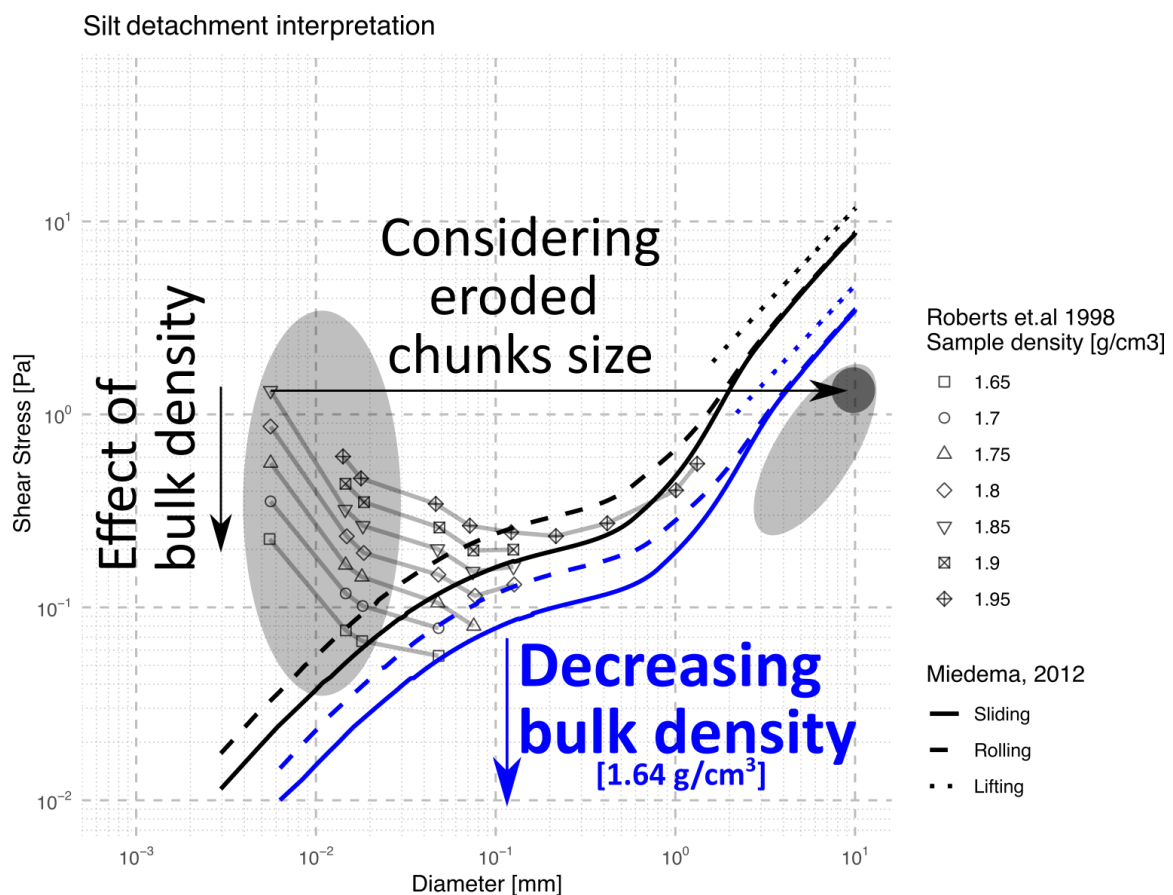


Figure 52. Possible reinterpretation of Roberts et al., 1998 data based on reported erosion in ‘chunks’ up to 1 cm for cohesive quartz particle with d₅₀ < 40 μm.

5.2 Considerations about mobilization of clusters/aggregates in clays

To the author's knowledge, the observation that erosion in reconstituted clay occurs via the detachment of flakes (Figure 18) rather has never been reported in the literature. However, there is a body of literature that supports indirectly the observed detachment mechanism.

Schieber et al. (2010) formed kaolin beds deposited from a suspension at ~ 0.1 g/L concentration consolidated under running recirculation flume. Upon erosion small clay rip-ups (i.e. flakes in this study) began to travel along the flume bottom. Initially of irregular shape, they became rounded after traveling around the track once or twice and formed clay balls of 0.5 to 2 mm size. By depositing a thicker bed in similar fashion (~ 0.1 g/L), the authors state that irregular shreds were torn from the topmost layer of the bed and formed rounded rip-ups in 0.5 to 2 mm size, as they travelled down the flume. It is likely that the detachment mechanism (i.e. prior the rounding action by saltation) occurred in flakes.

Einsele et al. (1974) showed that erosion from kaolinite beds formed at 60-65 volumetric water content occurred in the form of detachment of clay clasts (aggregates), suggesting that some consolidation is needed before muds can erode in chunks instead of simply being resuspended. Rip-up clasts formation appears to be aided by alternating layers of different erosion resistance and by bedding-plane discontinuities.

Perkey et al. (2024) performed flume erosion test on natural cohesive sediments (silt with clay up to 15% fraction) reconstituted into Shelby tubes. The flume was equipped with a sieve trap downstream to collect the eroded material. Upon testing the muddy cores with density in the range 1.2 - 1.5 g/cm³, the material retrieved in the sieve traps was made of clay macro-aggregates >1 mm (bed clasts). These types of aggregates were demonstrated to consistently account for 20% or more of the eroded mass. They appear thicker and rounder compared to the rip-ups described by Schieber et al. (2010) but this might have been due to the dominance of silt in the mud tested. The aggregates shown in Figure 7(b) of the paper by Perkey et al. (2022) resembles to the flakes observed to detach from the clay surface in this work (Figure 18).

5.3 Layered fabric

5.3.1 Effect of pH

The layered fabric responsible for the erosion in the form of detachment of flakes was observed in the samples prepared at pH4 but not in the samples prepared at pH9. The effect of the pH is to control the electrical charge of the particle edge, positive in acidic pore fluid (pH4) and negative in alkaline pore fluid (pH9). Under pH4 conditions, the positively charged edge is attracted by the negatively charged face of the particle, promoting edge-to-face attraction and generating an open ‘flocculated’ fabric in suspension. On the other hand, under pH9 conditions, the particles are negatively charged all around promoting a denser ‘dispersed’ fabric in suspension. This is well established in the literature of clay particle electrochemical interaction (Wang et al., 2006; Pedrotti, 2016).

To highlight the different electrical interaction in clay sediment under different pH, Figure 53 shows the final volume after sedimentation of two slurries prepared at a water content $w_c=2.0$ (~ 3.1 times the LL) at pH4 and pH9 respectively. The slurry at pH 4 maintain a more open fabric due to the edge-to-face contacts between the clay particles.



Figure 53. Self-weight consolidation of kaolin slurry at $w_c=2.0$ in plastic beaker after 30 days. (a) sample at pH4 showing a minor decrease of volume compared to the initial beaker volume (250 mL). (b) sample at pH9 with final volume at 170 mL.

The interaction between clay particles, which results from the balance between Coulombic interactions (either attractive or repulsive) and Van der Waals attraction, has been investigated extensively for the case of clay particles in suspension. The commonly accepted theory used to interpret

interactions observed experimentally is referred to as the DLVO theory, named after Boris Derjaguin and Lev Landau, Evert Verwey and Theodoor Overbeek (Derjaguin,1941; Verwey et al., 1948).

The charge of the particle face (surface charge on the basal planes) results from isomorphic substitutions and is always considered to be negative (Van Olphen, 1977), although its magnitude appears to be pH dependent. The charge of the particle edge results from the protonation or deprotonation of hydroxyl groups of edges and, unlike the face, the sign of the edge charge is pH dependent (Van Olphen, 1977; Mitchell & Soga, 2005; Wang & Siu, 2006).

Coulombic interaction between particle surfaces depends on the electric field generated by the particle charges. The interaction can be attractive if the surfaces are charged with opposite sign or repulsive if the sign of the charges is the same. In general, Coulombic forces depend on the dielectric permittivity and electrolyte concentration of the pore fluid, and the inter-particle distance (Coulomb's law). In an electrolyte-free suspension, Van der Waals forces are considered to be relevant (compared to the Coulombic forces) only at distances smaller than 10–20 nm (Van Olphen, 1977; Mitchell & Soga, 2005). Therefore, as the minimum pore size typically observed in soils usually appears to be at least one order of magnitude greater (10-20 nm), particle distance can be mainly assumed to be controlled by the Coulombic interactions. Particles are thus considered to interact in two different modes.

1. Face-to-face interaction (F-F): Coulombic repulsion exists between the two negatively charged faces.
2. Edge-to-face interaction (E-F): Coulombic attraction exists between the negative clay faces and the positive edges (edges are positively charged as long as the solution is acidic and no dispersant is added) for the case of acidic solutions or Coulombic repulsion between negatively charged faces and negatively charged edges for the case of alkaline solutions.

In summary particles are mainly arranged in E-F contact configuration for samples prepared at pH4 while particles are arranged in F-F no contact configuration for the samples prepared at pH9. Pedrotti and Tarantino (2018) showed how plastic deformation (i.e. consolidation in this case) are the results of slippage of E-F contacts between particles at pH4. The E-F contact slippage brings the clay particles in F-F non-contact configuration but differently from the samples at pH9 the edge is still positively charged. de Carvalho Faria Lima Lopes et al. (in prep.) have quantified the electrical charge of a well crystallised kaolinite identified as KGa-1 as reported in Figure 54 and further described in Appendix II.

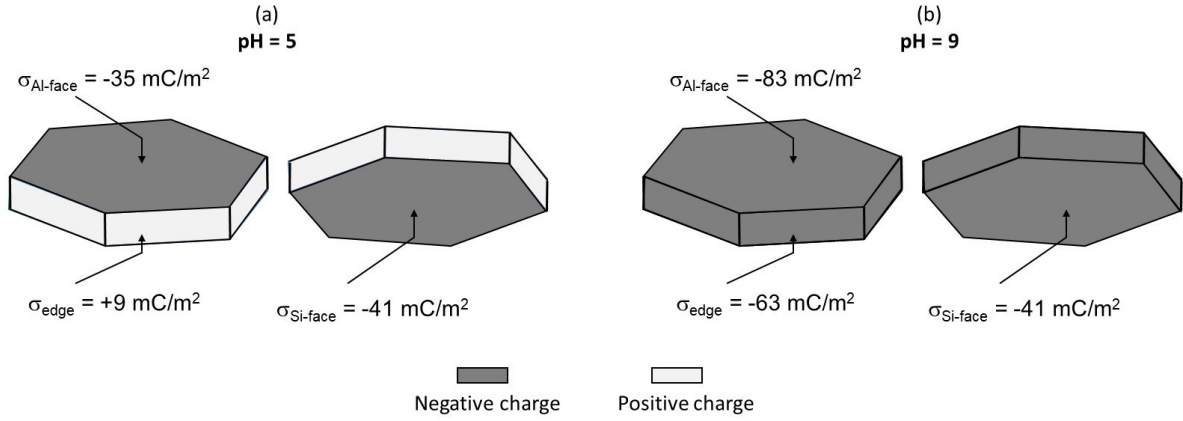


Figure 54. Surface charge density of faces and edges of kaolinite under (a) pH 5 and (b) pH 9 (de Carvalho Faria Lima Lopes et al., in prep.).

Figure 55 shows that simulation of the force per unit area required to bring two particle in face to face configuration into contact for the cases of acidic conditions (Figure 55a) and alkaline conditions (Figure 55b) (de Carvalho Faria Lima Lopes et al., in prep.). The cases of particles aligned or staggered were examined. The face-to-face configuration for the case of acidic conditions (pH4) is assumed to be reached once slippage occurs at the edge-to-face contact due to external loading. Figure 55 shows that

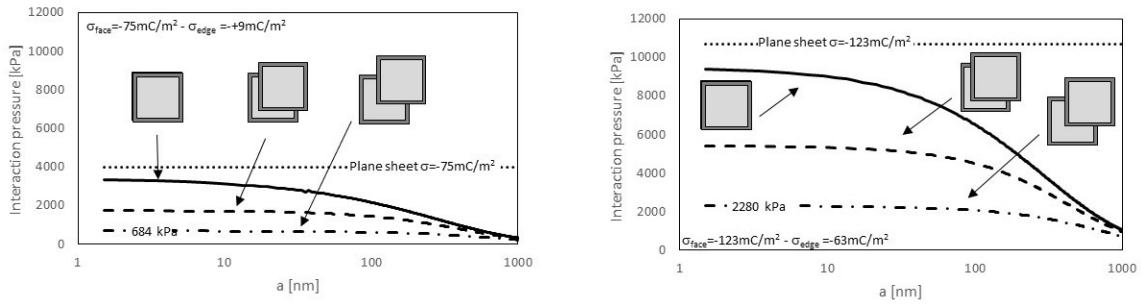
- i) the range of pressures required to bring two particles into contact for the cases where appears to be of the same order of magnitude of the macroscopic ‘continuum scale’ stress that generates plastic deformation in face-to-face configuration;
- ii) the interaction pressure reduces if the overlap is partial, i.e. particles are likely to ‘bond’ in a staggered pattern;
- iii) the maximum interaction pressure that, if exceeded by the external stress causes the particles to be brought into contact, is substantially lower for the case of acidic conditions (pH=5) compacted to alkaline conditions (pH=9).

To investigate the role of Van der Waals attractive forces, the interaction pressure was re-computed by superposing the (repulsive) Coulombic pressure with the attractive Van der Waals pressure according to Israelachvili (2011):

$$p_{vaw} = -\frac{A}{6\pi a^3} \quad (8)$$

As shown in Figure 55c,d, the Van der Waals forces only becomes active at very close distance from the particles and do not modify substantially the Coulombic pattern, i.e. to bring face-to-face particles into contact there is no need to invoke Van der Waals attractive forces, it is sufficient that the external pressure exceed the maximum Coulombic repulsion pressure that can be generated by the overlapping electrical fields. Van der Waals attractive forces only come into play to prevent that particles detach once the external pressure is released.

Coulombic forces only



Coulombic and Van der Waals forces

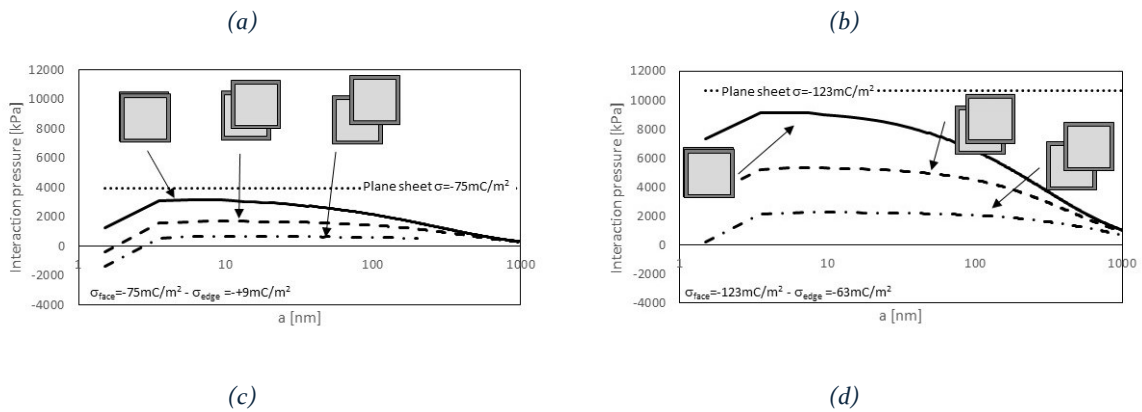


Figure 55. Interaction pressure between two kaolinite particles with 100%, 56% and 25% of their surfaces overlapping. (a) pH 5 - Coulombic forces only. (b) pH 9 - Coulombic forces only. (c) pH 5 - Coulombic and Van der Waals forces. (d) pH 9 - Coulombic and Van der Waals forces (de Carvalho Faria Lima Lopes et al., in prep.).

This theoretical investigation suggests that the clay particles in the samples at pH4 require less external pressure to reach a F-F contact stacking after E-F slippage to possibly generate a layer similar to the one observed in the jet erosion tests. On the other hand, it can be speculated that the external pressure was not sufficient to bring F-F particles into contact under alkaline conditions, then justifying the absence of layering in the samples consolidated at pH9.

The observation that the turbidity of the eroding fluid decreases with the pre-consolidation stress in pH9 samples might be explained by some degree of F-F contact stacks created during consolidation loading.

5.3.2 Effect of consolidation stress on layer thickness

As observed in Figure 22, the thickness (s) and planar dimensions (d) of the detaching flakes increases with the increasing pre-consolidation stress for samples prepared at pH4. Moreover, by increasing the consolidation stress, it appears that the layer becomes more rigid when lifted by the jet undermining the layer, consistent with the flexural stiffness D of a plate proportional to its thickness ($D \propto s^3$). The increase in thickness of the layer and, hence, the flake, can be possibly be explained by extending the theoretical analysis of clay particles in F-F interaction.

Figure 56 shows the interaction pressure when stacks are involved (only the case of stacks formed by particles overlapping 100% is shown in the figure for the sake of simplicity). Because the limiting Coulombic repulsion pressure varies with the square of the charge, bringing particle stacks together is much more difficult than bringing single particles together. Thicker layers require higher contact pressure to be formed (to bring stacks into contact). Increasing the pre-consolidation stress is therefore more likely to bring stacks into contact increasing the thickness of the detaching flakes. The consolidation stress could be increased by either the external stress or the ‘internal’ suction when shortly exposing the slurry to air drying (Figure 33).

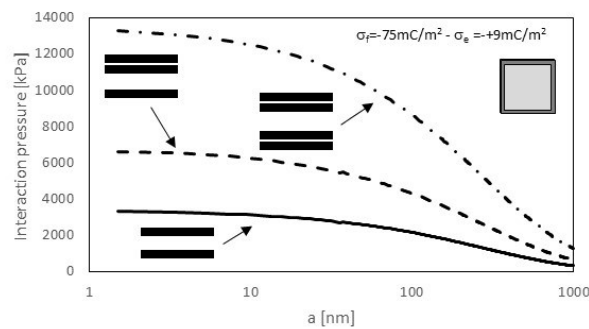


Figure 56. Interaction pressure between generated by particle stacks (de Carvalho Faria Lima Lopes et al., in prep.).

5.3.3 Effect of hydraulic gradient and on sample fabric formation

Figure 57 report the direct comparison of four sample subjected to the same final vertical stress upon consolidation (i.e. 888 kPa) but different drainage paths (marked by the arrows and excess pore water pressure during transient consolidation phase. For the case of vertical drainage, the flake dimension changed depending on whether the surface for draining or not during consolidation. It also changed for the case of draining surface depending on the magnitude of the excess pore-water pressure as shown in Figure 57. Radial consolidation did not produce layers parallel to the surface exposed to the impinging jet and, hence, no flake detachment was observed (Figure 30). The effect of drainage is interesting though a conceptual explanation could not be provided at this stage.

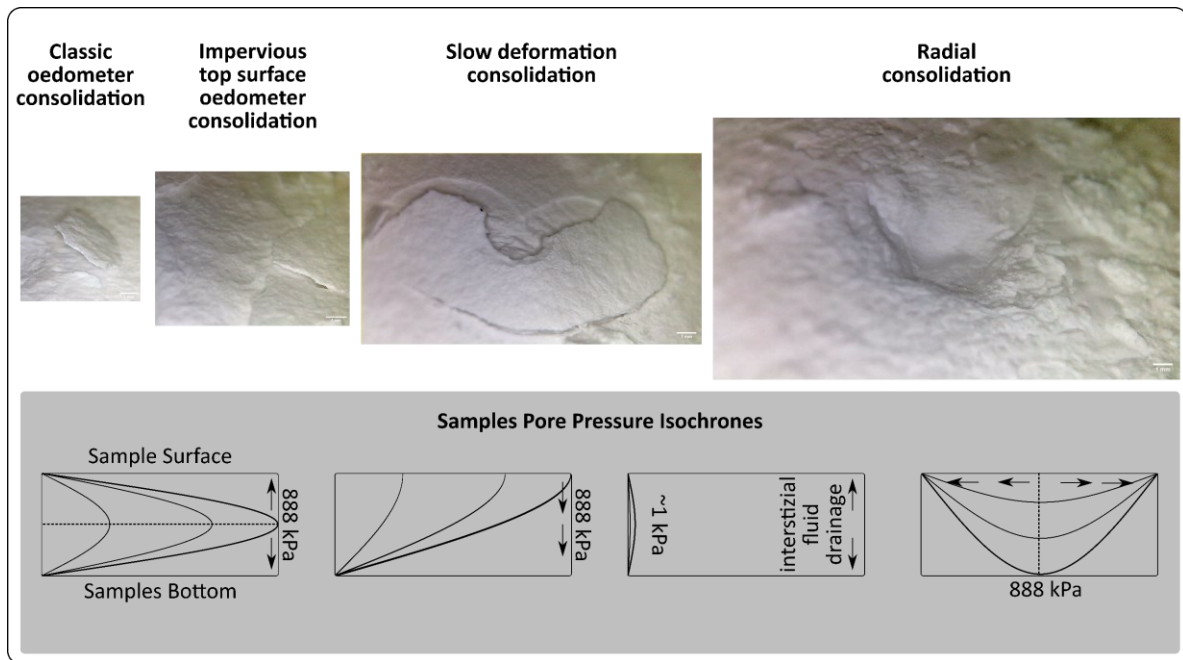


Figure 57. Drainage path effect on flake detachment, all four samples have been consolidated to the same nominal pressure of 888 kPa via vertical loading.

6 Conclusions

This study presented an experimental investigation of the detachment mechanism in clay. The observed detachment mechanism consisted in the detachment of clay flakes, i.e., flat and thin pieces of clay lifted by the impinging jet.

Erosion occurred in the form of flake detachment with two main features observed: i) the planar dimension d of the flakes increase as the sample is consolidated to a higher stress and ii) the thickness of the flake, s , also increases with the consolidation stress. Moreover, the flexural stiffness of the clay layer that is lifted by the impinging jet also appears to increase with the pre-consolidation stress (the clay layer consolidated by self-weight was ‘peeled off’ by the jet whereas the clay layer of the samples consolidated to 888 kPa remained planar when lifted before breakage). These two experimental observations are consistent with the flexural stiffness D of a plate increasing with cube of the plate thickness, s ($D \propto s^3$).

From the inspection of samples subjected to flake detachment due to the impinging jet, it appears that the reconstituted clay sample exhibits a ‘layered’ fabric, which extends below the sample surface.

The investigation of the interplay between the detachment mechanism and the fabric of the sample lead to the identification of three factors controlling the genesis of the layered fabric i.e., hydraulic, mechanical, and chemical modes of loading. The first major difference in detachment mechanism and underlying fabric is associated with the chemistry of the pore-fluid used in sample preparation. All the samples prepared at pH9 do not show any layered fabric and, hence, detachment in the form of flakes. On the other hand, almost all samples prepared at pH4 presented a layered fabric and detachment in

form of flakes (with the exception of the top surface of the sample consolidated by self-weight consolidation, which was subjected by zero effective stress).

The second major role is played by the hydraulic boundary conditions imposed to the samples prepared at pH₄ during consolidation, which appears to control the thickness of the layers forming in the sample and, hence, the dimension and thickness of the detaching flakes. Compared to the samples prepared under 'ordinary' oedometer drainage (top and bottom of the sample), different mechanisms and fabric were observed when making the sample surface non-draining during consolidation. For the case of impervious surface with zero flow orthogonal to the tested boundary (i.e. impervious surface), the detachment shear stress and flake dimensions both increased. For the case of impervious surface due to consolidation flow occurring parallel to the tested boundary (i.e. radial consolidation), the sample eroded in more rounded fragments of different size, similarly to the self-weight consolidated sample at the top surface.

Another role is played by the magnitude of the pre-consolidation effective stress imposed to the sample during consolidation. At zero pre-consolidation stress (top surface of the sample consolidated by self-weight), there is no layering forming. However, as the pre-consolidation stress increase to about 1 kPa, either generated mechanically (e.g. overburden) or hydraulically by the suction induced by air-drying, the clay shows a layered fabric and flake detachment.

The flake of first detachment were interpreted within the incipient motion in terms of bed shear stress threshold and representative dimension of the detaching unit. If the characteristic dimension adopted is the particle size as always done in the literature the experimental data appears to be very far from the critical shear stress threshold derive for granular material however if the characteristic dimension is chosen as the dimension of the flake the experimental data are indeed very close to the ones derived for granular materials suggesting a consistency in the critical shear stress controlling the incipient motion from fine-grained to coarse-grained materials.

The different fabric induced by the pore fluid pH can be explained by the different edge charge of clay particles (i.e. negative for pH₉ and positive for pH₄). When particles are in Face to Face and staggered configuration the particles at pH₉ require a much higher pressure to be brought in contact as derived considering particle interaction via Coulombic and Van der Waals forces and this is assumed to explain the absence of layered fabric in samples prepared at pH₉.

The characterized layered fabric triggers the detachment of flakes instead of individual particles or equidimensional aggregates (or fragments) and therefore plays a key role in the definition of the erosion mechanisms of reconstituted clay, this is key to develop robust semi-empirical models for the characterisation of the shear stress threshold in clayey sediments.

References

- Ariathurai, R. and Arulanandan, K., 1978. Erosion rates of cohesive soils. *Journal of the hydraulics division*, 104(2), pp.279-283.
- Bacakoglu, H. and Kamel, M.S., 1997. A three-step camera calibration method. *IEEE Transactions on Instrumentation and Measurement*, 46(5), pp.1165-1172.
- Badr, S., Gauthier, G. and Gondret, P., 2014. Erosion threshold of a liquid immersed granular bed by an impinging plane liquid jet. *Physics of Fluids*, 26(2).
- Benseghier, Z., Cuéllar, P., Luu, L.H., Delenne, J.Y., Bonelli, S. and Philippe, P., 2020. Relevance of free jet model for soil erosion by impinging jets. *Journal of Hydraulic Engineering*, 146(1), p.04019047.
- Bradski, G., 2000. The OpenCV library. *Dr. Dobb's Journal of Software Tools*.
- Brunier-Coulin, F., Cuéllar, P. and Philippe, P., 2020. Generalized Shields criterion for weakly cohesive granular materials. *Physical Review Fluids*, 5(3), p.034308.
- Chen, D., Zheng, J., Zhang, C., Guan, D., Li, Y. and Huang, H., 2022. Threshold of surface erosion of cohesive sediments. *Frontiers in Marine Science*, 9, p.847985.
- Cheng, N.S., 1997. Simplified settling velocity formula for sediment particle. *Journal of hydraulic engineering*, 123(2), pp.149-152.
- Debnath, K. and Chaudhuri, S., 2010. Cohesive sediment erosion threshold: A review. *ISH Journal of Hydraulic Engineering*, 16(1), pp.36-56.
- de Carvalho Faria Lima Lopes, B., Tarantino, A., Porfírio Cordão Neto, M. (in prep.). An experimental and theoretical investigation into the micromechanics of plastic deformation of clays: the role of attractive forces. In preparation
- Derjaguin, B.V., 1941. Theory of the stability of strongly charged lyophobic sol and of the adhesion of strongly charged particles in solutions of electrolytes. *Acta phys. chim. URSS*, 14, p.633.
- Dunne, K.B., Arratia, P.E. and Jerolmack, D.J., 2022. A new method for in situ measurement of the erosion threshold of river channels. *Water Resources Research*, 58(8), p.e2022WR032407.
- Einsele, G., Overbeck, R., Schwarz, H.U. and Unsöld, G., 1974. Mass physical properties, sliding and erodibility of experimentally deposited and differently consolidated clayey muds (approach, equipment, and first results). *Sedimentology*, 21(3), pp.339-372.
- Fadlallah, S.O., Anderson, T.N. and Nates, R.J., 2021. Flow behaviour and aerodynamic loading on a stand-alone heliostat: Wind incidence effect. *Arabian Journal for Science and Engineering*, 46, pp.7303-7321.
- Grabowski, R.C., Droppo, I.G. and Wharton, G., 2011. Erodibility of cohesive sediment: The importance of sediment properties. *Earth-Science Reviews*, 105(3-4), pp.101-120.
- Gopalakrishnan, R.N. and Disimile, P.J., 2017. Effect of Position of Wall Mounted Surface Protrusion in Drag Characteristics At Low Reynolds Number. *International Journal of Computational Engineering Research*, 7(11)
- Gupta, L.K., Pandey, M., Raj, P.A. and Shukla, A.K., 2023. Fine sediment intrusion and its consequences for river ecosystems: a review. *Journal of Hazardous, Toxic, and Radioactive Waste*, 27(1), p.04022036.
- Hanson, G.J. and Cook, K.R., 2004. Apparatus, test procedures, and analytical methods to measure soil erodibility in situ. *Applied engineering in agriculture*, 20(4), pp.455-462.
- Harrison, A.J.M. and Owen, M.W., 1972. Siltation of fine sediments in estuaries. *IN: HYDRAULIC RESEARCH AND ITS IMPACT ON THE ENVIRONMENT*.

- Hartley, R. and Zisserman, A., 2003. *Multiple view geometry in computer vision*. Cambridge university press.
- Israelachvili, J.N., 2011. *Intermolecular and surface forces*. Academic press.
- Jawahar, C.V. and Jain, P.K., 2006, June. Homography estimation from planar contours. In *Third International Symposium on 3D Data Processing, Visualization, and Transmission (3DPVT'06)* (pp. 877-884). IEEE.
- Kandiah, A. and Arulanandan, K., 1974. Hydraulic erosion of cohesive soils. *Transportation Research Record*, 497, pp.60-68.
- Lick, W., 1982. The transport of contaminants in the Great Lakes. *Annual Review of Earth and Planetary Sciences*, Vol. 10, p. 327, 10, p.327.
- Lüthi, M., 2011. *A modified hole erosion test (het-p) to study erosion characteristics of soil* (Doctoral dissertation, University of British Columbia).
- McAnally, W.H., Friedrichs, C., Hamilton, D., Hayter, E., Shrestha, P., Rodriguez, H., Sheremet, A., Teeter, A. and ASCE Task Committee on Management of Fluid Mud, 2007. Management of fluid mud in estuaries, bays, and lakes. I: Present state of understanding on character and behavior. *Journal of Hydraulic Engineering*, 133(1), pp.9-22.
- Mehta, A.J. and Partheniades, E., 1982. Resuspension of deposited cohesive sediment beds. In *Coastal Engineering 1982* (pp. 1569-1588).
- Mehta, A.J., Hayter, E.J., Parker, W.R., Krone, R.B. and Teeter, A.M., 1989. Cohesive sediment transport. I: Process description. *Journal of Hydraulic Engineering*, 115(8), pp.1076-1093.
- Mehta, A.J. and Lee, S.C., 1994. Problems in linking the threshold condition for the transport of cohesionless and cohesive sediment grain. *Journal of coastal research*, pp.170-177.
- Mehta, A. 2013. *An Introduction to Hydraulics of fine Sediment Transport* (World Scientific Publishing Company), ISBN 978-981-4449-48-9.
- Miedema, S.A., 2012. Constructing the Shields curve. Part A: Fundamentals of the sliding, rolling and lifting mechanisms for the entrainment of particles. *Journal of dredging engineering*, 12(1), pp.1-49.
- Miedema, S.A., 2013. Constructing the Shields Curve: Part C—Cohesion by Silt, Hjulstrom, Sundborg. In *International Conference on Offshore Mechanics and Arctic Engineering* (Vol. 55409, p. V006T10A023). American Society of Mechanical Engineers.
- Mitchell, J.K. and Soga, K., 2005. *Fundamentals of soil behavior* (Vol. 3, p. USA). New York: John Wiley & Sons.
- Partheniades, E., 1965. Erosion and deposition of cohesive soils. *Journal of the Hydraulics Division*, 91(1), pp.105-139.
- Partheniades, E., 2009. *Cohesive sediments in open channels: erosion, transport and deposition*. Butterworth-Heinemann.
- Pedrotti, M., 2016. *An experimental investigation on the micro-mechanics of non-active clays in saturated and partially-saturated states*. PhD thesis, University of Strathclyde, Glasgow, UK
- Pedrotti, M. and Tarantino, A., 2018. An experimental investigation into the micromechanics of non-active clays. *Géotechnique*, 68(8), pp.666-683.
- Perkey, D.W., Smith, S.J., Fall, K.A., Massey, G.M., Friedrichs, C.T. and Hicks, E.M., 2020. Impacts of muddy bed aggregates on sediment transport and management in the tidal James river, VA. *Journal of Waterway, Port, Coastal, and Ocean Engineering*, 146(5), p.04020028.
- Perkey, D.W., Smith, S.J., Fall, K.A., Tarpley, D.R. and Friedrichs, C.T., 2024. Production and abundance of macro-aggregate bed clasts from moderately consolidated cohesive beds and their implications for sediment management. *Journal of Sedimentary Research*, 94(1), pp.37-50.

- Püspöki, Z., Storath, M., Sage, D. and Unser, M., 2016. Transforms and operators for directional bioimage analysis: a survey. Focus on bio-image informatics, pp.69-93.
- Righetti, M. and Lucarelli, C., 2007. May the Shields theory be extended to cohesive and adhesive benthic sediments?. *Journal of Geophysical Research: Oceans*, 112(C5).
- Roberts, J., Jepsen, R., Gotthard, D. and Lick, W., 1998. Effects of particle size and bulk density on erosion of quartz particles. *Journal of Hydraulic Engineering*, 124(12), pp.1261-1267.
- Roberts, J.D., Jepsen, R.A. and James, S.C., 2003. Measurements of sediment erosion and transport with the adjustable shear stress erosion and transport flume. *Journal of Hydraulic Engineering*, 129(11), pp.862-871.
- Rueden, C.T., Schindelin, J., Hiner, M.C., DeZonia, B.E., Walter, A.E., Arena, E.T. and Eliceiri, K.W., 2017. ImageJ2: ImageJ for the next generation of scientific image data. *BMC bioinformatics*, 18, pp.1-26.
- Schieber, J., Southard, J.B. and Schimmelmann, A., 2010. Lenticular shale fabrics resulting from intermittent erosion of water-rich muds—interpreting the rock record in the light of recent flume experiments. *Journal of Sedimentary Research*, 80(1), pp.119-128.
- Schroth, Brian & Sposito, G. 1997. Surface Charge Properties of Kaolinite. *Clays and Clay Minerals*, 45(1): 85-91.
- Sheng, Y., 1986. Modeling bottom boundary layer and cohesive sediment dynamics in estuarine and coastal waters. *Estuarine cohesive sediment dynamics*, 14, pp.360-400.
- Shields, A., 1936. Anwendung der Aehnlichkeitsmechanik und der Turbulenzforschung auf die Geschiebebewegung. PhD Thesis Technical University Berlin.
- Sposito, G. 1998. On Points of Zero Charge. *Environmental Science & Technology*, 32(19): 2815-2819
- Tarantino, A. and Tombolato, S., 2005. Coupling of hydraulic and mechanical behaviour in unsaturated compacted clay. *Géotechnique*, 55(4), pp.307-317.
- Teslong, 2019. MS100 Portable USB Microscope – Sensor: 1.0 Megapixel CMOS, Resolution : 1280x720 pixels, Diameter : 8 mm - <https://teslong.com/products/ms100-industrial>
- Turton, R. and Levenspiel, O., 1986. A short note on the drag correlation for spheres. *Powder technology*, 47(1), pp.83-86.
- van Olphen, H. (1977). *An Introduction to Clay Colloid Chemistry*, 2nd Ed. John Wiley & Sons, New York, London, Sydney, Toronto
- Verwey, E.J.W., Overbeek, J.T.G. 1948. *Theory of the Stability of Lyophobic Colloids: The Interaction of Sol Particles Having an Electric Double Layer*.
- Voermans, J.J., Ghisalberti, M. and Ivey, G.N., 2018. A model for mass transport across the sediment-water interface. *Water Resources Research*, 54(4), pp.2799-2812.
- Walder, J.S., 2016. Dimensionless erosion laws for cohesive sediment. *Journal of Hydraulic Engineering*, 142(2), p.04015047.
- Wang, Y.H. and Siu, W.K., 2006. Structure characteristics and mechanical properties of kaolinite soils. I. Surface charges and structural characterizations. *Canadian Geotechnical Journal*, 43(6), pp.587-600.
- Winterwerp, J.C., Van Kessel, T., van Maren, D.S. and Van Prooijen, B.C., 2022. *Fine sediment in open water: From fundamentals to modeling*.
- Wu, W. and Wang, S.S., 2006. Formulas for sediment porosity and settling velocity. *Journal of Hydraulic Engineering*, 132(8), pp.858-862.
- Yao, P., Su, M., Wang, Z., van Rijn, L.C., Stive, M.J., Xu, C. and Chen, Y., 2022. Erosion behavior of sand-silt mixtures: Revisiting the erosion threshold. *Water Resources Research*, 58(9), p.e2021WR031788.
- Zhou Z, Gunter WD. 1992. The nature of the surface charge of kaolinite. *Clays Clay Miner* 40:365-368

Appendix I: Drag coefficient estimation of the plate detachment

General equation for Drag coefficient versus Re number

Many authors derived the drag coefficient of particles via settling velocity experiments. Since the particle shape and surface roughness affect the settling process, the C_d - R curve of natural sediment particles deviates from that of spheres. The drag coefficient estimated in those studies can generally be represented as done by Cheng 1997 in the equation below:

$$C_d = \left[\left(\frac{M}{R} \right)^{1/n} + N \frac{1}{n} \right]^n$$

where R is the particle Reynolds number while M , N and n are fitting parameters.

Wu et al., 2006 aggregated experimental data of multiple authors and fitted the M , N and n parameters so that they only depend on a shape factor parameter S_f as follows:

$$M = 53.5e^{-0.65S_f}; \quad N = 5.65e^{-2.5S_f}; \quad n = 0.7 + 0.9S_f$$

The case of a spherical particle

For $S_f=1$ the parametrization of Wu et al., 2006 allows to retrieve the Drag coefficient of a particle with shape similar to a sphere. Comparing this with the empirical equation derived by Turton & Levenspiel (1986) on smooth spheres there is good agreement for high Reynolds values where the drag coefficient is close to 0.445 as well as for low-Reynolds numbers where the two curves have the same value. In the intermediate range of Reynolds the fit function for the transitional region that has been derived by Turton & Levenspiel (1986) differs for the effect of the surface roughness of the particles considered by Wu et al., 2006. The equation by Turton & Levenspiel (1986) better approximates the drag coefficient of a smooth sphere and for this reason it has been used in the shield diagram derivation performed by Miedema, 2012.

$$C_D = \frac{24}{Re_D} \cdot (1 + 0.173 \cdot Re_D^{0.657}) + \frac{0.413}{1 + 16300 \cdot Re_D^{-1.09}}$$

where Re_D is the particle Reynolds number.

In Figure 58 the comparison between the two drag coefficient functions for spheres and spheroidal particles is reported.

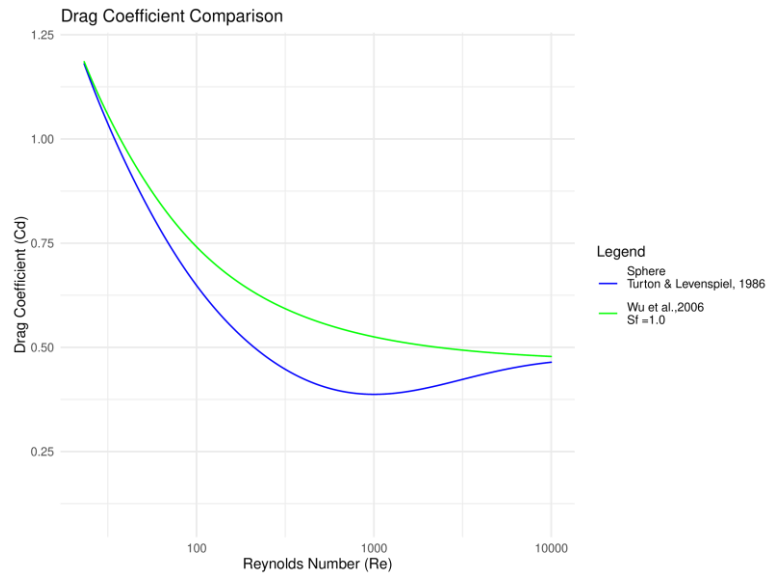


Figure 58. Drag coefficient of a sphere based on Turton and Levenspiel, 1986 and Wu et al., 2006 with $Sf=1$.

The case of inclined platy particle

As described in the result section the detaching units observed is mainly 2D with the geometry of a thin plate. The estimation of the drag coefficient with the Reynolds number is performed as follows. The drag coefficient at high Reynolds numbers is derived from literature where similar cases has been studied in CFD simulations, the curve is then propagated backwards from the Cd derived following the equation suggested by Wu et al., 2006

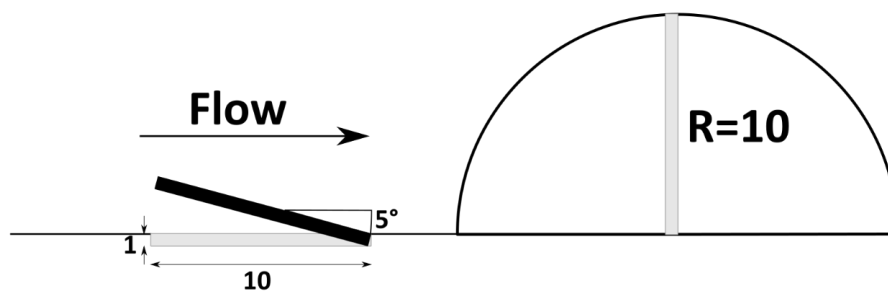


Figure 59. Geometric representation of flake detachment versus half-sphere.

In order to include the drag reduction in the case of a smooth bed with a protruding thin plate some assumptions have been made. The thin plate protrudes against the flow with an angle of 5 degrees, the plate has a length/thickness ratio ≥ 10 as visible in Figure 59. For comparison a half sphere of the same radius is plotted side by side.

Drag coefficient for Horizontal particle

Gopalakrishnan et al., 2017 studied a flat plate immersed in a fluid and derived its drag coefficient in different configurations.

When the plate was smooth the reported drag coefficient is of 0.06273 for the single plate immersed in the fluid at Reynolds numbers 1000.

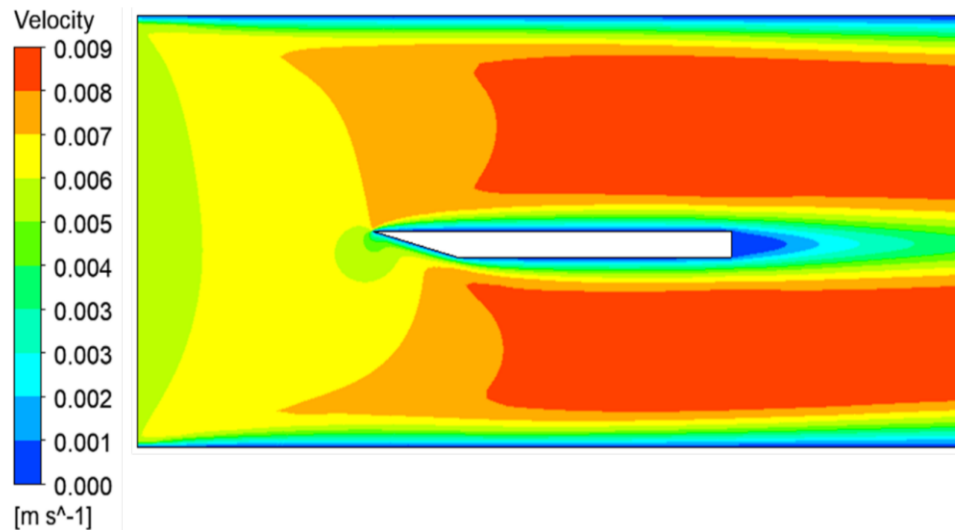


Figure 60. Contour of velocity profile along midplane for baseline case of plate, after Gopalakrishnan et al., 2017.

Meanwhile, when a sharp protrusion was added to the plate, as visible in the figure below, the drag coefficient increased by a 9.81 % to 0.06889.

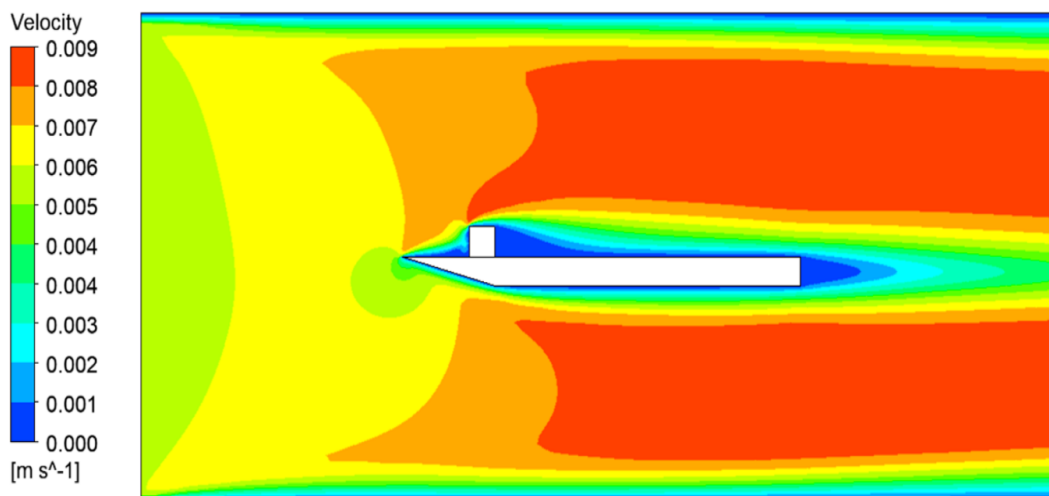


Figure 61. Contour of velocity profile along midplane for single asperity case of plate, after Gopalakrishnan et al., 2017.

Drag coefficient for small angle inclined particle

Fadlallah et al., 2021 performed CFD simulation of a heliostats at different inclination subjected to wind. Hereafter the configuration of most interest for the plate detachment are reported.

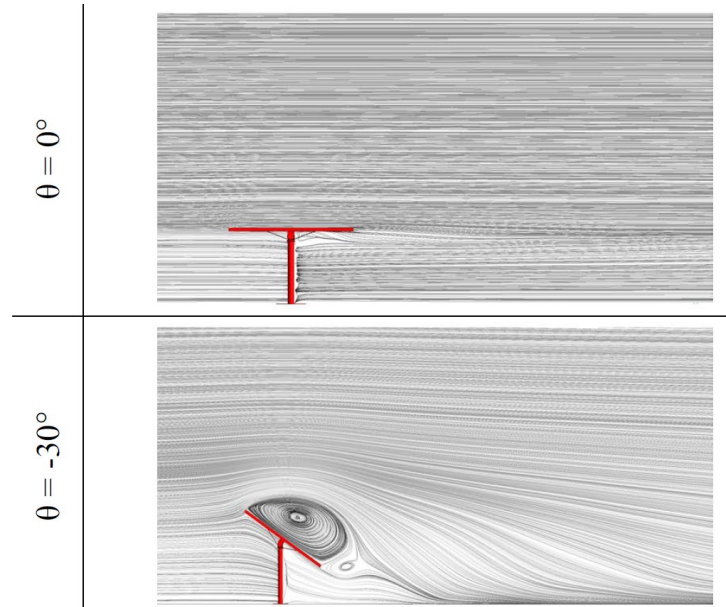


Figure 62. Flow visualization around a flat and inclined heliostat (flow left to right), after Fadlallah et al., 2021.

As visible in Figure 62 the flow is not much affected while the heliostat is horizontal ($\theta = 0$) while as it is inclined against the flow it influences the flow lines and creates drag and lift on the structure. The systematic investigation of different angles lead to the chart in Figure 63.

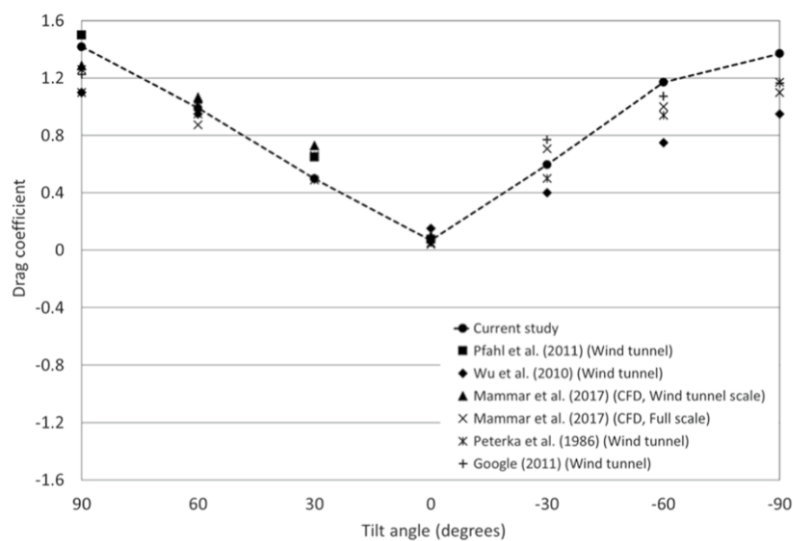


Figure 63. Drag coefficient for plate in fluid at different angles at high-Reynolds numbers, after Fadlallah et al., 2021.

The value corresponding to 5 degrees (i.e Tilt angle = -5 degrees) is of 0.15, this value is being used in the derivation of the drag coefficient for the thin plate.

Moreover the drag coefficient when the plate is horizontal is reported to be 0.0689, this has been also compared against the simulation performed by Gopalakrishnan et al., 2017 where a flat plate was studied and the value of 0.06273 was reported.

Drag coefficient versus Re number for small angle particle

Based on the CFD simulation of Fadlallah et al., 2021 and Gopalakrishnan et al., 2017 it is considered that the derived drag coefficient value of 0.15 at high Reynolds numbers is conservative of the conditions observed experimentally where even lower values of drag could be considered.

By adopting the S_f parameter of Wu et al., 2006 as a fitting parameter to match the C_d value of 0.15 at high Reynolds ($Re = 10^5$) numbers the C_d - R relation for the thin plate at 5 degree inclination from the bed has been found with a S_f of 1.5.

Hereafter the comparison between the Drag coefficient for a sphere (in blue) and the one estimated for a plate inclined by 5 degrees facing the flow (red) is reported.

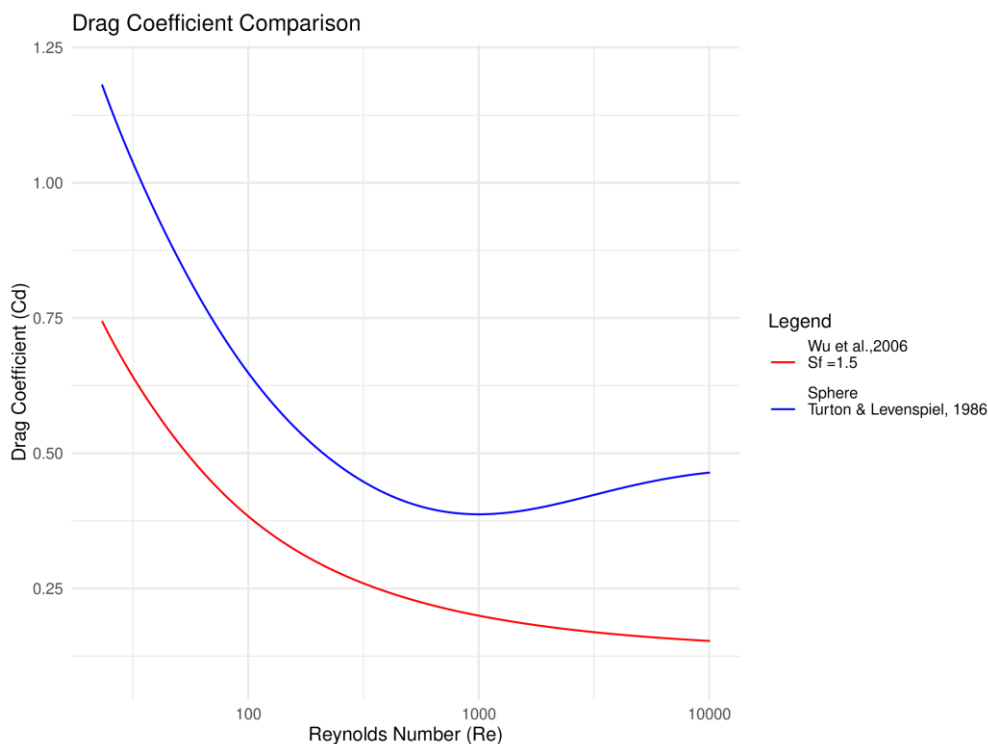


Figure 64. Drag coefficient for plate inclined 5 degrees (red) and sphere (blue).

Appendix II – Interaction of clay particles in Face-to-Face configuration

This appendix is part of the work presented in de Carvalho Faria Lima Lopes et al. (in prep.)

Characterization of kaolinite particle surface charge

Interaction of particles is controlled by their electrical charge and this needs to be characterized prior to performing any quantitative calculation. Data are available in the literature for a well crystallized kaolinite identified as KGa-1. A detailed analysis of the data available in the literature and their interpretation is presented hereafter.

According to Sposito (1998), clay particles develop surface charge from i) structural isomorphous substitutions referred to as ‘structural charge’ and denoted σ_0 and ii) proton adsorption and desorption reactions referred to as ‘proton charge’ denoted σ_H . The sum of these two charges is referred to as ‘intrinsic charge’ denoted σ_{in} :

$$\sigma_{in} = \sigma_0 + \sigma_H \quad (9)$$

The intrinsic charge is counterbalanced by the Stern layer surface charge denoted σ_S and the counterions in the diffuse double layer denoted σ_d (Figure 65).

The counterions in the Stern layer are immobilised in surface complexes, i.e. they do not engage in translational motions relative to the particle surface. Sposito (1989) therefore introduces the concept of total particle charge denoted σ_P , representing the net surface charge contributed by the adsorbent structure plus the adsorbed ions immobilised in the Stern layer:

$$\sigma_P = \sigma_{in} - \sigma_S = -\sigma_d \quad (10)$$

In this paper, the total particle charge σ_P is assumed to control clay particle interaction.

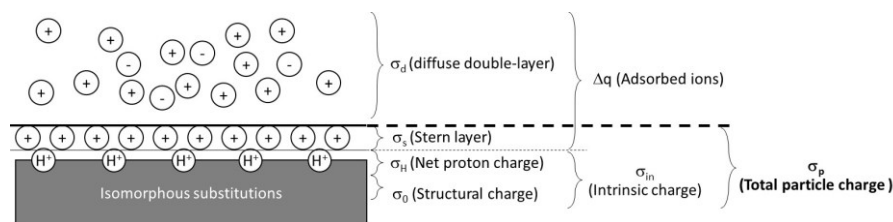


Figure 65. Operational categories of surface charge (after Sposito 1989)

Measurements of structural and proton charge have been carried out on reference kaolinite

identified as KGa-1, classified as ‘well crystallized’ kaolinite from the Source Clays Repository of the Clay Minerals Society. Scroth and Sposito (1997) measured a structural surface charge σ^* , equal to 6.3 mmol/kg (by measuring the cation exchange occurring in a solution saturated with Cs). The structural charge is attributed to the particle faces, i.e. the structural surface charge is determined by considering the specific surface area of the faces. If the particle is assumed to have hexagonal shape with size d and thickness t (Figure 66), the ratio between specific surface area of the faces denoted SSA_{faces} and the total specific surface area denoted SSA_{total} is given by

$$\frac{SSA_{faces}}{SSA_{total}} = \frac{\left(\frac{d}{t}\right)}{2 + \left(\frac{d}{t}\right)} \quad (11)$$

Assuming $d/t=10$, this ratio is $\cong 85\%$, in line with the assumption made by Zhou and Gunter (1992). The surface charge can therefore be calculated as follows:

$$\sigma_0 = 10^{-3} \frac{\sigma_0^* \cdot e \cdot N_A}{SSA_{face}} \quad (12)$$

where σ_0^* is the measured surface charge in mmol/kg, e is the electron charge, N_A is the Avogadro’s number, SSA is the specific surface area in m^2/g , and σ_0 is the surface charge in mC/m^2 . The calculated structural surface charge is reported in

Table 2.

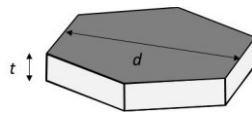


Figure 66. Kaolinite particle geometry

Proton charge of KGa-1 kaolinite has been measured by proton titration. Figure 67 shows data collected from two different sources, which appear to be in fair agreement. Protonation and deprotonation has often been assumed to involve only particle edge (e.g. Wang and Siu 2006) and, as a result, proton charge has often been attributed to the edge. However, Zhou and Gunter (1992) have demonstrated that the attribution of the proton charge only to the particle edge leads to values that exceed the physical limit imposed by kaolinite and concluded that the basal surface must also contribute to proton reactions. The assumption made in this paper is that proton charge is uniformly distributed over the edge and the alumina basal face, as both expose hydroxide groups. The proton charge was therefore calculated as follows:

$$\sigma_H = 10^{-3} \frac{\sigma_H^* \cdot e \cdot N_A}{SSA_{(Al-face+edge)}} \quad (13)$$

where σ_H^* is the measured proton charge in mmol/kg, $SSA_{(Al-face+edge)}$ is the specific surface area associated with the edge plus the alumina face in m^2/g , and σ_H is the proton surface charge in mC/m^2 . The calculated proton charge is reported in

Table 2. Finally, the intrinsic charge was calculated as the sum of the structural and proton charges as also given in

Table 2.

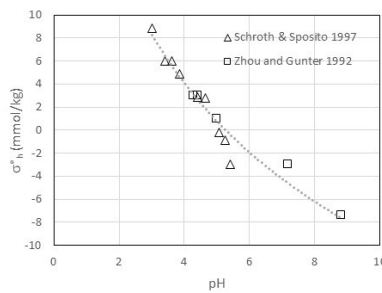


Figure 67. Effect of pH on proton charge σ_H^*

Table 2. Structural, proton, and intrinsic charge for KGa-1

pH		SSA_{total} [m^2/g] (*)	σ_o^* [mmol/kg]	SSA_{faces} [m^2/g] (**)	σ_o [mC/m^2]	σ_H^* [mmol/kg]	SSA_{Al-} face+edge [m^2/g] (***)	σ_H [mC/m^2]	σ_{in} [mC/m^2]
5	Silica face	12	-6.3	10.2	-60				-60
	Alumina face				-60		+11	-49	
	Edge					+0.77	6.9	+11	+11
9	Silica face	12	-6.3	10.2					-60
	Alumina face						-111	-171	
	Edge					-7.95	6.9	-111	-111

(*) after Zhou and Gunter (1992)

(**) assuming $SSA_{\text{faces}}/SSA_{\text{total}} = 0.85$

(***) assuming $SSA_{\text{Al-face + edge}}/SSA_{\text{total}} = 0.575$

The Stern charge σ_S was estimated according to Verwey & Overbeek (1948):

$$\sigma_S = \frac{N_1 v e}{1 + \left(\frac{N_A \rho_{\text{solvent}}}{M n_0} \right) \exp \left(- \frac{v e \Psi_\delta + \varphi}{kT} \right)} \quad (n_0 = c_0 \cdot 10^3 \cdot N_A) \quad (14)$$

where

N_1 [1/m²] = number of adsorption spots per unit area available at the surface

v [-] = valence of counter-ions

e [C] = electron charge ($1.602 \cdot 10^{-19}$ C)

N_A [1/mol] = Avogadro's number ($N_A = 6.022 \cdot 10^{23}$ 1/mol)

ρ_{solvent} [g/m³] = density of the solvent

M [g/mol] = molecular weight of solvent

n_0 [1/m³] = number of counter-ions per unit volume in the far field (at zero electrical potential)

c_0 [M] = counter-ion molar concentration in the far field (at zero electrical potential)

Ψ_δ [V] = potential on the border between Stern layer and Gouy layer

φ [V] = specific chemical adsorption potential of the counter-ions adsorbed on the wall ($\varphi=0$)

K [J/K] = Boltzmann's constant ($K = 1.38 \cdot 10^{-23}$ J/K)

T [K] = absolute temperature

On the other hand, the diffuse double layer charge σ_d , which counterbalances the total particle charge σ_P , can be written as follows according to Verwey & Overbeek (1948):

$$\sigma_P = -\sigma_d = (8n_0 \epsilon_0 \epsilon_r kT)^{\frac{1}{2}} \cdot \sinh \left(\frac{1}{2} \frac{v e \Psi_\delta}{kT} \right) \quad (15)$$

where

ϵ_0 [C²/Jm] = vacuum permittivity ($\epsilon_0 = 8.8542 \cdot 10^{-12}$ C²/Jm)

ϵ_r [-] = relative dielectric permittivity

By combining Eqs. (14) and (15), a relationship can be derived between the intrinsic charge σ_{in} and the total particle charge σ_p as shown in Figure 68 (parameters used in Eqs. (14) and (15) are reported in Table 3). More specifically, values of the electrical potential Ψ_δ were selected and i) the total particle charge σ_p was calculated according to Eq. (15) and ii) the intrinsic charge σ_{in} was calculated as

$$\sigma_{in} = \sigma_p - \sigma_s \quad (16)$$

according to Eqs. (14) and (15). The relationship established in Figure 68 was used to convert the values of intrinsic charge σ_{in} in

Table 2 into the total particle charge σ_p as shown in Table 4.

Table 3. Stern layer parameters

ν [-]	N_1 (*) [1/m ²]	ρ_{solvent} [g/m ³]	M [g/mol]	c_0 (**) [M]	T [K]	ϵ_r [-]
1.5	10^{19}	10^6 g/m ³	18	2×10^{-5} M	293	80

(*) According to van Olphen (1977)

(**) According to Pedrotti and Tarantino (2018)

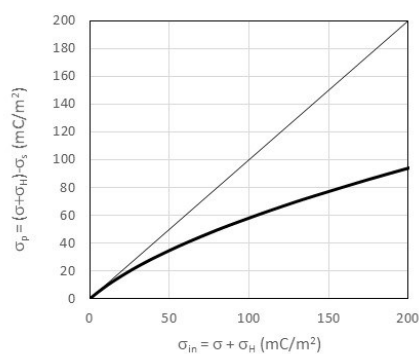


Figure 68. Total particle charge σ_p versus intrinsic charge σ_{in}

Table 4. Intrinsic and total charge for KGa-1.

pH	σ_{in} [mC/m ²]	σ_p [mC/m ²]	σ_{model} [mC/m ²]

]]]
5	Silica face	-60	-41	-75
	Alumina face	-49	-35	
	Edge	11	9	9
9	Silica face	-60	-41	-123
	Alumina face	-171	-83	
	Edge	-111	-63	-63

In summary, clay particles develop surface charge from i) structural isomorphous substitutions referred to as ‘structural charge’ and denoted σ_o and ii) proton adsorption and desorption reactions referred to as ‘proton charge’ denoted σ_H . The sum of these two charges is referred to as ‘intrinsic charge’ denoted σ_{in} , which is counterbalanced by the Stern layer surface charge denoted σ_S and the counterions in the diffuse double layer denoted σ_d . The counterions in the Stern layer are immobilised in surface complexes, i.e. they do not engage in translational motions relative to the particle surface.

Accordingly, this paper assumes that the particle charge is characterised by the net surface charge contributed by the adsorbent structure plus the adsorbed ions immobilised in the Stern layer (referred to as total particle charge σ_P):

$$\sigma_P = \sigma_o + \sigma_H - \sigma_S \quad (17)$$

The permanent charge σ_o is measured via the cation exchange occurring in a solution saturated with caesium (Cs) and is attributed to the basal planes in this paper. The proton charge σ_H , measured via titration methods, is pH dependent (positive at low pH and negative at high pH) and is attributed to the edges and the alumina face in this paper. Finally, the Stern layer surface charge σ_S was estimated based on the model proposed by Verwey and Overbeek (1948). This leads to the charge distribution shown in Figure 69, for acidic kaolinite (pH=5) and alkaline kaolinite (pH=9) respectively.

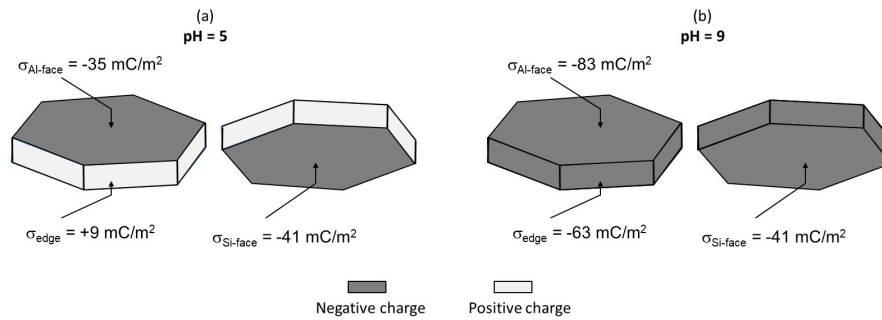


Figure 69. Surface charge density of faces and edges of kaolinite under (a) pH 5 and (b) pH 9.

Interaction pressure

To analyse electrical interaction, particles were modelled as square sheets (i.e. the charges on the alumina and silica faces were concentrated on a single plane). The principle of superposition was used to model the different charge possessed by the face and the edge (a ratio 85/15 was considered for the surface areas of the face and the edge respectively). The square sheet was assumed to have a side of 1 μm . The Coulombian interaction electrical potential was calculated numerically and the interaction pressure was derived as the derivative of the electrostatic energy as detailed hereafter.

Case of uniform charge

The case of two parallel square particles was examined. The particle 1 has its centroid centred on the origin of the reference system whereas the particle 2 has its centroid located at the point (x_a, y_a, z_a) .

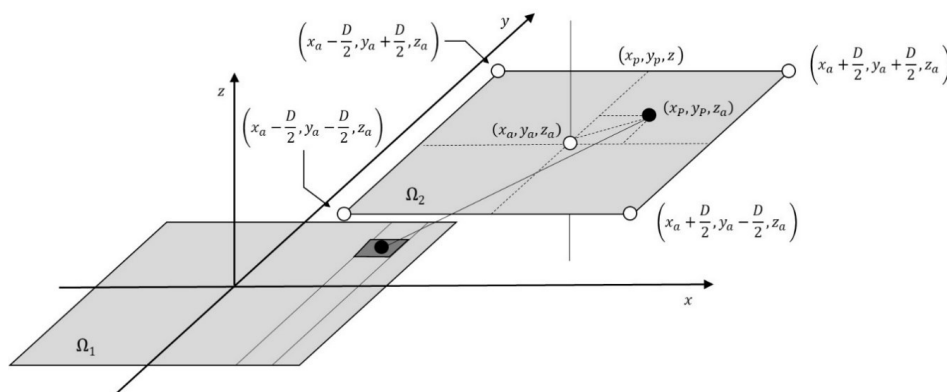


Figure 70. Electrical interaction between two square particles uniformly charged

The electrical potential dV_P generated by the an elementary surface $dx \cdot dy$ of the particle 1 on a generic point P on the particle 2 point is given by

$$dV_P = \frac{1}{4\pi\epsilon_0\epsilon_r} \frac{k \sigma \, dx \, dy}{\sqrt{(x_p - x)^2 + (y_p - y)^2 + z_a^2}} \quad (18)$$

Integration leads to the electrical potential V_P generated by the the particle 1 on a generic point P on the particle 2:

$$V_P = \iint_{\Omega_1} dV_P = \frac{1}{4\pi\epsilon_0\epsilon_r} \sigma \int_{-\frac{D}{2}}^{\frac{D}{2}} \left[\ln \left(\frac{-(x_p - \frac{D}{2}) + \sqrt{(x_p - \frac{D}{2})^2 + (y_p - y)^2 + z_a^2}}{-(x_p + \frac{D}{2}) + \sqrt{(x_p + \frac{D}{2})^2 + (y_p - y)^2 + z_a^2}} \right) \right] dy \quad (19)$$

The electrostatic energy of the particle 2 generated by the particle 1 is given by

$$U_{21} = \frac{1}{2} \sigma \int_{\Omega_2} V_P \cdot d\Omega \quad (20)$$

where σ is the uniform particle surface charge. By replacing (19) into (20), the term U_{21} can be calculated by solving numerically the following triple integral:

$$U_{21} = \frac{1}{2} \frac{\sigma^2}{4\pi\epsilon_0\epsilon_r} \int_{x_a - \frac{D}{2}}^{x_a + \frac{D}{2}} dx \int_{y_a - \frac{D}{2}}^{y_a + \frac{D}{2}} dy \int_{-\frac{D}{2}}^{\frac{D}{2}} \left[\ln \left(\frac{-(x_p - \frac{D}{2}) + \sqrt{(x_p - \frac{D}{2})^2 + (y_p - y)^2 + z_a^2}}{-(x_p + \frac{D}{2}) + \sqrt{(x_p + \frac{D}{2})^2 + (y_p - y)^2 + z_a^2}} \right) \right] dy \quad (21)$$

If the two particles have the same area

$$\Omega_1 = \Omega_2 = \Omega \quad (22)$$

then the electrostatic energy of the system made of two parallel particles is given by:

$$U = U_{21} + U_{12} = 2U_{21} \quad (23)$$

The interaction force F normal to the particles can then be derived by differentiating the electrostatic energy with respect to the interparticle distance z_a

$$F = \frac{dU}{dz_a} \quad (24)$$

Finally, the interaction pressure is calculated by normalising the force with respect to particle area Ω :

$$p = \frac{F}{\Omega} \quad (25)$$

Case of non-uniform charge

The case of particle having a different charge on the edge and the faces was analysed by i) concentrating the charge on the silica and alumina face on a single plane (σ_{model} in Table 4) and ii) using the principle of superposition as shown in Figure 71. The ratio between the particle size D and the width of the edge d was estimated based on the Eq. (11) and its value given in

Table 2:

$$\frac{d}{D} = 1 - \sqrt{\frac{SSA_{\text{faces}}}{SSA_{\text{total}}}} = 0.08 \quad (26)$$

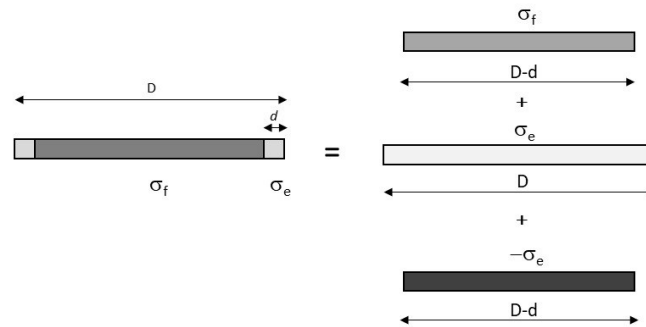


Figure 71. Principle of superposition used to calculate electrical field of non-uniformly charged particle

Figure 72a,b show the interaction pressure between two kaolinite particles with 100%, 56% and 25% of their surfaces overlapping under pH 5 and 9 respectively. For comparison, the interaction pressure between two infinite sheets p_{sheet} having the same charge of the face is also shown in this figure:

$$p_{\text{sheet}} = \frac{\sigma_{\text{sheet}}^2}{2\epsilon_0\epsilon_r} \quad (27)$$

where ϵ_0 is the vacuum permittivity, ϵ_r is the relative dielectric permittivity, and σ_{sheet} is the (uniform) charge of the infinite sheet.

The most striking aspect revealed by Figure 72a,b is that the interaction pressure arising from the overlapping of the particle electrical fields is a finite value, which approaches the value

of the infinite sheet (note that the interaction pressure of the infinite sheet is calculated by considering the charge of the face whereas the interaction pressure of the finite square sheet is computed by considering a non-uniform charge different for the face and the edge). In other words, it is sufficient that the external pressure applied to the pair of particles exceeds the maximum sustainable interaction pressure to bring particles in face-to-face configuration into contact. Once contact is achieved, it is reasonable to assume that attractive van der Waals forces prevent the particles to detach once the external pressure is relieved upon unloading. This is essentially the mechanism generating plastic deformation when particles are in face-to-face configuration (alkaline specimens at any stress or acidic specimens at high stress).

Figure 72a,b also shows that i) the range of pressures required to bring two particles into contact appears to be of the same order of magnitude of the macroscopic ‘continuum scale’ stress that generates plastic deformation in face-to-face configuration; ii) the interaction pressure reduces if the overlap is partial, i.e. particles are likely to ‘bond’ in a staggered pattern; iii) the maximum interaction pressure of acidic (pH=5) and alkaline (pH=9) is different due to the different surface charge but remain within the same order of magnitude.

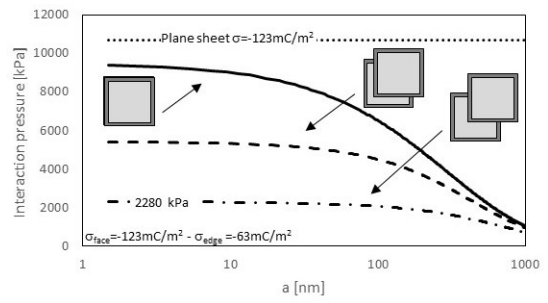
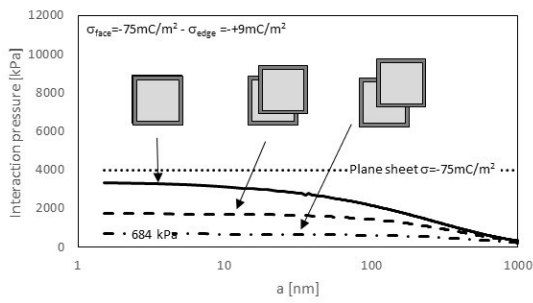
To investigate the role of Van der Waals attractive forces, the interaction pressure was re-computed by superposing the (repulsive) Colombian pressure with the attractive Van der Waals pressure according to Israelachvili (2011):

$$p_{vdw} = -\frac{A}{6\pi a^3} \quad (28)$$

As shown in Figure 72c,d, the Van der Waals forces only becomes active at very close distance from the particles and do not modify substantially the Colombian pattern, i.e. to bring face-to-face particles into contact there is no need to invoke Van der Waals attractive forces, it is sufficient that the external pressure exceed the maximum Coulombian repulsion pressure that can be generated by the overlapping electrical fields. Van der Waals attractive forces only comes into play to prevent that particles detach once the external pressure is released.

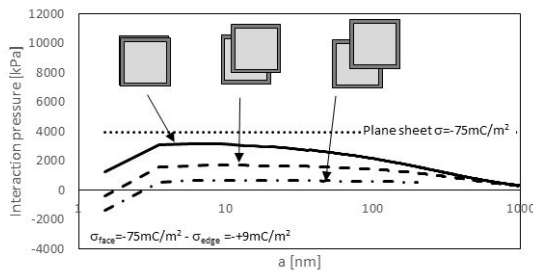
Once two particles are forming a ‘stack’, the stacks are more difficult to be brought into contact because the net charge of the stuck increases. As an example, Figure 73 shows the interaction pressure when stacks are involved (only the case of stacks formed by particles overlapping 100% is shown in the figure for the sake of simplicity). Because the limiting Coulombian repulsion pressure varies with the square of the charge (see Eq. (8)), bringing particle stacks together is much more difficult than bringing single particles together.

Coulombic forces only

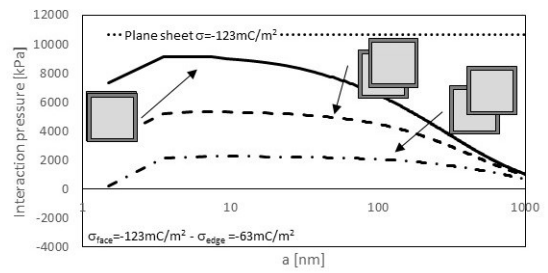


Coulombic and Van der Waals forces

(a)



(b)



(c)

(d)

Figure 72. Interaction pressure between two kaolinite particles with 100%, 56% and 25% of their surfaces overlapping. (a) pH 5 - Coulombic forces. (b) pH 9 - Coulombic forces. (c) pH 5 - Coulombic and Van der Waals forces. (d) pH 9 - Coulombic and Van der Waals forces

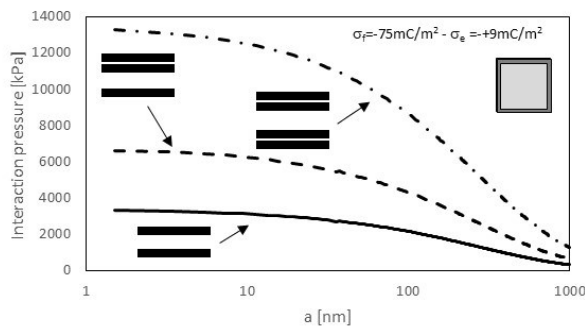


Figure 73. Interaction pressure between generated by particle stacks

Chapter IV: Effect of Submergence Time on Erosion Mechanisms of Clay in Jet Erosion Test

1 Introduction

The Jet Erosion Test (JET) is one of the few methods used to quantify the erodibility of fine-grained soils in geotechnical applications (Hanson and Cook, 2004). This test is employed in the laboratory and field to determine erosion rate coefficient (k_d) and critical shear stress (τ_c) of materials susceptible to erosion. The JET provides crucial insights into soil behaviour under erosive conditions (Wahl, 2021) and has been used in studies related to the erosion of flood embankment and reliability analysis of earth dams (Andreini et al., 2019).

Flood embankments and dams are often constructed with clayey geomaterials, compacted at prescribed water content and dry density. Data in literature show quite erratic patterns on the influence of compaction water content and dry density on erosion properties.

Hanson (1992) tested a clay loam (28% sand, 38% silt, 34% clay), by varying dry density and water content along the compaction curve and found that maximum scour depth is monotonically controlled by water content whereas dry density appears to have limited effect. Hanson and Robinson (1993) testing a sandy clay loam (34% sand, 39% silt, 27% clay) showed that maximum scour depth varies non-monotonically with water content (at given dry density) whereas it decreases monotonically with dry density (at given water content).

Hanson and Hunt (2007) tested a clay loam (25% sand, 49% silt, 26% clay) and observed that the erosion rate coefficient varied non-monotonically with water content (at given dry density) whereas it decreased monotonically with dry density (at given water content). They also observed that the scour depth decreases with increasing compaction water content along the 'dry' branch of the compaction curve (at constant compaction effort). In this case, the decrease in scour depth might have been due to either increasing water content or increasing dry density. Benahmed & Bonelli (2012) tested two kaolinite clays (IP=16% and IP=24% respectively) via Hole Erosion Test (HET) and showed conflicting trends for the variation of the critical shear stress

and erosion rate coefficient with compaction water content (at given dry density) for the two clays.

Nguyen (2014) and Nguyen et al. (2017) tested a clayey silt (82% silt, 18% clay fraction) and show different trends depending on soil dry density. Scour depth increased with compaction water content at low dry density (1.55 to 1.6 g/cm³) and decreased with compaction water content at dry density (1.65 to 1.75 g/cm³). In these two studies, the maximum scour depth and the scoured volume were both measured. Inspection of the relationship between maximum scour depth and scoured volume shows a non-monotonic variation, possibly suggesting the different scour depth vs water content trends observed at different dry densities is associated with different morphology of the scour.

Despite the utilization of the JET test there is not a clear and consistent experimental procedure in the JET literature: sample submergence time, length of jet exposure and head steps, drainage of the cell, scour measurement; thus making comparison between different tests and materials extremely difficult. As for any geomaterial there must be a strong time dependency in the hydromechanical behaviour and coupling. The resulting effect of submergence time and time-exposure to jet will depend on the hydraulic condition of the sample (e.g. water content, hydraulic conductivity).

In jet erosion test, the sample installed in the apparatus possesses a suction, even under saturated conditions. Once submerged, the zero-suction imposed at the surface propagates into the sample. Different submergence times are therefore expected to generate different distributions of suction in the sample and, hence, different erodibility. The effect of submergence time is expected to be more pronounced in fine-grained materials characterized by low hydraulic conductivity. For example, Nguyen (2014) showed very slow penetration of suction in the clayey silt tested (the zero suction front penetrated ~1cm after 10 min submergence time and ~3cm after 60 min submergence time). The effect of suction on the erodibility of clayey geomaterials has been investigated by Liu (2017) testing a clayey silt (5% sand, 56% silt, 39% clay). As expected, they observed that the erodibility is lower at higher suction.

The effect of submergence time of clayey samples prior to the commencement of the JET is then paramount in the measured erosion properties even if this effect has not been directly studied in the literature. Submergence time is also rarely reported with very few exceptions (e.g., Hanson (1993) who submerged samples for 20h prior to testing). Most of the authors do not report information on sample history prior-JET testing such as submergence time or they

provide limited information, whereas these are conditions that need to be controlled and not simply monitored.

This paper aims to shed light and provide a key of interpretation on the often inconsistent results via an experimental study investigating the effect of submergence time, compaction water content and dry density on erosion behaviour of compacted kaolin clay. To reveal possible different mechanisms underlying the different erosion responses at varying compaction water contents and dry densities, the full scour geometry was detected using a laser scanner. This enabled the measurement of both scour depth and scoured volume, the latter seldomly reported in the literature. To infer the effect of suction changes occurring in samples exposed to different submergence times, the water content was measured post-mortem on different horizontal slices.

2 Methods

2.1 Material and Specimen Preparation

Speswhite™ Kaolin from Imerys with a plastic limit $w_p = 0.32$ and a liquid limit $w_L = 0.64$ was chosen for the tests presented herein. The particle size distribution shows it to have a 0.20 silt fraction and a 0.80 clay fraction. Specimen preparation consisted of two stages: 1) compaction of the specimen (to target water content and dry density); 2) submersion of the compacted specimen for target submersion time.

To reach the target water content, oven dry kaolin powder was moisturized with distilled water in thin layers in a plastic tray, mixed with sharp spatula and let homogenise in sealed plastic bags for 24 hours, as described in Tarantino and Tombolato (2005). After moisture equalisation, the material was sieved using a 1 mm mesh sieve. Static compaction was carried out in an acrylic cylindrical mould 100 mm height, 100 mm internal diameter, and 5 mm wall thickness. A loading frame operating in displacement control was used to achieve the target dry density. Compaction was performed in one single layer to avoid any stratification that could affect the formation of the scour hole.

Compacted samples were stored in sealed bags for 24 hours before testing. The sample was then submerged with water directly in the JET apparatus with water level 200 mm above the top surface of the sample requiring 30 seconds from water touching the top of the sample to jet testing. The bottom of the sample was vented to allow the pore-air to be displaced as the waterfront advanced downward from the top of the sample.

Samples were compacted to two different water contents (0.16 and 0.32), and two different dry densities (1.09 and 1.30 Mg/cm³). The dry density and water content of the compacted samples are shown in the compaction plane in Figure 1 ('w16' and 'w32' stand for water content equal to 0.16 and 0.32 respectively and 'low' and 'high' stand for dry density equal to 1.09 and 1.30 Mg/cm³ respectively). All samples were compacted on the 'dry' side of optimum. Different submersion times were considered for each compaction state as shown in Table 1.

Table 1. Submergence time (in minutes) for samples compacted at different water contents, w , and dry densities ρ_d

	w=0.16	w=0.32
$\rho_d=1.09 \text{ Mg/cm}^3$	10 min	10 min
$\rho_d=1.30 \text{ Mg/cm}^3$	1,3,5,10,60,180,390 min	1,3,5,10,60,180,390 min

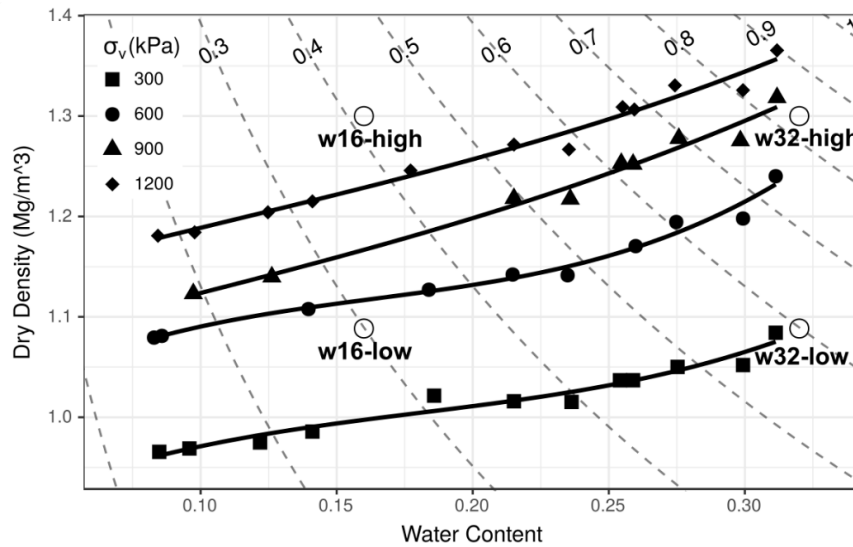


Figure 1. Compaction plane for Speshwite kaolin (after Tarantino and De Col, 2008) and samples tested in the JET apparatus (open circles)

2.2 Jet erosion test procedure

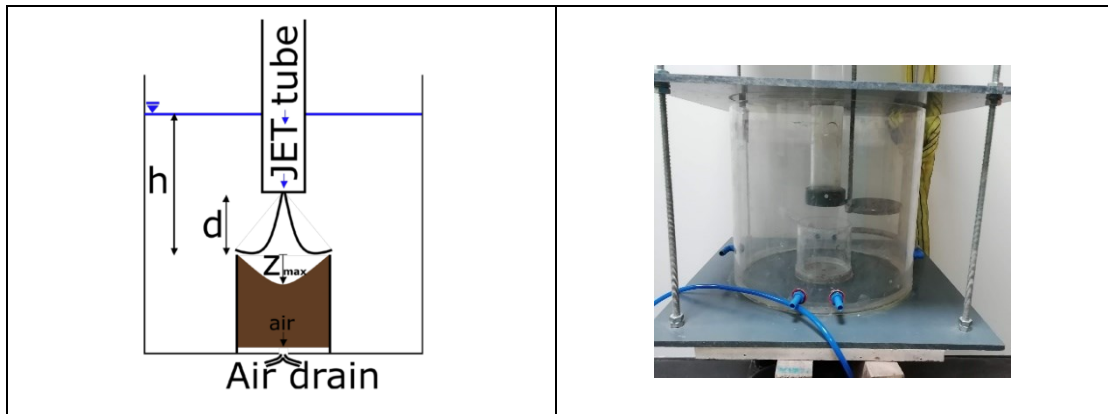


Figure 2. A) Schematic of the JET erosion test apparatus utilized in this study (after Beber et al. (2019)). The air drain is added to the original design (Hanson and Cook, 2004) to allow the expel of air pushed by the advancing wetting front from the surface of the sample to the bottom. B) Picture of the JET device realized at the University of Strathclyde (the blue tube is connected to the air drain at the base of the sample holder).

The specimens were tested within the JET apparatus described in Beber et al. (2019). The submerged impinging water jet (normal to the surface of the sample) was generated by a 6.4 mm diameter nozzle positioned at 40 mm from the surface of the sample and subjected to 1.24 m piezometric head. The impinging jet was generated under water with a free water surface maintained at 200 mm above the sample surface. The impinging jet was maintained for 5 min after which the sample was removed, scour geometry and water content were measured.

2.3 Scour morphology

The typical scour morphology after 5 min impinging jet is shown in Figure 3. The profile below the mould edge generally presents a step (e.g. a plateau) characterised by a depth z_0 and a scour hole with depth z_G (referred to the base of the step). During the submersion period, the compacted clay samples tended to swell by an amount Δz . As such, the total scour depth z_{tot} is given by:

$$z_{tot} = \Delta z + z_0 + z_G \quad [1]$$

Accordingly, the scoured volume is made of three components:

$$V_{tot} = \Delta V + V_0 + V_G \quad [2]$$

The volumes associated with Δz and z_0 were calculated assuming cylindrical shapes.

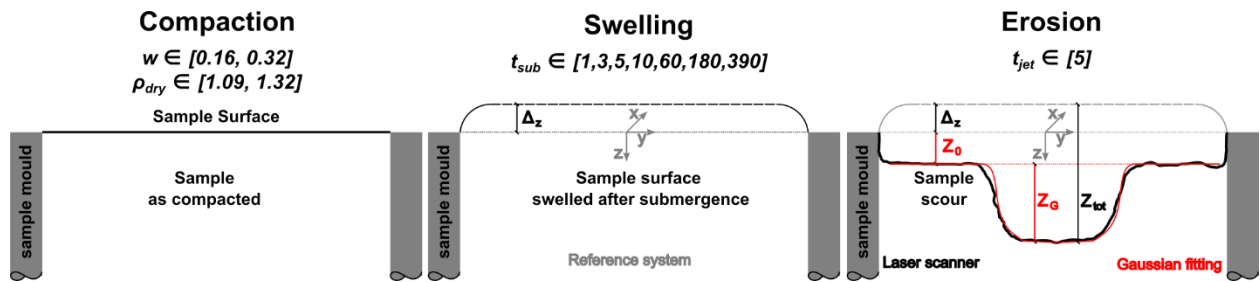


Figure 3. Sample history (i.e. static compaction, swelling, erosion) and scour hole geometry

2.3.1 Correction for swelling accumulated during submersion period

The amount of swelling prior to the application of the impinging jet (Figure 3) for the samples compacted at the higher density was measured via processing photography images taken at the start and end of the submersion period. Figure 4 show the variation of sample height, Δz , measured at 10, 60, 180, and 390 minutes (solid symbols). As expected, the swelling Δz increased with the duration of the submersion period. Samples at higher compaction water content ('w32-high') swelled more than the samples prepared at lower compaction water content ('w16-high'). The swelling was not measured for the samples subjected to submersion periods of 1, 3, and 5 minutes. The swelling was inferred by fitting the experimental data in the range 10-390 min with a power law and extrapolating the fitting curve to 1 min (open symbols in Figure 4).

The swelling occurring in the samples compacted at lower density and subjected to 10 min submersion time was not measured. Conservatively, their swelling was assumed to be equal to swelling of the samples compacted at higher density.

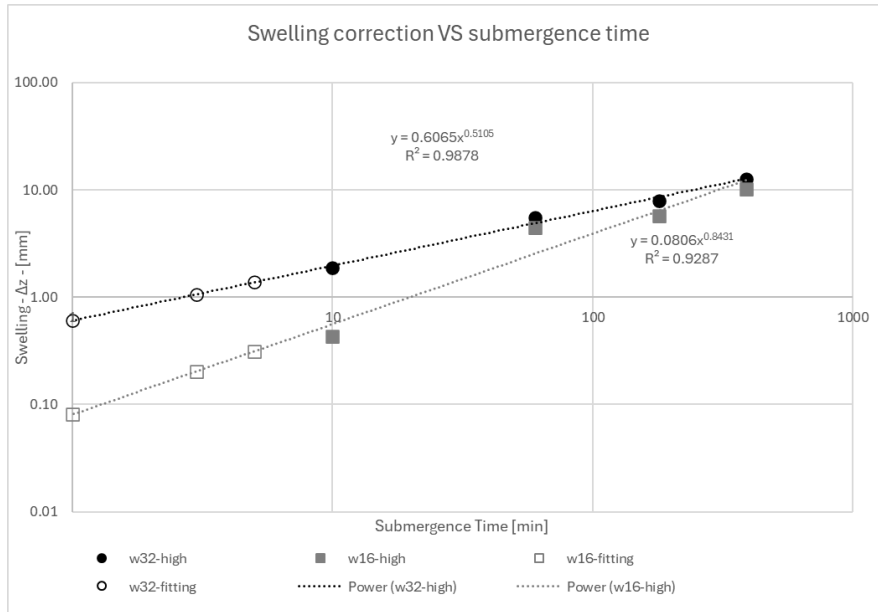
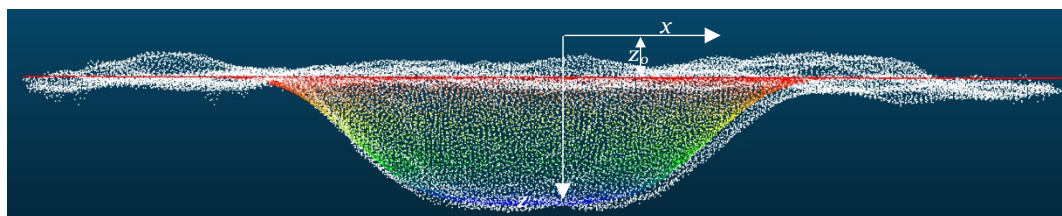


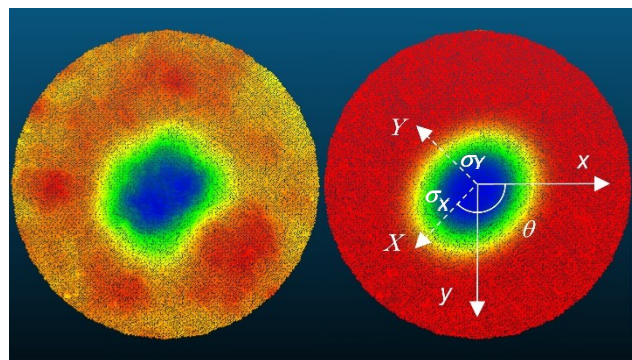
Figure 4. Variation of sample height Δz accumulated during the submersion period. Samples compacted at the higher density ($\rho_d=1.30 \text{ Mg/cm}^3$)

2.3.2 Measurement and geometrical representation of the scour hole

The surface of the sample before and after the erosion test was recorded using a scanCONTROL 2700-100/BL Laser Scanner from Micro-Epsilon. The point clouds coregistration and difference between pre and post erosion scans was performed with the software CloudCompare (version 2.6.2 -2016) and enabled the measurement of the scour hole morphology (Figure 5a).



(a)



(b)

(c)

Figure 5. (a) Side view of scour geometry derived from laser scanner in white. (b) Top view of Contour map of scour depths. (c) Top view of contour map of scour depths derived from the Super-Gaussian fitting

2.3.3 Scour surface modelling

The scour hole morphology (Figure 4a) was modelled with a flat-top super-Gaussian function (Parent et al., 1992), considering that the scour has quasi-radial symmetry and a bell shape:

$$z(x, y) = z_0 + z_G \cdot \exp\{-[a \cdot (x - x_0)^2 + 2b \cdot (x - x_0)(y - y_0) + c \cdot (y - y_0)^2]^p\} \quad [3]$$

where z_0 is the depth of the step, x_0 and y_0 are the coordinates identifying the position of the axis of symmetry in the xy plane, and z_G , a , b , c , and p are fitting parameters. The parameters a , b , c are related to i) the angle θ defining the inclination with respect to the x -axis of the major axis of any ellipse obtained by the intersection between the Gaussian surface and any plane parallel to the xy coordinate plane (Figure 5c) and ii) the standard deviation σ_X and σ_Y of the Gaussian curves obtained by intersecting the Gaussian surface with the planes Xz and Yz , with X and Y being the directions of major and minor axes of the intersection ellipse respectively (Figure 5c). The parameter p controls the flatness of the Gaussian cusp and a constant value $p=1.369$ was adopted to fit the scour morphology for all tests.

As an example, the comparison between the measured and the fitted scour morphology is shown in Figure 5b and Figure 5c respectively for the test w_{32} -high with submersion time of 60 min.

3 Results

3.1 Effect of compaction water content and density

The effect of compaction water content and density was investigated on specimens statically compacted and submerged for 10 minutes prior to imposing an impinging jet for 5 minutes. Two different water contents (0.16 and 0.32) and two different dry densities (1.09 and 1.30 g/cm³) were investigated. Specimens were tested in duplicate or triplicate as detailed in Table 2.

Table 2. Submergence time (in minutes) for samples compacted at different water contents, w , and dry densities ρ_d

	$w=0.16$	$w=0.32$
$\rho_d=1.09$ Mg/cm ³	10 (3 specimens)	10 (2 specimens)
$\rho_d=1.30$ Mg/cm ³	10 (2 specimens)	10 (3 specimens)

Figure 6a shows the total eroded volume, V_{tot} increased with compaction water content at both density values. The volume is reported in terms of measured value (full circles) and value derived from the Gaussian fitting (open circles) showing that these two values are very close.

Figure 6b shows the total erosion depth Z_{tot} against compaction water content. Again, the measured value and value derived from the Gaussian fitting are very close. The samples compacted at lower density show an increase in scour depth with compaction water content, in line with the eroded volume shown in Figure 6a. However, this trend is reversed at higher density, with the scour depth decreasing with compaction water content. The specimens compacted at higher density therefore show two opposite trends for the scoured volume and scoured depth respectively.

To illustrate the morphology of the scour as a whole, Figure 7a shows the volume of the step ($\Delta V + V_o$) normalised to total scoured volume V_{tot} (the volume of the step is calculated by multiplying the depth $\Delta z + z_o$ times the area of the specimen). Figure 7b shows the depth of the step ($\Delta z + z_o$) normalised to total scoured depth z_{tot} . The volumes and depths in Figure 7 are derived from Eq. [3] used to fit the scour geometry.

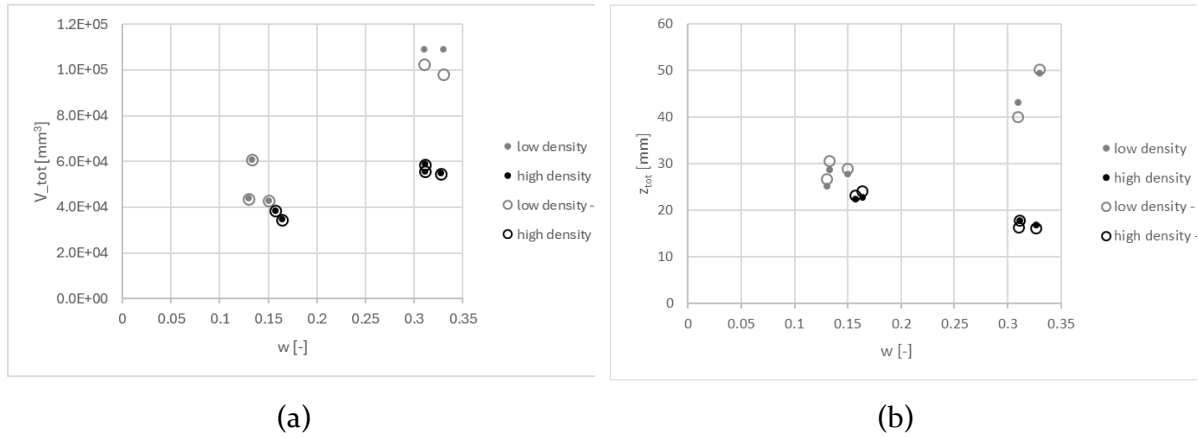


Figure 6 Scour depth and volume versus compaction water content (solid symbols refer to the measured values, open symbols refer to values derived from the Gaussian fitting). (a) Total scour volume V_{tot} . (b) Total scour depth z_{tot}

For the specimens compacted at lower density, the morphology of the scour does not vary significantly with the compaction water content. On the other hand, the morphology changes substantially at higher density. The increase in compaction water content generates a higher step depth/volume compared to the total scour depth/volume in particular the step represent the 55% of the total volume and the 25% of the total scour depth. It is worth noting that the change in scour morphology at higher density occurs for the same specimens that show an opposite trend for scoured volume and scoured depth at varying compaction water content (Figure 6).

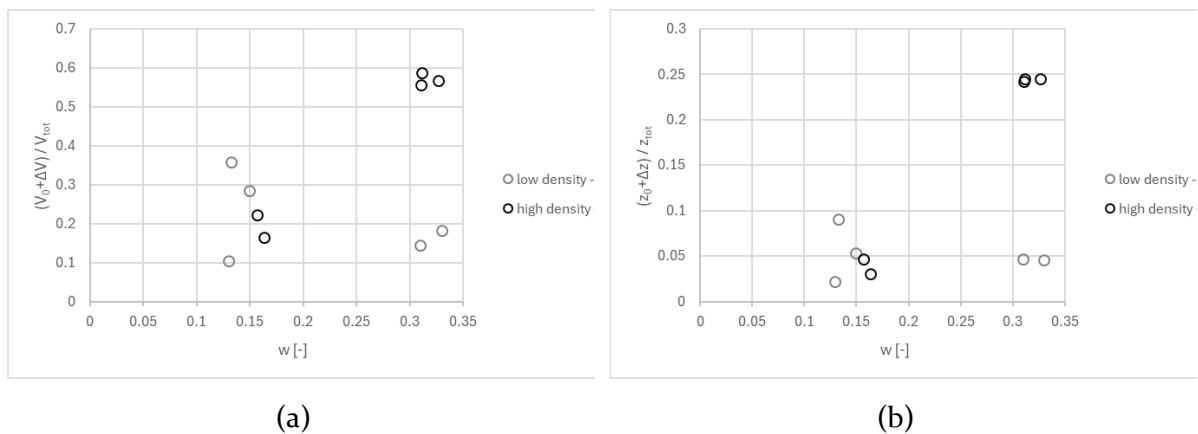


Figure 7. Geometry of scoured 'step'. (a) Volume of the step normalised to total scoured volume. (b) Depth of the step normalised to total scoured depth.

It is also interesting to inspect the morphology of the scour hole, i.e. the portion of scour below the step, by means of the σ_x and σ_y parameters controlling the width of the scour hole.

Figure 8a shows the scour hole depth z_G , normalised to the mean standard deviation of the Gaussian fitting function. This ratio decreases with increasing compaction water content for specimens compacted at higher density. In other words, an increase in compaction water content generates a scour hole that is shallower and wider with ratio close to unity. For the specimens compacted at lower density, an increase in compaction water content generates a scour hole deeper and narrower. Overall, at lower water content, the compaction dry density does not seem to affect much the geometry of the scour hole.

Figure 8b shows the ratio of standard deviation values of Gaussian fitting function along principal directions in the XY plane. The scour hole remains quasi symmetrical for specimens compacted at higher density whereas it becomes asymmetrical for the sample compacted at lower density and higher water content. Again, at lower water content, the compaction dry density does not seem to affect the geometry of the scour hole in terms of symmetry.

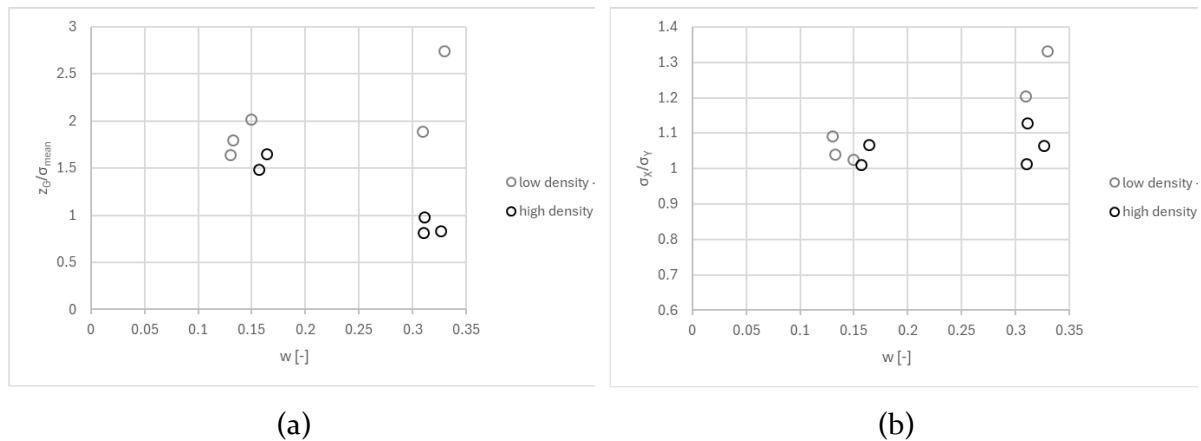


Figure 8. Geometry of scoured 'hole'. (a) Scour depth Z_G , normalised to mean standard deviation of Gaussian fitting function. (b) Ratio of standard deviation values of Gaussian fitting function along principal directions in the xy plane.

3.2 Effect of submergence time

The compaction water content was observed to have opposite effect on scour depth z_{tot} and scour volume V_{tot} respectively for the specimens compacted at higher density ($\rho_d=1.30 \text{ g/cm}^3$) as shown in Figure 6. However, these tests were carried out considering a single submergence time of 10 min. The effect of submergence time was therefore investigated for the samples compacted at the higher density ($\rho_d=1.30 \text{ Mg/cm}^3$) with submergence times ranging from 1 to 390 minutes (Table 3). During the submergence, the quasi-zero water pressure imposed at the specimen top boundary propagates into the initially unsaturated specimen, increasing the pore-water pressure from negative values to zero as the waterfront propagates downward.

Table 3. Submergence time (in minutes) for samples compacted at different water contents and higher dry density ($\rho_d=1.30 \text{ Mg/cm}^3$)

	w=0.16	w=0.32
$\rho_d=1.30 \text{ Mg/cm}^3$	1, 3, 5, 10 (x2), 60, 180, 390 min	1, 3, 5, 10 (x3), 60, 180, 390 min

Figure 9 shows the effect of submergence time on scour depth for the specimens compacted at two different water contents (the scour depth is derived from the Gaussian fitting). The total scour depth z_{tot} presents a different pattern for the two compaction water contents (Figure 9a). At low submergence time ($t < 5 \text{ min}$), the scour depth is lower for the specimen compacted at lower water content ($w=0.16$). At intermediate submergence time ($5 \text{ min} < t < 180 \text{ min}$), the scour depth for the specimen compacted at the lower water content ($w=0.16$) shifts to higher values compared to the specimen at higher compaction water content ($w=0.32$). Eventually, the total scour depths for the two compaction water contents tend to converge at long submersion times ($t \geq 180 \text{ min}$).

A similar pattern is observed for the scour hole depth z_G (Figure 9b) except for the lack of convergence at long submersion times ($t \geq 180 \text{ min}$). Indeed, the scour hole depth for the specimens at $w=0.32$ compaction water content remains nearly constant as the submersion time increases.

The depth of the step ($z_o + \Delta z$ in Figure 9c) remains very similar for the two compaction water contents at low submergence time ($t < 5 \text{ min}$). At longer submergence times, the step depth always remains higher for the higher compaction water content ($w=0.32$).

Overall, there is no inversion for the step depth (Figure 9c) as opposed to the scour hole depth (Figure 9b), indicating that the scour evolves with different morphology for the two compaction water contents. Figure 9b,c also shows that the inversion observed for the total scour depth z_{tot} (Figure 9a) is controlled by the inversion observed for the scour hole depth z_G .

Figure 9d shows the total scour volume V_{tot} . There is no inversion between the curves associated with the two different compaction water contents, with the scoured volume being greater for the higher compaction water content ($w=0.32$). The scour hole volume (Figure 9e) presents the same pattern as the scour hole depth (Figure 9b), with an inversion at 10 min submergence time and the scour volume for the specimens at $w=0.32$ compaction water content remaining nearly constant as the submergence time increases. This shows that the scour hole evolves nearly homothetically.

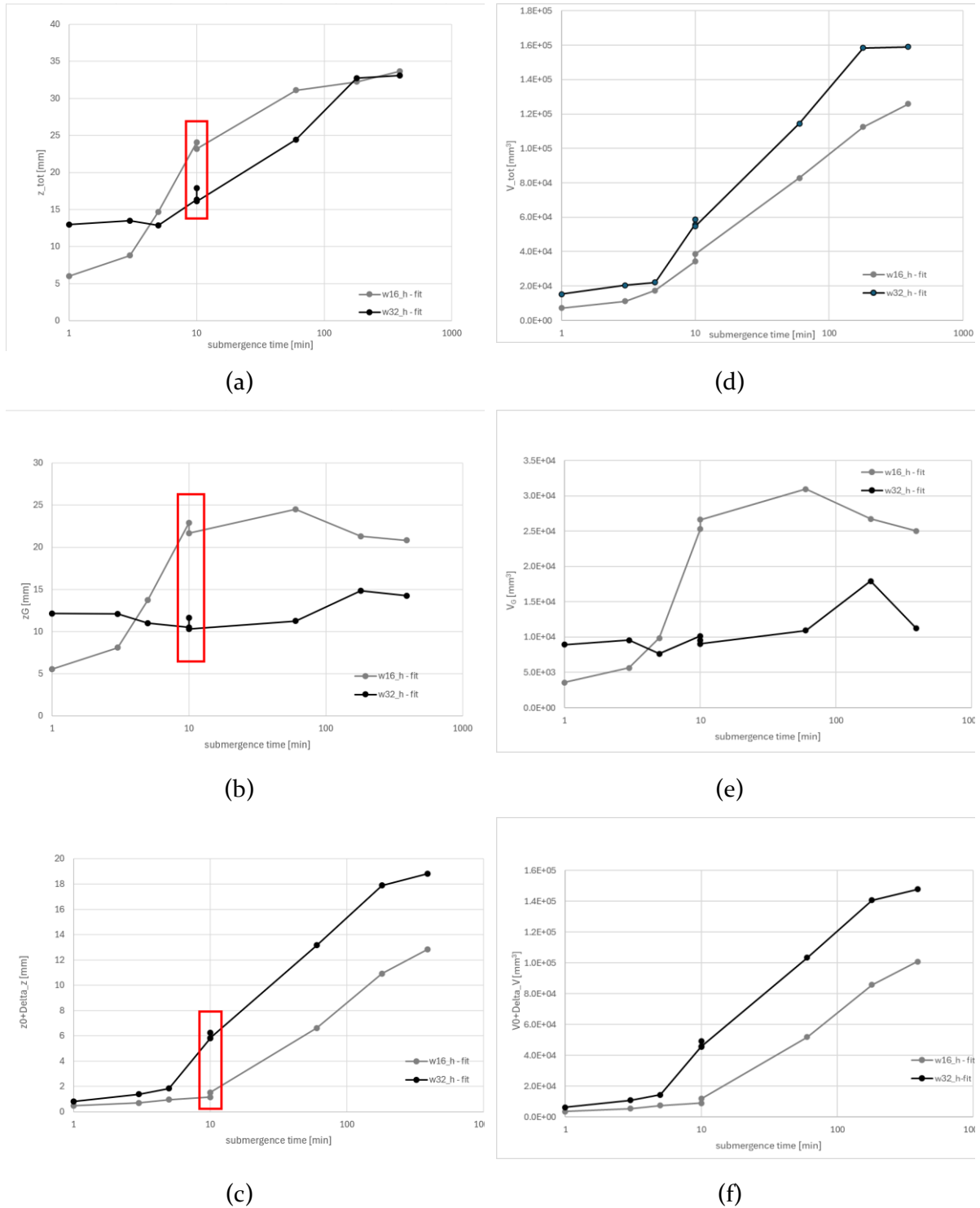


Figure 9. Effect of submergence time on scour depth and volume for specimens compacted at higher density (specimens in red rectangle are the same as reported in Figure 7 and Figure 8). (a) Total scour depth. (b) Scour hole depth. (c) Step depth. (d) Total scour volume. (e) Scour hole volume. (f) Step volume

The step volume (Figure 9f) obviously follows the same path as the step depth (Figure 9c) since the depth volume is calculated based on the assumption of cylindrical volume. The step

volume does not present an inversion and show that the total volume (Figure 9d) is dominated by the step volume.

Overall, Figure 9 confirms that from 10 min submersion time, the specimens compacted at $w=0.16$ and $w=0.32$ water content exhibits an opposite response in terms of scour volume and scour depth, i.e. scour total volume increases with compaction water content as opposed to the scour total depth that decreases with compaction water content.

The evolution of the morphology of the scour is better illustrated by plotting the total scour volume V_{tot} against the total scour depth z_{tot} (Figure 10). The specimens compacted at $w=0.32$ evolve parallel to the ‘cylinder’ line, implying that the erosion occurs with the deepening of the step while the scour hole maintains a nearly constant shape. The specimens compacted at $w=0.16$ shows a rapid increase in total scour depth associated with a rapid increase in the scour hole depth (while the step remains small) until 10 min submergence time. At larger submergence times, the erosion evolves parallel to the ‘cylinder’ line, again implying that the erosion occurs with the deepening of the step while the scour hole maintains a nearly constant shape.

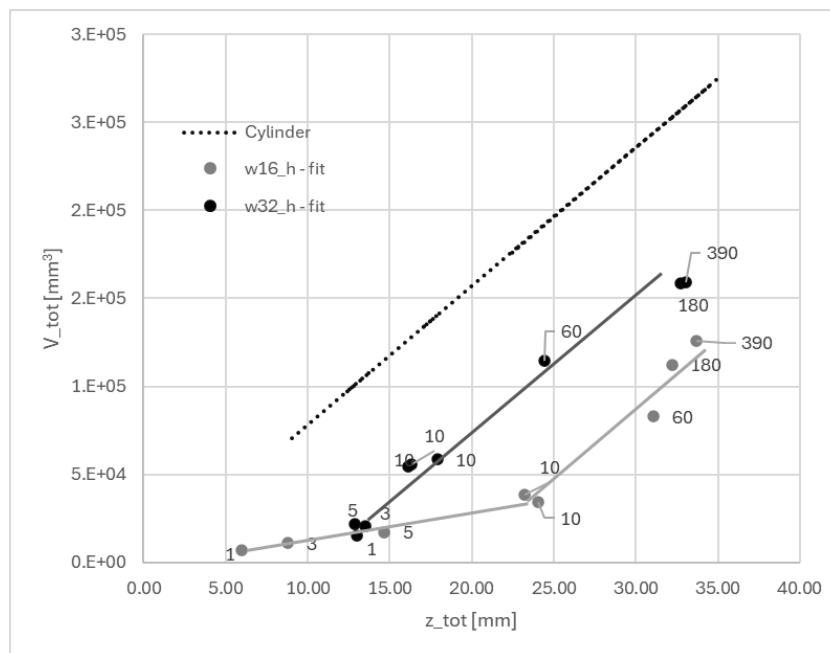


Figure 10. Relationship between total scour depth, z_{tot} , and total scour volume, V_{tot} , for specimens compacted at higher density (submergence times are also reported for each datapoint)

Water content profile was determined experimentally at the end of the erosion test by dissecting the specimens in four slices. Figure 11 shows the evolution of gravimetric water content profile with submersion time and show the progressive saturation of the specimens, with a relatively sharp waterfront for the sample compacted at $w=0.16$ (Figure 11a) and more uniform profile for the sample compacted at $w=0.32$.

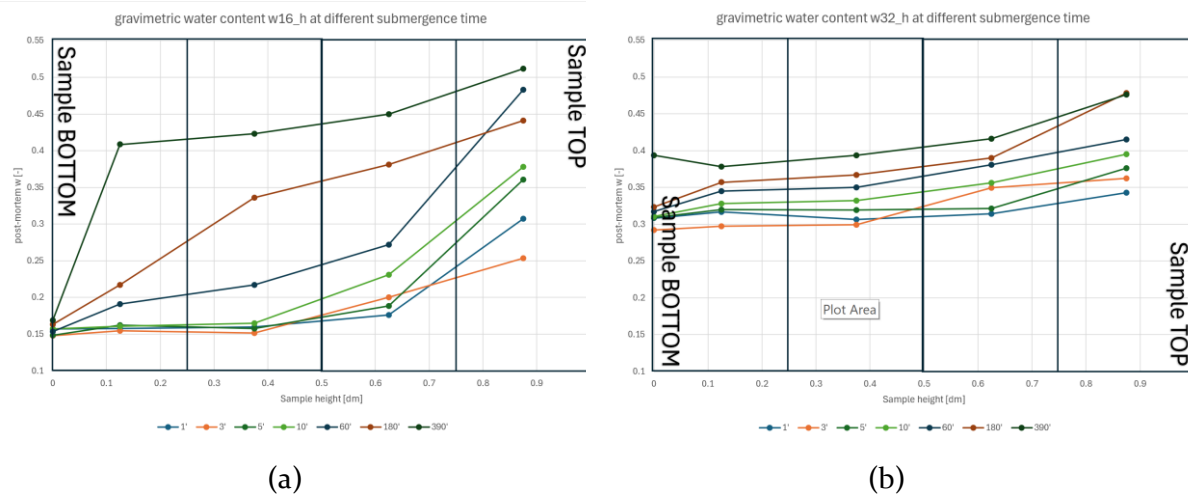


Figure 11. Water content profiles for the samples compacted at high density for different submersion times. (a) Compaction water content $w=0.16$. (b) Compaction water content $w=0.32$. For the sample w_{16} the wetting front has a sharper front compared to sample w_{32} where the gradient is diffuse on the entire depth of the sample. Similar water contents (i.e. and density) are achieved at advance swelling time (e.g. 390 minutes) showing the convergence of the swelling process.

4 Discussion

The experimental results have shown that the submerged water jet generates a scour with a relatively complex geometry, made of a step extending over the entire cross-sectional area of the sample (e.g. a plateau) and a scour hole localised in the centre of the sample. The depths of both the erosion step and the scour hole evolve with the submersion time in a different fashion depending on the compaction water content. At the same time, the compaction water content generates different rates and mode of penetration of the waterfront that propagates from the surface of the sample once the sample is submerged with water before the Jet Erosion Test starts. These experimental results prompt three questions:

- i) What does generate the two different modes of erosion?
- ii) What does generate a different mode and rate of propagation of the waterfront?
- iii) Why the depths of the step and scour hole evolve differently depending on the compaction water content?

To answer these questions the hydro-mechanical response of the compacted clay, of major implication in the behaviour of the partially saturated clay samples subjected to erosion, was modelled within the framework of unsaturated soil mechanics and the two modes of erosion were analysed by considering 'continuum scale' failure mechanisms.

4.1 Hydro-mechanical characterisation

The water retention behaviour of the compacted clay subjected to wetting paths was derived from Tarantino and De Col (2008), who characterised the void ratio-dependent water retention behaviour as follows:

$$S_r = \left[\frac{1}{1 + (\phi e_0 \psi s)^n} \right]^m \quad [4]$$

where S_r is the degree of saturation, e_0 is the void ratio at compaction, s is the suction, and ϕ , ψ , n , and m are soil parameters given in Table 4.

When wetted, compacted kaolin does not exhibit volume change until suction reaches very low values (Tarantino and Tombolato, 2005). It was therefore assumed that the void ratio, e , response of the kaolinite when subjected to wetting paths can modelled via a bilinear function:

$$e(s) = e_{sat} - (e_{sat} - e_0) \frac{\ln(1 + s)}{\ln(1 + s^*)} \quad (s < s^*) \quad [5]$$

$$e(s) = e_0 \quad (s \geq s^*)$$

where e_0 is the void ratio at compaction, e_{sat} is the void ratio under saturated conditions, and s^* is the suction at which the clay starts to swell when approaching saturated conditions, tentatively set at $s^*=10$ kPa. The change in void ratio in the low suction range was assumed to be linear on a semi-log scale.

By implementing Eqs. [4] and [5] in the definition of volumetric water content θ as follows one can account for degree of saturation and void ratio as functions of suction s :

$$\theta = S_r(s) \left(\frac{e(s)}{1 + e(s)} \right) \quad [6]$$

The water retention function expressed in terms of both degree of saturation and volumetric water content is shown Figure 12 for the case of the sample compacted at 32% water content to a dry density $\rho_d=1.30$ Mg/cm³.

The hydraulic conductivity was modelled via a Kozeny-Carman-type function:

$$k = k_{sat0} \left(\frac{e}{e_0} \right)^\alpha \left(\frac{1 + e_0}{1 + e} \right) S_r^\beta \quad [7]$$

where k_{sat0} is the saturated hydraulic conductivity at the reference void ratio e_0 and α and β are soil parameters, which were determined by inverse analysis of the water content profiles as discussed in the next section.

The shear strength was characterised according to Tarantino (2007):

$$\tau_{res} = \left(\sigma + s \frac{e_w - e_{wm}}{e - e_{wm}} \right) \tan \phi' \quad [8]$$

where τ is shear strength, σ is the normal stress, s is the suction, e is the void ratio, e_w is the water ratio, e_{wm} is the microstructural water ratio, and ϕ' is the friction angle (parameters given in Table 4).

Table 4. Hydro-mechanical parameters

Parameter	e_{wm} []	ϕ [kPa ⁻¹]	ψ []	n []	m []	e_0 []	e_{sat} []	ϕ' [°]	s^* [kPa]	k_{sat0} [m/s]	α []	β []
Value	0.4	0.00474	2.992	1.64	0.197	1.00	1.33	22	10	2 E-9	18	12
Source	Tarantino (2007)	Tarantino and De Col (2008)				Experimental		Wheeler (1995)	Best-fitting			

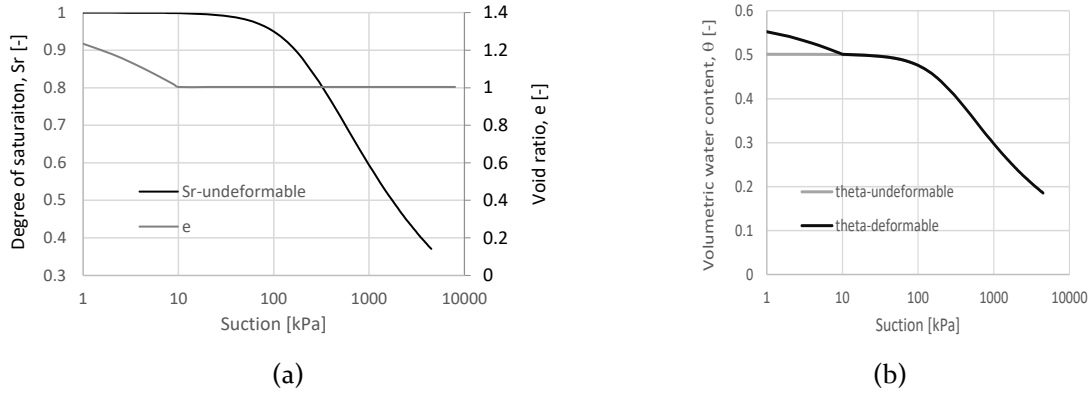


Figure 12. (a) Degree of saturation (Eq. [4]) and void ratio (Eq. [5]). (b) Volumetric water content (Eq. [6]) for the 'deformable' clay (sample compacted at 32% water content to a dry density $\rho_d=1.30 \text{ Mg/cm}^3$) The curves parametrizing the water retention behaviour of the tested material are reported. In particular the swelling in the model is allow to occur only for suction levels lower than 10 kPa.

4.2 Numerical modelling of water infiltration during submersion period

Water flow generated within the clay sample after submersion with water was modelled via the 1D Richards' equation:

$$\frac{\partial}{\partial x} \left[k \frac{\partial}{\partial x} \left(\frac{u_w}{\gamma_w} + z \right) \right] = \frac{\partial \theta}{\partial u_w} \frac{\partial u_w}{\partial t} \quad [9]$$

where z is elevation (positive upward), u_w is the pore-water pressure ($u_w=-s$), γ_w is the unit weight of water, θ is the volumetric water content, k is the hydraulic conductivity, and t is the time. Simulation of the pore-water pressure profiles for the samples compacted at 16% and 32% water content respectively (dry density $\rho_d=1.30 \text{ Mg/cm}^3$) are shown Figure 13.

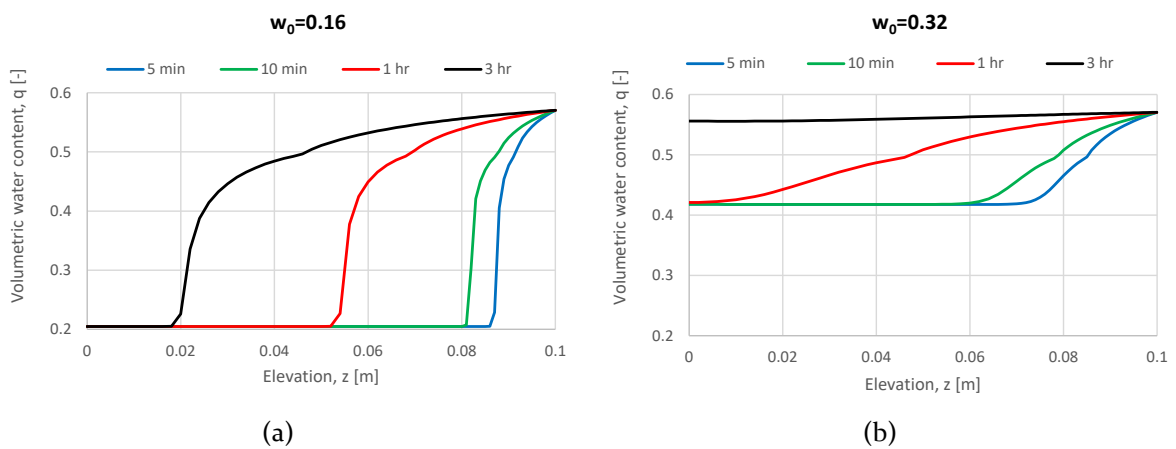


Figure 13. Evolution of volumetric water content profiles as submersion time increases. (a) $w_0=0.16$. (b) $w_0=0.32$. In the two figures the samples start at two different Volumetric water contents, during submersion

the water front propagates differently in the two samples: more sharply and slower in the sample compacted at lower water content due to the low relative hydraulic conductivity.

For the simulation, the bottom boundary was assumed to be impermeable whereas zero pore-water pressure was imposed at the top boundary. The initial condition was associated with the degree of saturation generated by the compaction process.

The numerical results are compared with the experimental results in Figure 14, where the gravimetric water content measured on the four horizontal slices sampled after the jet erosion test are compared with the global gravimetric water content derives numerically for the same slices. The numerical simulation captures satisfactorily the evolution of the water content profiles from a qualitative standpoint. An accurate simulation of the experimental data is outside the scope of this work if one considers that the simulation refers to the undisturbed sample just after submersion whereas the experimental data refer to the sample after submersion and 5 min jet erosion with the formation of erosion step and scour hole.

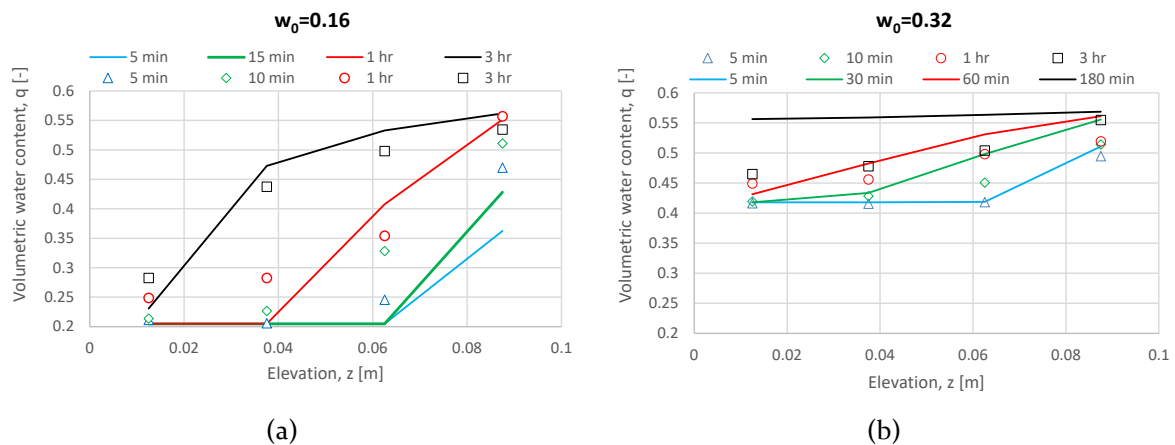


Figure 14. Comparison between the measured and simulated global volumetric water content of sample slices. (a) $w_0=0.16$. (b) $w_0=0.32$.

4.3 Hydrodynamic loading

The hydrodynamic loading associated with the submerged jet impinging on a planar surface has been studied extensively (Fitzgerald and Garimella, 1998; Beltaos and Rajaratnam, 1974; Phares et al., 2000). The maximum normal pressure P_{max} on the surface at the jet centre line was calculated semi-empirically by Beltaos et al. (1974):

$$P_{max} = C \left[\frac{\rho_w U_0^2}{(z_0/d_0)^2} \right] \quad [10]$$

where U_o is the velocity at the nozzle, d_o the nozzle diameter and z_o the distance of the jet outlet to the surface; C has been found experimentally to be 27.8 by Hanson et al., 1990.

The normal pressure distribution on the surface can be represented by an exponential function (Beltaos et al., 1974) (Figure 14a):

$$\frac{P(r)}{P_{max}} = e^{-144(r/z_o)^2} \quad [11]$$

where r is the distance from jet centre line.

Similarly, the maximum tangential stress τ_{max} can be estimated via the following semi-empirical equation by Beltaos et al. (1974):

$$\tau_{max} = 0.16 \left[\frac{\rho_w U_o^2}{(z_o/d_o)^2} \right] \quad [12]$$

The distribution of the tangential stresses can be represented by the following equation by Beltaos et al. (1974) (Figure 14b):

$$\frac{\tau(r)}{\tau_{max}} = 0.18 \left[\frac{1 - e^{-144(r/z_o)^2}}{r/z_o} \right] - 9.43(r/z_o)e^{-144(r/z_o)^2} \quad [13]$$

Ghaneezad et al., 2015 investigated the effect of flow confinement to the forcing exerted on the surface. It was found that in the setup used by the JET, Eq. [12] underestimates the maximum tangential stresses, τ_{max} , by a factor of 2.4. We thus corrected the constant from 0.16 to 0.38 as reported by Ghaneezad et al., 2015 .

In order to analyse the ‘continuum scale’ failure mechanisms and simplify its derivation, the two spatially varying normal and tangential stresses were approximated as reported by the dashed lines in Figure 15a and Figure 15b. The values of normal pressure, $q_{hydrodynamic}$, in the centre and the tangential stress, $\tau_{hydrodynamic}$, are given by Eqs. [14] and [15] respectively.

$$q_{hydrodynamic} = 11 \text{ kPa} \quad [14]$$

$$\tau_{hydrodynamic} = 85 \text{ Pa} \quad [15]$$

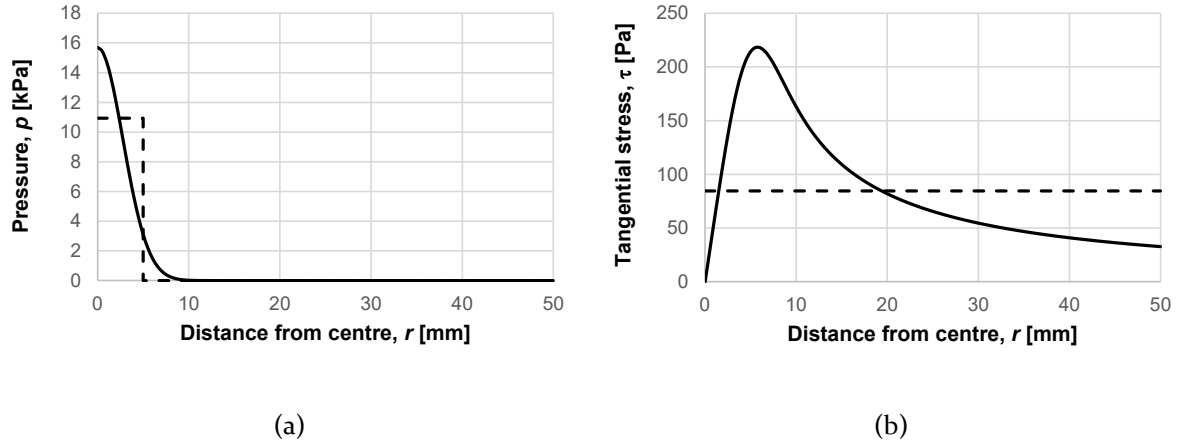


Figure 15. (a) Normal hydrodynamic pressure. (b). Tangential hydrodynamic stress

4.4 Formation of the erosion step

The mechanism leading to the formation of the erosion step, $z_o + \Delta z$, is conceptualised as an horizontal infinite layer subjected to the tangential hydrodynamic stresses, $\tau_{\text{hydrodynamic}}$, which are counterbalanced by the shear resistance, τ_{res} , developing along the potential horizontal failure surface (dashed line in Figure 16 right side).

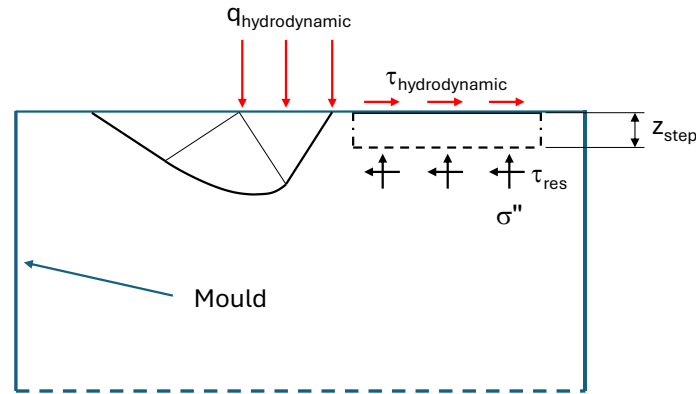


Figure 16. Failure mechanisms associated with normal and tangential hydrodynamic stresses

The shear strength for the unsaturated clay can be defined according to Tarantino (2007) as

$$\tau_{res} = \left(\sigma + s \frac{e_w - e_{wm}}{e - e_{wm}} \right) \tan \phi' \quad [16]$$

where σ is the total stress normal to the failure surface, s is the suction, e and e_w the void ration and water ration respectively, e_{wm} is the microstructural water ratio, and ϕ' is the friction angle. In turn, the normal total stress is given by:

$$\sigma = \gamma z_{step} \quad [17]$$

where γ is the unit weight of the soil (assumed here to be constant and equal to the saturated unit weight) and z_{step} is the depth of the failure surface ($z_{step} = z_o + \Delta z$)

Failure occurs when

$$\tau_{res} = \tau_{hydrodynamic} \quad [18]$$

i.e., the depth of the erosion step can be extracted by the following equilibrium equation:

$$\left(\gamma z_{step} + s \frac{e_w - e_{wm}}{e - e_{wm}} \right) \tan \phi' = 85 \text{ Pa} \quad [19]$$

Figure 17 shows the simulated evolution of the profile of tangent shearing resistance, τ_{res} , with submersion time for the two compaction water contents. The intersection with the line $\tau_{hydrodynamic}=85 \text{ Pa}$ returns graphically the failure depth at different submersion times.

The simulated evolution of depth of the erosion step with submersion time is shown in Figure 18 for the two compaction water contents. The simulation captures correctly the order of magnitude of the depth of the erosion step observed experimentally (Figure 9c) and also the qualitative evolution of the erosion step for the two different water contents.

The mechanisms of failure associated with the erosion step depicted in Figure 16 is clearly a simplification of the real, more complex, erosion process. However, the fair simulation of the evolution of the erosion step with submersion time clearly highlights the role of the evolving partial saturation in controlling the formation of the erosion step.

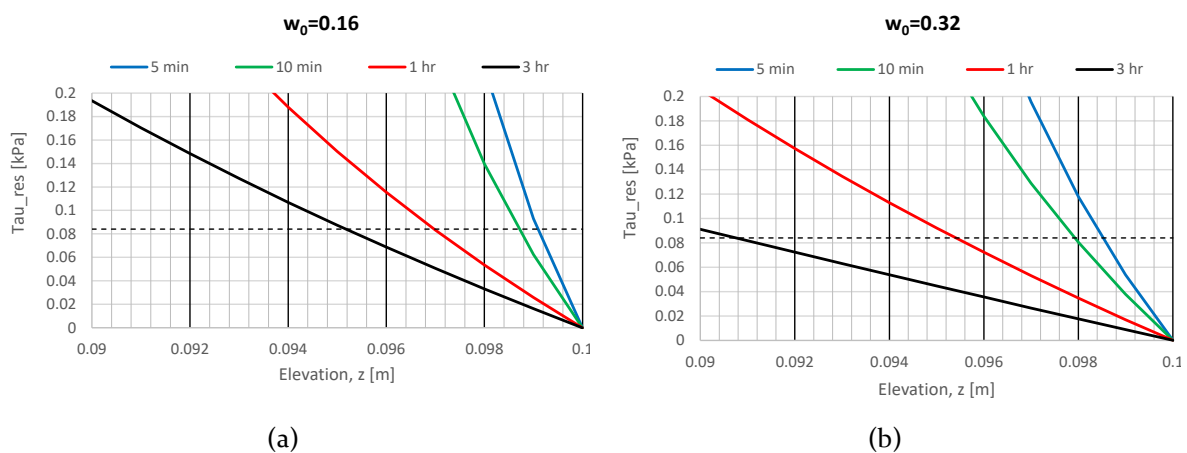


Figure 17. Evolution of the profile of tangent shearing resistance, τ_{res} , with submersion time (a) $w_0=0.16$. (b) $w_0=0.32$.

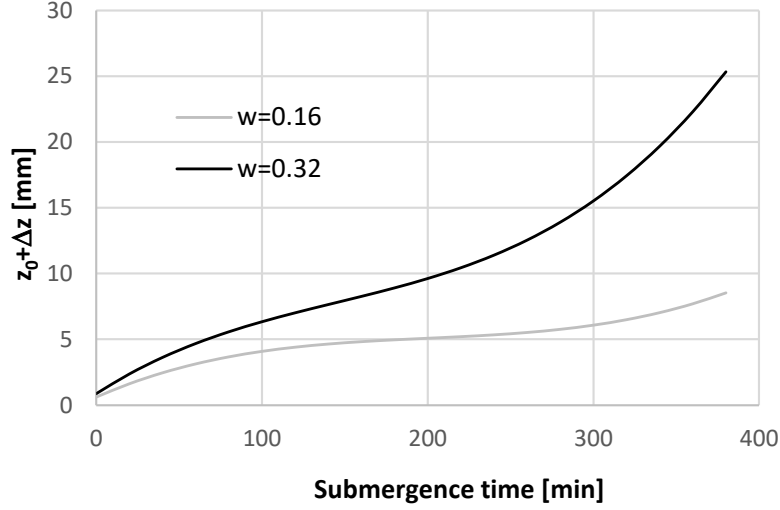


Figure 18. Evolution of depth of the erosion step with submersion time

4.5 Formation of the erosion hole

The mechanism leading to the formation of the scour hole, z_G , is conceptualised as bearing capacity failure triggered by the normal hydrodynamic stresses, $q_{\text{hydrodynamic}}$ (continuous line in Figure 16, left side). The bearing capacity can be written as (Hansen, 1970):

$$q_{lim} = c_{eq}N_c + \frac{1}{2}\gamma BN_\gamma + q_0N_q \quad [20]$$

where B is the load footprint ($B=10\text{mm}$), γ is the soil unit weight, N_γ , N_q and N_c are the bearing capacity factors, and c_{eq} is the equivalent cohesive term generated by the suction. The bearing capacity factors are given by:

$$\begin{aligned} N_\gamma &= 1.5(N_q - 1) \tan \phi' \\ N_c &= (N_q - 1) \cot \phi' \end{aligned} \quad [21]$$

$$N_q = e^{\pi \tan \phi'} \tan^2(45 + \phi'/2)$$

The equivalent cohesive term was calculated considering the suction at 5mm depth, approximately at mid-height of the region where the failure mechanics develops considering the time dependence:

$$c_{eq} = \frac{e_w(t) - e_{wm}}{e(t) - e_{wm}} \cdot s_{5mm}(t) \cdot \tan \phi' \quad [22]$$

where s_{5mm} is the suction at the depth of 5mm. The bearing capacity simulated at different submergence times for the two compaction water contents is shown in Figure 19 together with applied total normal stress, $q_{\text{hydrodynamic}}$. For the case of samples compacted at $w=16\%$, failure

with the corresponding generation of a scour hole occurs only after 6 min of submergence, and this agrees with the observation in Figure 9b. For the case of samples compacted at $w=32\%$, failure occurs earlier (after 2 min in Figure 19) and this is also in agreement with Figure 9b.

The bearing mechanism leads to the same depth of the scour hole once the applied $q_{\text{hydrodynamic}}$ exceeds the bearing capacity. This is in agreement with the constant scour hole depth observed for $w=32\%$ (i.e. since minute 1) and the constant scour hole depth observed for $w=16\%$ once failure is triggered (from minute 5). The bearing capacity mode of failure does not explain, however, the different depth of the scour hole observed for $w=16\%$ and $w=32\%$ respectively (i.e. in the early stage of sample $w=16\%$: 1 to 5 minutes). It is intuitive to assume that the mechanism leading to the formation of the scour hole is more complex than just a bearing capacity mechanism. Nonetheless, the bearing capacity mechanism still represents a valuable conceptualisation of the mechanism leading to the formation of the scour hole

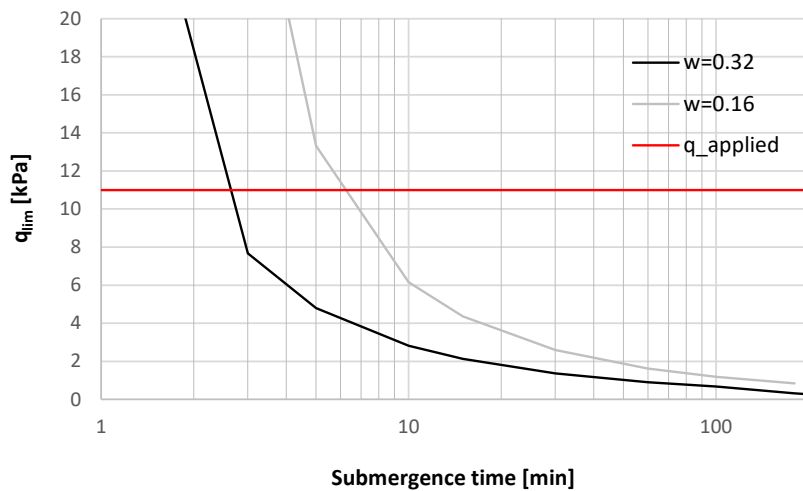


Figure 19. Bearing capacity versus applied hydrodynamic pressure

5 Conclusions

This study has presented an experimental campaign aimed at investigating the effect of submergence time on the scour behaviour of compacted kaolinite clay samples in Jet Erosion Tests. To reveal the different mechanisms underlying the different erosion responses at varying submersion time, compaction water contents and dry densities, the full scour geometry was measured using a laser scanner. This enabled the measurement of both scour depth and scoured volume. The experimental study also investigated the effect of submergence time (prior to the application of the impinging jet). To infer the effect of suction changes occurring in samples

exposed to different submergence times, the water content was measured post-mortem on different horizontal slices.

The experimental results have shown that the submerged water jet generates a scour with a relatively complex geometry, made of a step extending over the entire cross-sectional area of the sample (i.e. a plateau) and a scour hole localised in the centre of the sample. The parametrization of the scour via the fitting of a gaussian surface lead to the identification of the two erosion modes i.e., the step and the scour hole. The depths of both the erosion step and the scour hole evolve with the submersion time in a different fashion depending on the compaction water content. At the same time, the compaction water content generates different rates and mode of penetration of the waterfront that propagates from the surface of the sample once the sample is submerged with water before the Jet Erosion Test starts.

To interpret the different modes of scouring observed for different compaction water contents and dry densities, and their evolution with the submergence time, the hydro-mechanical response of the compacted clay was modelled within the framework of unsaturated soil mechanics and the two modes of erosion were analysed by considering 'continuum scale' failure mechanisms. The step developing at the top of the sample was modelled successfully by considering the failure of a horizontal infinite layer subjected to the tangential hydrodynamic stresses generated by the impinging jet. The central scour hole was assumed to be generated by a bearing capacity mode of failure triggered by the normal hydrodynamic stresses. The submergence time has been identified as a variable that needs to be controlled during JET test on partially saturated geomaterials.

References

- Andreini, M., Gardoni, P., Pagliara, S. and Sassu, M., 2019. Probabilistic models for the erosion rate in embankments and reliability analysis of earth dams. *Reliability Engineering & System Safety*, 181, pp.142-155.
- Beber, R., Tarantino, A., Pedrotti, M. and Lunn, R., 2019. The effect of clay water content in the Jet Erosion Test. In *E3S Web of Conferences* (Vol. 92, p. 02016). EDP Sciences.
- Beltaos, S. and Rajaratnam, N., 1974. Impinging circular turbulent jets. *Journal of the hydraulics division*, 100(10), pp.1313-1328.
- Benahmed, N. and Bonelli, S., 2012. Investigating concentrated leak erosion behaviour of cohesive soils by performing hole erosion tests. *European Journal of Environmental and Civil Engineering*, 16(1), pp.43-58.
- CloudCompare (version 2.6.2) [GPL software]. (2016). Retrieved from <http://www.cloudcompare.org/>
- Fitzgerald, J.A. and Garimella, S.V., 1998. A study of the flow field of a confined and submerged impinging jet. *International journal of heat and mass transfer*, 41(8-9), pp.1025-1034.
- Ghaneezad, S.M., Atkinson, J.F. and Bennett, S.J., 2015. Effect of flow confinement on the hydrodynamics of circular impinging jets: Implications for erosion assessment. *Environmental Fluid Mechanics*, 15, pp.1-25.
- Hansen, J.B., 1970. A revised and extended formula for bearing capacity.
- Hanson, G.J., 1992. Erosion resistance of compacted soils. *Transportation Research Record*, (1369).
- Hanson, G.J. and Cook, K.R., 2004. Apparatus, test procedures, and analytical methods to measure soil erodibility in situ. *Applied engineering in agriculture*, 20(4), pp.455-462.
- Hanson, G.J. and Hunt, S.L., 2007. Lessons learned using laboratory JET method to measure soil erodibility of compacted soils. *Applied engineering in agriculture*, 23(3), pp.305-312.
- Hanson, G.J. and Robinson, K.M., 1993. The influence of soil moisture and compaction on spillway erosion. *Transactions of the ASAE*, 36(5), pp.1349-1352.
- Hanson, G.J., Robinson, K.M. and Temple, D.M., 1990. Pressure and stress distributions due to a submerged impinging jet. In *Hydraulic engineering* (pp. 525-530). ASCE.
- Liu, Q.J., Wells, R.R., Dabney, S.M. and He, J.J., 2017. Effect of water potential and void ratio on erodibility for agricultural soils. *Soil Science Society of America Journal*, 81(3), pp.622-632.
- Nguyen, V.N., 2014. Caractérisation de l'érosion des sols par le Jet Erosion Test. Phd thesis Ecole Centrale Paris, 2014. (NNT : 2014ECAP0043).
- Nguyen, V.N., Courivaud, J.R., Pinettes, P., Souli, H. and Fleureau, J.M., 2017. Using an improved jet-erosion test to study the influence of soil parameters on the erosion of a silty soil. *Journal of Hydraulic Engineering*, 143(8), p.04017018.
- Parent, A., Morin, M. and Lavigne, P., 1992. Propagation of super-Gaussian field distributions. *Optical and quantum electronics*, 24, pp.S1071-S1079.
- Phares, D.J., Smedley, G.T. and Flagan, R.C., 2000. The wall shear stress produced by the normal impingement of a jet on a flat surface. *Journal of Fluid Mechanics*, 418, pp.351-375.
- Tarantino, A., 2007. A possible critical state framework for unsaturated compacted soils. *Géotechnique*, 57(4), pp.385-389.
- Tarantino, A. and De Col, E., 2008. Compaction behaviour of clay. *Géotechnique*, 58(3), pp.199-213.
- Tarantino, A. and Tombolato, S., 2005. Coupling of hydraulic and mechanical behaviour in unsaturated compacted clay. *Géotechnique*, 55(4), pp.307-317.

Wahl, T.L., 2021. Methods for analyzing submerged jet erosion test data to model scour of cohesive soils. *Transactions of the ASABE*, 64(3), pp.785-799.

Wheeler, S.J. and Sivakumar, V., 1995. An elasto-plastic critical state framework for unsaturated soil. *Géotechnique*, 45(1), pp.35-53.

Chapter V: Climate Change Adaptation of Elbe River Flood Embankments via Suction-Based Design

1 Introduction

The increase of extreme weather events is a well-established trend observed as a consequence of climate change. In the North Sea, storm surges are anticipated to increase in both intensity and duration (Barnard et al., 2019) and there is therefore a need to protect communities from the increased flood hazard.

Earthen structures such as flood embankments are the main asset to manage and mitigate flood risk. Increased extreme sea levels require upgrading flood embankments by raising their crest. Retrofitting measures should be designed to maximise social (reduced flood risk hazard) and economic (lowering costs of flood protection maintenance) benefits and minimise environmental impact due to habitat suppression and carbon emissions (Defra, 2002; Spencer and Harvey, 2012; Committee on Climate Change, 2013; Spalding et al., 2014).

If the flood embankments are raised with the same prescribed inclination of the landside slope (e.g. 1:3 in the Elbe River area in Germany), the footprint of the upgraded flood embankment would increase significantly posing two major problems. Existing earthen structures are often adjacent to the built environment and there is either no space available to increase the embankment footprint or this is associated with high land expropriation costs. At the same time, environmental legislation such as the European Birds and Habitats Directives (Sundseth, 2012) imposes constraints to prevent the loss and degradation of coastal habitats and associated biota. The increase in flood embankment footprint associated with the increase of its crest generates direct and indirect loss of habitat, which requires to be compensated elsewhere. The lesser the generation of footprint by the retrofitted flood embankment, the lower are the direct and indirect economic and environmental costs.

This calls for new approaches to embankment design, i.e. raising crest level by limiting the increase in embankment footprint. This would also limit flood embankment embodied carbon. Construction is one of the main sectors responsible for carbon emissions and geotechnical

engineers are challenged to develop new design concepts for carbon-efficient geo-infrastructures. Suction and partial saturation are commonly neglected in geotechnical design. However, suction is an extraordinary untapped natural ‘reinforcement’ and could significantly contribute to reduce economic and carbon costs of a geostructure if accounted for in geotechnical design.

In this respect, it is worth highlighting that design of river, estuarine, and coastal flood embankments based on transient water flow is now being introduced in national recommendations including Germany (Committee for coastal protection works of the German Society for Earthworks and Foundation Engineering and the Society for Port Engineering, 2020). This implicitly acknowledges the economic and environmental benefit of suction-based design. The importance of partial saturation and transient-state conditions for a realistic assessment of the existing safety conditions of flood embankments is also highlighted by Gragnano et al. (2021) who monitored a river embankment on the river Secchia (northern Italy) for 36 months. The importance of partial saturation in the analysis of the response of flood embankments is now widely acknowledged in the literature (Vahedifard et al., 2022; Ngo et al., 2022; Zhang et al., 2021; Johari et al., 2019; Khalilzad et al., 2015).

A critical aspect in suction-based design is that loss of suction due to rain-water and/or river-water infiltration. However, Showkat et al., (2022) showed that, if properly modelled, the suction-based design of earthen structures is feasible for practitioners that nowadays commonly use more advanced computational models. Another critical aspect of suction-based design is the reliable characterisation of the unsaturated soil hydraulic behaviour. For example, Bhaskar et al., (2022) observed that the saturated hydraulic conductivity was found to be 15 times lower after the soil experienced a drying and wetting cycle. This highlights the importance of considering the effect of hysteresis on hydraulic.

This paper aims at examining whether, and to what extent, the inclusion of soil suction and partial saturation in geotechnical design of flood embankments (including the analysis of water flow under transient conditions instead of the conventional steady-state approach) could reduce the flood embankment footprint and embodied carbon while keeping the performance of the flood embankment to the required geotechnical standard. The analysis is developed herein with reference to the design of the upgrade of Elbe River flood embankments in the Hamburg tidal area in Germany. However, similar concepts could be applied to the retrofitting of existing infrastructures that has to be raised in order to meet new design water levels in other countries.

2 The Hamburg flood defence system

2.1 Historical floods and upgrade of flood protection infrastructure

Hamburg is located on the Elbe River in northern Germany with 270 km² of its metropolitan area considered at risk of flooding (including 180k inhabitants and €10 billion worth of goods). The flood defence system extends over 260 km and consists of 130 km of earthen embankments. It is designed to prevent overflow of the Elbe River mainly associated with the storm surges in the North Sea.

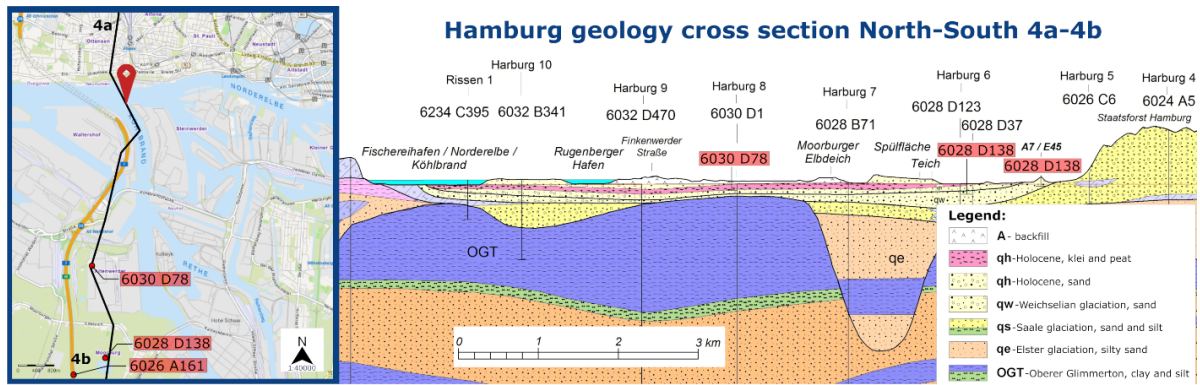
The two most catastrophic storm surge events in the 20th century occurred on 16-17 February 1962 and 3 January 1976. The first event was characterised by a water level mark of +5.7 m above NN (NN stands for Normal-Null, i.e. standard elevation zero adopted in Germany until 2000) and 80mm of rainfall in 24 h, which flooded 30% of the city and caused 315 fatalities. The second event devastated the harbour area with a water level mark of +6.45 m above NN (von Storch, 2017).

Since the 1976 event, the flood protection infrastructure has been upgraded repeatedly including a major investment of €660M in the period 1998-2015. The Hamburg city council has recently launched a programme to further raise flood defence embankments from 5.7 to 7m above landside ground level (7.7 to 9m above NN) to accommodate the increase extreme sea levels due to global warming (Vousdoukas et al., 2018).

2.2 Embankment typical cross section and geological setting

The typical cross section of the flood embankments in the Hamburg area consists of 1:3 slopes with a crest 3 m wide. The embankment core is generally constructed with locally sourced sand whereas the outer shell consists of an impermeable cover (clayey silt named 'Klei') with thickness greater than 1.3m and 1.0m on the waterside and landside respectively. The slope becomes gentler at the toe on the river side (1:10 or 1:6) often armoured with stones to prevent erosion of the bank due to tidal fluctuations and waves.

The Hamburg flood embankments are built on a Holocene sedimentary deposit. The upper soil layers are made of silty sand (qe-Elster glaciation) and/or klei (qh-Holocene) as shown in Figure 1.



Representative boreholes of the uppermost layers

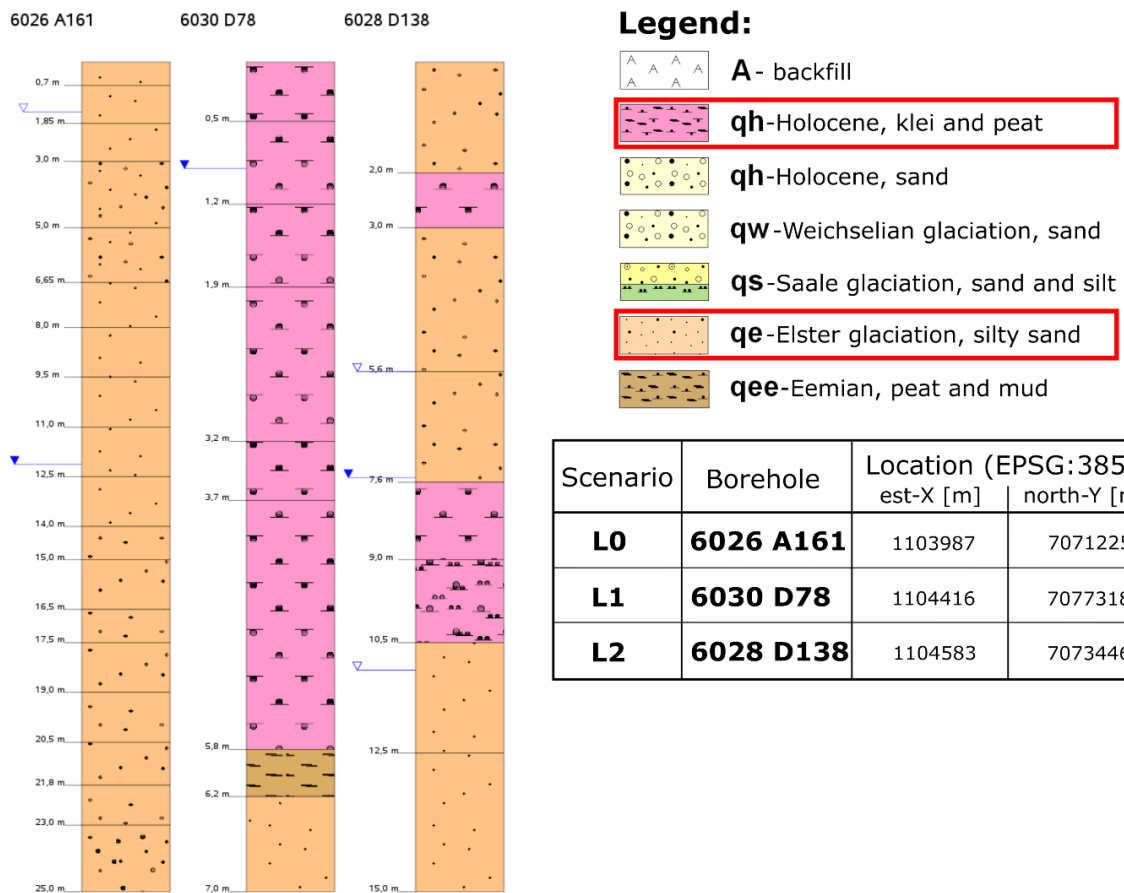


Figure 1. Geological cross section of the Hamburg Elbe harbour. (top) Uppermost layers consisting of Holocene klei & peat (pink) and Holocene silty sand (orange)(map data from BUE (2018b), geological section data from BUE (2018c). (bottom) Representative schematic borehole logs. Data from BUE (2018).

Three scenarios were considered to represent typical soil profiles under the flood embankments as illustrated in Figure 3, i) uniform silty sand layer (L0), ii) klei and peat layer overlying a layer of silty sand (L1), and iii) a sandwich of silty sand, klei and silty sand layers (L2).

2.3 Design storm surge

The Hamburg Port Authority (HPA) has developed a technical framework to design adaptation measures for private flood protection in the Hamburg tidal region (HPA 2008). This includes the adoption of standard design storm surges as shown in Figure 2. These two storm surges represent two different scenarios, that is relatively long duration of surge (~50h) with moderate peak surge elevation (6 m above NN) and relatively short duration of surge (~30h) with high peak surge elevation (7.3 m above NN). These two scenarios will be used as a basis for the analyses presented in this paper.

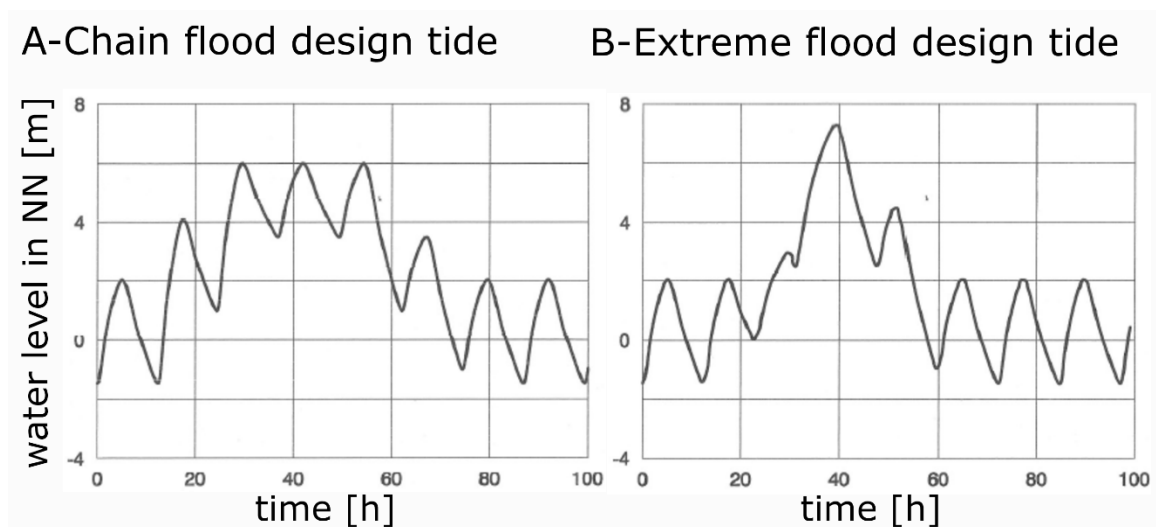


Figure 2 a) A-chain tide and b) B-peak tide used in the transient analysis, after *Technische Rahmenbedingungen (TR HWS-Bau)* according to HPA (2008),

3 Methodology

The standard design of flood embankments based on steady state water flow and assuming zero-pore water pressures above the phreatic surface was compared to the design based on transient water flow and assuming the soil to be unsaturated above the phreatic surface. To this end, numerical simulations were carried out to compare these two different design approaches. The soil was assumed to have a rigidly-perfectly plastic behaviour thus allowing uncoupling water flow analysis from slope stability analysis. The numerical analyses were intentionally kept simple to makes the analyse easily accessible to engineers.

3.1 Flood embankment cross section

The analyses were performed by considering the typical cross section with landside slope 1:3 and increasing progressively up to 1:1 (Figure 3). The aim was to explore whether and to what extent the embankment can be designed with steeper slopes if unsaturated soil and transient flow are considered.

Three different foundation scenarios (L₀, L₁, and L₂) were considered as shown in Figure 3 to be representative of borehole logs shown in Figure 1. The embankments and their foundations are formed by three materials, a clayey silt referred to as 'klei', a sand, and a silty sand.

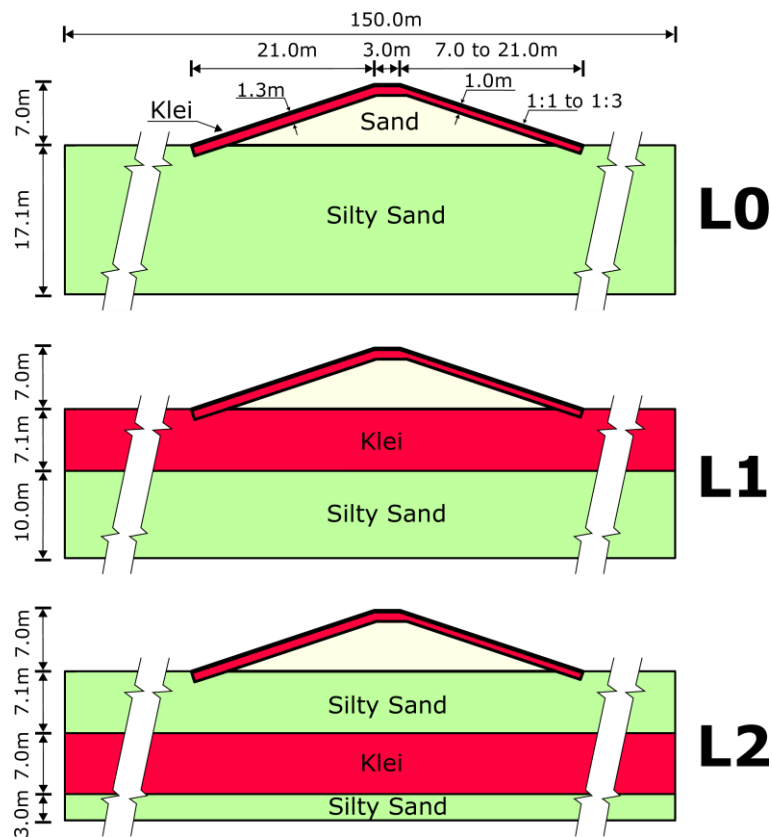


Figure 3. Geometry of the flood embankment (with the landside slope varied from 1:3 up to 1:1) and the layered foundation deposits analysed (L₀, L₁, and L₂).

3.2 Materials

The grain size distribution of materials forming the flood embankments and their foundations are shown in Figure 4 and were extracted from a database compiled the Hamburg Geological Survey (GLH, 2017).

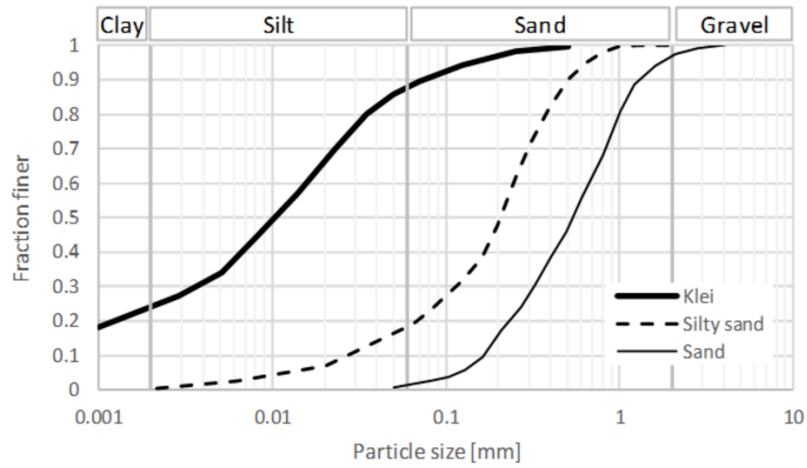


Figure 4. Representative grain size distributions of the materials forming the flood embankment and its foundation

3.2.1 Water retention and hydraulic conductivity characterisation

Standard geotechnical tests available for the Hamburg area have been carried out only on materials in the saturated state. A simple engineering approach was adopted to characterise the materials' water retention behaviour. The parameter that most characterises a water retention function is the air-entry suction because it varies by several orders of magnitude when moving from coarse-grained to fine grained materials. The air-entry suction is controlled by the larger pore-sizes in turn associated with the larger grain size as a first approximation. Tarantino and Di Donna (2019) have shown that the air-entry suction can be related to particle size corresponding to the 80% finer fraction, D_{80} (Figure 24 in Tarantino and Di Donna, 2019). Although such an empirical relationship was built on a relatively small dataset, its peculiarity is that it was developed by considering only undisturbed non-agricultural soils. The values of air-entry suction s_{AEV} derived from this empirical correlation based on the grain size distributions curves in Figure 4 are presented in Table 1.

Table 1. van Genuchten parameters of water retention and hydraulic conductivity functions

Material	D_{80} [mm]	s_{AEV} (empirical) [kPa]	α [kPa ⁻¹]	n [-]	k_{sat} [m/s]
Klei	0.035	44	0.010	1.7	1e-8
Silty Sand	0.4	5	0.100	2	1e-6
Clean Sand	1	4	0.142	3	1e-5

The 2-parameter van Genuchten soil water retention function shown in Eq. [1] (van Genuchten, 1980) was adopted to model water retention behaviour.

$$\theta_e = \frac{\theta}{\theta_s} = \left[\frac{1}{1 + (\alpha s)^n} \right]^m \quad \left[m = 1 - \frac{1}{n} \right] \quad [1]$$

where θ is the volumetric water content, θ_{sat} is the volumetric water content at saturation, θ_e is the effective degree of saturation, and α and n are soil-dependent parameters. The parameter n was estimated using engineering judgement considering that n increases as the grain size uniformity coefficient decreases. Once n was fixed, the parameter α was determined to match the air-entry suction s_{AEV} estimated empirically (Table 1). The resulting water retention functions are shown in Figure 5.

The hydraulic conductivity k was characterised based on van Genuchten (1980):

$$k = k_{\text{sat}} \cdot \left\{ \sqrt{\theta_e} [1 - (1 - \theta_e^{1/m})^m]^2 \right\} \quad [2]$$

where k_{sat} is the saturated hydraulic conductivity derived from the database made available by the Hamburg Geological Survey (GLH, 2017) as shown in Table 1.

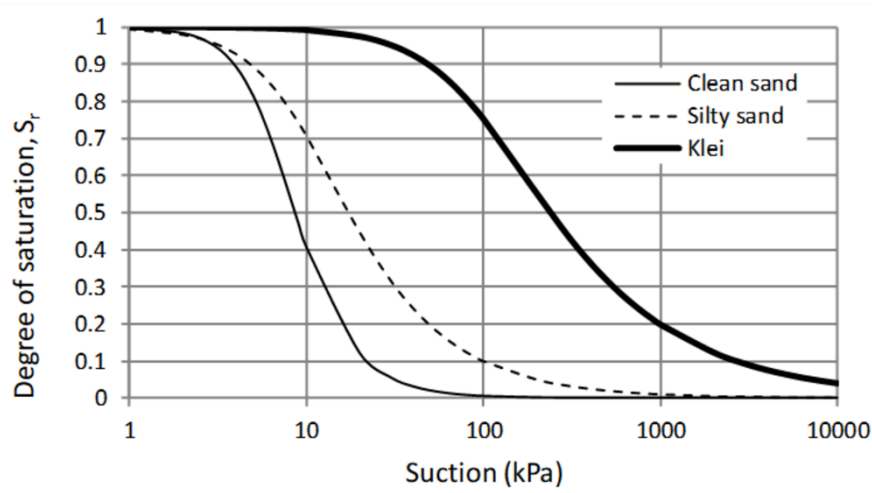


Figure 5. Water retention functions adopted for the materials forming the flood embankment and its foundation.

3.2.2 Shear strength characterisation

Shear strength parameters for the Sand and Silty Sand were derived from a table made available by the Hamburg Geological Survey (GLH, 2017) and are shown in Table 2. The values of the friction angle ϕ' and effective cohesion c' for these two materials are in the range expected for the grain size distributions shown in Figure 4. On the other hand, the values of ϕ' and c' for the

klei were somehow contradictory. Significantly different values were reported for Consolidated Drained (CU) and Consolidated Undrained (CU) triaxial tests and a wide range of pairs of (ϕ' , c') were provided (see Appendix I). Two options were therefore considered. The data for the values of ϕ' and c' reported by the Hamburg Geological Survey (GLH, 2017) for drained tests where first correlated (as expected the friction angle ϕ' decreases as the effective cohesion c' increases) and the average values were selected as shown in Table 2 as option 1 (see Appendix I). The available CU raw triaxial data were then examined and values $\phi'=30^\circ$ and $c'=0$ were selected as discussed Appendix I (shown in Table 2 as option 2). The two options allow considering the cases of zero and non-zero effective cohesion.

Embankment crest and slopes are generally turfed, i.e. the uppermost layer of the embankment is reinforced by the root system. To take into account the mechanical effects of roots, to the uppermost klei layer of the embankment (200 mm) was assigned an effective cohesion of 4 kPa. This is in line with the values reported in the literature (De Baets, 2008; Comino, 2010, Baral et al., 2019).

Table 2. Mechanical parameters

Material	γ_{dry} [kN/m ³]	γ_{sat} [kN/m ³]	ϕ' (°)	c' [kPa]
Klei top layer (200 mm) – option 1	12.5	17.5	27.4	11.7
Klei top layer (200 mm) – option 2			30	4
Klei – option 1	12.5	17.5	27.4	7.7
Klei – option 2			30	0
Sand	17	20	36	0
Silty Sand	18	20	33	0

3.3 Water-flow model

The Software GEOSTUDIO 2019 was used for the analyses. It includes the module SEEP/W to compute the pore-water pressure and the module SLOPE/W to perform the stability analysis using the simplified Bishop method of slices (GeoSlope 2019)

3.3.1 Governing equation

The governing equation (Lu and Likos 2004, Eq. S1 in Appendix III) was solved numerically using the FEM code SEEP/W. It was assumed that the soil skeleton is rigid and, hence, the hydraulic flow is uncoupled from the mechanical deformation (i.e. the volumetric water content θ only

depends on the pore water pressure u_w). A coupled hydro-mechanical model would have added unnecessary complexity considering that the water retention behaviour and the relative hydraulic conductivity thereof were estimated using informed engineering judgement.

3.3.2 Hydraulic initial and boundary conditions

The initial condition for the transient analysis was generated via a steady-state seepage analysis with hydraulic head on the river side set to 0 m NN. The hydraulic boundary conditions were assigned as follows (see also Figure S2 in Annex III):

- 1) Constant hydraulic head assigned to the vertical boundary on the landside to simulate far-field ground water table (0 m NN corresponding to 2m below the ground surface). The distance of the landside vertical boundary from the toe of the embankment was set to 52-67m depending on the embankment landside slope considered. The extension of the flow domain was wide enough to not affect the pore-water pressure distribution up to 10 m from the toe of the embankment.
- 2) Bottom boundary modelled as impermeable.
- 3) Crest of the embankment, landside slope and landside ground surface were modelled as potential seepage faces, i.e. water flux is imposed equal to zero as long as the pore-water pressures remains negative ($u_w < 0$), otherwise pore-water pressure is set equal to zero (Figure S2).
- 4) Transient water flow - Boundary condition on the water side was designed as shown in Figure 6. The river water level was allowed to fluctuate for 1 year to simulate the normal tide regime with the water level oscillating between the lower tide water level (MLT=-1.90m NN) and the high tide water level (MHT=+2.42m NN). This was followed by the storm surge over a period of 100h. Two different patterns were considered for the storm surge as shown in Figure 6 according to the standard design storm surges developed by Hamburg Port Authority (Figure 2) with water level peaks of 6m NN (A) and 7.3m NN (B) respectively.
- 5) Steady state flow - Water level was set equal to the peak of the two patterns considered for transient state, i.e. 6m NN and 7.3m NN respectively (Figure 2.).

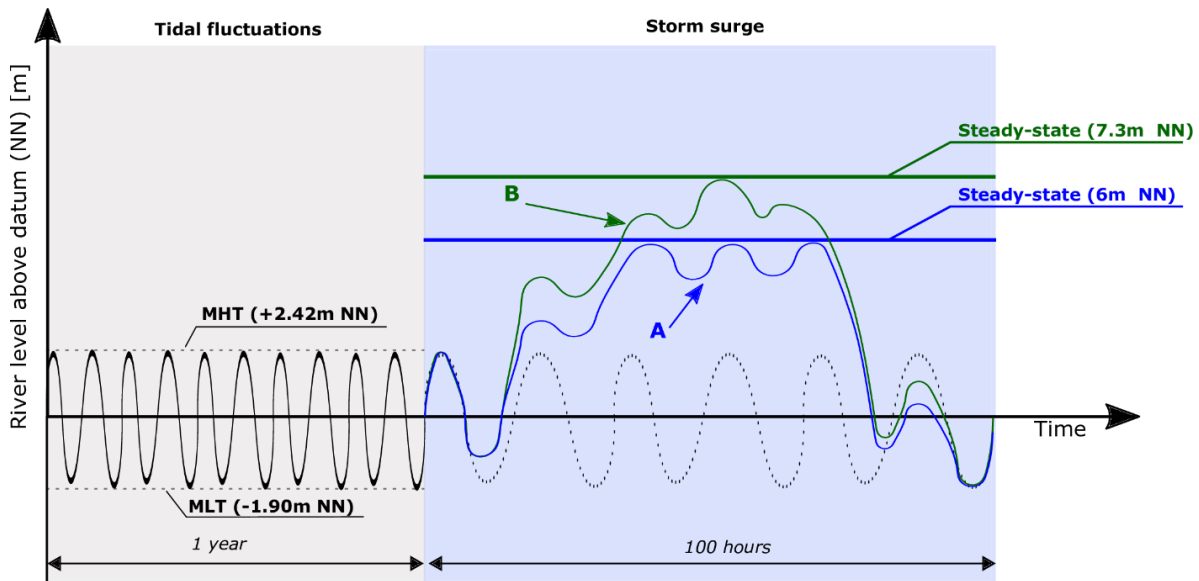


Figure 6. Hydraulic boundary condition imposed on the water side for transient and steady-state analyses.

3.3.3 Additional considerations

The mesh density in the regions where higher gradients develop was optimised (Figure S3) and constant time step of 30 min was used for both the ~1-year tide record (12,774 time steps) and the 100h storm surge.

The transient water flow analyses neglect the effect of transpiration and evapotranspiration at the embankment surface. These generate higher suction and neglecting these effects leads to a conservative estimation of the factor of safety of the slope.

3.4 Stability analysis model

The stability analysis was carried out using Bishop's simplified method (Bishop, 1955). The iterative procedure to calculate the Factor of Safety (FoS), was computed with the module SLOPE/W. The pore-water pressures derived from the water flow analysis (either steady-state or transient-state flow) were used to calculate the shear strength and, hence, the FoS. For the transient state analysis, the pore-water pressure and, hence, the FoS, varies with time. The FoS is taken as the minimum value over the duration of the storm surge event. The Bishop method is corrected in SLOPE/W, i.e. the critical slip surface is initially assumed to be circular and then refined with the optimisation algorithm based on the segmental technique.

The equation proposed by Vanapalli, et al. (1996) was used to account for the effect of suction on shear strength (Eq. S2 in Appendix III). The residual volumetric water content in Eq. S2 was

set to zero, which is appropriate for sandy and silty materials and materials with low content of clay as discussed by Tarantino & El Mountassir (2013).

4 Results & Discussion

4.1 Conventional versus suction-based design

The numerical analyses were aimed at comparing ‘prescriptive’ design based on steady-state water flow in saturated/dry embankment with ‘performance-based’ design based on transient-state water flow in unsaturated embankment:

- *SS-Ns (Steady-State – No suction)*. Steady state water flow analysis assuming saturated condition below the phreatic surface and a virtually dry soil above the phreatic surface; shear strength criterion formulated assuming zero pore-water pressure above the phreatic surface.
- *TR-s (Transient-state –suction)*. Transient state water flow analysis assuming unsaturated conditions above the phreatic surface; shear strength criterion accounting for partial saturation (Eq. [S2]).

To investigate whether and to what extent the inclination of the landside slope can be increased to raise the embankment while minimising its footprint, the FoS of the embankment was assessed for landside slopes varying from a 1:3 up to 1:1 ratio (Table 3). The factor of safety is expressed via the Overdesign Factor (ODF) according to the Eurocode 7:

$$ODF = \frac{R_d}{E_d} \quad [1]$$

where E_d is the design effect of actions and R_d is the corresponding design resistance. For the case of flood embankments, and ODF equal to unity is associated with partial factors for shearing resistance γ_ϕ and effective cohesion γ_c equal to 1.25.

For each embankment geometry, the FoS was then calculated considering:

- a) two types of analysis illustrated above (SS-Ns and TS-s)
- b) three different foundations scenarios as shown in Figure 3 (Lo, Li, and L2)
- c) two hydraulic loading patterns as shown in Figure 6 (A and B)

d) two options for the shearing resistance ϕ' and effective cohesion c' of the Klei layer as in Table 2

Table 3. Landslide slopes examined

H:L slope ratio	Slope Angle [°]
1:3.00	18.4
1:2.50	21.8
1:2.00	26.6
1:1.75	29.7
1:1.50	33.7
1:1.25	38.7
1:1.00	45.0

4.1.1 Homogenous silty sand foundation (foundation scenario L0)

As an example, the results for the case of storm surge at 6m NN and landside slopes 1:3 and 1:1.25 are shown in Figure 7. The conventional analysis based on steady-state water flow and saturated/dry approach is shown in Figure 7a, b for the cases $c'=0$ and $c'\neq 0$ respectively.

For the case $c'=0$, the failure surface develops through the Klei cover, fully or partially below the phreatic surface due to the high pore-water pressures developing at the toe whereas the failure surface tends to deepen into the sand core for case $c'\neq 0$ as one would expect. Under the assumption of steady-state flow and 'dry' soil above the phreatic surface, the landside slope 1:3 is not stable for $c'=0$ and an effective cohesion greater than zero is required for the Klei to make the landside slope stable. It is difficult to say whether the non-zero effective cohesion is a genuine mechanical property of the Klei or the effective cohesion is null (as the triaxial data shown in Appendix I seem to suggest) and $c'\neq 0$ is actually a 'design' value that takes into account implicitly the effect of suction effects. For avoidance of doubt, the numerical analyses are performed in parallel by considering either $c'=0$ or case $c'\neq 0$. Within the conventional design approach, the landside slope is not stable when inclined 1:1.25 even if $c'\neq 0$ and the slope 1:1.25 would therefore not be allowed.

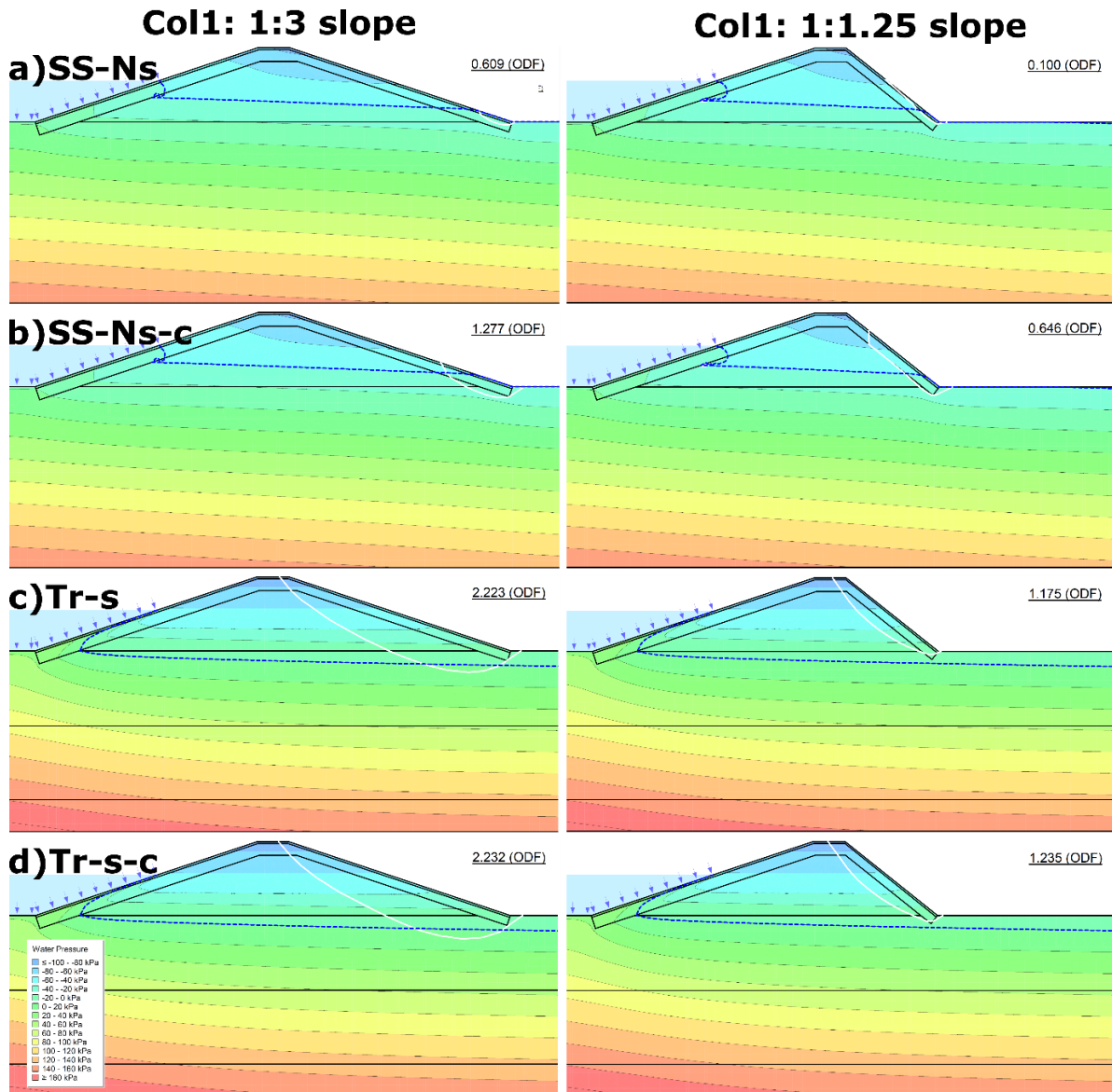


Figure 7. Stability analysis associated with river level at 6m NN for Lo scenario. (a) SS-Ns, Steady state analysis without suction effects, $c'=0$; (b) SS-Ns, Steady state analysis without suction effects, $c' \neq 0$; (c) TR – Ns, Transient analysis with suction effects, $c' = 0$ (minimum ODF at 53.5h from the start of the storm surge); TR – Ns, Transient analysis with suction effects, $c' \neq 0$ (minimum ODF at 53.5h from the start of the storm surge).

Figure 7c, d present the ODF for the case where water flow is modelled in the transient regime and the soil is assumed to be partially saturated. The phreatic surface remains well below the landside toe and the ODF increases substantially. For the 1:3 slope, the ODF increases from 0.61 to 2.22 for $c'=0$ and from 1.28 to 2.23 for $c' \neq 0$. The contribution of suction to shear strength makes the slope 1:1.25 stable even if $c'=0$.

Homogenous silty sand foundation - scenario L0

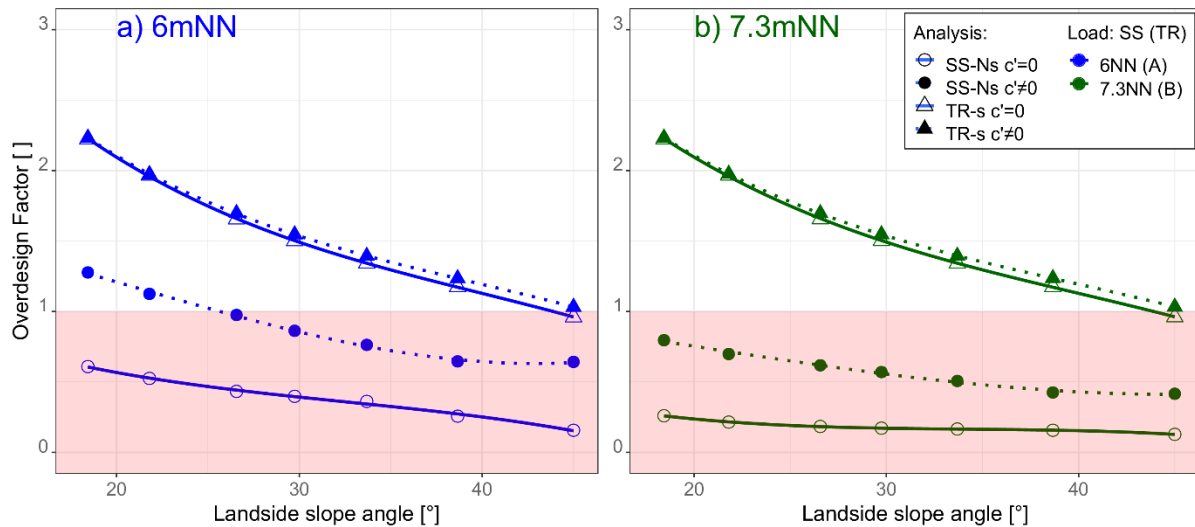


Figure 8. Effect of inclination of landside slope on Overdesign Factor for the homogenous silty sand foundation (scenario L0). (a) 6m NN – Pattern A (b) 7.3 m NN – Pattern B (SS-Ns= steady-state flow with no suction effects; TR-s= steady-state flow with suction effects, open symbols $c'=0$ and solid symbols $c'\neq 0$)

The results presented in Figure 7 refer to storm surge pattern A (Figure 6) and the extreme landside slopes 1:3 and 1:1.25. Stability analyses were also carried out for the surge pattern B (Figure 6). Figure 8 summarises the variation of the ODF with the inclination of the landside slopes for the two design approaches (SS-Ns for steady state flow with no suction effects and TR-s for transient flow with suction effects) and the two design storm surges. The increase in peak river level (from 6m NN to 7.3m NN) produces a significant effect on the ODF if the water flow regime is analysed under steady-state conditions. For the case of storm surge 7.3 NN, the gentlest slope 1:3 is unstable even if $c'\neq 0$ is considered (Figure 8b).

For the case of transient flow with suction effects, the ODF remains is greater than unity and approaches unity for a landside slope angle of 45° (1:1). This inclination could also be considered a practical limit dictated by other constraints (e.g. grass mowing or other slope maintenance interventions). The increase in peak river level (from 6m NN to 7.3m NN) does not produce significant effect on the ODF if the water flow regime is analysed under transient state conditions. This is because the water front propagating from the waterside slope hardly penetrates the embankment regardless of the peak water level.

4.1.2 Clayey foundation (foundation scenario L1)

The upper portion of the Holocene deposit in the Hamburg harbour area, which forms the foundation of the Elbe river flood embankments, is made of alternate layers of klei and silty sand (Figure 3). The previous section has analysed the scenario of uniform foundation deposit

made of silty sand. This section focuses on the case of a clay layer overlaying a silty sand layer (scenario L1 in Figure 3). The presence of a layer beneath the embankment characterised by a low hydraulic conductivity is expected to dampen down water flow underneath the flood embankment and concentrate water flow through the embankment. This scenario can potentially modify the pore-water pressure regime within the embankment and was therefore considered worth exploring.

Figure 9 shows the variation of the ODF with the inclination of the landside slopes for the two design approaches (SS-Ns for steady state flow with no suction effects and TR-s for transient flow with suction effects). For comparison, the results from the scenario Lo are reported with grey shaded symbols. For the steady-state flow analysis, the ODF reduces with respect to the foundation scenario Lo and becomes lower than unity for the storm surge 7.3 m NN even for the gentlest slope 1:3 and $c' \neq 0$ (Figure 9b). The presence of an impermeable foundation layer forces the water to flow through the embankment only and this raises the phreatic surfaces and the pore-water pressures at the landside toe of the embankment.

Clayey foundation - scenario L1

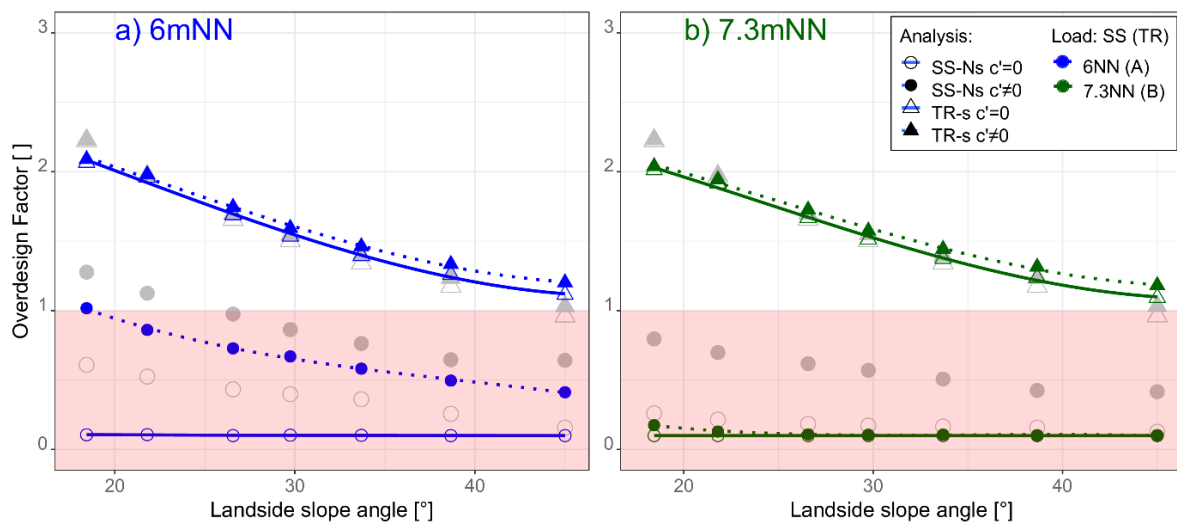


Figure 9. Effect of inclination of landside slope on Overdesign Factor for the homogenous clayey foundation (scenario L1). (a) 6m NN – Pattern A (b) 7.3 m NN – Pattern B (SS-Ns= steady-state flow with no suction effects; TR-s= steady-state flow with suction effects, open symbols $c'=0$ and solid symbols $c' \neq 0$, grey shaded symbols refer to foundation scenario Lo)

On the other hand, the ODF derived from the transient state analyses (TR-s) for the foundation scenario L1 is very similar to the one derived for the scenario Lo. A closer inspection of the ODF curves reveals that the L1 curve lies slightly below the Lo curve for the milder slopes (18.4° and 21.8°). This is due to the fact that the phreatic surface in the L1 scenario is slightly higher and that the failure surface partially develops below the phreatic surface. On the other

hand, the failure surface develops above the phreatic surface for the steeper slopes, in the region where the pore water pressure regime is only slightly affected by the change in hydraulic conductivity of the foundation, hence the ODF remains essentially the same.

4.1.3 Confined silty sand foundation (foundation scenario L2)

This section examines the case of silty sand layer confined by an underlying Klei layer (scenario L2 in Figure 3). The presence of a confined silty sand layer beneath the embankment is expected to promote uplift pressures at the downstream toe of the embankment.

Figure 10 shows the variation of the FoS with the inclination of the landside slopes for the two design approaches. For comparison, the results from the scenario L0 are reported with grey shaded symbols. It can be observed that there is essentially no difference between these two foundation scenarios.

Confined silty sand foundation - scenario L2

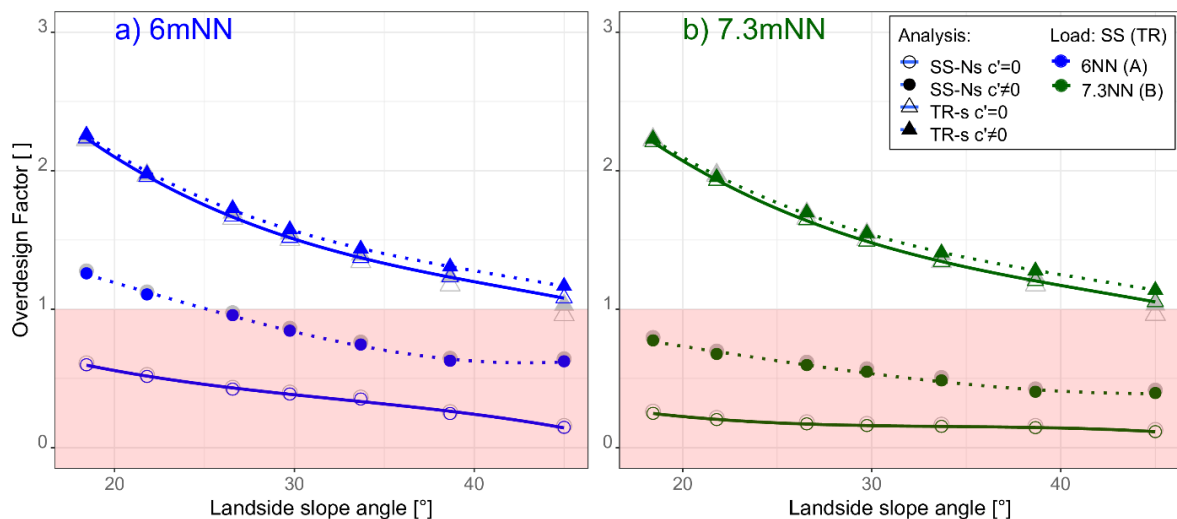


Figure 10. Effect of inclination of landside slope on Overdesign Factor for the confined silty sand foundation (scenario L1). (a) 6m NN – Pattern A (b) 7.3 m NN – Pattern B (SS-Ns= steady-state flow with no suction effects; TR-s= steady-state flow with suction effects, open symbols $c'=0$ and solid symbols $c'\neq 0$)

4.2 Sensitivity analysis: effect of the hydraulic conductivity of the klei cover

The high ODF derived for the case where pore-water pressures are derived from transient water flow in partially saturated embankment is associated with the low hydraulic conductivity of the Klei layer that hampers the propagation of the water front from the waterside slope (Figure 7).

The most critical soil parameter underpinning the ‘performance-based’ design of the Hamburg area flood embankments is therefore the hydraulic conductivity of the Klei. A sensitivity analysis was carried out to assess the influence of this parameter in the factor of safety of the flood embankment considering the variability of the saturated hydraulic conductivity generally encountered in the field. The saturated hydraulic conductivity of the Klei cover was therefore increased from $k_{sat}=10^{-8}$ m/s to $k_{sat}=10^{-6}$ m/s.

Hydraulic conductivity of klei cover $k_{sat}=10^{-6}$ m/s - scenario L0

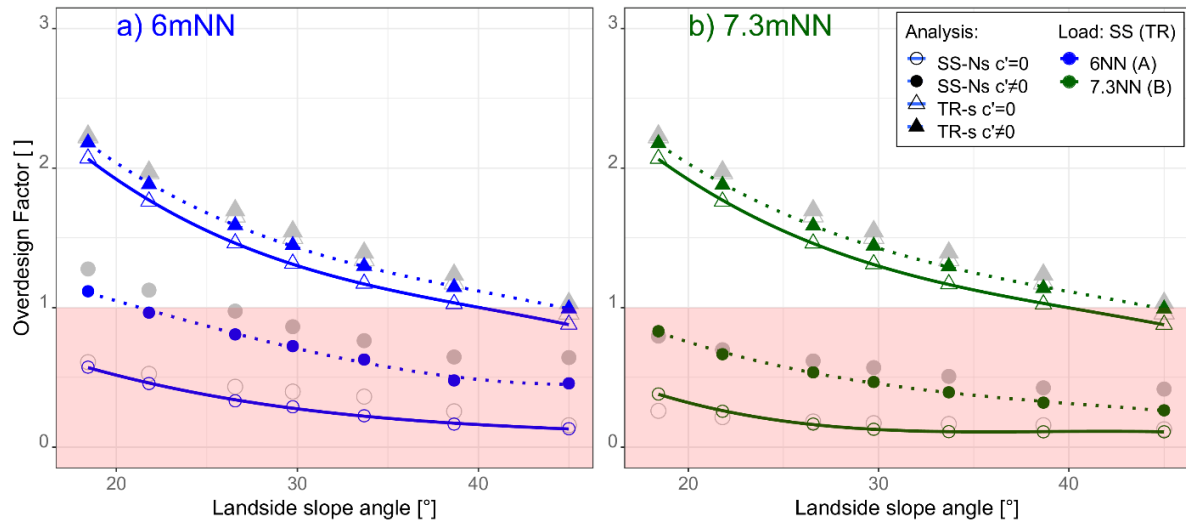


Figure 11. Effect of hydraulic conductivity of the Klei cover on the Overperformance Factor (foundation scenario L0). Saturated hydraulic conductivity increased from $k_{sat}=10^{-8}$ m/s to $k_{sat}=10^{-6}$ m/s. (SS-Ns= steady-state flow with no suction effect; TR-s= steady-state flow with suction effects, shaded grey symbols represent the case of $k_{sat}=10^{-8}$ m/s for comparison).

The results from these analyses are presented in Figure 11 and show that even an increase in hydraulic conductivity of the Klei cover by two orders of magnitude does not decrease the ODF significantly when the stability is analysed by considering transient water flow and partial saturation. This is because the contrast between the hydraulic conductivities of the quasi-saturated Klei and the partially saturated sand core remains still relatively high. Under the condition of Klei cover having hydraulic conductivity two orders of magnitude lower than the design value, the maximum landside slope is 40° .

4.3 Sensitivity analysis: Rainfall effects

The high factor of safety resulting from the performance-based design is in part associated with the transient nature of the water flow through the flood embankment and in part associated with the increase in shear strength generated by the suction along the potential failure surface. A critical step in suction-based design is the evaluation of the effect of rainfall on the potential

loss in suction and, hence, shear strength. For this reason, the factor of safety for the foundation scenario Lo was assessed assuming that i) a rainfall occurs at the same time and for the same duration as the storm surge and ii) an antecedent rainfall of 30 days occurs before the storm surge.

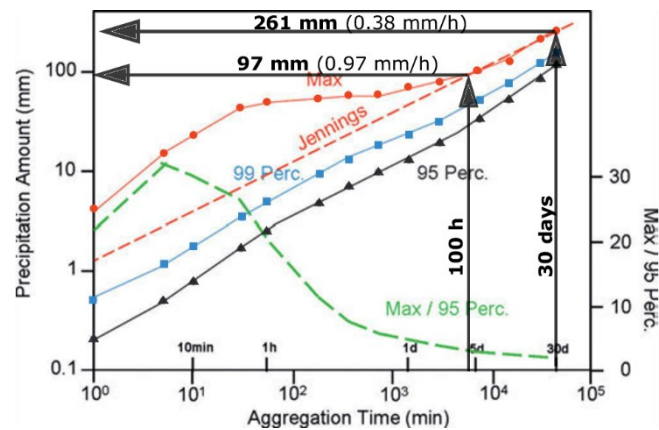


Figure 12. Cumulative rainfall versus aggregation time over 17-year observation period. Data measured at the Hamburg Weather Mast 1997–2014. Solid circle = max historical rainfall data, solid triangle = 95th percentile, solid square = 99th and the absolute maximum taken from the PDFs for the total (left scale) and maximum/95th percentile ratio versus aggregation time (right scale). (data from Weder, 2017).

Figure 12 reports the precipitation statistics of rainfall events in Hamburg over the observation period 1997–2014 (17 years). The red dotted curve shows the maximum cumulated rainfall recorded over a duration given by the ‘aggregation time’. For example, a cumulative rainfall of 97 mm is associated with an aggregation time of 100h. This means that the maximum cumulated rainfall recorded over a time window of 100h over the 17 year-period is equal to 97 mm. The blue dotted curve represents the same cumulative rainfall versus aggregation time associated with a return period of 100 years (99 percentile).

Two rainfall events were considered. The first consists of 97 mm over 100h, consistent with the maximum cumulative rainfall recorded over the aggregation time of 100h in the 17 year-period (Figure 12) and occurring at the same time as the storm surge (see Figure 6). The second event consists of 261 mm over 30 days, it initiates before the storm surge and ends when the storm surge ends. These two rainfall events are ‘extreme’ in the sense that they are associated with a return period >100 years.

Rainfall effects for $q_{in}=0.97\text{mm/h}$ & $q_{in}=0.38\text{mm/h}$ - scenario L0

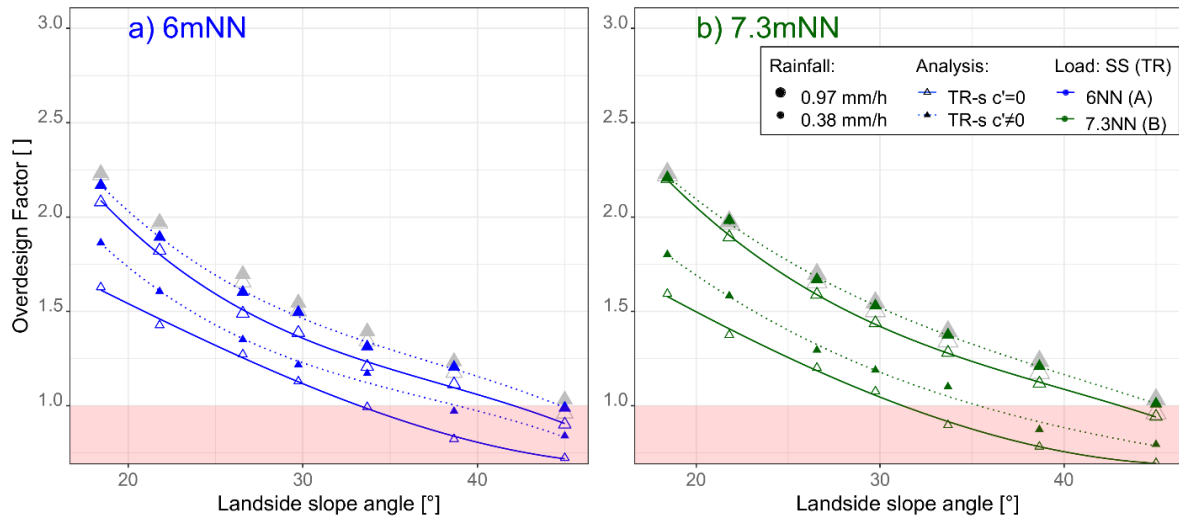


Figure 13. Effect of rainfall on the Overdesign Factor (foundation scenario L0). Rainfall 0.97mm/h for 100h duration and rainfall 0.38 mm/h for 30 d duration for the two design storm surges. Shaded grey triangles represent the foundation scenario L0 in the absence of rainfall for comparison.

Figure 13 shows the ODF for the foundation scenario L0 and storm surge pattern 7.3m NN for the cases of rainfalls of 97mm/100h and 261 mm/30d. The ODF is compared with the ODF in the absence of rainfall (shaded grey triangles). The ODF decreases but only marginally for both rainfall events. The reason why the rainfall events do not cause a significant drop in suction is that most of the rainfall tends to run off once pore water pressure increases up to zero at the boundary. Under the condition of concomitant or antecedent rainfall, the maximum landside slope is 43°.

5 Economic and environmental implications of prescriptive and performance-based design

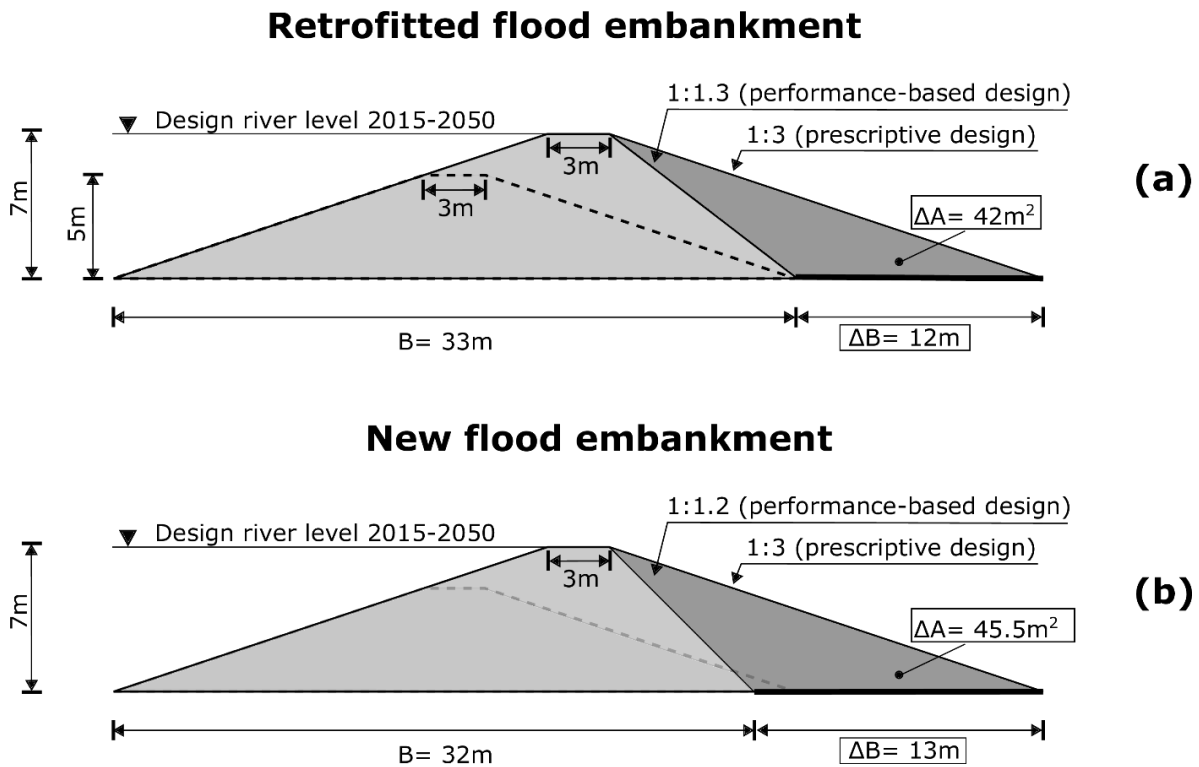


Figure 14. Comparison between prescriptive design (dark grey) and performance-based design (light grey). (a) flood embankment retrofit with no footprint increase. (b) new flood embankment with 1:1,2 landside slope.

5.1 Land expropriation

Figure 14a shows the case where the flood embankment is raised from 5m to 7m without changing its footprint. This would result in a landside slope 1:1.3 (37°) that would still allow for a ODF greater than 1 if the embankment is designed by assuming transient water flow and partial saturation (Figure 8 to Figure 11, Figure 13). Compared with the prescriptive design where the landside slope is maintained 1:3, this would allow for a footprint saving of 12 m² per linear meter of embankment and volume saving of 42 m³ per linear meter of embankment. If a new embankment must be built with a landside slope 1:1.2 (40°), the footprint saving would be 13 m² per linear meter of embankment and volume 45.5 m³ per linear meter of embankment (Figure 14b).

A survey of land values on real estate market in Hamburg reveals that, at the time of writing, the price of land with building permits is around €250-400/m² in the harbour area and

Wilhelmsburg island on the south side of the river Elbe (LBS, 2020). Assuming an average price of land of €325/m², the saving of expropriation cost moving from the prescriptive design (SS-Ns) to the performance-based design (TR-s) would therefore be €3.9M/km for the flood embankment retrofit and €4.5M/km for a new embankment.

5.2 Habitat suppression

The retrofit of the flood embankment using the performance-based design (Figure 14a) could be achieved with no habitat suppression compared to the prescriptive design that would cost at least 1.2 ha per linear km of compensatory habitat to be restored somewhere else. It should be noted that habitat compensation need to take into account not only direct loss due to the portion of land covered by the upgraded flood embankment but also indirect losses due to the time required to restore the ecological function of the adjacent habitat that will be damaged during the construction period (Esteves and Thomas, 2014).

If a new flood embankment must be built, the habitat to be compensated for the case of the performance-based designed flood embankment would be limited to 3.1ha per linear km compared to the traditional prescriptive-based design that would require 3.8ha per linear kilometre of compensatory habitat.

5.3 Embodied carbon savings

A full Life Cycle Analysis (LCA) should be developed (Glass 2013) for an accurate quantification of the embodied carbon savings associated with the performance-based design in comparison with the conventional prescriptive design. However, a LCA is out of the scope of this work and a simplified approach was pursued to estimate the order of magnitude of the carbon that can be saved by the performance-based design proposed. The embodied carbon per unit volume of embankment was estimated on the basis of the data available for the Cobbins Brook flood embankment that present characteristics similar to the flood embankments in the Hamburg area as discussed in Appendix II. The computation of the overall carbon emission for the Cobbins Brook flood alleviation scheme led to an embodied carbon between 64-84 kg of CO₂e/m³.

The volume saved by the performance-based design was found to be equal to 42,000 m³/km for the retrofitted embankment (Figure 14a) and 46,000 m³/km for a new embankment (Figure 14b). If this volume is multiplied by the estimated embodied carbon (64-84 kg of CO₂e/m³), the carbon saving would result in 2,678-3,525 tCO₂e/km for the retrofitted embankment and 3,125-4,113 tCO₂e/km for a newly built, which roughly corresponds to 12.5-16.8 million car/km or more

than 3700-5000 flights London-New York/km. These figures are significant if one considers that earthen flood-protection infrastructure in the Hamburg area extends over 130 km.

6 Conclusions

The paper has discussed the problem of retrofitting flood embankments in a climatic-change scenario by raising their crest with reference to the case of the Elbe River in Hamburg. If the embankments are raised by maintaining the same 'prescriptive' landside slope, the cost in terms of land expropriation, habitat compensation, and embodied carbon would be significantly high.

The paper has made the case that performance-based design based on transient water flow analysis and accounting for the partial saturation of the embankments can lead to substantial economic and environmental saving compared to the tradition prescriptive design, which is based on steady-state flow analysis and the assumption that the soil above the phreatic surface is dry.

To demonstrate the differences between prescriptive and performance-based design, the landside slope was varied from the prescriptive value of 1:3 up to 1:1, which might be considered an upper limit of the landside slope dictated by maintenance operations. It has been shown that design based on transient water flow and partial saturation (performance-based design) allows for the landside slope to be increased potentially up to 1:1 still maintaining the Overdesign Factor (ODF) substantially greater than the one derived from traditional analysis (steady-state water flow and saturated/dry approach).

The high factor of safety resulting from the performance-based design is in part associated with the transient nature of the water flow through the flood embankment (the water front propagating from the riverside slope hardly penetrates the embankment) and in part associated with the increase in shear strength generated by the suction along the potential failure surface.

The performance-based design would allow the embankment to be raised without increasing its footprint (in contrast with the prescriptive design where the raising of the crest is achieved at the expenses of significant increase in embankment footprint). In the Hamburg area, this would allow savings expropriation cost of the order of €3.9M per linear kilometre and carbon savings of the order of 2600-3500 tCO₂ per linear kilometre.

The suction-based design of flood embankments relies on the low (unsaturated) hydraulic conductivity of the embankment materials, and this poses a challenge in practice due to the difficulty associated with the reliable characterisation the hydraulic properties of the

embankment geomaterials and their potential degradation over time (e.g. effect of drying and wetting cycles, fine fissuring and/or surface cracks). Suction-based design of flood embankments would therefore require an additional investment in terms of laboratory and field characterisation of unsaturated hydraulic conductivity of embankment materials and possibly low-cost field monitoring. This paper aimed at demonstrating that such an additional investment could be worthwhile in the light of the economic, carbon, and environmental savings enabled by the suction-based design.

References

- Baets, S. D., Torri, D., Poesen, J., Salvador, M. P., & Meersmans, J. (2008). Modelling increased soil cohesion due to roots with EUROSEM. *Earth Surface Processes and Landforms: The Journal of the British Geomorphological Research Group*, 33(13), 1948-1963.
- Baral S. Wang JX, Alam S. and Patterson WB (2019). Experimental and Analytical Studies on the Root Reinforcement Effect of a Grass Species, *Spartina alterniflora*. Eighth International Conference on Case Histories in Geotechnical Engineering
- Barnard, P.L., Erikson, L.H., Foxgrover, A.C. J.A. Finzi Hart, P. Limber, A.C. O'Neill, M. van Ormondt, S. Vitousek, N. Wood, M.K. Hayden & J.M. Jones (2019). Dynamic flood modeling essential to assess the coastal impacts of climate change. *Sci Rep* 9, 4309. DOI: 10.1038/s41598-019-40742-z.
- Bhaskar, P., Puppala, A. J., & Boluk, B. (2022). Influence of Unsaturated Hydraulic Properties on Transient Seepage and Stability Analysis of an Earthen Dam. *International Journal of Geomechanics*, 22(7), 04022105.
- Bishop, A. W. (1955). The use of the slip circle in the stability analysis of slopes. *Geotechnique*, 5(1), 7-17.
- BUE (2018) Behörde für Umwelt und Energie (BUE), Geologisches Landesamt , <https://suche.transparenz.hamburg.de/dataset/bohrarchiv13> (last accessed 01/06/2020)
- BUE (2018b) Behörde für Umwelt und Energie (BUE), Geologisches Landesamt , <https://suche.transparenz.hamburg.de/dataset/digitale-stadt-karte-hamburg-historisch6> (last accessed 01/06/2020)
- BUE (2018c) Behörde für Umwelt und Energie (BUE), Geologisches Landesamt , <https://suche.transparenz.hamburg.de/dataset/geologische-profil-schnitte-hamburg18> (last accessed 01/06/2020)
- Comino, E., Marengo, P., & Rolli, V. (2010). Root reinforcement effect of different grass species: A comparison between experimental and models results. *Soil and Tillage research*, 110(1), 60-68.
- Committee for coastal protection works of the German Society for Earthworks and Foundation Engineering and the Society for Port Engineering (Ausschuss für Küstenschutzwerke der Deutschen Gesellschaft für Erd- und Grundbau und der Hafenbautechnischen Gesellschaft) (2020). Recommendations B 2002 - Geotechnical investigations of sea and tidal current dike (Empfehlungen B 2002 - Geotechnische Untersuchungen von See- und Tidestromdeichen). In: *Die Küste* 88. Karlsruhe: Bundesanstalt für Wasserbau. S. 303-337.
- Committee on Climate Change (2013) Managing the land in a changing climate. Adaptation Sub-Committee Progress Report 2013. Committee on Climate Change, London
- Department for Environment, Food and Rural Affairs (Defra) (2002). Directing the Flow: Priorities for Future Water Policy. Department for Environment, Food and Rural Affairs, Defra Publications (<http://www.defra.gov.uk>).
- Esteves, L. S., & Thomas, K. (2014). Managed realignment in practice in the UK: Results from two independent surveys. *Journal of Coastal Research*, Special Issue, 70, 407–413.
- GeoSlope (2019) Seepage modelling with SEEP/W 2012 – An engineering methodology, 4th Ed., GeoSlope International, Alberta, Canada
- Glass, J., Dyer, T., Georgopoulos, C., Goodier, C., Paine, K., Parry, T., ... & Gluch, P. (2013). Future use of life-cycle assessment in civil engineering. *Proceedings of the Institution of Civil Engineers-Construction Materials*, 166(4), 204-212.
- GLH (2017). Geologisches Landesamt Hamburg, <http://ingdata.hamburg.de/> (last accessed 01/06/2020)
- GLH (2017)b. Geologisches Landesamt Hamburg, http://ingdata.hamburg.de/pdf/KLabf3axKohaeReibD_s.pdf (last accessed 01/06/2020)

- GLH (2017)c. Geologisches Landesamt Hamburg, http://ingdata.hamburg.de/pdf/KLabf3axKohaeReibCU_s.pdf (last accessed 01/06/2020)
- GLH (2017)d. Geologisches Landesamt Hamburg, <http://ingdata.hamburg.de/pdf/tvc-DBrue-B83-1,90-22,33-7,29.pdf> (last accessed 01/06/2020)
- GLH (2017)e. Geologisches Landesamt Hamburg, <http://ingdata.hamburg.de/pdf/tvc-CND-B3-2,50-19,57-8,28.pdf> (last accessed 01/06/2020)
- Gragnano, C. G., Rocchi, I., & Gottardi, G. (2021). Field Monitoring and Laboratory Testing for an Integrated Modeling of River Embankments under Transient Conditions. *Journal of Geotechnical and Geoenvironmental Engineering*, 147(9), 05021006.
- Hammond, G. P., & Jones, C. I. (2008). Embodied energy and carbon in construction materials. *Proceedings of the Institution of Civil Engineers-Energy*, 161(2), 87-98.
- HPA (2008). Technische Rahmenbedingungen (TR HWS-Bau). Hamburg Port Authority.
- Johari, A., & Talebi, A. (2019). Stochastic analysis of rainfall-induced slope instability and steady-state seepage flow using random finite-element method. *International Journal of Geomechanics*, 19(8), 04019085.
- Khalilzad, M., Gabr, M. A., & Hynes, M. E. (2015). Deformation-based limit state analysis of embankment dams including geometry and water level effects. *International Journal of Geomechanics*, 15(5), 04014086.
- Lee, S., Cass, J., Cornick, S., & Bradley, M. (2010). Cobbins Brook Flood Storage Reservoir. In *Managing dams Challenges in a time of change* (pp. 364-375). Thomas Telford Ltd.
- LBS (2020). Immobilien markt atlas 2020 Hamburg und Umland. https://www.lbs.de/unternehmen/schleswig_holstein_hamburg_6/regionales_thema_68/regionales_thema_63.jsp(last accessed 01/06/2020)
- Lu, N. And. Likos, W.J. (2004). *Unsaturated Soil Mechanics*. Wiley.
- Ngo, P. S. N., Garciano, L. E. O., De Leon, M. P., Lopez, N. S. A., Ishii, H., Iimura, K., ... & Shibayama, T. (2022). Experimental and Numerical Modeling of a Tide Embankment Section Subjected to Storm Surge in Tacloban City, Philippines. *Natural Hazards Review*, 23(4), 05022007.
- Quast, P.: Ein Beitrag zum Kriechverhalten eines norddeutschen Kleis, *Mitteilungen des Lehrstuhls für Grundbau, Bodenmechanik und Energiewasserbau der TU Hannover*, Heft 11, 1977
- Showkat, R., Mohammadi, H., Babu, G. S., & ASCE, F. (2022). Effect of Rainfall Infiltration on the Stability of Compacted Embankments. *International Journal of Geomechanics*, 22(7).
- Spalding, M. D., Ruffo, S., Lacambra, C., Meliane, I., Hale, L. Z., Shepard, C. C., & Beck, M. W. (2014). The role of ecosystems in coastal protection: Adapting to climate change and coastal hazards. *Ocean & Coastal Management*, 90, 50-57.
- Spencer, K. L., & Harvey, G. L. (2012). Understanding system disturbance and ecosystem services in restored saltmarshes: integrating physical and biogeochemical processes. *Estuarine, Coastal and Shelf Science*, 106, 23-32.
- Stubbs, B. (2008). Plain English guide to sustainable construction. *Construction-Excellence in the Built Environment*. Available at: <https://constructingexcellence.org.uk/wp-content/uploads/2015/02/SUSTAINGUIDE.pdf> accessed 8/7/2020.
- Sundseth, K. (2012). *The EU Birds and Habitats Directives*. European Commission, Environment Directorate General
- Tarantino A. & El Mountassir G. (2013). Making unsaturated soil mechanics accessible for engineers: Preliminary hydraulic–mechanical characterisation & stability assessment *Engineering Geology*, 165: 89-104
- Tarantino A. (2010). Basic concepts in the mechanics and hydraulics of unsaturated geomaterials. In: L. Laloui (Ed.), *Mechanics of Unsaturated Geomaterials*, pp. 1-23. Wiley.

- Tarantino, A. & Di Donna, A. (2019). Mechanics of unsaturated soils: simple approaches for routine engineering practice. *Italian Geotechnical Journal*, 4/2019: 6-46.
- Vahedifard, F., Jasim, F. H., Tracy, F. T., Abdollahi, M., Alborzi, A., & AghaKouchak, A. (2020). Levee fragility behavior under projected future flooding in a warming climate. *Journal of Geotechnical and Geoenvironmental Engineering*, 146(12).
- van Genuchten, M. T. (1980). A closed-form equation for predicting the hydraulic conductivity of unsaturated soils. *Soil science society of America journal*, 44(5), 892-898.
- von Storch, H., Meinke, I., & Claußen, M. (2017). *Hamburger Klimabericht–Wissen über Klima, Klimawandel und Auswirkungen in Hamburg und Norddeutschland* (p. 302). Springer Nature.
- Vanapalli, S. K., Fredlund, D. G., Pufahl, D. E., & Clifton, A. W. (1996). Model for the prediction of shear strength with respect to soil suction. *Canadian geotechnical journal*, 33(3), 379-392.
- Vousdoukas, M., Mentaschi, L. & Voukouvalas, E., Verlaan, M. & Feyen, L. (2017). Extreme sea levels on the rise along Europe's coasts. *Earth's Future*, 5: 304–323. DOI: 10.1002/2016EF000505.
- Weder, C., Müller, G., & Brümmer, B. (2017). Precipitation extremes on time scales from minute to month measured at the Hamburg Weather Mast 1997-2014 and their relation to synoptic weather types. *Meteorologische Zeitschrift*, 26, 507-524.
- Zhang, Z., Fu, X., Sheng, Q., Du, Y., Zhou, Y., & Huang, J. (2021). Stability of cracking deposit slope considering parameter deterioration subjected to rainfall. *International Journal of Geomechanics*, 21(7), 05021001.

Appendix I – Klei Shear Strength Parameters

The Hamburg Geological Survey made available a database of hydraulic and mechanical properties of the soils in the Hamburg area (GLH, 2017). Shear strength data for klei are provided via two datasets including Consolidate-Drained (CD) and Consolidated-Undrained (CU) triaxial data tests. As shown in Figure 15, the two datasets are not very consistent. It is not surprising that shear strength at relatively high stresses can be represented by either a relatively high friction angle ϕ' and zero effective cohesion ($c'=0$) or a lower friction angle and $c'>0$. However, the values of friction angle would have been expected to be similar (at similar effective cohesion values).

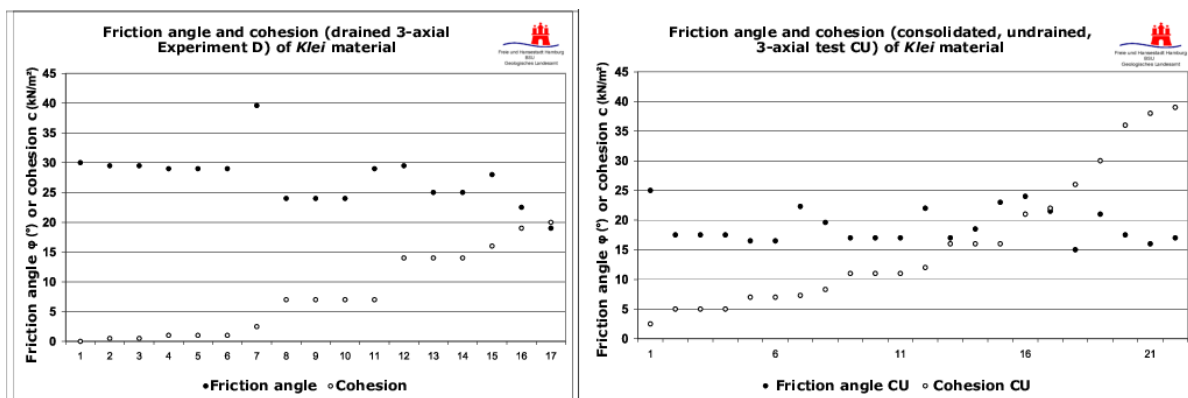


Figure 15. Shear strength data in terms of friction angle ϕ' and effective cohesion c' provided by the Hamburg Geological Survey. (a) CD triaxial test data from Klei samples (Data from GLH (2017)) (b) CD triaxial test data from Klei samples (Data from GLH (2017)) (c)

When predicting shear strength at relatively high stresses, the combination of high friction angle ϕ' and zero effective cohesion ($c'=0$) and the combination of lower friction angle and $c'>0$ can be considered equivalent. This is not the case at low stresses because even a small cohesive term in the shear strength criterion can radically change the results of a stability analysis.

Two options were considered. The values of friction angle ϕ' and effective cohesion c' from Figure 15a were plotted as in Figure 16. As expected, the friction angle decreases with effective cohesion. As per option 1, the Klei effective cohesion was set equal to its average value ($c'=7.7$ kPa) and the friction angle derived from the linear correlation as shown in Figure 16 ($\phi' = 27.4^\circ$).

The raw data available from the Triaxial-CU dataset reported in the Hamburg Geological Survey database (GLH, 2017) were also re-interpreted (i.e. specimens 6 and 7 in Figure 15b). As shown in Figure 17, the triaxial stress path seem to be satisfactorily enveloped by a straight line

passing through the origin, i.e. the Klei seems to show zero effective cohesion. This is further supported by the finding of Quast (1977, pages 134-136).

As shown in Figure 15a, the value of the friction angle associated with zero effective cohesion is $\phi' = 30^\circ$ and this value was adopted in the analysis. However, it should be noted that the null effective cohesion exhibited by the two samples in Figure 17 could just be an artefact of sampling disturbance.

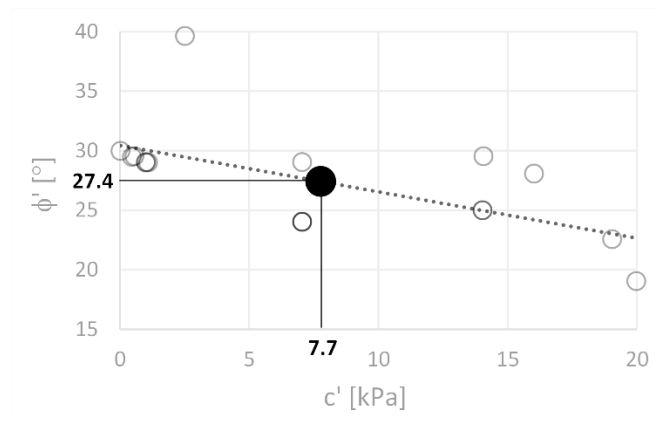


Figure 16. Friction angle ϕ' versus effective cohesion c' derived from CD triaxial test data and average value for friction angle ϕ' and effective cohesion c' .

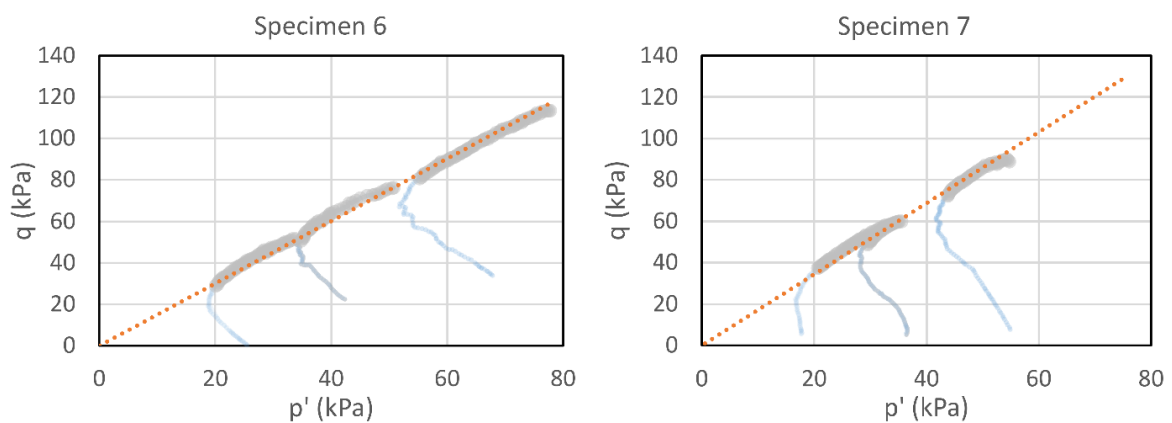


Figure 17. Re-interpreted triaxial Consolidate-Undrained tests of specimen 6 (data from GLH (2017)d) and 7 (data from GLH (2017)e) in figure 19b database (isotropic stress p' versus deviator stress q).

Appendix II – Embodied Carbon for Cobbins Brook Embankment

The Cobbins Brook flood alleviation scheme protects the town of Waltham Abbey in Essex UK and a 1.3 Million Flood Storage Reservoir (FSR) located 2km upstream of Waltham Abbey was constructed in 2009. The earth dam has a maximum height of 7.5m, length of 750 m with 1:3 slopes on both sides except for the 1:6 slope of the spillway on the landside slope. The embankment has been fully constructed using nearby won London Clay compacted to an optimum water content of 21.5% to achieve a maximum air voids of ~5%. Considering the water content and porosity of the compacted materials as reported by Lee et al (2010) and a specific gravity for London Clay of 2.7 according to Monroy et al (2010), the density of the as-compacted material can be estimated in the range 1971-2075 kg/m³ with an average value of 2023 kg/m³.

The carbon footprint associated with the construction phase of the Cobbins Brook flood alleviation scheme has been assessed by Defra (2010). In particular, Table A4.22 of the Defra report lists the tonnes of CO₂ generated for each material and task during the construction phase. The items that are relevant to the flood embankment in the Hamburg area are listed in the table below, with the exception of the item 'Quarried Material (clay + aggregates)' that has been added.

The carbon associated with this item appeared to be out of range (probably miscalculated) and was estimated differently. The embodied carbon associated with the quarried material was assumed to be equal to 0.024 tCO₂ per tonne according to the ICE V3 database (Hammond, 2008) and multiplied by the mass of material forming the Cobbins Brook flood embankment. In turn this mass was estimated in two independent ways:

- i) using the information directly provided by Defra (2010) about the mass of material used to construct the embankment, i.e. 152,000t of clay and 8,300t of aggregates. This leads to a carbon contribution for the quarried material of 3847 tCO₂.
- ii) using the information provided by Lee (2010) about the volume of embankment (~ 56000 m³) and the estimated bulk density of 2023 kg/m³ as shown above. This leads to a carbon contribution for the quarried material of 2718 tCO₂.

The computation of the overall carbon emission for the Cobbins Brook flood alleviation scheme during the construction phase is reported in Table 4. By dividing the total carbon emission for the Cobbins Brook embankment by its volume (56,000 m³), the embodied carbon of a flood embankment can be estimated between 64-84 kg of CO₂e/m³.

Table 4 Carbon emission during construction of the Cobbins Brook embankment. The contribution of quarried material is re-calculated with two different approaches * & **

Subtotal	CO₂ tonnes	CO₂ tonnes
Quarried Material (clay + aggregates)	3847*	2718**
Material Transport	424	424
Plant Emissions	344	344
Personnel Travel	36	36
Portakabins	19	19
Timber	19	19
Waste Removal	7	7
Miscellaneous	4	4
Total	4700	3571

*the amount of quarried material reported by DEFRA/EA (2010) is multiplied by the carbon factor for soil in Hammond (2008), ** the mass of won clay is calculated from the volume and density provided by Lee (2010) and then multiplied by the same carbon factor.

Appendix III – Supplemental Materials

Equation S1 – Water flow equation

$$\frac{\partial}{\partial x} \left[k \frac{\partial}{\partial x} \left(\frac{u_w}{\gamma_w} + z \right) \right] + \frac{\partial}{\partial z} \left[k \frac{\partial}{\partial z} \left(\frac{u_w}{\gamma_w} + z \right) \right] = \frac{\partial \theta}{\partial u_w} \frac{\partial u_w}{\partial t} \quad [S1]$$

x = horizontal coordinate

z = elevation,

u_w = pore-water pressure,

γ_w = unit weight of water,

θ = volumetric water content,

k = hydraulic conductivity (assumed to be isotropic)

t = the time

Equation S2 – Shear strength equation

$$\tau = \left(\sigma + s \frac{\theta - \theta_r}{\theta_s - \theta_r} \right) \tan \phi' \quad [S2]$$

τ = shear strength

σ = normal stress

s = suction

θ = volumetric water content

θ_{sat} = saturated volumetric water content,

ϕ' = friction angle.

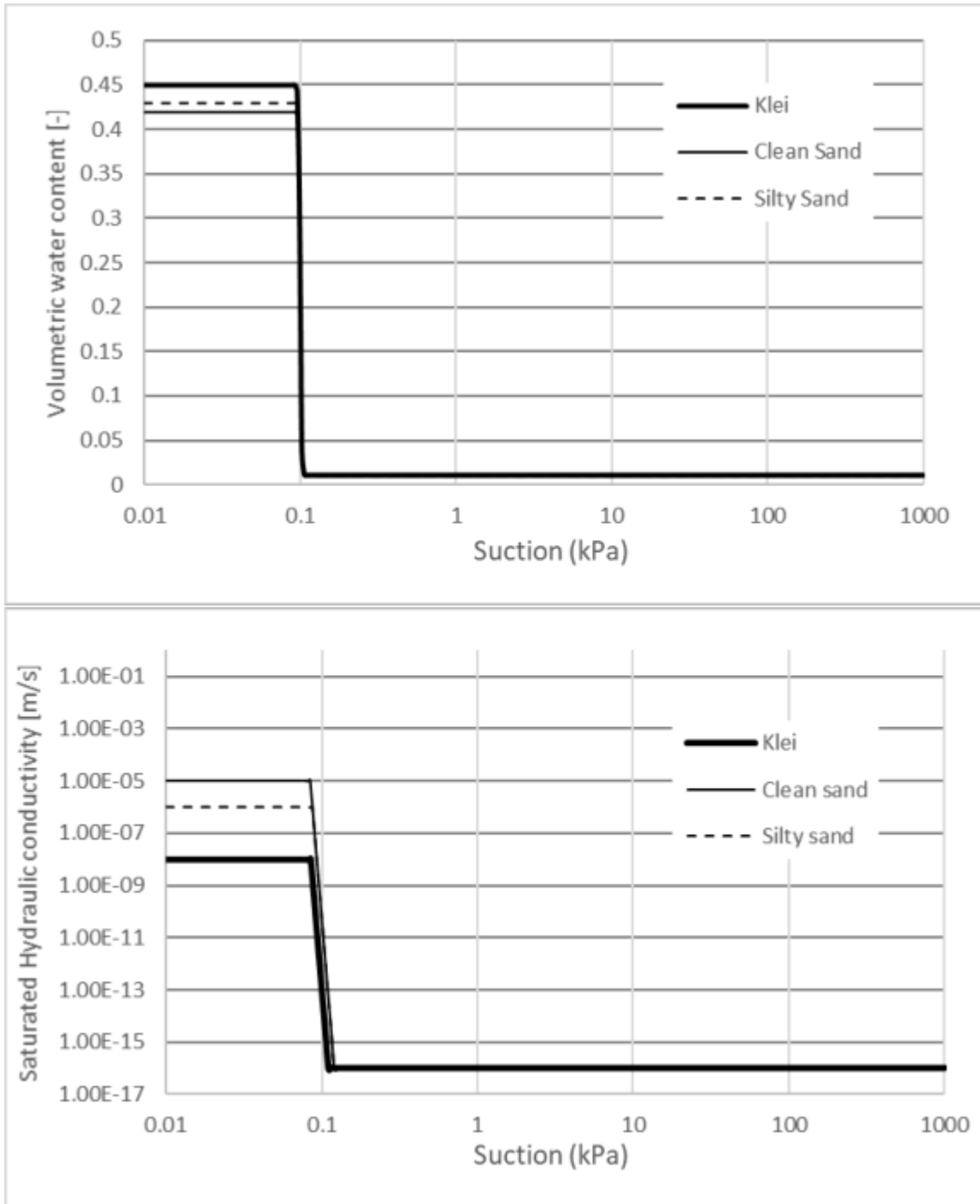


Figure S18 Step functions were adopted for the water retention and hydraulic conductivity functions to simulate dry/saturated conditions.

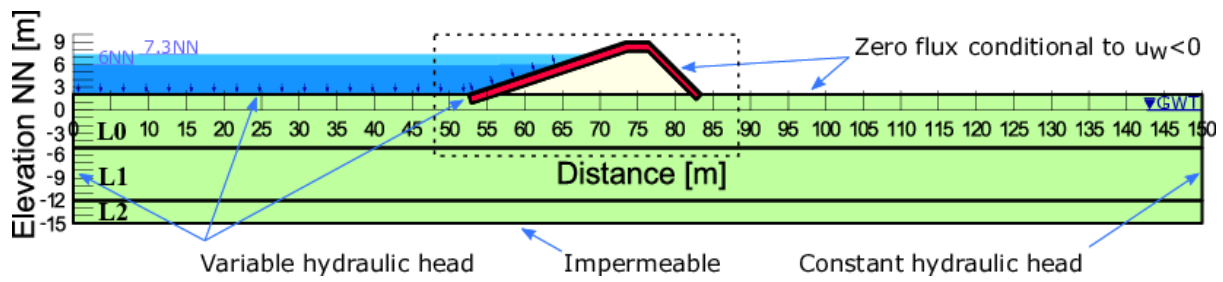


Figure S19 Hydraulic boundary conditions including highest water river level considered for both steady-state and transient.

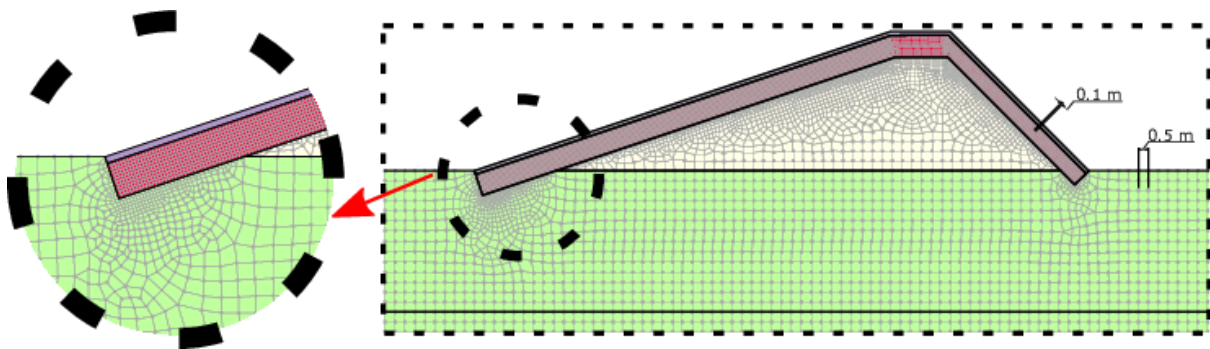


Figure S20 Zoom from Figure S2, Unstructured mesh of quadrilateral and triangular elements. Mesh density in regions where higher gradients develop was optimised by reducing the element size until no significant change in simulated pore-water pressure was observed (~ 0.5 kPa). Elements with size equal to 0.1m were adopted for the embankment cover and elements with size equal to 0.5m were used for the embankment core and foundation layers.

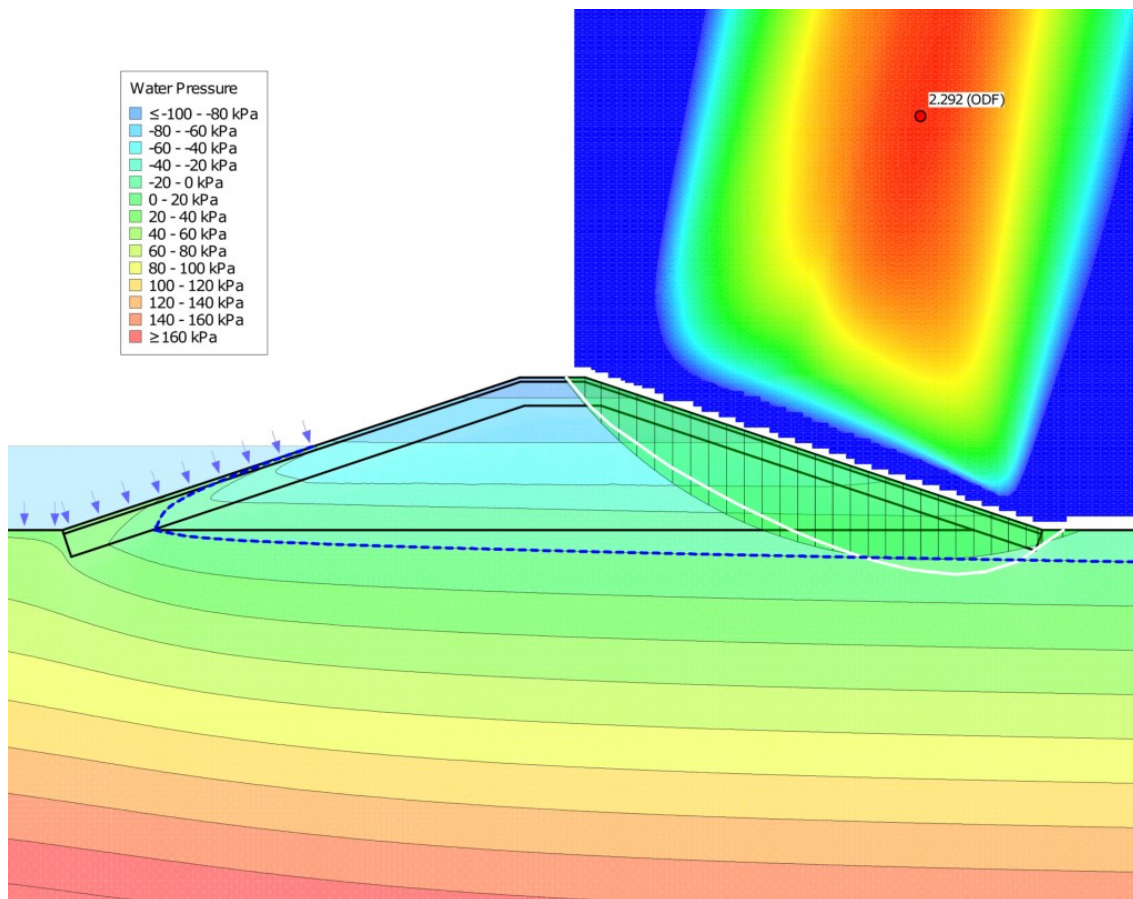


Figure S21 Stability analysis using the modified Bishop method (non-circular failure surface in white). The contour plot shows the Factor of Safety associated with the centre of the initially circular failure surface (before refinement) to check that the centre of the circular failure surface associated with the minimum Factor of Safety falls well within the grid inputted to search the critical failure surface.

Chapter VI: Summary and Conclusions

This thesis presented an experimental investigation of the erosion behaviour of clay, both in saturated and unsaturated states. In addition the thesis has presented a numerical simulation study to promote the adoption of performance-based design in flood embankments upgrading. In the following a summary of the findings of the three main chapters and answers to the research questions presented in the introduction are reported.

RQ-1: What is the erosion detachment mechanism in reconstituted clay?

The erosion detachment mechanism of saturated reconstituted clay have been investigated with a miniaturized jet erosion device (μ -jet) and a imaging system. Direct observation of the detaching unit, identified as 'flake' (the planar dimensions are much more prominent than its thickness), during erosion has been performed and characterized based on sample preparation. A layered fabric within the samples has been identified as genesis of the flake detachment mechanism and further investigated based on clay particle physio-chemical interaction. A micro-mechanical interpretation of the observed detaching unit and layered fabric have been put forward.

RQ-2: Is partial saturation controlling the results of JET erosion test performed in compacted clay?

The unsaturated soil mechanics framework have been used to re-interpret a well known, standard de facto, test to measure erosion: the Jet Erosion Test. Different erosion responses at varying compaction water contents and dry densities were detected using a laser scanner. This enabled the measurement of both scour depth and scoured volume. The experimental study mainly investigated the effect of submergence time. The experimental results have shown that the submerged water jet in clay generates a scour with a relatively complex geometry, made of a step extending over the entire cross-sectional area of the sample and a scour hole localised in the centre of the sample. The depths of both the erosion step and the scour hole evolve with the submersion time in a different fashion depending on the compaction water content. At the same

time, the compaction water content generates different rates and mode of penetration of the waterfront that propagates from the surface of the sample once the sample is submerged in water before the Jet Erosion Test starts. The step developing at the top of the sample was modelled successfully by considering the failure of a horizontal infinite layer subjected to the tangential hydrodynamic stresses generated by the impinging jet. The central scour hole was assumed to be generated by a bearing capacity mode of failure triggered by the normal hydrodynamic stresses and modelled accordingly.

Answering the second research question, yes, by characterizing the transient behaviour of a unsaturated compacted clay is possible to interpret the JET erosion test within a unique framework for unsaturated samples.

RQ-3: Does unsaturated soil mechanics-based design help minimize the material required to upgrade flood embankments?

The numerical simulation work examines the case of flood embankments in the tidal area of the Elbe River in Germany. These embankments require to be retrofitted by raising their crest from 5m to 7m because of the new projection of extreme river levels due to climate change. The conventional 'prescriptive' design consisting of raising the embankment by maintaining the 1:3 inclination of the landside slope was compared with the 'performance-based' design where the inclination of the slope on the landside could be potentially increased up to 1:1, which is shown to be sustainable if partial saturation and transient water flow are considered. Raising the flood embankment with 1:1 landside slope (rather than 1:3) lead to expropriation cost savings of the order of €3.9M/km. For the case of a newly built embankment of 7 m height, the saving would become €4.5M/km. An approximate estimation of embodied carbon suggests that the carbon saving would be of the order of 3,100-4,200tCO₂e/km.

Perspective

The core findings of the thesis is the flake detachment mechanism observed in reconstituted clay together with the layered fabric of the samples identified as genesis of the flake detachment mechanism. This micro scale observation alongside the finding on the effect of submergence time in the Jet Erosion Test at the representative element volume scale need to be incorporated in larger model dealing with the surface erosion of geotechnical infrasturctures. It has been shown that different processes are at play at different scales and that both impact the final

surface erosion. Since such a concept is considered by the author as a starting point for new research rather than a conclusive piece of work, many different topics have been investigated in this thesis. Often not definitive conclusions have been made (e.g. chapter 3) but new approaches or ideas have been tested and have been proven to be promising. Significant amount of work has still to be carried out to test and validate this approach. So far, there are three main limitations of the work presented in this thesis:

1. The findings and observations have been drawn from a cohesive soil prototype, Speswhite Kaolin, although frequently used in the laboratory due to its well documented behaviour and characteristics, is not fully representative of the real world. Testing of more clay types and mixtures with silts and sand would be required to verify the range of applicability of the results presented in this thesis.
2. For the methodology adopted in the Jet testing an invasive method has been used for the determination of the water content, an application of NMR imaging (Nuclear Magnetic Resonance) could solve this issue considering the REV samples are sufficiently large in size.
3. The adoption of the laser scanner to measure the eroded surface lead to the disadvantage of concluding the JET test at each stage and repeat the tests on twin samples. A underwater laser scanner situated in the JET device could solve this issue allowing for continuous measurements of the erosion.